Numerical Assessment of Caprock Integrity in SAGD Operations Considering Mechanical Anisotropic Behavior of Shale Layers

by

Ehsan Rahmati

A thesis submitted in partial fulfillment of the requirements for the degree of

Doctor of Philosophy

in
Petroleum Engineering

Department of Civil and Environmental Engineering
University of Alberta

Abstract

There has been an increasing awareness of the importance of caprock integrity during Steam Assisted Gravity Drainage (SAGD) operations. However, mathematical tools that have been developed for caprock integrity studies have not incorporated an important characteristic of cap shales, which is the anisotropic behavior of the shales. This study focuses on the numerical assessment of the Maximum Operating Pressure (MOP) in SAGD projects accounting for the anisotropic behavior of cap shales. This research demonstrates the importance of capturing shale anisotropy and considering the effect of Natural Fractures (NFs) in the accurate prediction of MOP for SAGD projects.

A coupled hydro-thermo-mechanical model was developed to assess the MOP of SAGD projects. A constitutive model was incorporated and verified to consider the effect of NFs and intrinsic anisotropy of the caprock shale. The coupled numerical tool was validated against field data and utilized to determine the MOP for a SAGD operation. Also, the numerical model was utilized in a series of simulations to investigate the effects of sensitivity of the results to several characteristics of the NFs and intrinsic anisotropy.

Results of the coupled tool show that neglecting NFs and intrinsic anisotropy can result in MOP overestimation. The MOP was found to be highly sensitive to the fracture density, direction, and height. For the case study, results displayed horizontal fractures had minor effect on the MOP while fractures with the dip angle between 25° to 65° had a significantly lower MOP and could not be neglected. Furthermore, results showed that neglecting the intrinsic anisotropy of caprock shales resulted in an overestimation of the MOP by 7% for the case study.

This research incorporated the intrinsic and structural shale anisotropy in the caprock failure analysis model for the first time. Existing numerical models for evaluating the integrity of caprocks during SAGD operations employ isotropic constitutive laws. These models are believed to be deficient in capturing strongly intrinsic and structural anisotropic response of shales and mudstones, which have been well documented in applications other than SAGD studies. The isotropy assumption for the cap shale in caprock integrity analysis can lead to the overestimation of the MOP in SAGD operations. Results of this research can be of significant benefit to avoid choosing high MOPs which could lead to caprock failure in SAGD operations.

Dedication

To my parents

Acknowledgments

I sincerely thank my parents and brothers for their love, devotion, and continued encouragement to gain further education.

I am very thankful to my supervisor, Dr. Alireza Nouri, for having faith in me, for giving me an opportunity to work on this project, for all of his encouragement and support, and for granting me freedom to explore my ideas.

I wish to extend my deep gratitude to my co-supervisor, Dr. Japan Trivedi, for his advice and feedback over the course of this project.

I would also like to thank all of my committee members, Dr. Carlos Lange, Dr. Alireza Bayat, Dr. Dmitry Garagash, and Dr. Lijun Deng, for their valuable suggestions to improve my thesis.

I would like to acknowledge Alberta Energy Regulator (AER) and Natural Sciences and Engineering Research Council of Canada (NSERC) through their Collaborative Research and Development (CRD) Grants Program for providing the funding for this research. Finally, I would like to thank all those who assisted me throughout my research.

Table of Contents

List of Tables

List of Figures

List of Symbols

A = Constant in McLamore and Gray strength criterion

A_s = Surface area which convection heat transfer takes place

B = Constant in McLamore and Gray strength criterion

B_g = Gas formation volume factor

B_o = Oil formation volume factor

B_w = Water formation volume factor

C = Constant in McLamore and Gray strength criterion

c = Cohesive strength

c_b = Bulk compressibility

c_D = Cohesive strength of discontinuity

c_f = Cohesive strength of fracture

C_{ijkl} = Compliance tensor

c_{IR} = Cohesive strength of intact rock

c_r = Rock compressibility

c_{RM} = Cohesive strength of rock mass

c_s = Solid (grain) compressibility

D = Constant in McLamore and Gray strength criterion

E_i = Young's modulus in i^{th} direction

f_i = Body forces

f^s = Shear yield function

f^t = Tensile yield function

G = Shear modulus

g_i = Components of gravitational acceleration (body force)

G_{ij} = Cross-shear modulus

g^s = Shear potential function

GSI = Geological Strength Index

g^t = Tensile potential function

h = coefficient of heat convection

K = Bulk modulus

k = Permeability

k_0 = Initial permeability

K_L = Linear degree of seperation

l = Length of core run

m = Anisotropy type factor

m_b = Material constant in Hoek-Brown model

n = Anisotropy type factor

P_a = Atmospheric pressure

P_c = Confining pressure

P_{CgO} = Capillary pressure between oil and gas

P_{CWO} = Capillary pressure between oil and water

P_p = Pore pressure

$\dot{Q}_{cond}$ = Rate of heat conduction

$\dot{Q}_{conv}$ = Rate of heat convection

q_g = Gas well rate

q_o = Oil well rate

q_w = Water well rate

r_S = Solution gas oil ratio

S_g = Gas saturation

S_o = Oil saturation

S_w = Water saturation

T = Temperature

t = Time

T_s = Surface temperature

T_∞ = Fluid temperature far from the surface

u_i = Displacement components

α_T = Temperature coefficient

β = Constant in Touhidi-Baghini equation

γ_g = Gas specific weight

γ_o = Oil specific weight

γ_P = Plastic shear strain

γ_w = Water specific weight

δ = Kronecker delta

${\varepsilon_{ij}}^e$ = Elastic strains tensor

ε_V = Volumetric strain

θ = Angle between bedding plane and max principal stress

$\theta_{min,c}$ = Value of θ corresponding to the minimum cohesion

$\theta_{min,\varphi}$ = Value of θ corresponding to the minimum friction angle

λ_g = Gas mobility factor

λ_o = Oil mobility factor

λ_s = Constant of proportionality for shear yield mode

λ_t = Constant of proportionality for tensile yield mode

λ_w = Water mobility factor

υ_{ab} = Poisson’s ratio

ξ = Angle between the fracture plane and global horizontal direction

ρ = Fluid density

σ_{ij} = Stress tensor

σ_n = normal stress

σ'_1 = Maximum principal effective stresses

σ'_2 = Intermediate principal effective stresses

σ'_3 = Minimum principal effective stresses

τ = Shear stress

ϕ = Porosity

ϕ_0 = Initial porosity

φ = Friction angle

φ_D = Friction angle of discontinuity

φ_f = Fracture friction angle

φ_{IR} = Friction angle of intact rock

φ_{RM} = Friction angle of rock mass

ψ = Dilation angle

ψ_f = Fracture dilation angle

Chapter 1: Introduction

1.1 Motivation

Alberta has one of the largest proven oil reserves in the world of which 170 billion barrels are heavy oil from oil sands having total area of 140,200 km^2 (ERCB, 2011). Two types of production methods have been used to extract the oil sands reserves: surface mining and in-situ Enhanced Oil Recovery (EOR). The area of surface mineable oil sands is only ~3% of the total oil sands area in Alberta (CAPP, 2011). Thus, several in-situ thermal and non-thermal techniques have been utilized to stimulate and enhance the recovery of heavy oil from deeper oil sands reservoirs.

One of the most important in-situ recovery techniques in Alberta is the Steam Assisted Gravity Drainage (SAGD) method. SAGD operation involves the injection of large volumes of steam into the reservoir, resulting in considerable stress, pore pressure, and temperature changes as well as deformations in the reservoir and surrounding strata. Steam injection into the reservoir increases the pressure and temperature in the reservoir. The outcome is the reservoir rock expansion in the steam chamber and stress alteration in the chamber and surrounding strata. As a result, localized shear and/or tensile fractures can develop in the reservoir and the cap rock.

Having a sealing caprock in SAGD operations is of prime importance for petroleum operators. The vital objective is the prevention of the escape of reservoir fluids and injected steam into the shallower, environmentally sensitive horizons or even to the surface. Subsequent to the catastrophic steam release event at Total's Joslyn Creek SAGD project in May 2006 due to mechanical and hydraulic failure of the caprock, ensuring integrity of caprock has gained even further prominence by the Alberta Energy Regulator (AER) as well as petroleum producers in Alberta, Canada.

Shales comprise the majority of sedimentary rocks that are drilled to reach the hydrocarbon reservoir. Thus, shale research has been at the forefront of research in the petroleum industry (Tutuncu, 2010). Experimental evidence indicates that most sedimentary rocks, particularly shales and mudstones, behave anisotropically (Karakul et al., 2010; Kwasniewski, 1993; Ramamurthy, 1993; Horino and Ellickson, 1970; McLamore and Gray, 1967; Hoek, 1964; Donath, 1964). Shales exhibit strong inherent anisotropy due to the existence of bedding planes and the platelet shape of shale grains. This anisotropy manifests itself in directional dependency of deformation and strength properties (Duveau, 2001). Understanding the anisotropy and its causes is crucial as they strongly influence the reservoir and caprock responses.

Another type of anisotropy, which is called structural anisotropy, has been observed in the caprock (Tutuncu, 2010). Structural anisotropy can be caused by the Natural Fractures (NFs) in shale. Natural Fractures have been observed in SAGD caprocks in Alberta (Chou, 2014). Natural fractures can provide preferential flow paths through the caprock for the escape of bitumen and injected steam and compromise the caprock integrity. These fractures may be triggered and connected to form larger fractures that can compromise the caprock integrity.

These NFs also influence the caprock response by inducing structural anisotropy in the caprock.

Several researchers have studied caprock integrity in SAGD projects assuming isotropic elasto-plastic behavior for the caprock and neglecting the effect of NFs and discontinuities in caprock layers (Smith, 1997; McLellan and Gillen, 2000; Collins, 2007; Chalaturnyk, 2011; Khan et al., 2011; Rahmati et al., 2013). Isotropic elasto-plastic constitutive laws are believed to be deficient in capturing strongly anisotropic response of shale and mudstones. Neglecting intrinsic and structural anisotropy could result in significant overestimation of Maximum Operating Pressure (MOP) in SAGD projects.

In this research, a coupled hydro-thermo-mechanical model was developed for the assessment of caprock integrity in thermal operations. The coupled tool was utilized to assess the MOP in a SAGD case study. The numerical tool was validated against field data and employed to determine the effect of shale intrinsic and structural anisotropy on the pressure associated with caprock breach.

A constitutive model was incorporated in this research to capture the effect of intrinsic anisotropy and the existence of multiple sets of NF in the cap shale. In this constitutive model, a transversely isotropic constitutive model in the elastic range was combined with an anisotropic failure criterion to capture the intrinsic anisotropy of the cap shale. To consider the effect of multiple NF sets, one yield criterion for each single fracture set was added to the constitutive law.

The coupled tool was used in conjunction with the new constitutive model to assess the MOP for a SAGD project. The importance of considering anisotropy in the caprock was demonstrated by comparing the result of the anisotropic and isotropic models. Furthermore, different case scenarios in terms of fracture density, dip angle, height, and number of fracture sets were considered to investigate their effect on the MOP.

1.2 Problem statement

Some progresses have been achieved in the last decade in quantifying the MOP for thermal operations. However, the effect of intrinsic anisotropy and NFs in the cap shale on the MOP in SAGD projects has not been accounted for.

Intrinsic and structural anisotropy have commonly been observed in shale formations around the globe, critically impacting their flow and mechanical properties (Tutuncu, 2010; Chou, 2014). Existing numerical models for caprock integrity assessment have neglected both the intrinsic and structural anisotropy of the cap shale. In this research, a constitutive law capable of capturing both intrinsic and structural anisotropy of shales was coded, implemented and utilized in conjunction with a coupled hydro-thermo-mechanical model for caprock integrity assessment. The model was used in a case study to demonstrate the significance of incorporating shale anisotropy on the MOP.

1.3 Research objectives

The main aims of this research are as follows:

- Incorporate a constitutive law to capture the effect of shale's elasto-plastic intrinsic anisotropy and multiple sets of NFs in the cap shale on the MOP. The constitutive model has to be robust to allow handling a coupled hydro-thermo-mechanical field-scale model for multiple years of SAGD operation with significant number of elements (around 100,000 elements) in a reasonable time.

- Implement the constitutive model in an integrated geomechanics-fluid flow workflow for caprock integrity analysis and assess the MOP. This aim is attained by developing an iteratively coupled hydro-thermo-mechanical model to capture important phenomena in the SAGD reservoir and caprock.
- Investigate the influence of caprock anisotropy on the MOP, and the design of SAGD operations.
- Investigate the effect of different parameters including height, density, and number of NF sets on the MOP of SAGD reservoirs.

These objectives are achieved by coding and implementing an anisotropic constitutive model, validation and the verification of the constitutive model, development of a coupled hydro-thermo-mechanical model, validation of the coupled tool against field data, and the investigation of the effect of anisotropy (intrinsic and structural) on the MOP in SAGD reservoirs.

1.4 Research hypothesis

The injection of high temperature and pressure steam into the reservoir increases the reservoir temperature and pressure causing vertical and horizontal expansion of the oil sands. The reservoir expansion results in the variation of stresses in and around the reservoir.

Figure 1.1 presents schematically the vertical stress in a horizontal cross section in the caprock. Vertical stress directly above the steam chamber increases due to the expansion of the reservoir oil sands in the vertical direction. As the amount of the overburden weight on each horizontal cross section is constant, the increase of the vertical stress above the steam chamber is compensated by the decrease of the vertical stress at the flanks of the steam chamber.

Figure 1.2 shows schematically the horizontal stress profile for a vertical cross section. The lateral expansion of the steam chamber due to the steam injection results in an increased horizontal stress at the reservoir level. The increase in the horizontal stress at the reservoir interval is compensated by the decrease of the same at the over- and underburden strata. The increased vertical stress and decreased horizontal stress in the caprock lead to higher shear stresses in the caprock and increase the potential for shear failure across the caprock.

For the same vertical stiffness, anisotropic caprocks possess higher stiffness in the bedding direction. A hypothesis for this research is that the amount of drop in horizontal stresses is more substantial for anisotropic caprocks due to their higher horizontal stiffness. Therefore, higher shear stresses develop in the anisotropic compared to the corresponding isotropic caprock during the SAGD operation resulting in a lower MOP.

Furthermore, the NFs in the caprock decrease the strength properties of the cap shale. Stress alterations in the caprock during the steam injection could trigger the NFs and compromise the caprock integrity. The existence of NFs could decrease the MOP of SAGD reservoirs and should be taken into account.

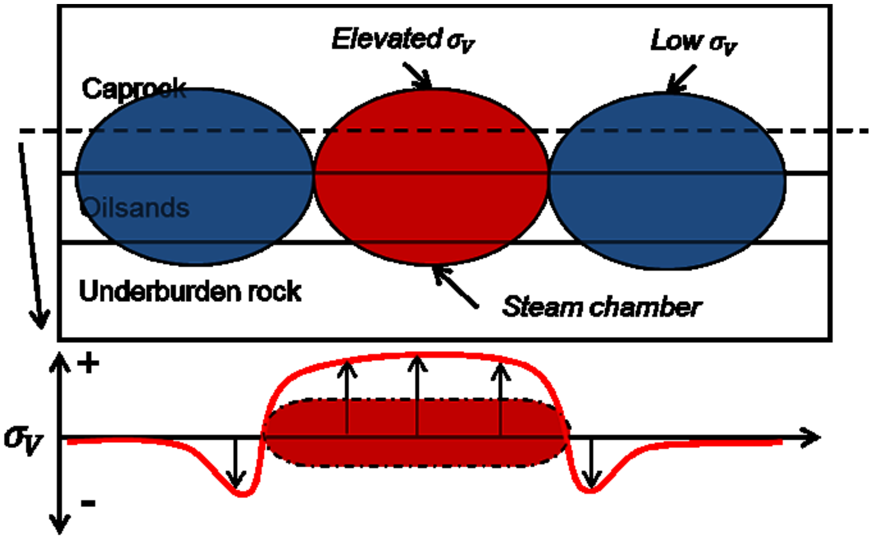

Figure 1.1 Expected vertical stress profile due to injection

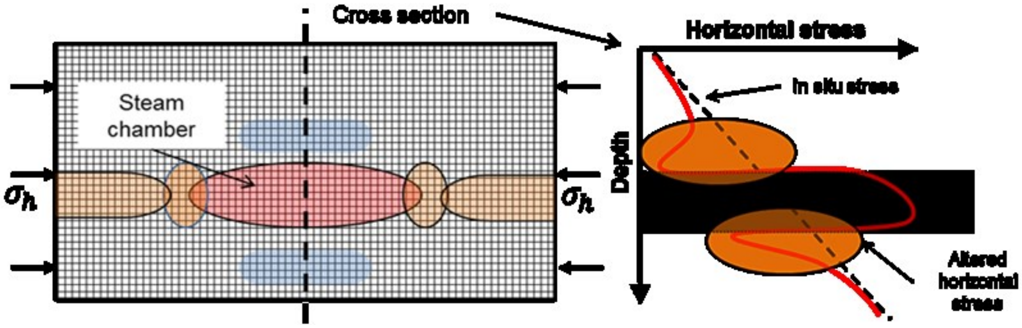

Figure 1.2 Expected horizontal stress profile due to injection

1.5 Thesis outline

This thesis is organized in five chapters:

Chapter 1 (the current chapter) provides the background and the scope of this research.

Chapter 2 contains a literature review on SAGD phenomena with particular emphasis on the caprock integrity assessment and the anisotropic behavior of caprock shales. This review also presents different factors that influence the mechanical properties of shales, and the existing constitutive models for anisotropic rocks. A review of existing numerical models for caprock integrity assessment in SAGD operations is also presented. The nature of shale anisotropy is reviewed and observations of the NFs in Alberta shales and their origin are discussed in this chapter.

Chapter 3 presents the theoretical background and verification of the coupled tool and the anisotropic constitutive law. This chapter also presents the governing equations for SAGD analysis and describes the coupled hydro-thermo-mechanical model and the constitutive law for this research along with their verification.

Chapter 4 presents the validation of the coupled hydro-thermo-mechanical model, the caprock integrity analysis for a SAGD project considering only the intrinsic anisotropy of the cap shale, and the comparison of the results with the corresponding case with isotropic cap shale.

Chapter 5 numerically investigates the effect of both intrinsic anisotropy of shale layers and NFs on the MOP of SAGD reservoirs. A sensitivity analysis is conducted to study the effects of fracture parameters such as fracture height, density, dip angle, and number of fracture sets on the MOP.

Chapter 6 summarizes the major findings of this research and presents suggestions for future research on this topic.

1.6 Significance of the work

There is 1.6 to 2.5 trillion barrels of oil in place in western Canada. However, most of it is embedded in oil sands and hence difficult to be produced with conventional methods (Jun et al., 2012). SAGD is one of the most popular techniques to produce oil from these oil sands. In Northern Alberta, Canada, caprock integrity is an important environmental concern in heavy oil production. On May 18, 2006, steam injection at Joslyn Creek thermal bitumen project induced a catastrophic disaster due to the loss of caprock containment. This resulted in a steam release to the ground surface, forming a 75 m by 125 m surface crater, throwing rocks nearly 300 m away from the release point, and creating 1-km high dust plume (ERCB, 2010). Increased attention was given to ensure caprock integrity after this catastrophic incident.

On January 3, 2009, a surface release of bitumen emulsion was discovered in the Primrose East development area operated by the Canadian Natural Resources Limited's (CNRL) (ERCB, 2013). Alberta Energy Regulator (AER) is of the view that the caprock was likely breached by high-pressure steam injection due to the failure of a series of pre-existing fractures and faults (ERCB, 2013).

Most of the numerical models that have been developed to study caprock integrity are based on isotropic and homogenous assumptions for the cap shale. Shale anisotropy and existence of NFs are important features that should be accounted for in the formulation of constitutive models, particularly in caprock integrity studies. Shale layers exhibit inherent anisotropy due to their micro and macro structure and also they show structural anisotropy due to the existence of NFs. Isotropic models for shale layers can lead to incorrect results and MOP overestimation for SAGD operations.

Using the proposed constitutive model in conjunction with the hydro-thermo-mechanical coupled tool can significantly improve the stress and deformation predictions within the reservoir and the caprock. The proposed model increases the accuracy of calculated MOP for SAGD projects.

This research provides evidence to highlight the need to consider the influence of anisotropy in the design of SAGD operations and the analyses of caprock integrity. The modelling and result analysis in this research enhances the understanding of the role of shale anisotropy on caprock deformation and failure during SAGD operations. Such improved understanding can help reservoir engineers in better reservoir management and field development.

This research can be of significant benefit in optimizing engineering performance, maintaining safety and minimizing environmental footprint.

1.7 Sign conventions

The following sign conversions are used in this thesis.

- Stress: Positive stresses indicate tension; negative stresses indicate compression.
- Strain: Positive strains indicate extension; negative strains indicate contraction.
- Pore pressure: Fluid pore pressure is positive in compression.
- Gravity: Positive gravity pulls the mass of a body downward.

Chapter 2: Literature Review

2.1 Introduction

This chapter presents a brief literature review on the geological aspects of Alberta oil sands and surrounding strata, a few cases of caprock failure in thermal projects, SAGD-induced stress alterations in the SAGD reservoir and surrounding strata, and the potential causes of caprock integrity breach. A review is also presented on the comparison of different coupling methods between geomechanical and hydro-thermal calculations and different exiting models for caprock integrity assessment.

This chapter also contains a literature review of the mechanical behavior of shales and discusses the effect of different parameters including temperature, confining pressure, mineralogy, and swelling on the mechanical behavior of shales. Also, existing constitutive models that have been designed to capture the anisotropic behavior of shales are reviewed.

Existence of NFs could be the source of structural anisotropy in the caprock. A literature review on the origin of NFs in Alberta, Canada is also presented in this chapter.

2.2 Caprock definition

Caprock is an impermeable layer of rock above a hydrocarbon reservoir, providing a seal in containing the reservoir fluids or gases. Caprock formation is usually located immediately above or near the edge of reservoir.

Caprock integrity refers to the preservation of the physical boundary created by the overburden layer directly above a formation that is under increased pressure due to the injection of a substance not normally present in the formation. This injection causes an increase in the pressure that, if greater than the loading capacity of the overburden layer, can cause the breach of the caprock allowing for the release of pressurized gas and/or produced fluids to the surface.

2.3 Geological overview of Alberta oil sands

Alberta oil sands are located in three major deposits in Northern Alberta. They include Athabasca, Cold Lake, and Peace River oil deposits. Below, we focus on the geology of Athabasca oil sands, and from this region, we zoom on MacKay River area, which is the area of focus in the case study for this research.

The following geological description has been adopted from Petro-Canada Corp. (2005a). Cretaceous McMurray formation contains the main oil sands deposits in the MacKay River area. McMurray formation in this area is confined from the top with Clearwater formations and from the bottom with Beaverhill Lake limestones. The Glacial Quaternary Deposits are laid on top of the Clearwater formations. Stratigraphic column of MacKay River area is presented in

Table 2.1.

Clearwater formation in the MacKay River area is divided to Wabiskaw member (shale/sandstone) and Clearwater shale. The Wabiskaw member (which is divided to Wabiskaw A, B, C, and D) is located under deposits of Clearwater shale.

Pleistocene deposits are laid on top of the Clearwater formation and have thickness of up to 70 m.

Table 2.1 General stratigraphic column in general MacKay River region, Alberta (after Petro-Canada Corp., 2005a)

Quaternary		Holocene Deposits Pleistocene Glacial Drift		
Cretaceous	Early	Mannville Group	Clearwater Fm	Clearwater shale Wabiskaw A Wabiskaw B Wabiskaw C Wabiskaw D
			McMurray Fm	Middle: Estuarine Lower: Continental
Devonian	Late	Beaverhill Lake Group		
	Middle Early	Elk Point Group	Watt Mountain Prairie Evaporite Winnpegosis/Keg River Contact Rapids Basal Red Beds Granite Wash	
Precambrian		Precambrian Basement		

2.3.1 Devonian sediments

In the MacKay River area, the Devonian formation consists of limey shale and argillaceous carbonate of Waterways formation in the Beaverhill Lake Group (Petro-Canada Corp., 2005a). Devonian formation in this area is impermeable; therefore, it forms an effective base rock for the SAGD operation. Furthermore, this formation does not contain bitumen resources in this area (Southern Pacific Resource Corp., 2011).

2.3.2 McMurray formation

The McMurray formation is typically divided into the lower, middle, and upper McMurray in the Athabasca oil sands area (Petro-Canada Corp., 2005a). However, McMurray formation is mainly composed of upper McMurray in the MacKay River area. The upper McMurray member contains the main oil sands deposits in this area (Southern Pacific Corp., 2011).

The upper member of McMurray formation shows the highest evidence of marine influence on sedimentation in comparison with lower and middle McMurray. Also, the upper McMurray shows more regionally extensive deposition pattern and more trace of fossils (Southern Pacific Corp., 2011).

2.3.3 Clearwater formation

Clearwater formation is divided into the Wabiskaw and Clearwater members.

2.3.3.1 Wabiskaw member

Wabiskaw member in MacKay River area is divided into Wabiskaw A, B, C, and D. In the MacKay River area, the Wabiskaw D thickness ranges from 0 to 22 m and consists of sandstone. Wabiskaw C consists of sandstone, shale, and siltstones. The Wabiskaw C thickness varies between 1 to 5 m in this area. Wabiskaw B and A members are mainly composed of shale and have thickness of 6 to 8 m and cap the Wabiskaw C sandstone unit (Petro-Canada Corp., 2005a).

2.3.3.2 Clearwater member

In the MacKay River area, most of the Clearwater member consists mainly of shale and minor siltstone. Clearwater shale is laid directly on top of the Wabiskaw member. Clearwater shale has a thickness between 17 to 86 m in the MacKay River area (Petro-Canada Corp., 2005a).

2.3.3.3 Quaternary Deposits

Quaternary Glacial Deposits have been deposited above the Clearwater shale. The Glacial drift consists of clay, silt, and sand and has 15 to 25 m thickness (Petro-Canada Corp., 2005a).

2.4 Caprock failure cases in thermal projects in Alberta, Canada

Several cases of caprock failure have been reported in Alberta. In this section, these incidents are listed in chronological order.

- Texaco/ Fort McMurray/ 1980s

In the 1980s, Texaco created a geyser of bitumen and salt water in Fort McMurray area (Nikiforuk, 2014). There is a little literature on the blowout.

- Imperial Oil/ Cold Lake/ 1988

In the Cyclic Steam Stimulation (CSS) operated by Imperial Oil Company, high pressure and temperature steam broke through an evaluation well. The incident resulted in the spread of 6,000 barrels of oil and 4,000 barrels of toxic water in the forest. The blow-out contaminated shallow aquifers in the area with chlorides (Nikiforuk, 2013).

- Total/ Joslyn Creek/ 2006

On May 18, 2006, a loss of caprock containment occurred at the Total Joslyn Creek SAGD project located about 60 km north of Fort McMurray, Alberta. This incident resulted in a steam release at ground surface, which lasted about 5 minutes. The incident formed a 75 m by 125 m surface crater, and threw rocks nearly 300 m away from the release point (ERCB, 2010).

- CNRL/ Primrose East/ 2009

At Primrose East, Canadian Natural Resources Limited's (CNRL) injected high-pressure steam into 80 wells at four pads in a CSS operation. On January 3, 2009, a surface release of bitumen emulsion was discovered in the Primrose East area (ERCB, 2013). Bitumen broke through to the surface at two well sites. The operator removed more than 12,000 tons of bitumen, water, snow, and muskeg to a landfill (Nikiforuk, 2013).

2.5 Geomechanical phenomena in the reservoir and surrounding strata

The injection of steam into the SAGD reservoir may trigger several subsurface and ground surface phenomena as schematically illustrated in Figure 2.1.

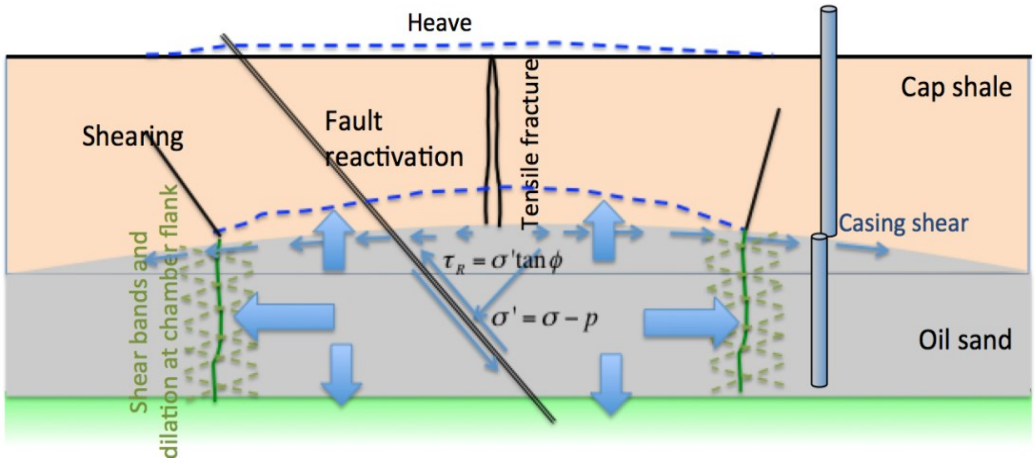

Figure 2.1 Possible geomechanical phenomena in SAGD (after Rahmati et al., 2014)

Thermal expansion of reservoir oil sands is an important aspect of SAGD operations. Influx of heat in the reservoir causes vertical and lateral expansion of the oil sands, transferring strain and deformation to the surrounding strata.

Typically, conductive thermal expansion of the saturating fluids at the flanks of the steam chamber exceeds that of the sand pore space, resulting in increased pore pressures, reduced effective stresses, and increased potential to the shear yield at the reservoir flanks. Further, thermal expansion of the oil sands alters the total stress in the lateral direction due to the restraint against lateral deformation by the side-burden. The lateral stress increase at the reservoir interval is compensated by the lateral stress decrease at the cap and base rock intervals. Increased pore pressure, induced lateral stresses, and decrease in the vertical stress at the side burden increase the shear stresses and this may result in shear yielding and dilative deformation at the flanks of the steam chamber.

The reservoir expansion is also partially resisted in the vertical direction resulting in an increase in the vertical stresses in the cap rock and some surface heave. The increase in vertical stress above the steam chamber is compensated by the vertical stress decrease at the reservoir flanks, a phenomenon called thermal jacking (Collins, 2006).

The thermal conduction of reservoir heat into the cap shale increases the pore pressures there. The Mohr circle diagram in Figure 2.2 demonstrates the effect of increasing fluid pressure on the effective stress state in the caprock. From the figure, it is obvious that increasing fluid pressure reduces effective normal stress and shifts the Mohr circle to the left. The increased pore pressure combined with the increased vertical stress and reduced lateral stress in the caprock increases the shear stress. Shear failure occurs once the circle intersects with the envelope. The caprock shear strength must withstand the shear stresses developed by the SAGD operation in order to sustain the caprock integrity throughout the development procedure. Furthermore, decreased lateral stresses in the caprock increases the risk of tensile failure in the caprock. Another potential hazards resulting from these induced stress changes is the reactivation of existing faults or NFs and inducing new fractures, which may breach the hydraulic integrity of the caprock that bounds the reservoir.

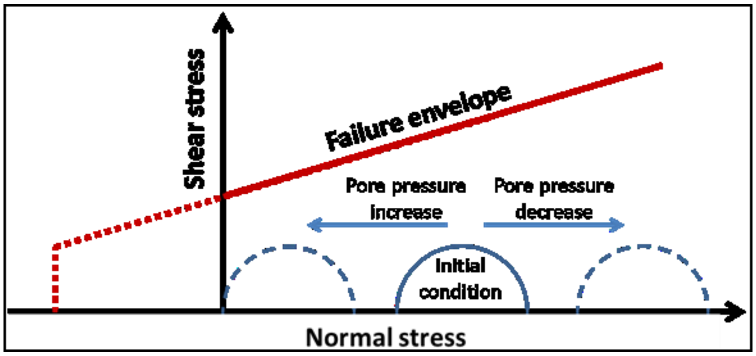

Figure 2.2 Effect of pore pressure increase/decrease associated with injection/production on Mohr’s circle

2.6 Existing models for the analysis of stress variations during reservoir operation

There are two main groups of models for stress analysis within and around reservoirs: semi-analytical models and numerical models. Semi-analytical models implement analytical solutions accompanied with numerical integration procedures to find the stress distribution throughout a field. These models are based on simplified geometrical and fluid flow assumptions, and are usually developed using the assumption of linear poro-elasticity for the reservoir and surrounding rocks (e.g., Segall, 1985).

To analyze more complicated reservoirs, accounting for more realistic geometries and rock/fluid behavior, the use of numerical models is required. Numerical models use discretization methods in both the space and time domains and solve the resultant equations to find displacements, strains, fluid pressure, and stresses. The most important advantages of numerical models are their ability to model discontinuities, complex reservoir geometries and fluid flow.

2.6.1 Semi-analytical analysis

Although semi-analytical models are not able to capture some of the complexities of real problems, usually they are faster and the solution process is more stable than numerical models. Semi-analytical solutions for poro-elastic stress and strain fields induced by subsurface fluid pressure changes are useful because of their relative ease of implementation and their suitability for parameter sensitivity analyses (Wong and Lau, 2008), which facilitates gaining an insight to the physics of the problem. These methods generally try to solve the poro-elastic equilibrium equations which, in their general form, are (Segall, 1992):

$$G\nabla^2 u_i + \frac{G}{1-2\nu}\frac{\partial^2 u_j}{\partial x_i \partial x_j} - \alpha\frac{\partial P_p}{\partial x_i} + f_i = 0 \qquad (1)$$

where u_i are the displacement components, G denotes the shear modulus, ν is the Poisson’s ratio, Pp is the pore pressure and f_i represents body forces. There are four types of semi-analytical models proposed by different researchers: (1) theory of strain nuclei, (2) theory of inclusions, (3) theory of inhomogeneity, (4) borehole stability model.

2.6.1.1 Theory of strain nuclei

One of the first solutions for homogeneous, poro-elastic media was derived using the “nuclei of strain” concept (Love, 1944; Mindlin and Cheng, 1950). This model was used by Geertsma (1966) to find the subsidence of reservoirs where the pore pressure change within the reservoir was considered constant over the entire reservoir. Wong and Lau (2008) also used this theory to study the observed ground surface heave resulting from steam injection in Cold Lake oil sand reservoir in Alberta, Canada.

Rahmati et al. (2013) applied the inverse of nuclei of strain concept to study caprock integrity in MacKay River SAGD operation located in Alberta, Canada. In this study, the nucleus-of-strain inversion formula was coded into a computer program to calculate the reservoir volumetric strains, using heave data at the surface. Then, the reservoir volumetric strains were used in a forward model to calculate stress alterations in the surrounding strata (Rahmati et al., 2013).

Among several restricting assumptions in the theory of strain nuclei is the uniform properties for all strata above the reservoir.

2.6.1.2 Theory of Inclusions

According to Eshelby (1957), an inclusion is a region in a homogeneous isotropic elastic medium that would undergo an arbitrary strain if it was unbounded, but due to the constraint imposed by the matrix that surrounds it, the strain field within it, is modified. In his well-known papers on this subject, Eshelby (1957, 1959) showed that the inclusion problem is equivalent to solving the equations of elastic equilibrium for a homogeneous body with a known body force distribution.

Segall and Fitzgerald (1998) suggested using the theory of inclusions for an ellipsoidal inclusion (i.e., reservoir) in a full-space, to evaluate the possibility of fault reactivation within a reservoir during its depletion. For an axisymmetric reservoir with a thickness considerably less than its lateral dimensions, they proposed using a formulation for stress change within a reservoir given by Mura (1982). They applied this formulation to study the induced stress change within the Ekofisk reservoir. The main limitations of this model are: surrounding rock that extends to infinity in all directions, a very particular form for the reservoir geometry (i.e., elliptical), and identical material properties for both reservoir and surrounding rock.

2.6.1.3 Theory of Inhomogeneity

The inability to account for material property contrasts is a key limitation of the previously discussed methods. Most reservoirs have remarkably different mechanical properties than the surrounding rock. The contrasts between the reservoir and surrounding rock may significantly affect the magnitudes of induced stresses (Khan et al, 2000).

When the inclusion (i.e., reservoir) and matrix (i.e., surrounding rock) have different elastic properties, the inclusion is referred to as an inhomogeneity. Eshelby (1957) showed that the problem of an ellipsoidal inhomogeneity with constant Eigen-strains can be transformed into an equivalent inclusion problem.

2.6.1.4 Borehole stability model

Chen and Teufel (2001) used a plane strain model which had been proposed by Ochs et al. (1997) for the the assessment of stress alterations due to production from an openhole within a horizontal, elastic, isotropic and homogeneous layer with impermeable upper and lower boundaries. Integration of two-dimensional Green functions was applied for solving the problem.

Considering the fact that the method was developed for a transient fluid flow-stress coupling condition around a borehole, it looks too local to be applied to large reservoirs. In addition, there are some important, inconvenient assumptions for the model. One important fact is that the reservoir in this model is of cylindrical shape with unit thickness, neglecting the vertical compaction/expansion of the reservoir.

2.6.2 Numerical analysis

Numerical analysis allows obtaining more accurate solutions by relaxing many assumptions that are necessary in analytical models of complex multi-physics problems.

A numerical study of caprock integrity in a non-thermal polymer flooding project was carried out by Ansari et al. (2012). They presented a case study of hydraulic and mechanical integrity of Wabiskaw caprock for multiple injection scenarios. They concluded that coupled reservoir-geomechanical modeling is necessary for predicting caprock failure (Ansari et al, 2012).

Jun et al. (2012) applied a coupled reservoir-geomechanical model to find the potential for tensile and shear failure associated with high pressure-temperature steam injection into a reservoir. They concluded keeping the injection pressure below the caprock fracturing pressure does not guarantee the caprock integrity and other failure modes should also be checked.

Other notable numerical studies of caprock integrity in the SAGD context include Uwiera-Gartner et al. (2011), Zhang et al. (2012), Walters and Settari (2012), and Khan et al. (2010). Table 2.2 lists some of the numerical studies of caprock integrity in different types of projects around the world. In these studies, the caprock is assumed to be isotropic.

It is well known that the shales exhibit significant anisotropy with respect to stiffness and strength (Donath, 1964; Hoek, 1964; McLamore and Gray, 1967; Horino and Ellickson, 1970; Kwasniewski, 1993; Ramamurthy, 1993; Karakul et al., 2010). Hence, isotropic models are believed to be deficient for use in the simulation of anisotropic caprock behavior.

Table 2.2 Different numerical models in caprock integrity studies

Author	Context	Coupling method	Failure criterion
Ansari et al., (2012)	Polymer flooding	Coupled	Mohr-Coulomb
Uwiera-Gartner et al., (2011)	SAGD	Coupled	Mohr-Coulomb
Zhang et al., (2012)	Waterflooding	Non-coupled	Linear Elastic
Walters et al., (2012)	SAGD	Iteratively coupled	Mohr-Coulomb
Jun et al. (2012)	SAGD	Iteratively coupled	Mohr-Coulomb
Khan et al. (2010)	Carbon storage	Iteratively coupled	Mohr-Coulomb
Khan et al. (2011)	SAGD	Iteratively coupled	Mohr-Coulomb

Current techniques for coupling fluid flow and geomechanical analysis include the classical, one-way coupling, iterative coupling, and fully coupled approach. The following discussion on the suitability of these approaches is based on Li and Chalaturnyk (2006) and Gutierrez et al. (2001).

The classical approach is the most simplistic coupling method by including the rock compressibility in the flow equations to consider the solid-fluid interaction.

The one-way coupling approach involves no feedback of changes in the reservoir porosity and permeability from the geomechanical simulator into the fluid flow simulator. The solution in this method is fast but accurate solutions cannot be guaranteed.

In the iterative coupling approach, fluid pressures calculated by the reservoir simulator are transmitted to the geomechanical simulator that computes stresses and strains which are then fed back into the flow simulator to alter the permeability and porosity. The deformation and flow calculations are performed in several iterations for each time step until the solutions converge within a tolerance. The solution then moves to the next time step.

In the fully coupled approach, displacements, pressures, and saturations are calculated simultaneously. The fully coupled approach provides the most accurate solutions. However, it is computation demanding and can present severe convergence problems (Dusseault and Rothenburg, 2002; Settari, 2005).

Tran et al. (2005) indicated that the "iterative coupling method is the most preferable method for field-scale simulation" so far. Settari (2005) also concluded that when "there is convergence on the iterative coupling process, the solution is similar to the one obtained by a fully coupled simulation". Samier et al. (2006) also commented about fully coupled systems and highlighted that the "feasibility and accuracy of such simulators, as far as complex and large-scale reservoir systems are concerned, have yet to be proven". Settari (2005) concluded that the "most appropriate method should allow the incorporation of the physics of the problem". For example, in the cases of elastic-plastic problems with history matching, a tighter coupling should be used, i.e., an iterative coupled solution.

Tran et al. (2005) introduced a porosity formula that improved the accuracy of the coupling and reduced the number of iterations to converge. However, in his formula a simplifying assumption is that the pore volume before and after the application of heat is considered constant. For the choice of coupling method,

2.7 Shales mechanical behavior

In this section, several aspects of the shale mechanical behavior are discussed. These include mechanical anisotropy, strain softening response, and shale swelling due to exposure to water.

2.7.1 Mechanical anisotropy of shales

Almost 80% of sedimentary rocks drilled for hydrocarbon production are shales (Tutuncu, 2010). Shales mainly consist of clay minerals and quartz with feldspar, carbonates, phosphates, and pyrite also being common inclusions (Potter et al., 2005). The clay platelets (Figure 2.3) at the micro- and macro-scale offer a key source of intrinsic anisotropic characteristics to shales (Tutuncu, 2010).

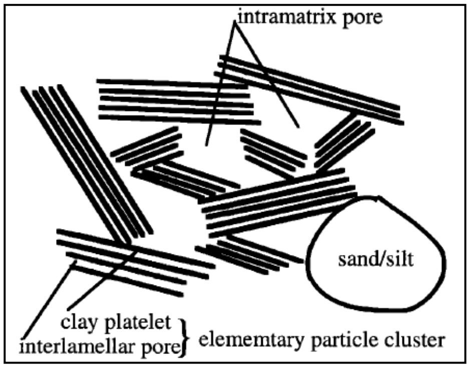

Figure 2.3 Shale fabric structure (after Wong, 1996)

Intrinsic (fabric) anisotropy in shale is generated by the preferred orientations of the clay matrix, shape/distribution of organics, and alignment of elongated fossils. The aggregates of aligned clay minerals can be observed under Scanning Electron Microscope (SEM) (Sone, 2012).

The existing experimental evidence (Donath, 1964; Hoek, 1964; McLamore and Gray, 1967; Horino and Ellickson, 1970; Kwasniewski, 1993; Ramamurthy, 1993; Nasseri et al., 2003; Colak and Unlu, 2004; Karakul et al., 2010) indicates that most sedimentary and metamorphic rocks, especially shales, display a strong anisotropy of strength. Rocks flow and recrystallize under new tectonic stresses and form weak foliation planes. These planes of weakness (i.e. schistosity and foliation) affect the strength and deformational behaviors of rocks with orientation of applied stresses (Saeidi et al., 2014). Hence, these types of rocks usually exhibit some preferred orientation of fabric or possess distinct bedding planes, which result in transversely isotopic behavior at the macro-scale (Lo et al., 1986).

Donath (1964) investigated the fracture strength of shale and slate from samples cored at various orientations relative to the cleavage plane. He showed that the strength parameter as well as the deformation characteristics of the material is highly dependent on the orientation of anisotropy with respect to the principal stress directions. He also showed that the cohesive strength and the coefficient of internal friction were functions of the anisotropy.

Chenevert (1965) determined the variation of the elastic constants, Young's modulus and Poisson's ratio, for three types of laminated rocks. He determined that there was insignificant variation in Young's modulus within the plane of anisotropy (bedding plane) but considerable variation in Young's modulus between this plane and planes perpendicular to the lamination.

McLamore and Gray (1967) performed series of undrained triaxial tests on different shale and slate samples. They concluded that the compressive strength behavior of anisotropic rocks is a function of both the effective confining stress and the orientation of the plane of anisotropy with respect to the applied stress. They also stated that the anisotropic behavior tends to decrease with increasing effective confining stress. Figure 2.4 presents the peak deviatoric stress as a function of the angle between the maximum principal stress and the lamination direction (θ). The minimum strength for this sample occurred at θ angles close to 45°.

Figure 2.5 shows stress-strain behavior for different confining stresses in different directions for a shale sample (McLamore and Gray, 1967).

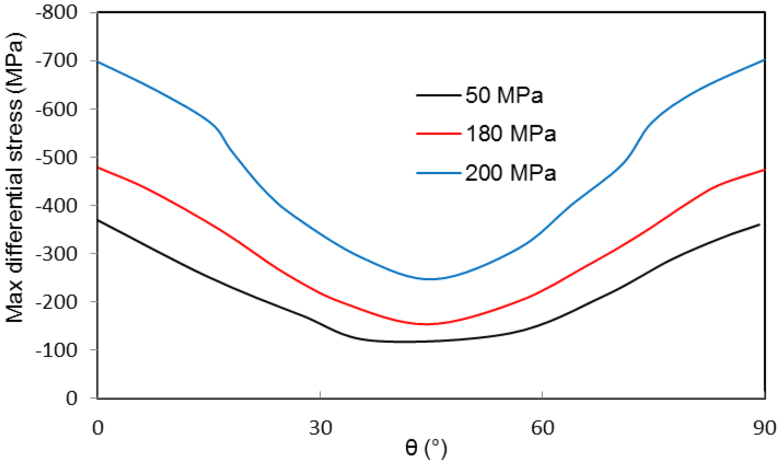

Figure 2.4 Variation of the peak deviatoric stress for triaxial compression test with the core plug direction (after McLamore and Gray, 1967)

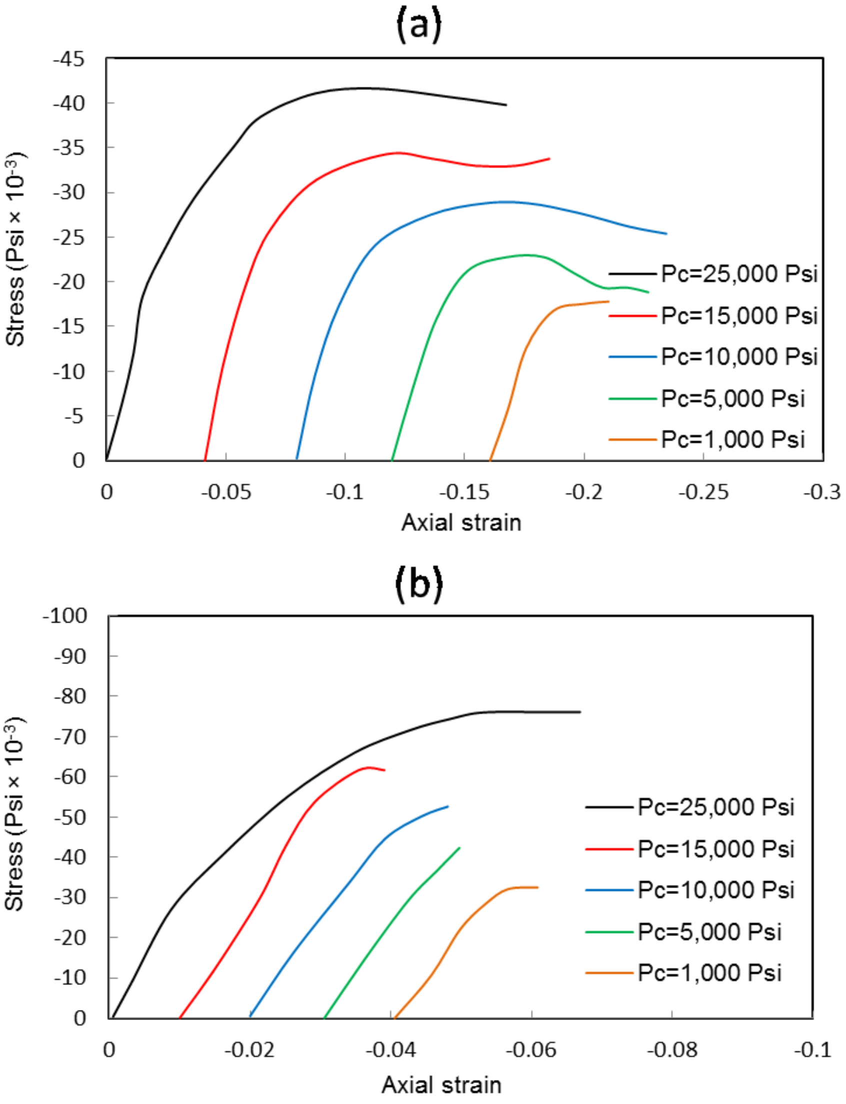

Figure 2.5 Stress-strain curves for a shale sample for various confining pressures: (a) θ=10°, (b) θ=90° (after McLamore and Gray, 1967)

Gautam and Wong (2006) performed a series of drained triaxial tests and confined torsion tests on Colorado shale core samples, taken from Alberta, to investigate transversely isotropic stiffness parameters at small strain deformation. They concluded that Colorado shale could be approximated by a transversely isotropic elasticity model at small strain. For small strain (less than 1%), the Colorado shale is anisotropic with an anisotropy ratio $E_h/E_v = 1.98$ and $G_{hh}/G_{vh} = 1.86$ and 1.5 for those second White Specks and Westgate formations, respectively. Table 2.3 shows the results of triaxial tests conducted for the investigation of anisotropy for Second White Specks and Westgate of Colorado shale group (Gautam and Wong, 2006).

Table 2.3 Results of triaxial tests for the investigation of anisotropy (after Gautam and Wong, 2006)

Test No.	Formation	Depth (m)	E_V (MPa)	v_{vh}	E_h (MPa)	v_{hh}
TRIAXV5	SWS	196.0-197.5	726	0-0.12	-	-
TRIAXV7	WG	294.8-296.2	400	0-0.08	-	-
TRIAXV8	SWS	196.0-197.5	582	0-0.2	-	--
TRIAXV9	WG	236.0-237.5	630	0-0.3	-	-
TRIAXH14	SWS	196.6-203.5	-	-	1198	-
TRIAXH15	WG	236.0-237.5	-	-	1250	-
TRIAXH16	WG	294.0-295.5	-	-	1150	0-0.11

Note: TRIAXV, triaxial test on vertically oriented core sample; TRIAXH, triaxial test on horizontally oriented core sample.

Wong et al. (2008) studied the Colorado shale samples from Cold Lake, Alberta, Canada. They used ultrasonic waves to determine the five elastic parameters and compare the results with those obtained in drained triaxial tests. They showed that shale samples display higher elastic moduli in the horizontal direction compared with the vertical direction because of the preferred clay fabric orientation. Figure 2.6 shows their result for the elastic properties of Colorado shale in different directions.

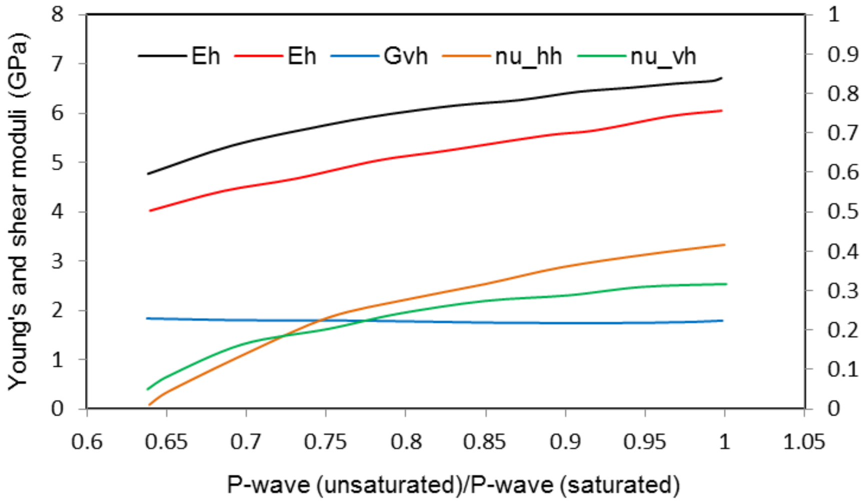

Figure 2.6 Estimation of Young's modulus and shear modulus in drained conditions (after Wong et al., 2008)

2.7.2 Softening behavior and Young's modulus in relation to confining pressure and temperature for shale samples

Niandou et al. (1997) performed a series of undrained triaxial tests on Tournemire shale samples. They studied the elastic response, plastic deformation and failure behavior of the shale samples. They concluded shale exhibits a large anisotropic plastic deformation. Figure 2.7 shows the triaxial data presented by Niandou et al. (1997). As it can be seen from their tests, softening behavior of the anisotropic shale increases with the decrease of confining pressure.

Another set of triaxial tests have been performed by Islam et al. (2013) to study the anisotropic mechanical properties of shale through undrained tests. They used Pierre-1 shale samples for their triaxial tests. Figure 2.8 shows the stress-strain behavior of shale samples cored in different directions.

Figure 2.9 shows the stress-strain curves at different confining pressures for Pierre1 shale sample on vertical core samples (Islam et al., 2013). The plot indicates higher peak strength and Young's modulus at higher confining stresses.

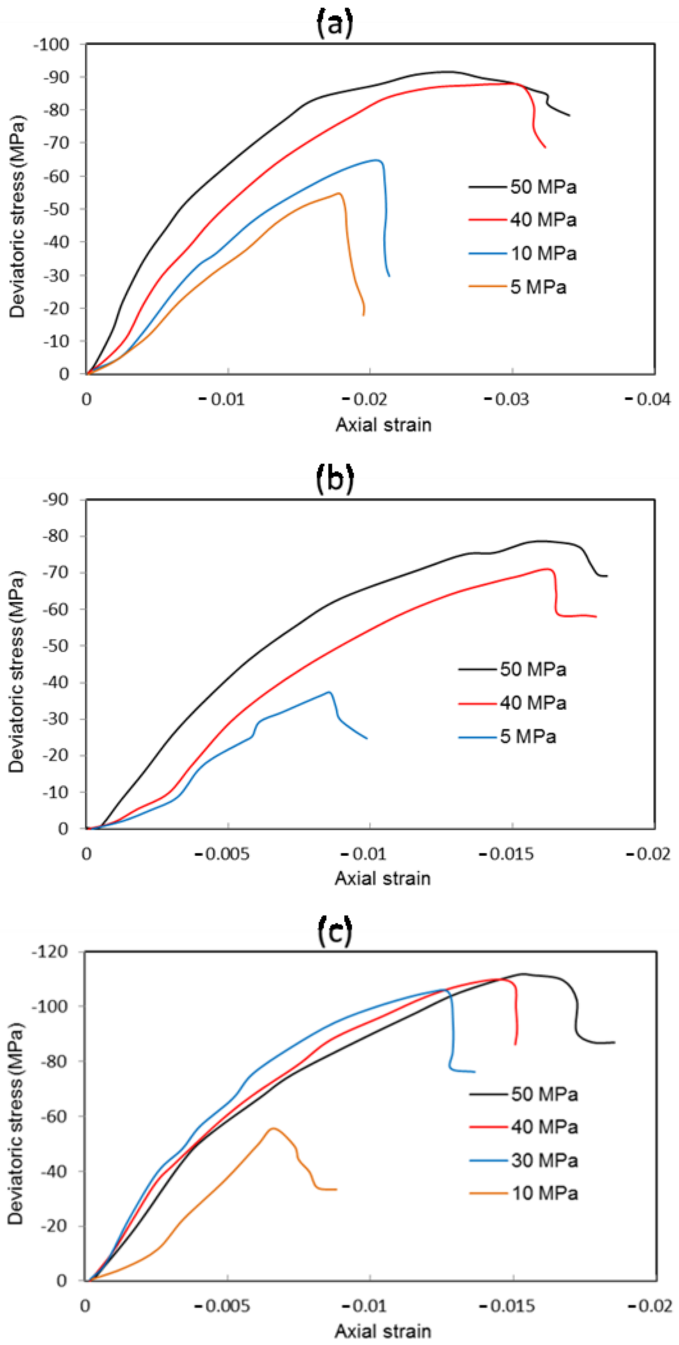

Figure 2.7 Triaxial tests in different directions on Tournemine shale samples: a) θ=90°, b) θ=45°, and c) θ=0° (after Niandou et al., 1997)

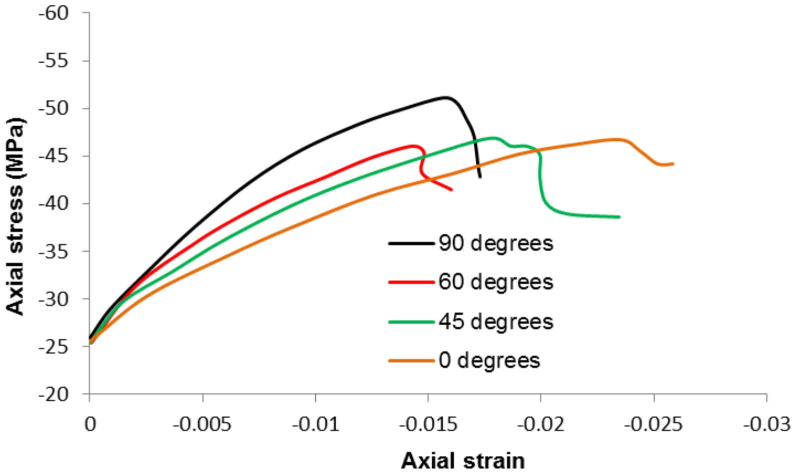

Figure 2.8 Strain-stress curves at confining pressure of 25 MPa for core plugs in different directions (after Islam et al., 2013)

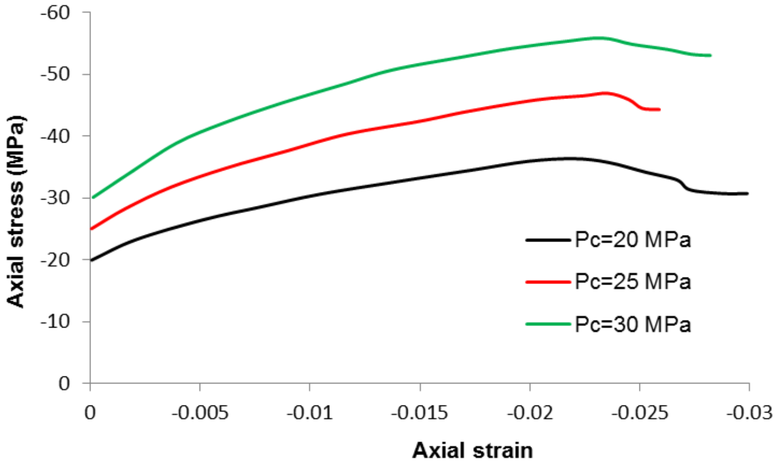

Figure 2.9 Strain-stress curves for Pierre-1 shale sample for vertical core samples at different confining pressures (after Islam et al., 2013)

Triaxial tests have been performed by Islam et al. (2013) on Pierre-1 shale samples indicating a small softening behavior for the shale particularly at high confining pressures. It can be seen that the shale samples show more ductile behavior at high confining pressures.

Zeuch (1983) performed a series of triaxial tests on Anvil Points oil shale at elevated temperatures and confining pressures. He concluded that the strength of the oil shale samples increases approximately linearly with confining pressure and decreases nonlinearly with temperature. He also concluded that ductility is greatly enhanced by the application of confining pressure. Elevated temperatures have little influence on ductility at low confining pressures; however, temperature exerts a progressively more pronounced influence on ductility with increasing the confining pressure (Zeuch, 1983). Figure 2.10 shows the stress-strain curve at 200°C on horizontal samples (Zeuch, 1983).

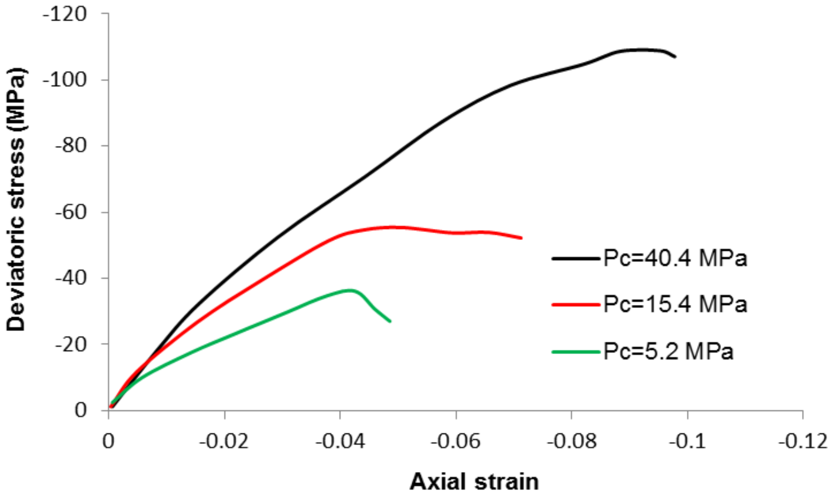

Figure 2.10 Compressive stress versus axial strain at 200°C and various confining pressures (after Zeuch, 1983)

Wong (1998) performed a series of drained triaxial tests on La Biche shale. Figure 2.11 shows stress-strain curves for La Biche shale at different confining stress. The results indicate nearly the same Young’s modulus at different low confining pressures for this rock.

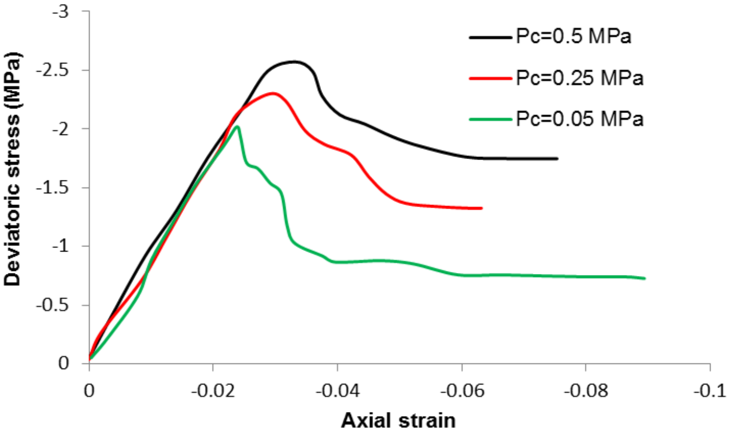

Figure 2.11 Results of drained triaxial compression tests on intact shale specimens (after Wong, 1998)

Figure 2.14 and 2.15 show the results of drained triaxial tests performed on upper and lower McMurray Formation shale at different confining pressures (Chalaturnyk, 1996). The results show small softening effects at high confining pressures.

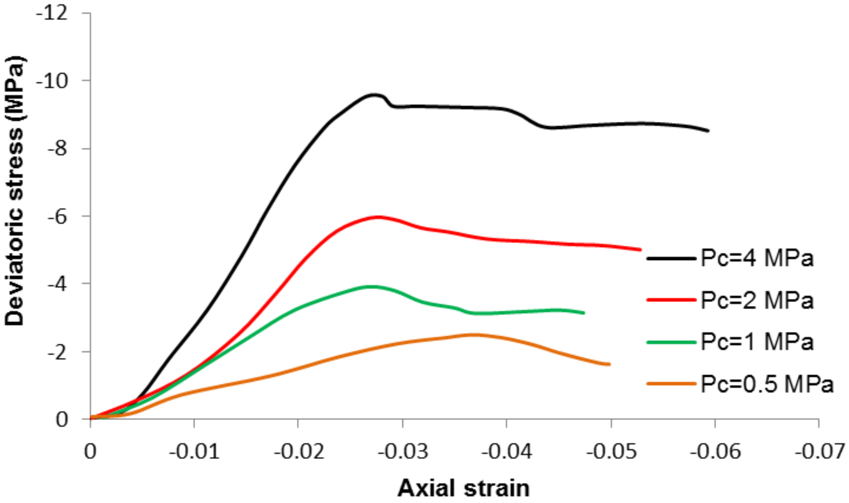

Figure 2.12 Consolidated-drained triaxial compression tests on upper McMurray Formation Shale (after Chalaturnyk, 1996)

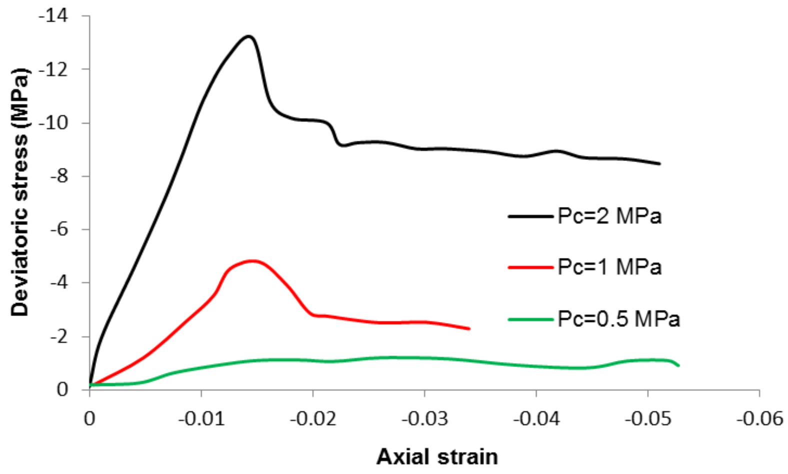

Figure 2.13 Consolidated-drained triaxial compression tests on lower McMurray Formation Shale (after Chalaturnyk, 1996)

Mohamadi et al. (2013) performed a series of undrained triaxial tests on Colorado shale samples in different confining pressures and temperatures. Figure 2.14 shows the result of triaxial tests in 25, 85, and 135 °C. The results show that at constant confining pressure with the increase of temperature, shale samples show more ductile behavior and effect of strain softening is less.

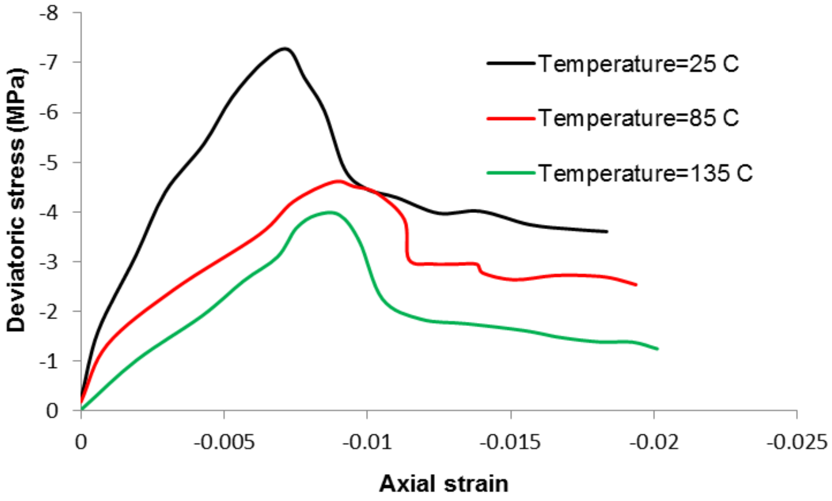

Figure 2.14 Results of triaxial compression tests at different temperatures and at 1 MPa confining pressure (after Mohamadi et al., 2013)

In summary, shale formations show softening behavior. However, the increase of confining stress and temperature reduces the softening effect and enhances ductility.

2.7.3 Effect of mineralogy on mechanical properties of shales

Mineralogy of shale formations can significantly impact the mechanical properties of shale samples. Figure 2.15 is the result of an experimental study on different shale samples and shows the increase of clay minerals in shale formation leads to higher ductility of the shale formation (Alqahtani et al., 2013).

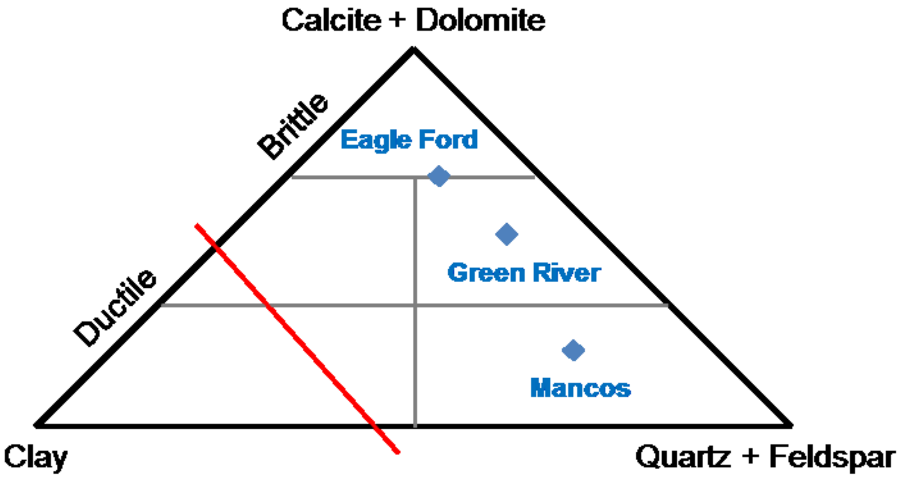

Figure 2.15 Composition of different shale samples (after Alqahtani et al., 2013)

Table 2.4 presents the X-Ray Diffraction analysis of Clearwater formation shale (Cenovus, 2011). The total clay content of the Clearwater ranges from 44% to 74% and total smectite content from 14 to 47%. Average clay content of the Clearwater formation shale is 62.1%. By considering the total clay content of Clearwater formation and Figure 2.15, one may expect Clearwater shale should be on the ductile side.

Table 2.4 Summary of Clearwater formation mineralogy (after Suncor Energy, 2009)

Sample depth	Clays					Total Clay
	Kaol	Chl	Ill	ML	Smec	
141.88-141.93 m	14	0	16	0	14	44
154.32-154.37 m	13	0	17	0	36	65
160.88-160.93 m	3	0	24	0	28	66
170-170.05 m	9	0	18	0	47	74
174.45-174.5 m	11	0	14	0	42	57
178.6-178.65 m	10	0	17	0	40	67

2.7.4 Effect of shale anisotropy on thermal characteristics

Many researchers have reported significant differences between thermal conductivity corresponding to heat flow in the direction perpendicular to the shale bedding and that corresponding to heat flow in the direction parallel to the stratigraphic planes (e.g., Dell'Amico et al., 1967; Nottenburg et al., 1978; Sladek, 1971; Robertson, 1979). In general, thermal conductivities parallel to the bedding planes are higher than those obtained perpendicular to the bedding planes. For shale from the Conassauge Group, Dell'Amico et al. (1967) reported that thermal conductivity values parallel to the bedding plane were 30% higher than those obtained perpendicular to the bedding plane; while Nottenburg et al. (1978) reported that the increase exhibited by shales from the Green River Formation was around 50%.

2.7.5 Swelling effect of shales

This part is retrieved from “Petroleum Related Rock Mechanics” by Fjaer et al. (2008).

The most important minerals in shaly rocks are clay minerals, which are composed of layers of sheet shaped crystals. Two basic structural units exist: One type of sheet is built from silica tetrahedral linked together in a hexagonal structure. The second type is an octahedral sheet in which silicon is replaced by cations like Al^{3+}, Mg^{2+}, Fe^{3+}, or Fe^{2+}, surrounded by six hydroxide groups. Usually, mainly because of oxygen and hydroxide at the surfaces, these have negative excess charge, and will therefore attract cations.

The basic sheets are kaolinite, illite, and smectite. Kaolinite is a two-layer mineral, consisting of alternate layers of gibbsite and silicon tetrahedron sheet. A basic unit is 0.7 nm thick, while typical composite crystals may be 70-100 layers, have six-fold symmetry and are flake shaped, up toward the micrometer range in lateral extent. The successive layers are strongly bonded to each other with a hydrogen bonding, and therefore water is not permitted to enter in between layers. Mineral density is 2.6-2.7 ${}^{g}/_{cm^3}$.

Smectite is a 2:1 layer mineral, composed of a central gibbsite sheet embedded between two silicon tetrahedron sheets, with a combined thickness of about 1nm. Isomorphous substitutions are common both within the central octahedral sheet and in the tetrahedral sheet. The bonding between two silica sheets connecting the unit layer is very weak. In smectite, this permits water and exchangeable ions to enter between the platelets, leading to a swelling capacity: at surface conditions, smectite minerals may absorb up to 10 times their own weight in water ("swelling clays").

Montmorillonite is a name often used synonymously with smectite, or as a common term for expandable clay minerals. In principle, this is a member of the smectite group. Another well-known smectitic clay is Bentonite, which is hydrated muscovite (a mica mineral) and has much less swelling capacity than the clay minerals mentioned above.

Illite is another clay mineral, formed by weathering of feldspars, degradation of muscovite, and transformation of smectite to illite at depth. Some of the silicon atoms in smectite are replaced by aluminum, causing a negative charge which is balanced by potassium ions that provide bonding between the silica tetrahedron sheet. This bond is much stronger than in smectite, preventing hydration and swelling, but it is considerably weaker than in kaolinite.

Common clay minerals are Kaolinite, Illite, and Montmorillonite. Kaolinite is essentially non-expansive because of the presence of strong hydrogen bonds that hold clay particles together. Illite contains weaker potassium bonds that allow limited expansion and Montmorillonite is weakly linked thus water can flow into the clays and separate the particles (Chan, 2014). Table 2.5 shows swelling potential of pure clay minerals.

Table 2.5 Swell potential of pure clay minerals (after Chan, 2014)

Load		Swell Potential (%)		
lb/ft^2	kPa	Kaolinite	Illite	Montmorillonite
200	9.6	Negligible	350	1500
400	19.1	Negligible	150	350

Swelling pressure of the soil sample is determined by reloading the soil sample at the end of a loaded swell test (Figure 2.16).

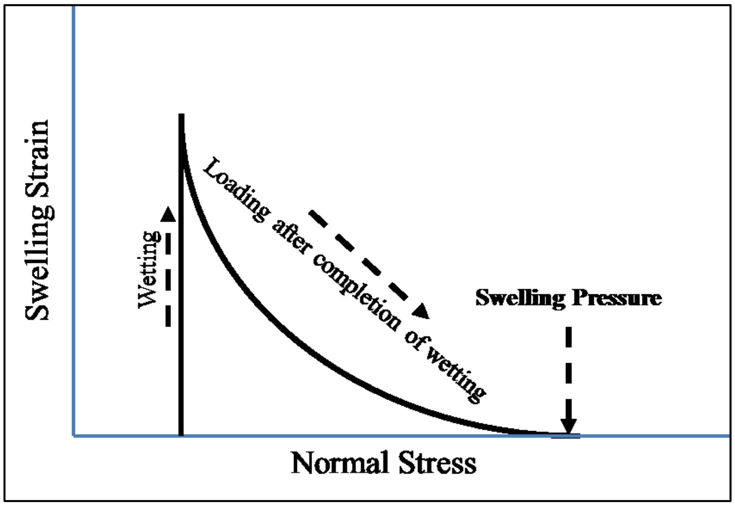

Figure 2.16 Swelling pressure of soils (after Chan, 2014)

Wong (1998) performed a series of Oedometer swell tests on La Biche shale, which is an over-consolidated, compact shale, to determine the axial swelling strain or pressure developed in an oedometer cell. Figure 2.17 shows the swelling pressure build up versus time. The development of swelling pressure in the specimens was fairly steady and leveled off after 22-27 days. The swelling pressure of the specimens in water and 1% NaCl solution reached maximum values of 272 kPa and 173 kPa, respectively, in Wong's tests.

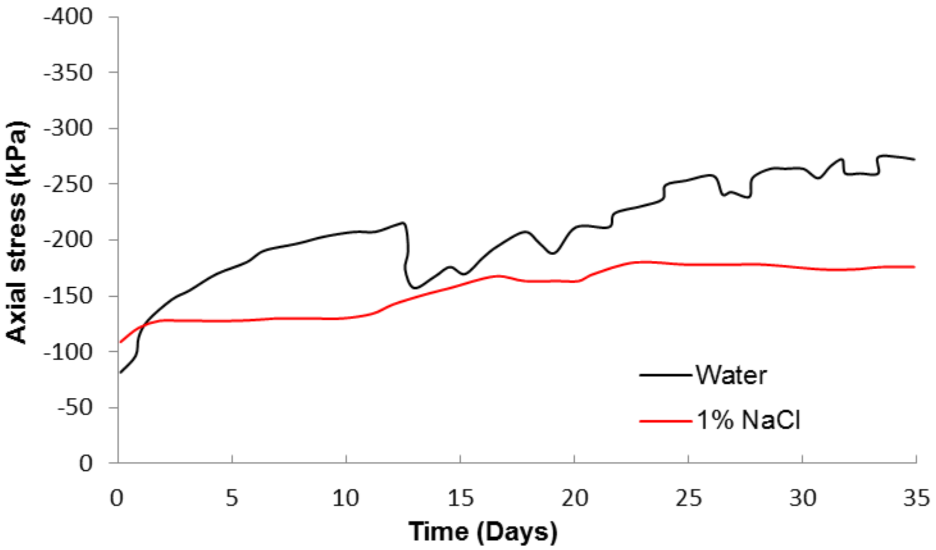

Figure 2.17. Swelling pressure build-up measured in oedometer cell with water and 1% NaCl solution (after Wong, 1998)

2.7.6 A review of constitutive models for anisotropic rocks

Although many attempts have been made in the past to describe the strength anisotropy of transversely isotropic rocks, no general methodology has emerged yet (Saeidi et al., 2014). There are few failure theories for anisotropic rocks that can be applied with different degrees of success to experimentally generated data. These theories will be briefly discussed in the following. Two groups of constitutive models are noted in the literature. The first group considers only the minimum and maximum principal stresses while the second group considers all three principal stresses in the yield criterion of anisotropic rocks.

2.7.6.1 Anisotropic constitutive models that neglect the intermediate principal stress

Single Plane of Weakness Theory: This approach seems to be the first attempt to describe the anisotropic behavior of sedimentary rocks such as shales. As opposed to the Walsh-Brace theory which assumes failure can only occur due to tensile stress, the single plane of weakness theory, proposed by Jaeger (1960), assumes that the body can only fail in shear. This theory is a generalization of the well-known Mohr-Coulomb linear envelope failure theory and describes an isotropic body that contains a single plane or a system of parallel planes of weakness. The failure of the matrix material is given by:

$$\tau = c - \acute{\sigma_n} \, tan \, \varphi \tag{2}$$

where c is the cohesive strength of the matrix material and tan φ is the coefficient of internal friction. Failure along the plane of weakness is described by:

$$\tau_W = c_W - \acute{\sigma_W} \, tan \, \varphi_W \tag{3}$$

where $c_W$and $\varphi_W$are the cohesive strength and friction angle of the weakness plane. Using the Mohr circle relationship, the final form of the single plane of weakness theory can be derived from above equations. For failure within the matrix, the equation is:

$$(\acute{\sigma_1} - \acute{\sigma_3}) = \frac{2c - 2\acute{\sigma_3} \, tan \, \varphi}{[tan \, \varphi - sin \, 2\gamma - cos \, 2\gamma \, tan \, \varphi]} \tag{4}$$

where γ is failure angle. The fracture strength of the material in the plane of weakness is given by:

$$(\acute{\sigma_1} - \acute{\sigma_3}) = \frac{2c_W \, cos \, \varphi_W - 2\acute{\sigma_3} \, tan \, \varphi_W}{[sin \, \varphi_W - sin(2\theta + \varphi_W)]} \tag{5}$$

where θ is the angle between $\acute{\sigma}_1$ and the plane of weakness and in both cases $\acute{\sigma}_3$ represents the minimum effective principal stress.

Walsh-Brace Theory: The Walsh-Brace theory (1964) assumes that failure is tensile in nature and that the body is composed of long, non-randomly oriented cracks that are superposed on an isotropic array of randomly distributed smaller cracks. The long and short crack arrays are such that the cracks close at relatively low values of applied stress thus transmitting both normal and shearing stresses. Walsh and Brace assume that fracture may occur through the growth of either long or small cracks depending upon the orientation of the long crack system to the applied deviatoric load $(\acute{\sigma}_1 - \acute{\sigma}_3)$.

Variable Cohesive Strength Theory: The variable cohesive strength theory was proposed by Jaeger (1960) to describe a body that fails in shear and has a variable cohesive strength c, and a constant value of internal friction, $\tan\varphi$. The governing equation describing failure for this case is:

$$(\acute{\sigma}_1 - \acute{\sigma}_3) = \frac{2c - 2\acute{\sigma}_3 \, tan\,\varphi}{\left[tan\,\varphi - \sqrt{tan\,\varphi^2 + 1}\right]} \qquad (6)$$

where

$$c = A - B[cos\,2(\theta - \beta)] \qquad (7)$$

and

$$tan\,\varphi \cong constant \qquad (8)$$

A and B are constants and θ represents the stress orientation; θ=β corresponds to the minimum value of c; usually β=30°. This theory can be evaluated by conducting compressive tests at 0°, 30°, and 90° at several pressures, plotting Mohr-Coulomb envelopes, determining the respective values of $\tan \varphi$ and c for each orientation and evaluating the constants A and B. The variable cohesive strength theory requires a wider range of tests to adequately evaluate the variation of cohesion with respect to θ.

Variable Cohesion and Friction Angle: McLamore and Gray (1967) proposed the use of variable cohesion and friction angle for sedimentary rocks. From triaxial testing data, the authors noted that the variation of c can be described by the following relationship:

$$c = A_{1,2} - B_{1,2}[cos\,2(\theta - \beta)]^n \tag{9}$$

where A_1 and B_1 are constants that describe the variation over the range of $0° \leq \theta \leq \beta$ and A_2 and B_2 over the range of $\beta < \theta \leq 90°$. The factor n is an anisotropy type factor and has the value of 1 or 3 for "planar" type of anisotropy (cleavage and possibly schistosity) and the value of 5 or 6 or greater for the "linear" type of anisotropy associated with the bedding planes. Tests on shale and slate, which exhibit a planar or cleavage type of anisotropy, indicate that the mechanical behavior of such rocks is best described by values of $\mathrm{n} = 1$ or 3, as the rock anisotropy appears to influence the failure over the entire range of $0° \leq \beta \leq 90°$.

The authors also noted that value of $\tan \varphi$ may also vary with respect to β or may, for some rocks, be reasonably constant. This variance is of the same nature as that of c and can be described by the following equation:

$$tan\,\varphi = C_{1,2} - D_{1,2}[cos\,2(\theta - \beta)]^m \tag{10}$$

where the constants C_1 and D_1 are the calibration parameters for the variation of $\tan \varphi$ over the range of $0° \leq \theta \leq \beta$ and C_2 and D_2 over the remaining range of θ. The same relationship between the type of anisotropy and the numerical value of m exists in this case for the value of n.

The fracture strength of an anisotropic rock may be predicted by utilizing this modified theory and performing compression tests at 0°, 30°, and 90° orientations for several values of confining pressure and determining the values of c and $\tan \varphi$ for different orientations.

If the rock being tested possesses a planar type of anisotropy, an additional orientation, say 45° or 50°, should be tested to determine if the orientation of the minimum value of $\tan \varphi$ corresponds to that of c.

Hoek-Brown Model: The Hoek-Brown failure criterion is an empirical relation for the description of failure in intact rock and rock masses. This model has been used successfully in design approaches that use limit equilibrium solutions. However, its use in numerical simulations has been limited (ICG, 2011). The generalized Hoek-Brown criterion is (Hoek and Brown, 1997):

$$\acute{\sigma}_1 = \acute{\sigma}_3 - \sigma_{ci}\left\{s - m_b\frac{\acute{\sigma}_3}{\sigma_{ci}}\right\}^a \qquad (11)$$

where $\acute{\sigma}_1$ and $\acute{\sigma}_3$ are the maximum and minimum effective principal stresses, and σ_{ci}, m_b, s and a are material constants that can be related the geological strength index and rock damage (Hoek et al., 2002).

More recently, Hoek and Brown (1997) assumed that the strength parameters m_b and s in their well-known failure criterion are not constant but vary with the direction of weakness plane. However, although the values of m_b and s are selected based on the orientation of weakness planes, it should be noted that the formulation remains isotropic, so it remains doubtful whether the orientation of failure plane predicted by this approach is realistic (Saeidi et al., 2014).

Modified Hoek-Brown Model: Saroglou and Tsiambaos (2008) modified the Hoek-Brown criterion by testing some metamorphic rocks from Greece in different orientations of the foliation's plane. In their study, they modified the Hoek-Brown model by incorporating a new parameter (k_β) to account for the effect of strength anisotropy. The proposed modification was studied for metamorphic rocks, but was not verified for sedimentary rocks such as shales.

Hoek and Brown (2000) introduced their failure criterion for the analysis and design of underground excavations in hard rocks (Hoek et al., 2000). The criterion started from the properties of intact rock and then factors were introduced to reduce these properties on the basis of the characteristics of joints in a rock mass. They sought to link the empirical criterion to geological observations by means of a rock mass classification schemes, i.e. Rock Mass Rating proposed by Bieniawski (1976). They modified the parameters "m_b", "s”, and “a" as follows:

$$m_b = m_i exp\left(\frac{GSI - 100}{28 - 14D}\right) \tag{12}$$

$$s = exp\left(\frac{GSI - 100}{9 - 3D}\right) \tag{13}$$

$$a = \frac{1}{2} + \frac{1}{6}\left(e^{-GSI/15} - e^{-20/3}\right) \tag{14}$$

where D is a factor which depends upon the degree of disturbance to which the rock mass has been subjected by blast damage and stress relaxation, and GSI is Geological Strength Index defined by Hoek et al. (1992). This index was subsequently extended for weak rock masses in a series of papers by Hoek et al. (1998, 2000), and Marinos et al. (2001).

2.7.6.2 Anisotropic constitutive models considering all three principal stresses

The first attempt to consider anisotropy in mechanical behavior of geomaterials seems to be Hill’s 1948 criterion (Hill, 1948):

$$F\left(\acute{\sigma}_y - \acute{\sigma}_z\right)^2 + G(\acute{\sigma}_z - \acute{\sigma}_x)^2 + H\left(\acute{\sigma}_x - \acute{\sigma}_y\right)^2 + 2N\tau_{xy}^2 = \bar{\sigma}^2 \tag{15}$$

where F, G, H, and N are constants in Hill’s 1948 criterion. The quadratic Hill yield criterion depends only on the deviatoric stresses and is pressure independent. It predicts the same yield stress in tension and in compression and neglects out of plane shear terms. Hill (1979) proposed a generalized form of his criterion as follow:

$$f|\acute{\sigma}_3-\acute{\sigma}_2|^m+g|\acute{\sigma}_1-\acute{\sigma}_3|^m+h|\acute{\sigma}_2-\acute{\sigma}_1|^m+a|\acute{\sigma}_2+\acute{\sigma}_3-2\acute{\sigma}_1|^m \\ +b|\acute{\sigma}_1+\acute{\sigma}_3-2\acute{\sigma}_2|^m+c|\acute{\sigma}_1+\acute{\sigma}_2-2\acute{\sigma}_3|^m=\left(-\bar{\sigma}\right)^m \qquad (16)$$

where the constants $\mathrm{f, g, h, a, b, c}$ and m are to be evaluated with various tests. The general form of Hill's 1979 criterion recognizes the possibility of planar anisotropy, but it cannot be used for loading conditions which involve shear relative to the axes (Hosford, 1985).

In 1993, Hill proposed another yield criterion for plane stress problems with planar anisotropy (Hill, 1993).

$$\left(\frac{\acute{\sigma}_1}{\acute{\sigma}_0}\right)^2+\left(\frac{\acute{\sigma}_2}{\acute{\sigma}_0}\right)^2+\left[(p+q-c)-\frac{p\acute{\sigma}_1+q\acute{\sigma}_2}{\acute{\sigma}_b}\right]\left(\frac{\acute{\sigma}_1\acute{\sigma}_2}{\acute{\sigma}_0\acute{\sigma}_{90}}\right)=1 \qquad (17)$$

where $\acute{\sigma}_0$ is the uniaxial tensile yield stress in the rolling direction, $\acute{\sigma}_{90}$ is the uniaxial tensile yield stress in the direction normal to the rolling direction, σ_b is the yield stress under uniform biaxial tension, and $\mathrm{c, p, q}$ are constant parameters. The original versions of Hill's yield criterion were designed for material that did not have pressure-dependent yield surfaces. Extensions of Hill's criterion incorporates pressure in the yield criterion (e.g. Caddell et al., 1973; Deshpande et al., 2001).

Imam (1998) used results of triaxial compression, triaxial extension, and hollow cylinder tests on different sand samples to investigate and formulate the effect of loading direction and intermediate principal stress on sand's behavior (Imam, 1998a). Imam's yield criterion is as follow:

$$f = \eta^2 + M_p^2\left[1 - \left({}^{P}\!/_{P_c}\right)^{1/2}\right] = 0 \tag{18}$$

where

$$\eta = \frac{q}{P} = \frac{\acute{\sigma}_1 - \acute{\sigma}_3}{(\acute{\sigma}_1 + \acute{\sigma}_2 + \acute{\sigma}_3)/3} \tag{19}$$

and

$$M_p = \frac{q_p}{P_p} \tag{20}$$

The pressure P_c is the value of P at $q = 0$ and the stress ratio M_p is the value of η at the peak point.

3D anisotropic yield criterions presented above are difficult to calibrate and require different experimental tests to fully characterize them. Instead, many researchers used two-dimensional anisotropic yield criteria for different applications. among these, the variable cohesion and friction angle theory proposed by McLamore and Gray (1967) is a well-known theory. Soreide et al. (2009) used the variable cohesion and friction angle theory in CamClay yield criterion to capture the anisotropic behavior of a shale formation in Norway. They performed a series of triaxial tests and compared the simulation results with testing measurements. Figure 2.18 and Figure 2.19 show the comparison between the experimental data and simulations results.

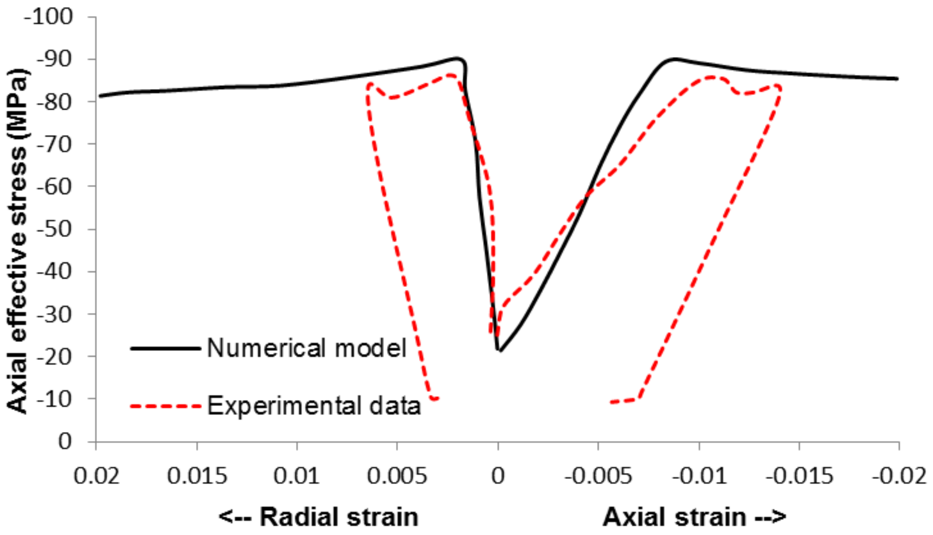

Figure 2.18 Undrained triaxial test with loading perpendicular to the bedding (after Soreide et al., 2009)

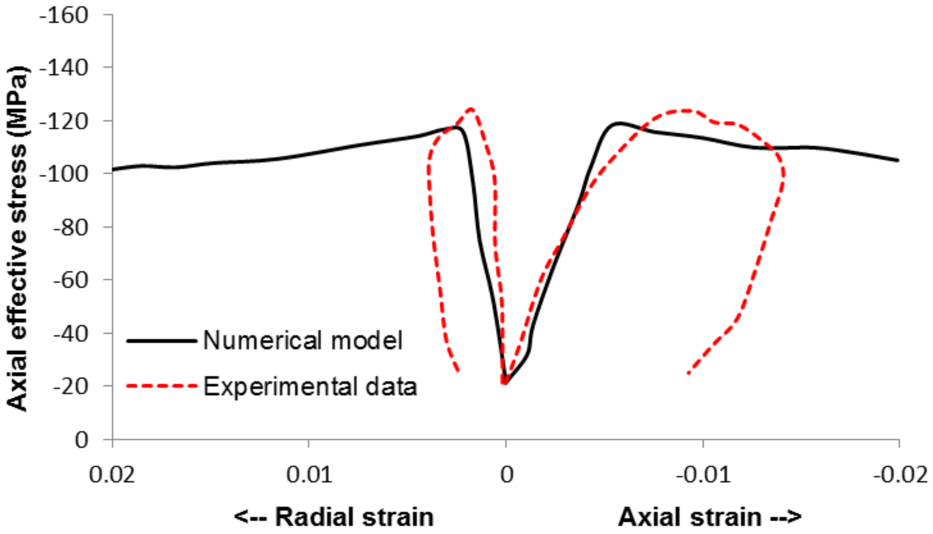

Figure 2.19 Undrained triaxial test with loading parallel to the bedding (after Soreide et al., 2009)

Xu et al. (2010) implemented variable cohesion and friction angle theory proposed by McLamore and Gray (1967) in conjunction with Drucker-Prager strength criterion to study the deformation of layered rock masses such as shales. They conducted a series of uniaxial compression numerical tests for a specimen of layered rock for different loading directions. The analysis results for uniaxial compressive strength tests are shown in Figure 2.20.

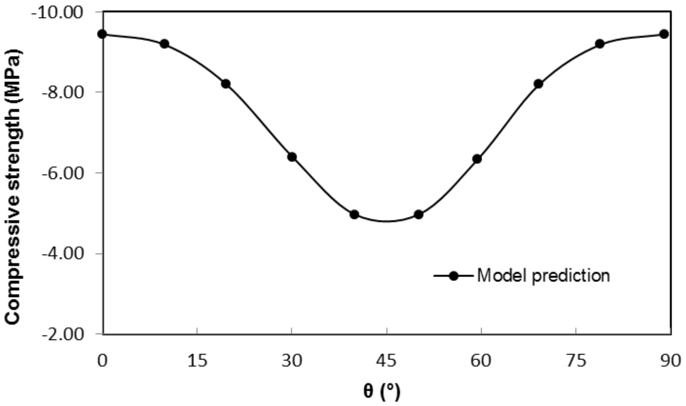

Figure 2.20 Numerical analysis results for uniaxial compression tests for different loading direction with respect to the bedding planes (after Xu et al., 2010)

Cazacu et al. (1996) used variable cohesive strength theory with a failure criterion to study Tournemire shale deformation behavior. Figure 2.21 shows the comparison between the experimental and calculated results. They concluded that the numerical model describes reasonably well some important features of the behavior of anisotropic rocks subjected to triaxial compression tests. They also stated that more complicated experimental tests were needed to verify the performance of the numerical model for more complex loading paths.

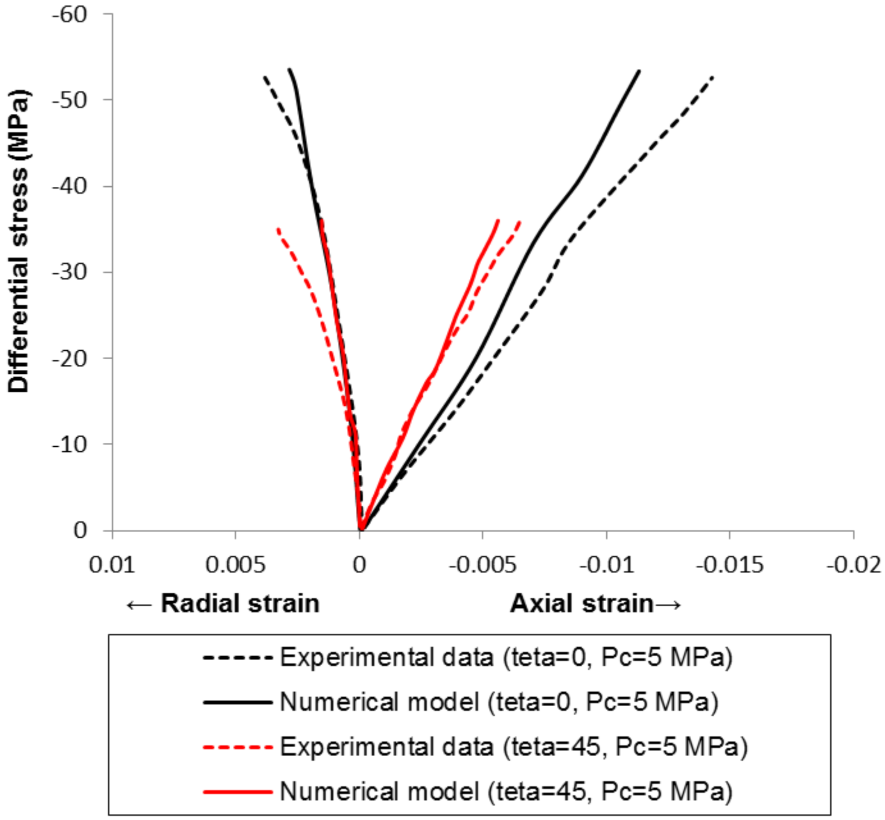

Figure 2.21 Comparison of numerical calculations and test measurements for triaxial tests with different orientation for the core plug axis (after Cazacu et al., 1996)

2.8 Natural fracture observations in shale (structural anisotropy)

Natural fracture sets have been observed in caprock layers of SAGD reservoirs in Canada (Chou, 2011). These natural fractures could be the source of structural anisotropy in caprock formations.

In this section, observations and evidence of NFs for shale formations in Alberta are discussed. Also, the causes of NFs in Alberta are briefly explained.

2.8.1 Observations on NFs in Alberta, Canada

Published information on the characterization of NFs in SAGD caprock layers in Alberta was found to be limited. Natural fractures in two SAGD projects are discussed in this part. The first one is the MacKay River SAGD project (Suncor Energy, 2009), which is the case study in this work. The second one is the pilot project (AOS, 2010).

The stratigraphic column of the pilot project and MacKay River project are shown in Table 2.1. The geological layers in the pilot project and MacKay River SAGD project are analogous but the pilot project is 10 m shallower than the MacKay River SAGD project (AOS, 2010).

2.8.1.1 NFs in MacKay River SAGD project

Suncor Energy (2013) conducted a fracture characterization work in this area. They observed a higher fracture frequency for the lower part of Clearwater shale (2.4 frac./m) and Wabiskaw A shale (2.6 frac./m) than for Wabiskaw D Mudstone (0.2 frac./m) in this area. No evidence of hydraulically conductive fractures in MacKay project area has been observed by Suncor Energy (2013). They also confirmed there is no mineralization or bitumen staining in the fractures crossed by the intersecting wells (Suncor Energy, 2013).

2.8.1.2 NF Observations in a pilot project

Uwiera-Gartner et al. (2011) completed a core based evaluation of the caprock and underburden units for a pilot project. The Pilot Project is owned and operated by Alberta Oilsands Inc. (AOS) and located 8 km southeast of Fort McMurray, Alberta. They used the data from core analyses and photographs, x-ray images, wireline logs, Formation MicroImage (FMI) logs, and a geotechnical borehole log to characterize and identify the NFs.

Uwiera-Gartner et al. (2011) developed a generalized RQD classification for the pilot project for assessing the NF information from core photographs of the Clearwater caprock. Generalized RQD was calculated based on the following equation (Goodman and Smith, 1980):

$$RQD = \left(\frac{l_{sum\ of\ 100}}{l_{total\ core\ run}}\right) \times 100\% \tag{21}$$

where l_{sum} of 100 is the sum of length of core sticks longer than 100 mm measured along the center line of the core, and $l_{total\ core\ run}$ is the total length of the core run.

The categories specified for the pilot project were "Good" (>75% RQD), 'Fair" (50-75% RQD), and 'Poor" (<50% RQD) (Uwiera-Gartner et al., 2011).

Table 2.6 summarizes the core recovery results determined from core photographs and the geotechnical log of the Clearwater formation caprock.

Table 2.6 Summary of generalized RQD for the Clearwater caprock (after Uwiera-Gartner, 2011)

Parameter	Maximum	Minimum	Average
Core length (m)	23.9	0.9	11.1
RQD (%)	37	0	13
Spacing (%)	24	0	4

Uwiera-Gartner et al. (2011) categorized natural fractures in the caprock of pilot project based on fracture spacing into three different groups: 'Closely' (<15 cm spacing), 'Moderate' (15-60 cm spacing), and 'Blocky' (>60 cm spacing) spacing.

They concluded: “A significant length of the caprock core fell in the ‘Closely’ category, which is not likely representative of the entire caprock unit at the pilot project”.

Uwiera-Gartner et al. (2011) calculated the fracture density at different depth intervals in the Clearwater caprock. The average fracture density based on their work is around 2 frac./m in the Clearwater formation caprock. Figure 2.22 shows the fracture frequency at different depth intervals of Clearwater formation caprock.

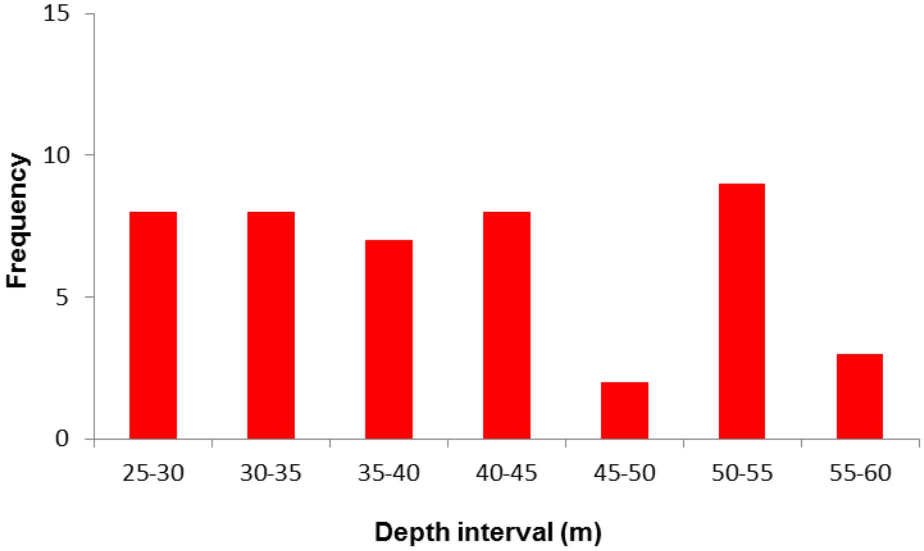

Figure 2.22 Fracture frequency from the geotechnical borehole log (after Uwiera-Gartner et al., 2011)

Uwiera-Gartner et al. (2011) categorized infill fracture materials from core photographs in the following groups: ‘None’ (0% occurrence), ‘Seldom’ (<10% occurrence), ‘Occasional’ (10-50% occurrence), and ‘Frequent’ (>50% occurrence). They concluded that most of the fractures categorized as either ‘None’ or ‘Seldom’ in terms of infill materials.

2.8.2 Origin of NFs in Alberta, Canada

Different possible mechanisms for the development of NFs include (Canadian Natural Resources Limited, 2014):

- Glacio-tectonic disturbance
- Gravity slumping
- Tectonic deformation
- Diagenetic mineral conversion
- Salt dissolution and associated collapse at depth
- Glacial loading and unloading
- Valley rebound

Evidence of the first three mechanisms (Glacio-tectonic disturbance, Gravity slumping, and Regional fracturing) have been observed in outcrops in Alberta, Canada. A brief literature review of these three mechanisms is brought next in the Alberta context. Later, a brief discussion is provided about mineral diagenesis in NFs.

2.8.2.1 Glacio-tectonic disturbance

Disturbed glacio-tectonic structures observed in both outcrop and cores have been described in several studies. Tsui et al. (1988) studied the mesofabric, microfabric, and submicrofabric of ice-thrust bedrock in Highvale mine, Wabamun Lake area, Alberta. They concluded that the characteristics of a typical ice-thrust shear zones are similar to those of shear zones formed by large-scale tectonic activities.

Stauffer et al. (1990) attributed many features observed in core and outcrop samples in the Maymont landslide in the North Saskatchewan River valley, Alberta, to a Glacio ice-thrust origin.

2.8.2.2 Tectonic deformation

Regional fracturing has been studied in Alberta and Saskatchewan by many researchers using data from a variety of sources. Babcock (1975) studied Cretaceous McMurray Formation outcrop in the Fort McMurray area. Babcok (1975) showed the presence of two orthogonal fracture sets. The first set has joints that strike N-S and E-W, while the second orthogonal fracture set has joints that strike parallel and perpendicular to the mountain front, NW-SE and NE-SW.

Babcock (1973) observed that both orthogonal sets are present at some locations in southern Alberta with one set normally being more dominant. Babcock (1973) observed that the joints in shale have the same trend and degree of curvature as those in associated sandstones, but are more closely spaced. Spacing in the sandstone varies from 15 cm to 100 cm, while in shale it is from 0.5 cm to 20 cm.

2.8.2.3 Gravity slumping

Karsting and salt dissolution in Devonian formation and Prairie Evaporite in Alberta could result in voidage into which the overlying oil sand and caprock can drape. If this occurred after the deposition of the caprock formations, it would result in a reduction in rock stress and fracture development in overlying units. Gregor (1997) concluded that much of the dissolution of Evaporites Formation is due to meteoric water flow along high angle faults in Lloydminster area. His studies of this area show that the timing of dissolution was after deposition of the Colorado Group in that area. He also believed that the salt dissolution has been episodic rather than continuous, and related to tectonic events.

2.8.2.4 Diagenetic mineral conversion

Abnormal high fluid pressures in rock can lead to development of NFs. Combination of clay minerals conversion and dehydration, hydrothermal pressurizing, and cementation can create abnormally high fluid pressure in shales (Ding et al., 2012). For instance, transition from montmorillonite to illite at about $100^{o}C$ involves the expulsion of water from montmorillonite. Abnormally high-pressure fractures may be produced when excessive fluid pressure equals to 1/2 or 1/3 of matrix pressure (Wenlong et al., 2003). Fractures tend to be closed when fluid pressure in pores is less than that in fractures. Generally, the opening and closing of fractures under abnormally high pressure is a multi-cycle process. During this process, small fractures formed early are continuously extended by later rupture, and it can result in forming larger vertical tensile fractures, a large number of micro fractures, and some shear fractures (Ding et al., 2012).

2.9 Conclusions

Shales display a significant anisotropic mechanical behavior in elastic and plastic ranges. Different parameters including confining pressure, temperature, and mineralogy were shown to affect the mechanical behavior of shales. Also, structural anisotropy, due to the existence of NFs, has been observed in the cap shales of SAGD operations in Alberta, Canada.

Different numerical models to assess the caprock integrity and prediction of MOP during thermal or non-thermal operations were also reviewed in this chapter. All these numerical tools consider the caprock as isotropic elasto-plastic or linear elastic rock and also neglect the role of NFs in the caprock. It seems that the incorporation of a model capable of capturing shale anisotropy is necessary for accurate prediction of MOP in SAGD operations.

Chapter 3: Theoretical background, numerical model development, and verification

3.1 Introduction

Butler and his former colleagues at Imperial Oil introduced the SAGD technique in early 1980s (Butler et al., 1981; Butler and Stephens, 1981). In SAGD, the force of gravity causes the flow of oil in the direction parallel to the surface of the steam chamber towards the producer (Figure 3.1). The SAGD process is governed by a combined conduction-convection mechanism. Cold bitumen cannot be displaced at economical rates. The injection of steam exposes the reservoir bitumen to heat and reduces its viscosity. Conduction heats a thin layer of oil sands adjacent to the steam chamber and mobilizes the bitumen and steam condensate towards the bottom of the chamber. This process will continue as long as steam is injected and the bitumen and condensate are removed from the bottom of the chamber (Edmunds et al., 1993).

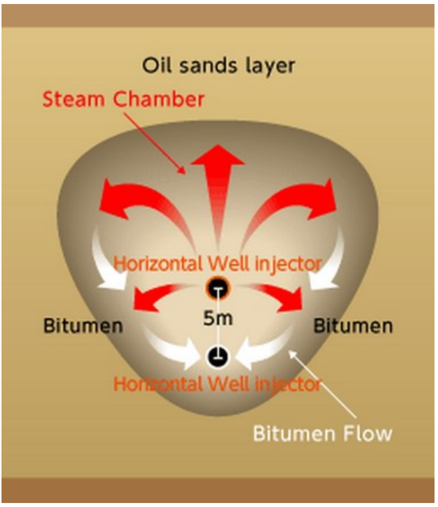

;

Figure 3.1 SAGD concept (Source: JAPEX)

This chapter presents the governing equations for SAGD analysis and the coupling scheme that was used to link these governing equations. An Anisotropic Ubiquitous (AU) constitutive model was implemented to consider the effect of intrinsic anisotropy and multiple NF sets (structural anisotropy) in shale. The formulation and verification of the AU model is also presented in this chapter.

3.2 Governing equations

The governing equations for fluid flow, heat transfer and force equilibrium are briefly discussed herein.

3.2.1 Fluid flow equations

The following equations describe the mass flow of oil, water, and gas, for laminar flow in porous media for which Darcy’s law is assumed to apply (Ertekin et al., 2001):

$$\nabla[\lambda_W(\nabla P_W - \gamma_W \nabla z)] = \frac{\partial}{\partial t}\left(\frac{\emptyset S_W}{B_W}\right) + q_W \tag{22}$$

$$\begin{aligned} &\nabla\left[\lambda_O(\nabla P_O - \gamma_O \nabla z) + r_s \lambda_g\left(\nabla P_g - \gamma_g \nabla z\right)\right] \\ &\qquad = \frac{\partial}{\partial t}\left(\frac{\emptyset S_O}{B_O} + \frac{r_s S_g}{B_g}\right) + q_O + q_g r_s \end{aligned} \tag{23}$$

$$\begin{aligned} &\nabla\left[\lambda_g\left(\nabla P_g - \gamma_g \nabla z\right) + r_s \lambda_O(\nabla P_O - \gamma_O \nabla z)\right] \\ &\qquad = \frac{\partial}{\partial t}\left(\frac{\emptyset S_g}{B_g} + \frac{r_s S_O}{B_O}\right) + q_g + q_O r_s \end{aligned} \tag{24}$$

where $\lambda_W, \lambda_O, \lambda_g$ are water, oil, and gas mobility factors, respectively; P_W, P_O, P_g are water, oil, and gas pressures, respectively; $\gamma_W, \gamma_O, \gamma_g$ are water, oil, and gas specific weights, respectively; S_W, S_O, S_g are water, oil, and gas saturations, respectively; B_W, B_O, B_g are water, oil, and gas formation volume factors, respectively; q_W, q_O, q_g are water, oil, and gas well rates at standard condition, respectively; and r_S is the solution gas-oil ratio.

Additional equations include the sum of saturations and the equations that relate capillary pressures to saturations.

$$S_W + S_O + S_g = 1 \tag{25}$$

$$P_{CWO} = f(S_W) \tag{26}$$

$$P_{CgO} = f(S_g) \tag{27}$$

where P_{CWO} and P_{CgO} are capillary pressure between oil and water and capillary pressure between gas and oil, respectively.

The relationship between bulk, rock and solid (grain) compressibilities is provided by Li et al. (2006):

$$C_r = C_b(1 - \emptyset_0) - C_S \tag{28}$$

where C_r, C_b, and C_S are rock, bulk, and solid compressibilities, respectively. $\emptyset_0$ is the initial porosity of the porous medium.

3.2.2 Heat transfer equations

The general energy balance for a process can be expressed in words as (Cengel, 2007):

$$\begin{aligned} &Accumulation\ of\ energy\ in\ the\ system \\ &\qquad = Input\ of\ energy\ into\ the\ system \\ &\qquad - Output\ of\ energy\ from\ the\ system \end{aligned} \tag{29}$$

The three basic mechanisms of heat transfer are: conduction, convection, and radiation (Cengel, 2007). However, heat transfer within the reservoir can only be by two mechanisms: thermal conduction through stationary materials and convective transport by fluids in movement. Radiant heat transfer is usually considered negligible (Butler, 1997). Heat conduction in a medium is three dimensional and time dependent. Fourier's law of heat conduction in one-dimensional form reads (Cengel, 2007):

$$\dot{Q}_{cond} = -kA\frac{dT}{dx} \tag{30}$$

where $\dot{Q}_{cond}$ is the rate of heat conduction; k is the thermal conductivity of the material; A is the cross sectional area through which the heat is flowing; dT/dx is the temperature gradient in x direction.

Convection is characterized by the heat transfer between a solid surface and the adjacent liquid or gas that is in motion. Despite the complexity of the convection mechanism, the rate of convection heat transfer is observed to be proportional to the temperature difference, and is expressed by Newton's law of cooling as (Cengel, 2007):

$$\dot{Q}_{conv} = hA_S(T_s - T_\infty) \tag{31}$$

where A_S is the surface area through which convection heat transfer takes place, T_s is the surface temperature and T_∞ is the temperature of the fluid sufficiently far from the surface. The convection heat transfer parameter is not a property of the fluid. Rather, it is an "experimentally determined parameter whose value depends on all the variables influencing convection such as the surface geometry, the nature of fluid in motion, the properties of the fluid, and the average fluid velocity" (Cengel, 2007). There are different correlations to calculate h parameter in terms of Rayleigh number, Prandtl number, and thermal conductivity (Cengel, 2007). Rayleigh number and Prandtl number are a function of the fluid velocity and, therefore, the h parameter is also a function of fluid velocity.

3.2.3 Geomechanical equations

The solution of solid-body problems in FLAC invokes the equations of motion and constitutive relations. This part reviews the basic governing equations for the stress and deformation analysis.

3.2.3.1 Motion and equilibrium

The momentum conservation law in a continuous solid body is generalized as follows (Malvern, 1969):

$$\rho \frac{\partial \dot{u}_i}{\partial t} = \frac{\partial \sigma_{ij}}{\partial x_j} + \rho g_i \tag{32}$$

where: ρ =mass density;

t =time;

x_i =components of coordinate vector;

$\dot{u}_i$ =velocity components;

g_i =components of gravitational acceleration (body force); and

σ_{ij} =components of stress tensor;

In this equation, subscript "i" denotes components in a Cartesian coordinate frame.

3.2.3.2 Constitutive relation

The other set of equations that apply to a deformable body is known as the constitutive relation, or stress-strain law. First strain rate is derived from velocity gradient as follows (e.g. Malvern, 1969):

$$\dot{e}_{ij} = \frac{1}{2}\left[\frac{\partial \dot{u}_i}{\partial x_j} + \frac{\partial \dot{u}_j}{\partial x_i}\right] \tag{33}$$

where $\dot{e}_{ij}$ is strain-rate components, and $\dot{u}_i$ is velocity components.

Mechanical constitutive laws are of the form (e.g. Malvern, 1969):

$$\sigma'_{ij} := M\left(\sigma'_{ij}, \dot{e}_{ij}, k\right) \tag{34}$$

where: $M(\,)$ is the functional form of the constitutive law;

k is a history parameter which may or may not be present; and

$:=$ means “replaced by”.

The simplest example of a constitutive law is that of isotropic elasticity (e.g. Fjaer, 2008):

$$\sigma'_{ij} = \lambda\delta_{ij}\varepsilon_{vol} + 2Ge_{ij} - 3\alpha_T K\Delta T\delta_{ij} \tag{35}$$

where: δ_{ij} is the Kronecker delta;

α_T =temperature coefficient;

σ'_{ij} =effective stress; and

ΔT =temperature difference; and

G, K =shear and bulk modulus, respectively.

The effective stress concept was originally introduced in soil mechanics by Terzaghi (1923) on an empirical basis. It relates the pore pressure, total stress, and effective stress. The effective stress law is as follows (e.g. Fjaer, 2008):

$$\sigma'_{ij} = \sigma_{ij} - P_p \tag{36}$$

where P_P is pore pressure.

The particular formulation for anisotropic constitutive laws used in this study is provided in Section 3.3.

3.2.4 Coupling parameters among the governing equations

Steam injection and the production of fluids in SAGD alter the pore pressures, temperatures, and effective stresses in the reservoir and result in reservoir deformation. Reservoir deformations, in turn, alter the permeabilities and porosities of the reservoir, which influence the pore pressures and temperatures. Therefore, the pore pressure, temperature, and deformation parameters are linked and are the coupling parameters of the governing equations.

3.3 Anisotropic Ubiquitous (AU) constitutive law and verification

This section presents the formulation and verification of the proposed AU constitutive model that incorporates intrinsic and structural anisotropy of shales.

3.3.1 Formulation of proposed AU constitutive model

Stratification of shale formations leads to transversely isotropic symmetry (Hemsing, 2007). In an elastic medium with transversely isotropic symmetry, stresses and strains are related by the Hooke's law as in Eq. (37) for plane strain condition (Puzrin, 2012).

$$\begin{bmatrix} e^e_{xx} \\ e^e_{yy} \\ e^e_{zz} \\ e^e_{xy} \end{bmatrix} = \begin{bmatrix} 1/E_x & -\upsilon_{yx}/E_y & -\upsilon_{zx}/E_z & 0 \\ -\upsilon_{xy}/E_x & 1/E_y & -\upsilon_{zy}/E_z & 0 \\ -\upsilon_{xz}/E_x & -\upsilon_{yz}/E_y & 1/E_z & 0 \\ 0 & 0 & 0 & 1/2G_{xy} \end{bmatrix} \begin{bmatrix} \sigma'_{xx} \\ \sigma'_{yy} \\ \sigma'_{zz} \\ \sigma'_{xy} \end{bmatrix} \tag{37}$$

where $\acute{\sigma}$ is the second-order effective stress tensor; e is the second-order strain tensor; E_i is the Young moduli in different directions; G_{xy} is the cross-shear modulus between a plane of isotropy and the perpendicular plane; υ_{ab} is the Poisson's ratio, where "a" indicates the stress direction , and "b" indicates the direction of the strain component caused by this stress. In this paper, x and z show the horizontal coordinates and y shows the vertical coordinate. Due to the transversely isotropic assumption, the material elastic strength properties in horizontal directions are equivalent ($E_x = E_z$; $\upsilon_{zx} = \upsilon_{xz}$; $\upsilon_{xy} = \upsilon_{zy}$). Eq. (37) contains five independent constants: $E_x, E_y, \upsilon_{xz}, \upsilon_{yx}, \upsilon_{xy}$. McLamore and Gray (1967) proposed variable cohesion and friction angle theory for shales based on triaxial test results:

$$c(\theta) = A_{1,2} - B_{1,2} cos\left(2(\theta_{min,c} - \theta)\right)^n \tag{38}$$

$$\varphi(\theta) = arctan\left(C_{1,2} - D_{1,2} cos\left(2(\theta_{min,\varphi} - \theta)\right)^m\right) \tag{39}$$

where θ is the angle between the maximum principal stress and the bedding plane direction; $c(\theta)$ and $\varphi(\theta)$ are cohesion and friction angle, respectively; $\theta_{min,c}$ and $\theta_{min,\varphi}$ are the value of θ corresponding to the minimum cohesion and friction angle, respectively; A_1, B_1 and C_1, D_1 are constants that describe variations over the range of $0^{\circ} \leq \theta \leq \theta_{min,c}$ and $0^{\circ} \leq \theta \leq \theta_{min,\varphi}$, respectively; A_2, B_2 and C_2, D_2 are constants that describe variations over the range of $\theta_{\mathrm{min,c}} < \theta \leq 90^{\circ}$ and $\theta_{\mathrm{min,\varphi}} < \theta \leq 90^{\circ}$, respectively; n and m are "anisotropy type" factors and have the value of 5 or 6 or greater for the linear type of anisotropy associated with bedding planes (McLamore and Gray, 1967).

In this study, the variable cohesion and friction angle theory (McLamore and Gray, 1967) was used in conjunction with the Mohr-Coulomb criterion as the shear yield criterion to describe shale's intrinsic anisotropy. A tension cut-off was adopted as the tensile yield criterion. Non-associated and associated flow rules were adopted in the shear and tensile constitutive models, respectively. Ubiquitous joints model theory (Clark, 2006) was adopted to account for the NFs which induce structural anisotropy. Ubiquitous joints model represents a set of fractures that are triggered when their yield criterion is satisfied.

In this constitutive model, yield may occur in the rock matrix or NFs or, in the extreme, both (matrix and fractures). In the implementation of the constitutive model, in the first step, matrix yield is analyzed and if yield is detected in the rock matrix, relevant plastic deformations are calculated. Next, the new stress state, obtained from the previous step is transformed to obtain fracture stresses to examine fracture yield. If fracture yield is detected, plastic deformations due to fracture yield is calculated and added to the plastic strain obtained from the previous step. This step is repeated for each set of fractures. Mohr-Coulomb criterion is used for fracture yield detection in the ubiquitous joints model:

$$\tau = -\acute{\sigma_n} tan\varphi_f + c_f \tag{40}$$

where τ and $\acute{\sigma_n}$ are the shear stress and effective normal stress on the fracture plane, respectively; φ_f is the fracture friction angle; and c_f is the fracture cohesive strength.

Figure 3.2 illustrates the global $(x\ y)$ and local $(`x\ `y)$ coordinate frames for the presentation of NFs. Angle ξ denotes the angle between the fracture plane and the global horizontal coordinate. If ξ is less than or equal to 90°, it is equal to the dip angle. If ξ is greater than 90°, it is equal to the sum of dip angle and 90°.

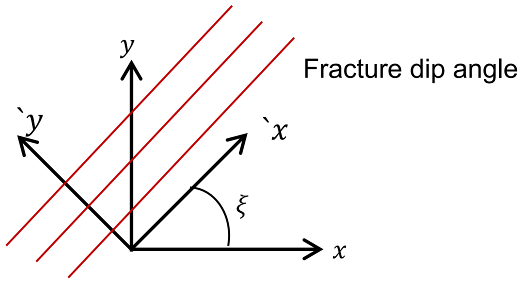

Figure 3.2 A fracture set with the dip angle of ξ with respect to the x axis of the global reference frame

The global and local effective stress components are denoted by σ'_{ij} and $`\sigma'_{ij}$, respectively. These global stresses are resolved into local components by stress transformation (Fjar et al., 2008):

$$\begin{bmatrix} `\sigma'_{xx} \\ `\sigma'_{yy} \\ `\sigma'_{zz} \\ `\tau = `\sigma'_{xy} \end{bmatrix} = R \begin{bmatrix} \sigma'_{xx} \\ \sigma'_{yy} \\ \sigma'_{zz} \\ \sigma'_{xy} \end{bmatrix} \tag{41}$$

where rotational matrix $[R]$ is as follows:

$$R = \begin{bmatrix} \cos\xi^2 & \sin\xi^2 & 0 & 2\sin\xi\cos\xi \\ \sin\xi^2 & \cos\xi^2 & 0 & -2\sin\xi\cos\xi \\ 0 & 0 & 1 & 0 \\ -\sin\xi\cos\xi & \sin\xi\cos\xi & 0 & \cos\xi^2 - \sin\xi^2 \end{bmatrix} \tag{42}$$

With this notation, the local expression of incremental elastic stress has the form:

$$\begin{bmatrix} \Delta`\sigma'_{xx} \\ \Delta`\sigma'_{yy} \\ \Delta`\sigma'_{zz} \\ \Delta`\tau \end{bmatrix} = [`K] \begin{bmatrix} \Delta`e^{e}_{xx} \\ \Delta`e^{e}_{yy} \\ \Delta`e^{e}_{zz} \\ \Delta`e^{e}_{xy} \end{bmatrix} \tag{43}$$

in which

$$[`K] = [R][K][R]^{-1} \tag{44}$$

where matrix $[K]$ is the stiffness matrix, and $`e^{e}_{ij}$ is the strain in the local coordinate system, and the superscript "e" stands for "elastic".

Yield criteria may be presented in the $(`\sigma'_{yy}, `\tau)$ plane, as illustrated in Figure 3.3:

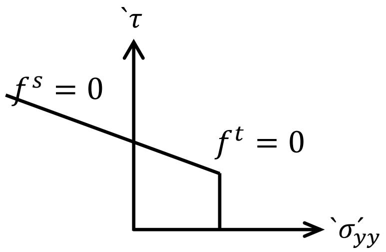

Figure 3.3 Fracture's yield criterion

Mohr-Coulomb criterion is used as the shear yield envelope for the NF:

$$f^{S} = -`\tau - `\sigma'_{yy} tan\varphi_{f} + c_{f} \tag{45}$$

And the tensile yield criterion for the NF is represented by:

$$f^{t} = \sigma^{t}_{f} - `\sigma'_{yy} \tag{46}$$

where σ^{t}_{f} is the tensile limit of the fractures.

The shear and tensile potential functions (g^{S}, and g^{t}) correspond to non-associated flow rules with dilatancy, ψ_{f}, as follows:

$$g^S = -`\tau - `\sigma'_{yy}\, tan\, \psi_f \tag{47}$$

$$g^t = -`\sigma'_{yy} \tag{48}$$

Non-associated flow rule for the shear and tensile yield are defined as follows (Fjar et al., 2008):

$$\Delta e^P_{ij} = \lambda_S \frac{\partial g^s}{\partial \sigma_{ij}} \tag{49}$$

$$\Delta e^P_{ij} = \lambda_t \frac{\partial g^t}{\partial \sigma_{ij}} \tag{50}$$

where λ_S and λ_t are the constants of proportionality for shear and tensile yield modes, respectively, and superscript "p" stands for "plastic".

Combining Eq. (47) and Eq. (49), plastic strain increments due to the shear yield along the fracture are expressed as follows:

$$\begin{bmatrix} \Delta`e^P_{xx} \\ \Delta`e^P_{yy} \\ \Delta`e^P_{zz} \\ \Delta`e^P_{xy} \end{bmatrix} = \begin{bmatrix} 0 \\ -\lambda_S\, tan\, \psi_f \\ 0 \\ -\lambda_S \end{bmatrix} \tag{51}$$

Plastic strain increments due to tensile yielding can be obtained by combining Eq. (48) and (50):

$$\begin{bmatrix} \Delta`e^P_{xx} \\ \Delta`e^P_{yy} \\ \Delta`e^P_{zz} \\ \Delta`e^P_{xy} \end{bmatrix} = \begin{bmatrix} 0 \\ -\lambda_t \\ 0 \\ 0 \end{bmatrix} \tag{52}$$

Elastic strain increments are obtained by subtracting the plastic strain increments from the total strain increments. Assuming that the plastic contributions of intact rock and NFs are additive, the elastic guesses in Eq. (43) are the stresses here, obtained after the application of plastic corrections related to the yielding of intact material. Using this approach, it may be shown that the new stress state in the case of shear and tensile yield may be expressed as follows, respectively.

$$\begin{bmatrix} `\sigma'_{xx}{}^{N} \\ `\sigma'_{yy}{}^{N} \\ `\sigma'_{zz}{}^{N} \\ `\tau^{N} \end{bmatrix} = \begin{bmatrix} `\sigma'_{xx} \\ `\sigma'_{yy} \\ `\sigma'_{zz} \\ `\tau \end{bmatrix} + \begin{bmatrix} `K(1,2)\, tan\, \psi_f\, \lambda_S + `K(1,4)\lambda_S \\ `K(2,2)\, tan\, \psi_f\, \lambda_S + `K(2,4)\lambda_S \\ `K(3,2)\, tan\, \psi_f\, \lambda_S + `K(3,4)\lambda_S \\ `K(4,2)\, tan\, \psi_f\, \lambda_S + `K(4,4)\lambda_S \end{bmatrix} \tag{53}$$

$$\begin{bmatrix} `\sigma'_{xx}{}^{N} \\ `\sigma'_{yy}{}^{N} \\ `\sigma'_{zz}{}^{N} \\ `\tau^{N} \end{bmatrix} = \begin{bmatrix} `\sigma'_{xx} \\ `\sigma'_{yy} \\ `\sigma'_{zz} \\ `\tau \end{bmatrix} + \begin{bmatrix} `K(1,2)\lambda_t \\ `K(2,2)\lambda_t \\ `K(3,2)\lambda_t \\ `K(4,2)\lambda_t \end{bmatrix} \tag{54}$$

where superscript "*N*" stands "new stress state", and $`K(i,j)$ is the component of stiffness matrix.

Considering that the new stresses should lie on the shear yield envelope, shear constant of proportionality may be calculated by combining Eq. (45) and Eq. (53), and expressed as follows:

$$\lambda_S = \frac{f^{s}\left(`\sigma'_{yy}, `\tau\right)}{\left(`K(4,2)\, tan\, \psi_f + `K(4,4) + `K(2,2)\, tan\, \psi_f\, tan\, \varphi_f + `K(2,4)\, tan\, \varphi_f\right)} \tag{55}$$

Using the same reasoning as described above, tensile constant of proportionality may be calculated by combining Eq. (46) and Eq. (54), and expressed as:

$$\lambda_t = \frac{f^{t}\left(`\sigma'_{yy}\right)}{`K(2,2)} \tag{56}$$

Finally, after calculating the new stresses in the local coordinate system, the stresses resolve back into the global coordinate system by using Eq. (42).

The aforementioned yield criterion is adequate to consider the effect of a single fracture set. To consider the effect of multiple fracture sets, one yield criterion for each single fracture set is added. The proposed AU constitutive law is capable of considering shale intrinsic anisotropy in elastic and plastic ranges. In addition, it is capable of considering the effect of multiple fracture sets in the caprock. The criterion was imbedded in FLAC software (ICG, 2011) for the caprock integrity analysis and the MOP assessment in SAGD projects. Detailed formulation of the AU model is presented in Appendix A and the coding and implementation of the model is presented in Appendix B.

3.3.2 Verification of the proposed AU constitutive model

One issue for the verification of AU constitutive law was the lack of testing data to compare the results with. Therefore, verification of the AU constitutive law was divided to two separate parts.

The first part was designed to verify the transversely elastic isotropy and intrinsic plastic anisotropy of the constitutive law without involving natural fractures. The results of the numerical model with the AU model were verified against (1) the results of Uniaxial Compressive Strength (UCS) data presented by Xu et al. (2010), and (2) numerical analysis of a triaxial test by FLAC assuming isotropic strength properties.

The second part was designed to include natural fractures. Results of the numerical model were compared to the results of numerical triaxial tests using the built-in Ubiquitous joint model of FLAC software.

3.3.2.1 Verification of the AU constitutive law for transversely elastic isotropy and intrinsic anisotropy

The AU constitutive law was verified against numerical triaxial and UCS data in the literature.

3.3.2.1.1 Model geometry and boundary conditions

Model geometry and boundary conditions of the numerical UCS and triaxial tests are presented in Figure 3.4. It is common to simulate triaxial experiments using an axisymmetric configuration; however, an axisymmetric configuration does not allow localization of deformation. Therefore, a plane strain configuration was used for the simulation of UCS and triaxial test in this study.

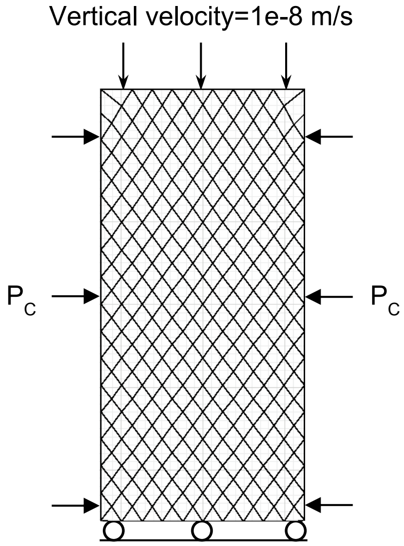

Figure 3.4 Model geometry of triaxial and UCS tests

The triaxial samples are 1 in. (2.54 cm) in diameter and 2 in. (5.08 cm) in length. The bottom boundary of the finite element mesh was fixed in the vertical direction. The radial and axial loads were applied on the boundaries, and then a small velocity (1e-8 m/s) in the vertical direction was applied on the top boundary.

3.3.2.1.2 Verification of the AU model against numerical UCS data

Xu et al. (2010) extended the isotropic Drucker-Prager strength criterion to an anisotropic elasto-plastic constitutive model for layered rock masses. They embedded the anisotropic constitutive model in ABAQUS software. The proposed constitutive law in this study was used to simulate the same model. Table 3.1 lists the model parameters. Mohr-Coulomb strength parameters were obtained using the relationships between the Mohr-Coulomb and Drucker-Prager strength parameters (Xu et al., 2010).

Table 3.1 The properties of the AU verification model (after Xu et al., 2010)

Property	**Value**	**Property**	**Value**	**Property**	**Value**
$E_x\ (MPa)$	21,000	$\theta_{min,\varphi}$ (°)	45	D_2	0.24
$E_y\ (MPa)$	12,000	$B_1\ (MPa)$	0.67	n	4
υ_{xy}	0.25	$B_2\ (MPa)$	0.67	m	2
υ_{yx}	0.2	C_1	1.27	$A_1\ (MPa)$	1.63
$G_{xy}\ (MPa)$	8,750	C_2	1.27	$A_2\ (MPa)$	1.63
$\theta_{min,C}$ (°)	45	D_1	0.24	☒	☒

A series of numerical UCS analysis was conducted for different loading directions by using the proposed anisotropic elasto-plastic constitutive model. In these analyses, the angle between the applied load and the horizontal direction (θ) changed from 0° to 90° in 10° increments.

The results of UCS test and the comparison with the results presented by Xu et al. (2010) are shown in Figure 3.5. It can be seen that the results of the proposed model and the results presented by Xu et al. (2010) are in close agreement.

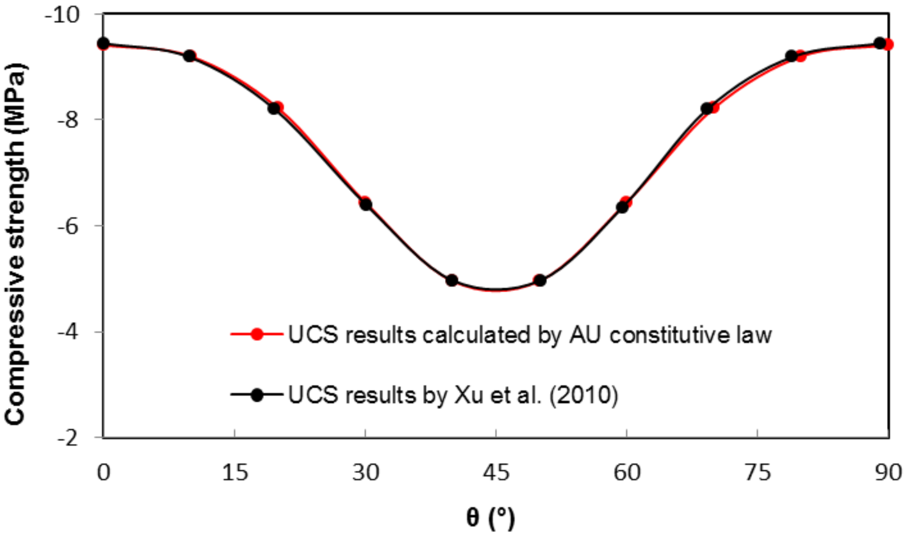

Figure 3.5 Results of the UCS tests for the verification model

3.3.2.1.3 Validation of the AU model against experimental triaxial data

The proposed constitutive model was validated against experimental triaxial tests. The experimental data are from upper Toarcian massive shale taken from Tournemire site in Massif Central (France). Detailed experimental data can be found in Niandou (1994) and Niandou et al. (1997). The elastic constants for Tournemire shale have been identified in Niandou (1994). The following values have been assigned:

Table 3.2 Values of elastic constants for Tournemire shale (after Niandou et al., 1997)

Property	**Value**	**Property**	**Value**
$E_x\ (MPa)$	35,000	υ_{xy}	0.4
$E_y\ (MPa)$	13,000	υ_{yx}	0.22
		υ_{xz}	0.17

Duveau et al. (2001) showed the variation of Tournemire shale strength with orientation for three different confining pressures based on the triaxial tests have been done by Niandou (1994). Figure below shows the variation of material strength with orientation at different confining pressures.

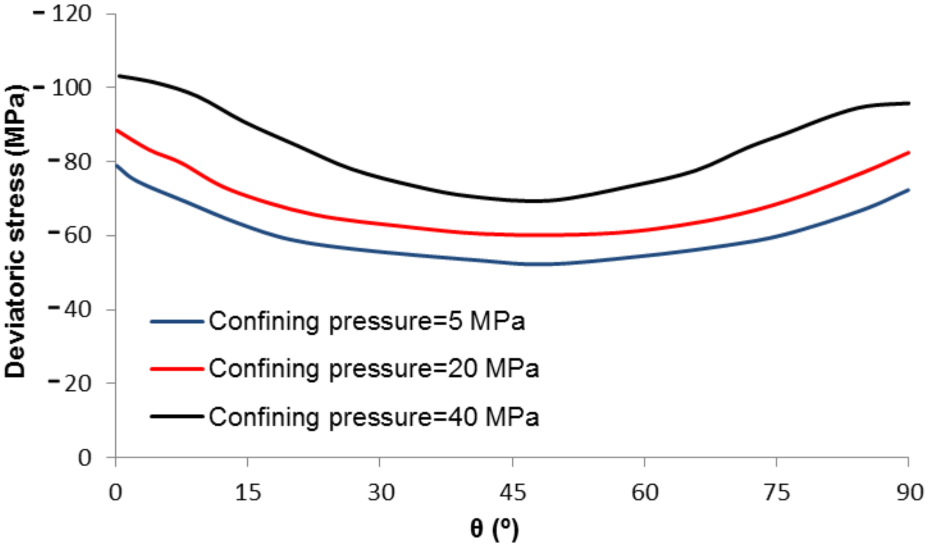

Figure 3.6 Strength variation vs orientation (after Duveau et al., 2001)

Figure below shows the comparison between numerical model predictions and experimental data for horizontal and vertical cores at the confining pressure of 40 MPa. The results show a good agreement between the numerical model results and experimental data for the case of θ=0, 90°. For the case of θ=45°, results show a good agreement in the elastic region. All of the cases predict the strength of the sample to be the same as what is shown in Figure 3.6 at the confining pressure of 40 MPa.

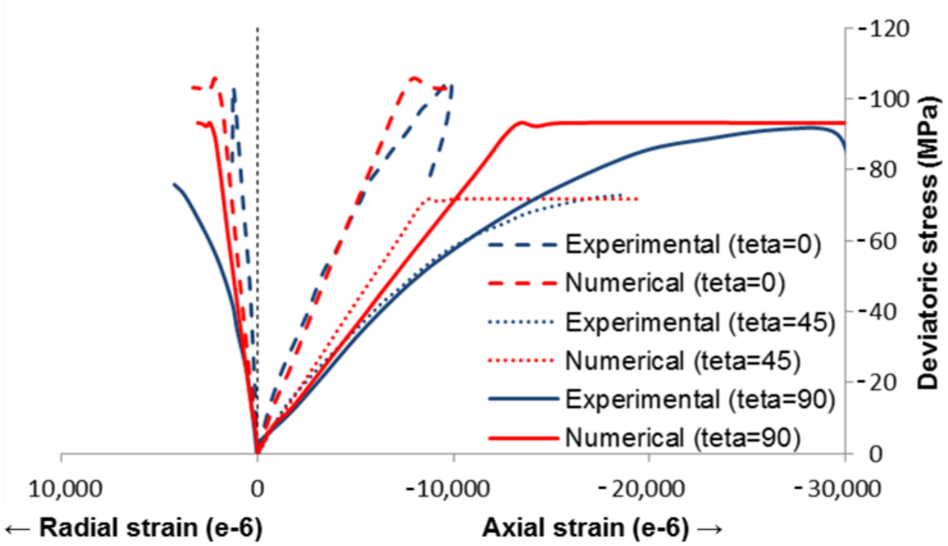

Figure 3.7 Comparison of calculated and measured data for θ=0, 45, and 90° and confining pressure of 40 MPa

3.3.2.1.4 Verification of the AU model against numerical triaxial data

The proposed constitutive model was verified against the results of numerical triaxial data from the literature. Both models used isotropic elastic and strength parameters. In both cases, MC criterion was used within an elastic-perfectly plastic framework, which means all elastic and strength properties were assigned the same values in different directions in the proposed model. Table 3.3 shows the model parameters for the MC strength criterion and AU constitutive model.

Table 3.3 Strength parameters of the verification model

Property	**Value**	**Property**	**Value**
Young's modulus (MPa)	4,830	**Cohesion (MPa)**	9.03
Poisson's ratio	0.12	**Friction angle (°)**	25
Bulk modulus (MPa)	2.12e3	**Dilation angle (°)**	16
Shear modulus (MPa)	2.16e3	**Tensile limit (MPa)**	0

Numerical analysis was performed for two different confining pressures (P_C=2.89, 6.89 MPa). Figure 3.8 compares the results of the numerical analysis with the literature data. Results indicate a perfect match.

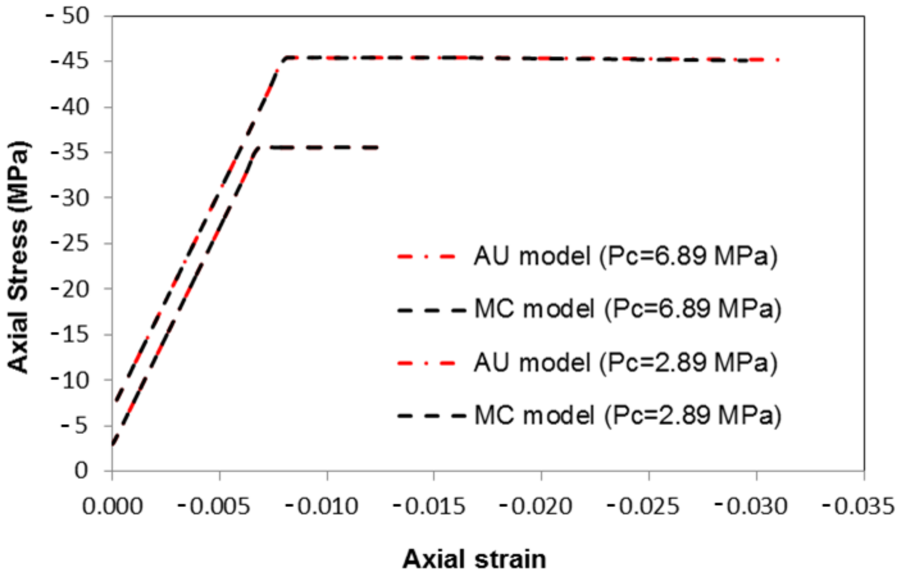

Figure 3.8 Axial stress vs. strain for the triaxial tests in the verification model

3.3.2.2 Verification of the AU model against Ubiquitous Joint model in FLAC

A series of numerical triaxial tests was performed to verify the AU constitutive law against the built-in Ubiquitous Joint model of FLAC. Isotropic elastic and strength properties were assumed as the Ubiquitous Joint model in FLAC is isotropic. One set of NFs with different dip angles for different cases ($\xi = 0°, 60°, 80°$) was considered for the triaxial tests (Figure 3.9). The mesh design of the numerical model is depicted in Figure 3.10. Confining pressure of 2.14 kPa was considered in all tests performed here.

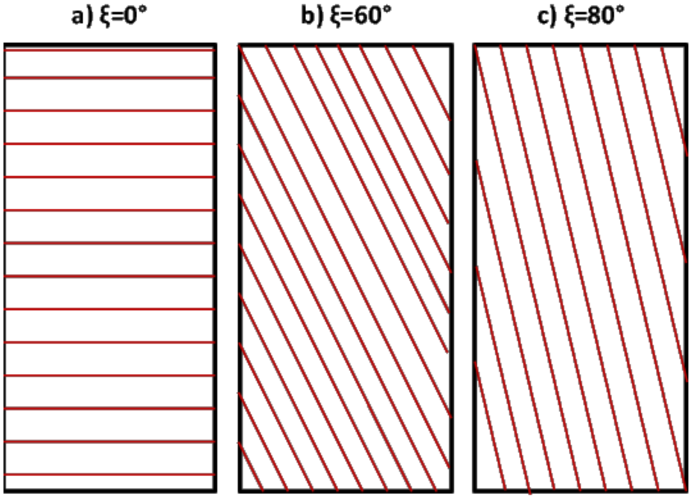

Figure 3.9 Schematic of triaxial samples and different dip angles of NFs

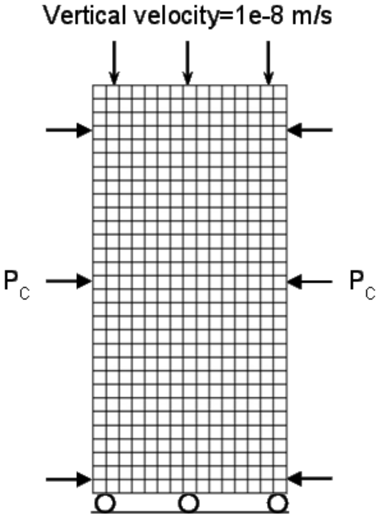

Figure 3.10 Model geometry, boundary conditions, and mesh deign of triaxial tests

Strength properties of the rock samples and also NFs are listed in Table 3.4 and Table 3.5, respectively.

Table 3.4 Strength properties of the rock matrix

Property	**Value**	**Property**	**Value**
Young's modulus (MPa)	350	**Cohesion (MPa)**	0.2
Poisson's ratio	0.25	**Friction angle (°)**	25

Table 3.5 Strength properties of natural fractures

Property	**Value**
Cohesion (MPa)	0
Friction angle (°)	15
Tensile limit (MPa)	0

Figure 3.11 to Figure 3.13 show the axial stress against axial strain for both models for NFs with different dip angles (0°, 60°, and 80°). Results of the FLAC built-in Ubiquitous joint model and the proposed AU model are in close agreement in the elastic range and they have the same peak yield points for different dip angles. However, there are some inconsistencies after the yield point in the figures. These inconsistencies could be due to different truncation errors of the built-in and the AU constitutive models. The max difference between the calculations of the two models is 4% and it is related to the case with the dip angle of 60° (Figure 3.12).

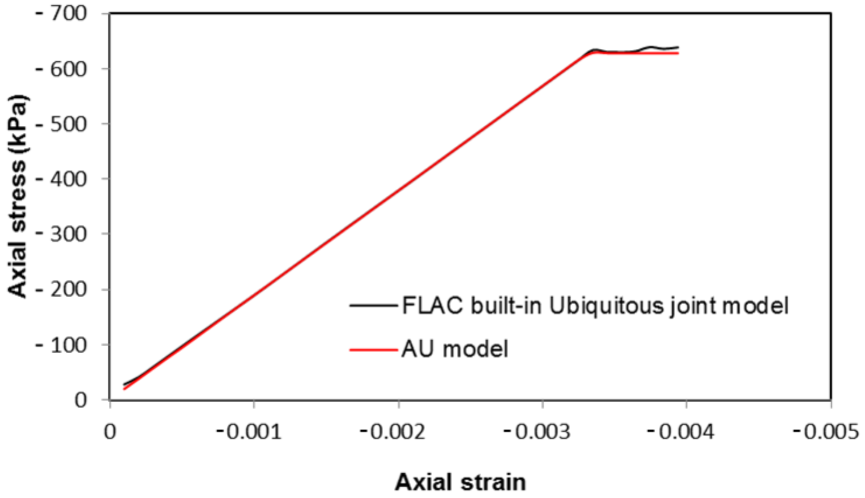

Figure 3.11 Axial stress vs. strain for fracture dip angle=0°

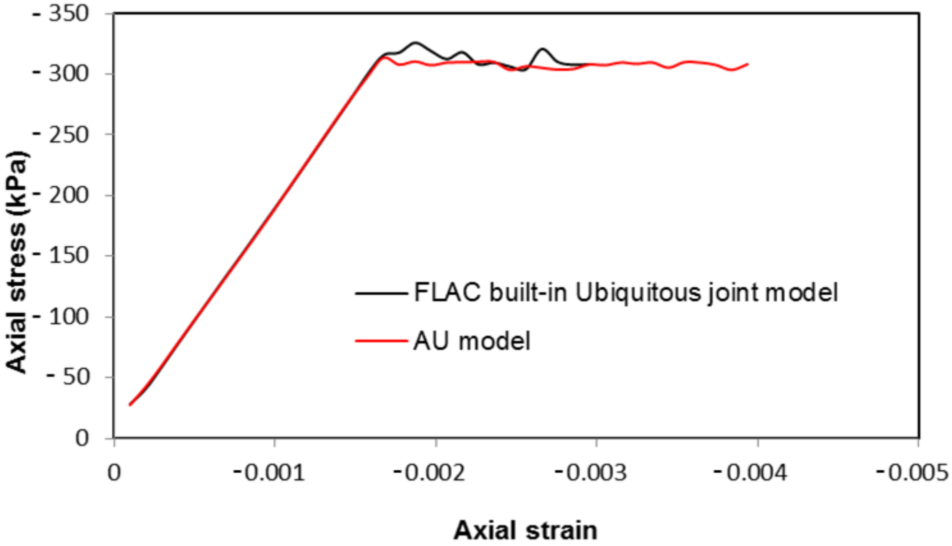

Figure 3.12 Axial stress vs. strain for fracture dip angle=60°

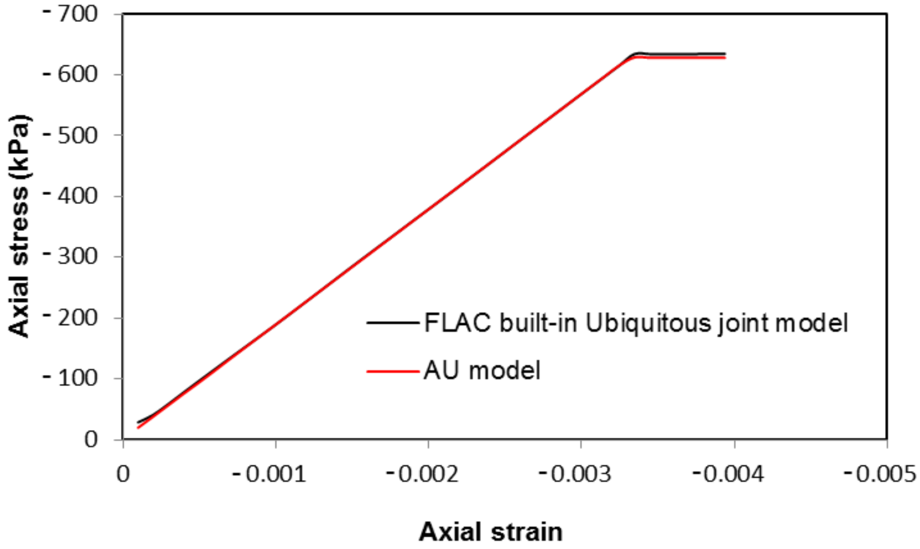

Figure 3.13 Axial stress vs. strain for fracture dip angle=80°

A series of numerical triaxial tests was performed to explore the effect of NFs on the results. Three cases were simulated: (1) No NFs, (2) NFs with dip angle=60°, and (3) NFs with dip angle=70°. The results are presented in Figure 3.14, which indicate significant difference in the yield points among these three cases.

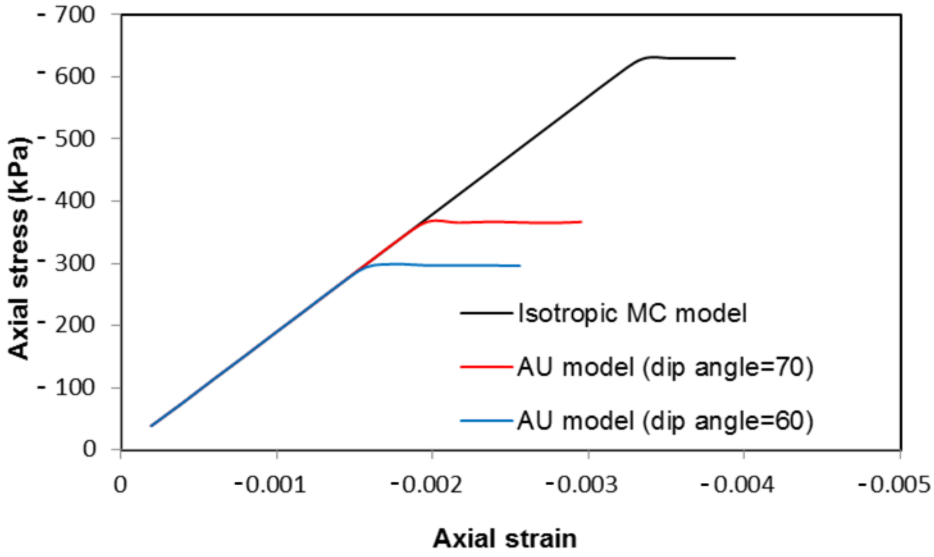

Figure 3.14 Axial stress vs. strain for the cases with: (1) No NFs, (2) NFs with ξ=60°, and (3) NFs with ξ=70°

3.4 Sequential coupling scheme and verification

Fluid and heat flow in SAGD operations change the state of stress, deformation, and temperature in the caprock (Azad and Chalaturnyk, 2011). To capture different phenomena involved in the SAGD operation, a coupled hydro-thermo-mechanical model is required, which is described herein.

3.4.1 Coupled hydro-thermo-mechanical model

Two commercial finite difference software packages (FLAC, geomechanical module developed by ITASCA (ICG, 2011) and STARS, fluid flow simulator developed by Computer Modeling Group (CMG, 2013) were linked to perform the simulations. A MATLAB code was used as an interface to run the modules and also update the shared parameters (Figure 3.15). In each time step, simulations were iterated between FLAC and STARS. The flow simulator calculated the pressures and temperatures that were transferred to the geomechanical module where deformations and stresses were calculated. The deformations were then used to update the porosities and permeabilities in the entire reservoir space by using Eq. (57)-(58) proposed by Touhidi-Baghini (1998).

$$ln\left(\frac{k}{k_0}\right) = \frac{\beta}{\phi_0}\varepsilon_V \tag{57}$$

$$\phi = \frac{\phi_0 + \varepsilon_V}{1 + \varepsilon_V} \tag{58}$$

where ε_V is volumetric strain, k is permeability, ϕ is porosity, and the subscript ‘0’ indicates initial permeability and porosity. In this study, β was assumed to be 2 and 5 for horizontal and vertical permeability, respectively (Azad and Chalaturnyk, 2011).

The updated porosities and permeabilities were then transferred to STARS for the next flow-temperature iteration. In each time step, the iterations continued till convergence was achieved within 5% tolerance for the maximum difference for pressures, temperatures, porosities, and permeabilities between two subsequent iterations.

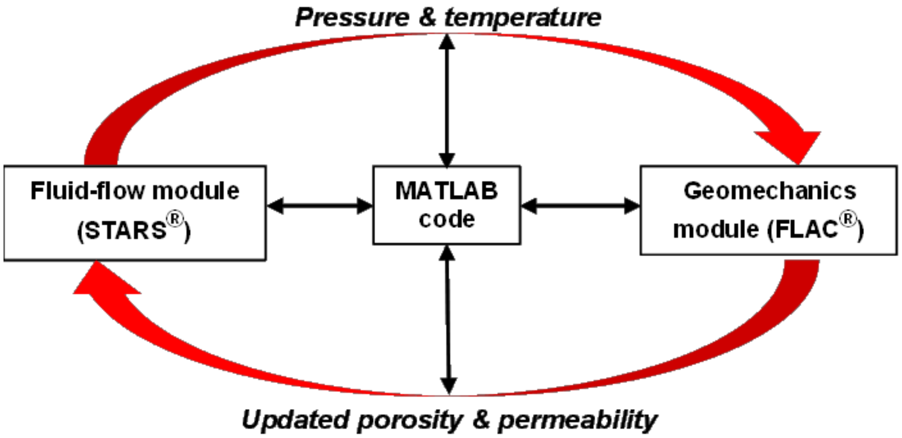

Figure 3.15 Sequential coupling scheme (after Rahmati et al., 2015)

3.4.2 Verification of coupled hydro-thermo-mechanical model

Results of the linked hydro-thermo-mechanical package (STARS-FLAC) were compared against the outcome of hydro-thermo-mechanical analysis by STARS. A synthetic case study with simplistic assumptions was considered for verification purpose.

3.4.2.1 Model geometry and boundary conditions

One well pair was modeled assuming 2-D plain strain conditions (see Figure 3.16). Plain strain condition considers no deformation along the horizontal well. The model length and depth were chosen large enough to minimize boundary effects on the results (Figure 3.16).

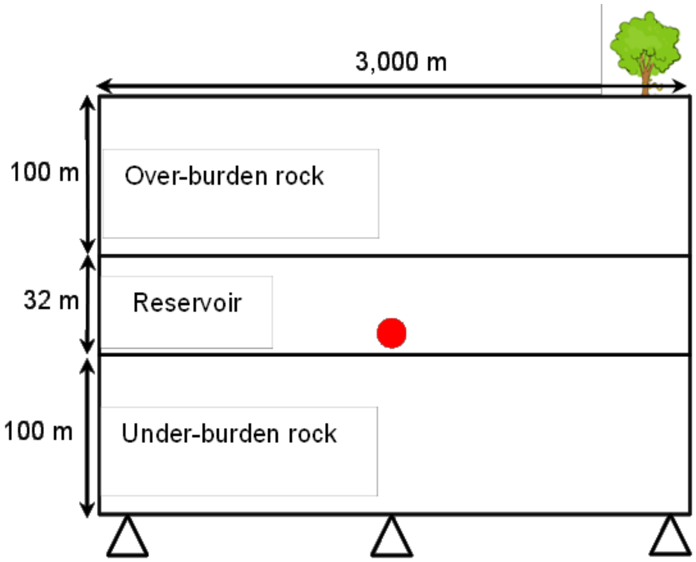

Figure 3.16 Model geometry

The model was fixed in the horizontal direction at the vertical boundaries. The bottom of the model was also fixed in the vertical direction. A uniform mesh size (4 m by 4 m) was used in both models (Linked model and STARS model). The coupling scheme for the linked model is presented in section 3.4.1.

3.4.2.2 Input data

3.4.2.2.1 Hydraulic, thermal, and mechanical properties

Over-burden rock, reservoir, and under-burden rock were assumed to be the Clearwater shale, McMurray formation, and Devonian limestone, respectively. Hydraulic, thermal and mechanical input data are summarized in Table 3.6, Table 3.7, and Table 3.8, respectively. These data have been obtained from laboratory tests, geophysical logs, and field data in published papers and reports for Alberta oil sand projects.

Table 3.6 Permeability for different layers

Zone	**Horizontal permeability** $(\mathbf{mD})$	**Vertical permeability** $(\mathbf{mD})$	**Reference**
Clearwater shale	0.001	0.001	AER, 2014
McMurray formation	6400	3400	Petro-Canada Corp. (2005b)
Devonian limestone	[1]115	[2]0.001	[1]Uwiera-Gartner (2011) [2]Thomas and Sands (2010)

Table 3.7 Thermal properties of the reservoir sand

Parameter	**Value**	**Reference**
Rock Expansion Coefficient $(\mathbf{1}/_{\mathbf{C}})$	3.84e-5	Chalaturnyk (1996)
Rock Thermal Conductivity $(\mathbf{W}/_{\mathbf{m.°K}})$	1.736	Chalaturnyk (1996)
Rock Heat Capacity $(\mathbf{kJ}/_{\mathbf{kg.°K}})$	1865	Chalaturnyk (1996)

Table 3.8 Isotropic geomechanical properties for different layers

Zone	Layer	Parameter	Value	Reference
Over-burden	Clearwater shale	Young's modulus (MPa)	175	Kosar (1989)
		Poisson's ratio	0.13	Thomas and Sands (2010)
		Cohesion (kPa)	200	Thomas and Sands (2010)
		Friction angle (°)	25	Thomas and Sands (2010)
Reservoir	McMurray formation	Young's modulus (MPa)	500	Li et al. (2005)
		Poisson's ratio	0.3	Li and Chalaturnyk (2009)
		Cohesion (kPa)	0	Chalaturnyk, (1996)
		Friction angle (°)	35	Li et al. (2005)
Under- burden	Devonian limestone	Young's modulus (MPa)	1,500	Chalaturnyk (1996)
		Poisson's ratio	0.3	Thomas and Sands (2010)
		Cohesion (kPa)	200	Thomas and Sands (2010)
		Friction angle (°)	40	Thomas and Sands (2010)

3.4.2.2.2 In-situ stresses

Figure 3.17 presents the in-situ stress and initial pore pressure profiles for verification purpose.

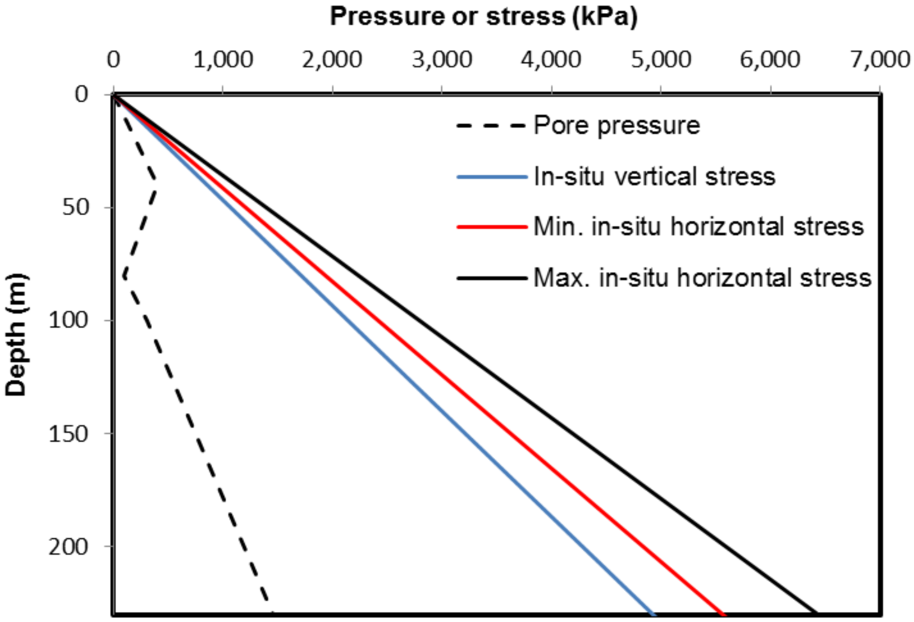

Figure 3.17 In-situ stress and pore pressure profiles

3.4.2.3 Comparison of the results of the linked model with STARS model

The results of linked hydro-thermo-mechanical model are compared with the results of STARS model in terms of stresses and deformations. The models simulated the first 60 days of injection-production operation. In this part, the operational constraints for the producer were considered to be the minimum Bottom Hole Pressure (BHP) of 500 kPa, steam trap of 10 °C, and maximum surface liquid rate of 0.2 m^3/day; injector constraints were considered to be the maximum BHP of 1700 kPa, and maximum surface water rate of 0.2 m^3/day. Results are correspond to those at the end of 60 days.

Figure 3.18 shows the measured heave for FLAC-STARS and STARS models at the surface. The results demonstrate a close agreement between the linked FLAC-STARS and STARS models. The maximum heave difference was found to be 4.49%. This difference is believed to be due to the different calculation schemes of FLAC and STARS software. For instance, FLAC uses nodal based calculations for pore pressure while STARS employs element based finite difference scheme.

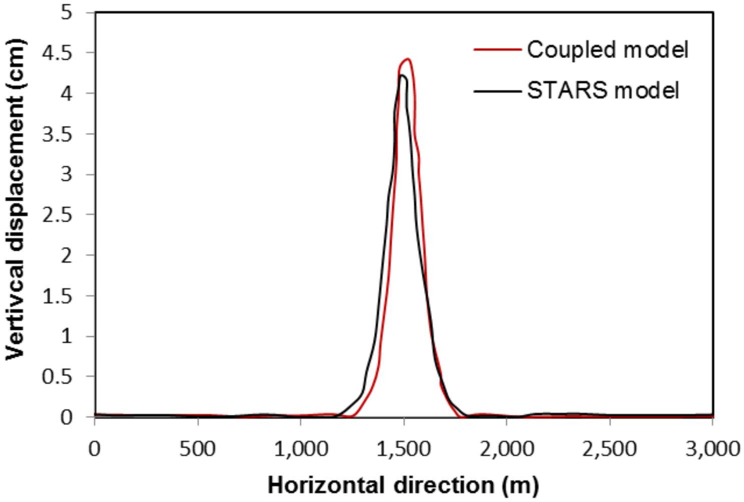

Figure 3.18 Comparison of calculated heave between the coupled and STARS model

Figure 3.19 and Figure 3.20 present the total vertical stress for horizontal profiles at 65 m and 110 m depth, respectively. Using the in-situ stress as the reference stress, the maximum differences between the profiles at 65 m and 110 m depth are 0.69% and 2.86%, respectively.

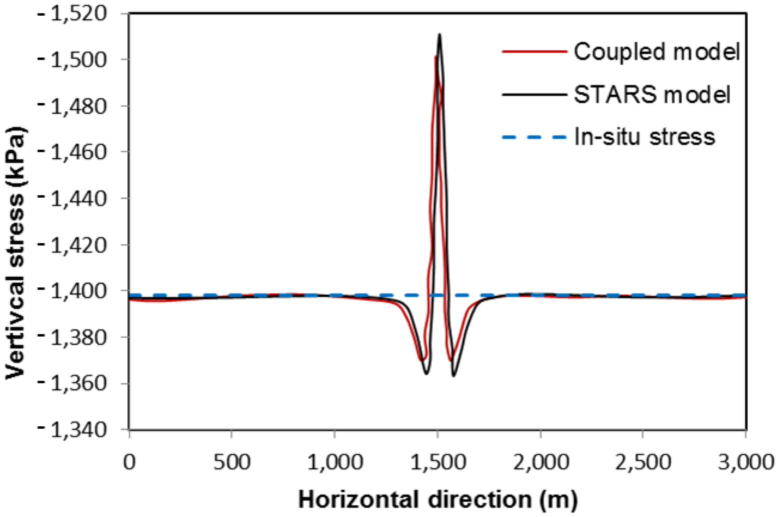

Figure 3.19 Comparison of the total vertical stress between FLAC-STARS and STARS models at 65 m depth

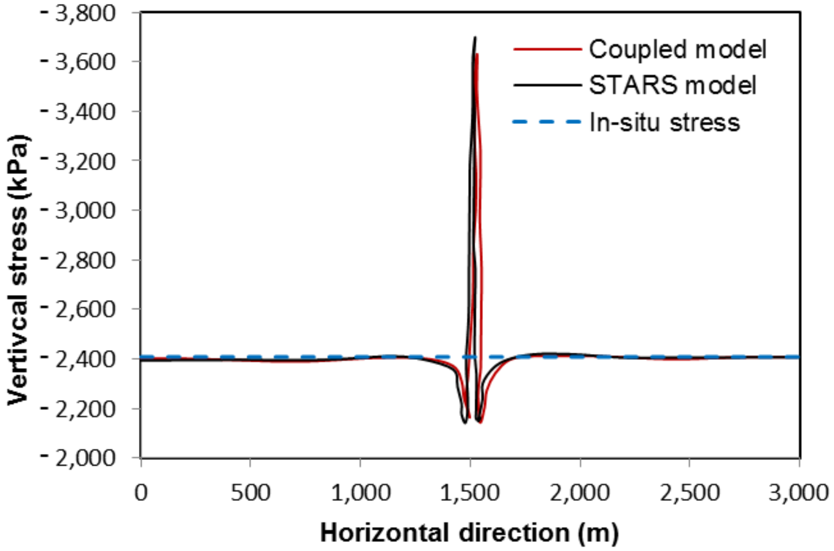

Figure 3.20 Comparison of the total vertical stress between the FLAC-STARS and STARS models at 110 m depth

Figure 3.21 shows the total horizontal stresses for a vertical section that passes through the injector and producer. The result show a general agreement but a sizeable maximum difference the horizontal stresses. The difference could be due to the different solution schemes for FLAC and STARS. FLAC software uses nodal based finite difference scheme while STARS uses the element based finite difference method. Also, mapping of coupling parameters in the coupled model and STARS model are different. Another source of difference could be due to the different truncation errors for FLAC and STARS and, therefore, different cumulative errors in the calculations.

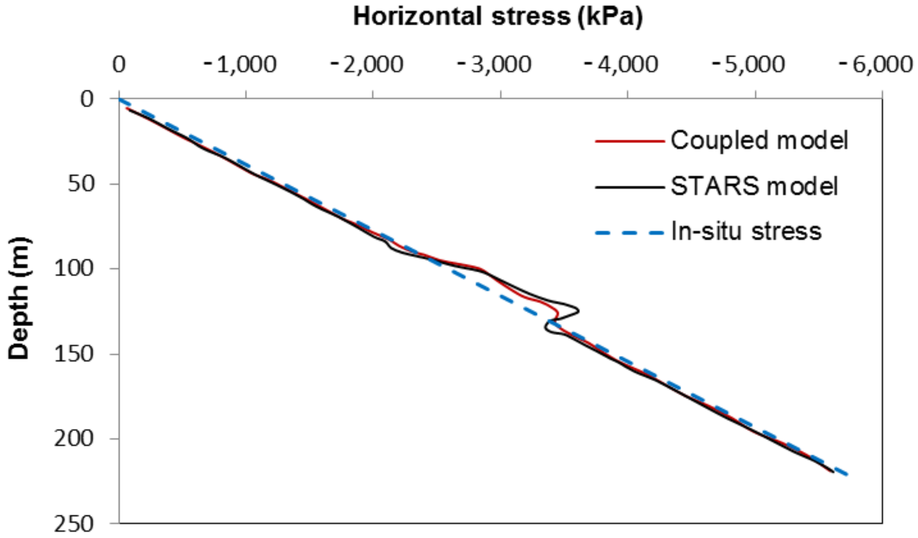

Figure 3.21 Comparison of the total horizontal stress between the FLAC-STARS and STARS models

3.5 Conclusions

In this chapter, a coupled hydro-thermo-mechanical model was developed for the assessment of caprock integrity based on the sequential coupling scheme. In this coupled model, two commercial software packages were linked together (FLAC (ICG, 2011), and STARS (CMG, 2013)) by a MATLAB code. The coupled model was verified against STARS software for a hypothetical case study. The results showed close agreement between the results of the two models.

An Anisotropic Ubiquitous (AU) constitutive model was developed to consider the effect of shale anisotropy in SAGD caprock studies. The proposed AU constitutive law is capable of considering shale intrinsic anisotropy in elastic and plastic ranges. In addition, it is capable of considering the effect of multiple fracture sets in the caprock. The criterion was imbedded in FLAC software (ICG, 2011) for the MOP assessment in SAGD projects. The proposed AU constitutive model was verified against the results of numerical triaxial and UCS tests. The results showed a good match for the attempted cases.

Chapter 4: Numerical assessment of the MOP in SAGD projects considering intrinsic anisotropy of the cap shale

4.1 Introduction

This chapter investigates the effect of intrinsic anisotropic behavior of caprock shales on the MOP in SAGD projects. As discussed in Chapter 2, shales and mudstones exhibit strong anisotropy at the micro and macro scales. However, the anisotropic behavior has been neglected in the existing published works on caprock integrity assessment.

In this chapter, the coupled hydro-thermo-mechanical model and the AU constitutive model (see Chapter 3) were utilized for the assessment of caprock integrity for a SAGD site. The coupled tool was validated against field data and employed in a case study to determine the effect of shale intrinsic anisotropic behavior on the MOP.

This chapter demonstrates the importance of capturing shale anisotropy in the accurate prediction of the MOP in SAGD projects. The role of shale anisotropy is highlighted by comparing the results of the AU constitutive model and isotropic model. Results display the effect of shale anisotropy on the caprock response in terms of deformations, stresses and failure pressure. The assumption of isotropic shale behavior in caprock integrity assessment for the case study resulted in the overestimation of the MOP by about 7%.

4.2 Case study

The importance of including cap shale's intrinsic anisotropy in caprock studies is demonstrated by presenting the results of a case study. We selected Pad C of MacKay River oil sands project (Suncor Energy, 2009) located northwest of Fort McMurray, Alberta, Canada (Figure 4.1) for the case study.

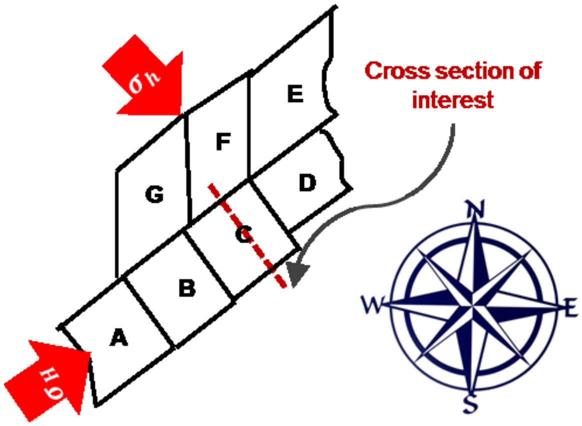

Figure 4.1 Cross section of interest in relation to in-situ stresses in Pad C, MacKay River SAGD Project (after Suncor Energy, 2013)

4.3 Geometry and boundary conditions of the numerical model

A cross section of Pad C was simulated by assuming 2-D plane strain condition (no deformation along the horizontal wells). This approach is deemed applicable for this problem because (1) the length of wellbores is large in comparison with the distance between the wells; (2) thermocouple measurements show uniform distribution of temperature along the producers (Suncor Energy, 2013). The latter indicates relatively uniform steam injection and production along the wells.

Log data for Pad C indicate the thicknesses of different formations from top to bottom: Quaternary Deposits (40 m), Clearwater shale (40 m), Wabiskaw member (20 m), McMurray formation (30 m), and Devonian limestone (300 m).

Clearwater formation, which is considered as the main caprock (Southern Pacific Resource Corp., 2011), consists of different layers of mudstone, shale, siltstone and sandstone. For simplicity, Clearwater formation shale was assumed as homogenous anisotropic shale in terms of mechanical properties. Similarly, Wabiskaw member, which consists, from top to bottom, of (1) Wabiskaw A shale, (2) gas-saturated Wabiskaw C sand, and (3) the lower-most Wabiskaw D mudstone (ERCB, 2010), was considered as a homogenous layer with mechanical properties equivalent to Wabiskaw A shale.

There are six well pairs called C1 to C6 in Pad C. In this study, symmetry was assumed and only half of the pad which includes well pairs C4 to C6 was simulated. Figure 4.2 shows the model geometry. The model length and depth were chosen large enough to minimize boundary effects on the results.

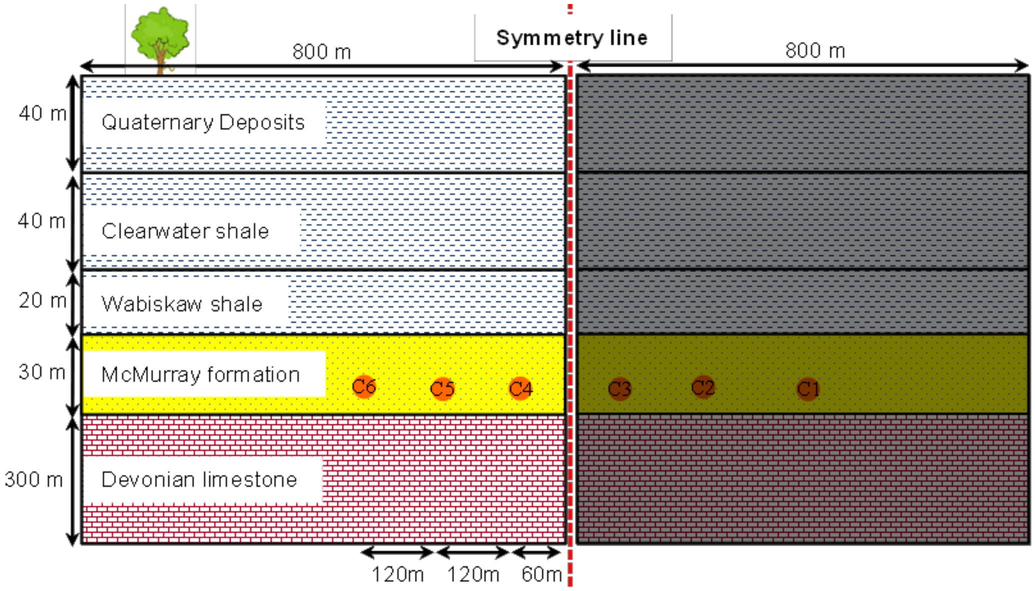

Figure 4.2 Model geometry

Side boundaries of the model were fixed in the horizontal direction and the bottom boundary was fixed in the vertical and horizontal directions. Preheating period of 90 days was simulated and the pad production was simulated using the injection and production data from September 2002 to January 2008.

4.4 Numerical mesh design

Figure 4.3 shows the mesh design of the model for the geomechanical analysis. Different element sizes were used in the geomechanical model to reduce the computation time of the coupled model. Continuous 2 m × 1 m element size was used in the fluid flow simulator (see Figure 4.4). The total number of elements in the geomechanical and fluid flow models were 26,500, and 92,000, respectively. Coupling parameters (pressure, temperature, porosity, and permeability) were mapped from one module to another by using the cubic spline data interpolation method (Michiel, 2001).

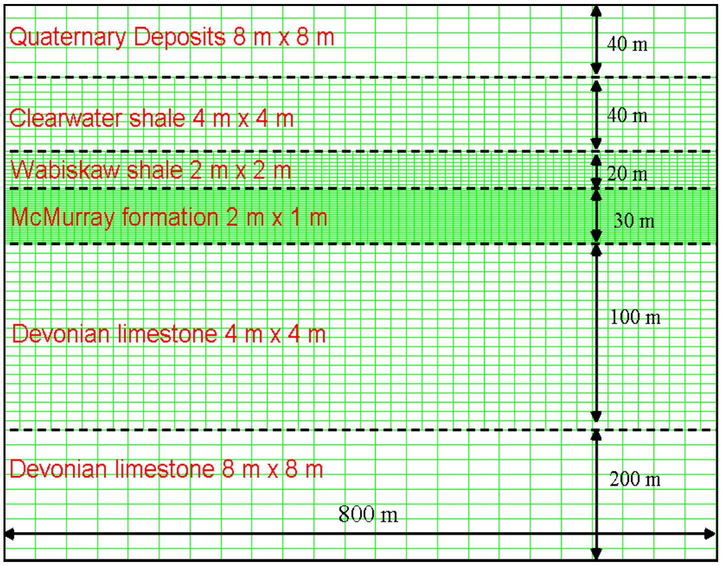

Figure 4.3 Grid-block design for the Geomechanical module

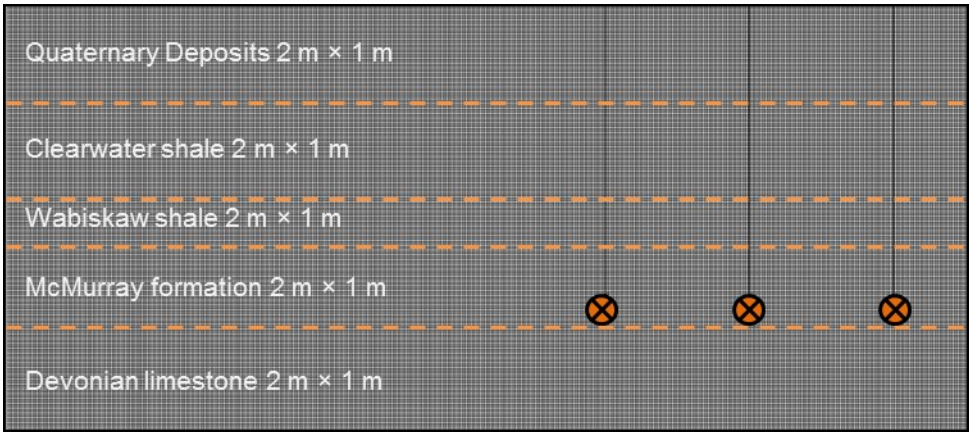

Figure 4.4 Grid-block design for the fluid flow module

4.5 Input data

We used public data related to Pad C of MacKay River oil sands project for this case study. Some input data were assumed as they were not publically available. Thus, this work should not be regarded as caprock integrity investigation for this particular project. It should only be regarded as an effort to understand the impact of intrinsic anisotropy of cap shale on the MOP in SAGD projects.

4.5.1 Hydraulic, thermal, and mechanical properties

Hydraulic, thermal and mechanical input data are summarized in Table 4.1, Table 4.2, and Table 4.3, respectively. These data have been obtained from laboratory tests, geophysical logs, and field data in published papers and reports for Alberta oil sand projects but not specifically for MacKay River SAGD project. In the tables, the data that specifically relate to MacKay River project are italicized.

Table 4.1 Permeability of different layers

Zone	Horizontal permeability (mD)	Vertical permeability (mD)	Reference
Clearwater shale	0.001	0.001	AER (2014)
Wabiskaw A shale	0.001	0.001	ERCB (2010)
Wabiskaw C sand	2,000	2,000	ERCB (2010)
Wabiskaw D mudstone	0.001	0.001	ERCB (2010)
McMurray formation	*6,400*	*3,400*	Petro-Canada Corp. (2005b)
Devonian limestone	[1]115	[2]0.001	[1]Uwiera-Gartner (2011) [2]Thomas and Sands (2010)

Table 4.2 Thermal properties of the reservoir sand

Parameter	Value	Reference
Expansion Coefficient ($^{1}/_{C}$)	3.9e-5	Kosar (1989)
Thermal Conductivity ($^{W}/_{m.\,°K}$)	1.736	Chalaturnyk (1996)
Heat Capacity ($^{kJ}/_{kg.\,°K}$)	1865	Chalaturnyk (1996)

Note the mechanical properties in Table 4.3 have been obtained by laboratory testing on vertical core samples (i.e., sample axis being perpendicular to sedimentary layers). For Quaternary deposits, McMurray sand, and Devonian limestone, the same properties were assumed to be valid for all other directions. For Clearwater and Wabiskaw shale, the numbers were assumed to apply only for the vertical direction and determined the values of the properties in all other directions as discussed in the next section.

Table 4.3 Isotropic geomechanical properties of the caprock and underburden layers

Layer	Parameter	Value	Reference
Quaternary Deposits	Young's modulus (MPa)	25	Uwiera-Gartner et al. (2011)
	Poisson's ratio	0.45	Uwiera-Gartner et al. (2011)
	Cohesion (kPa)	200	Thomas and Sands (2010)
	Friction Angle (°)	25	Thomas and Sands (2010)
Clearwater shale	Young's modulus (MPa)	[1]$E=-76.67\sigma'_3+23.33$	Kosar (1989)
	Poisson's ratio	0.13	Thomas and Sands (2010)
	Cohesion (kPa)	200	Thomas and Sands (2010)
	Friction angle (°)	25	Thomas and Sands (2010)
Wabiskaw shale	Young's modulus (MPa)	250	Kosar (1989)
	Poisson's ratio	0.15	Kosar (1989)
	Cohesion (kPa)	1,085	Khan et al. (2011)
	Friction angle (°)	20	Khan et al. (2011)
Devonian limestone	Young's modulus (MPa)	1,500	Chalaturnyk (1996)
	Poisson's ratio	0.3	Chalaturnyk (1996)

	Cohesion (kPa)	200	Thomas and Sands (2010)
	Friction angle (°)	40	Thomas and Sands (2010)

[1] based on Kosar (1989) triaxial tests. E is Young's modulus and $\acute{\sigma}_3$ is minimum effective principal stress.

Figure 4.5 and Figure 4.6 show the relative permeability curves and also the variation of bitumen viscosity with temperature.

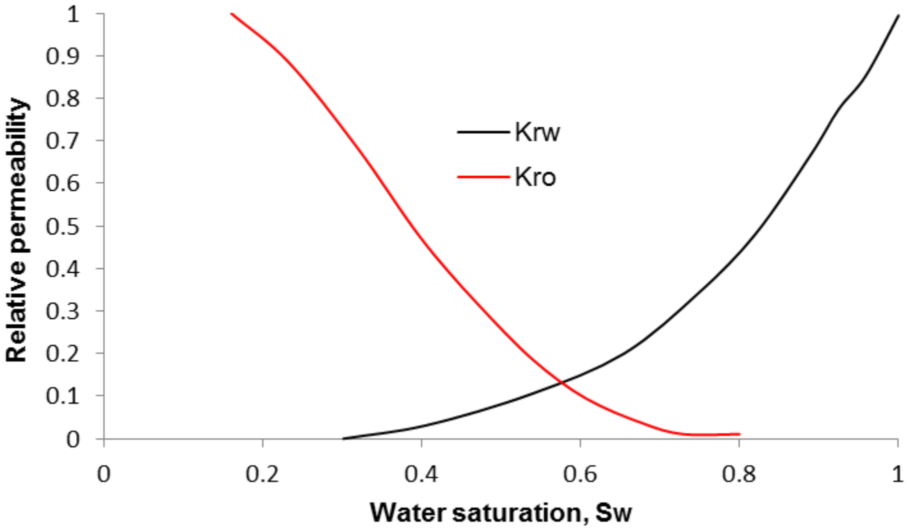

Figure 4.5 Relative permeability curves (after Chalaturnyk, 1996)

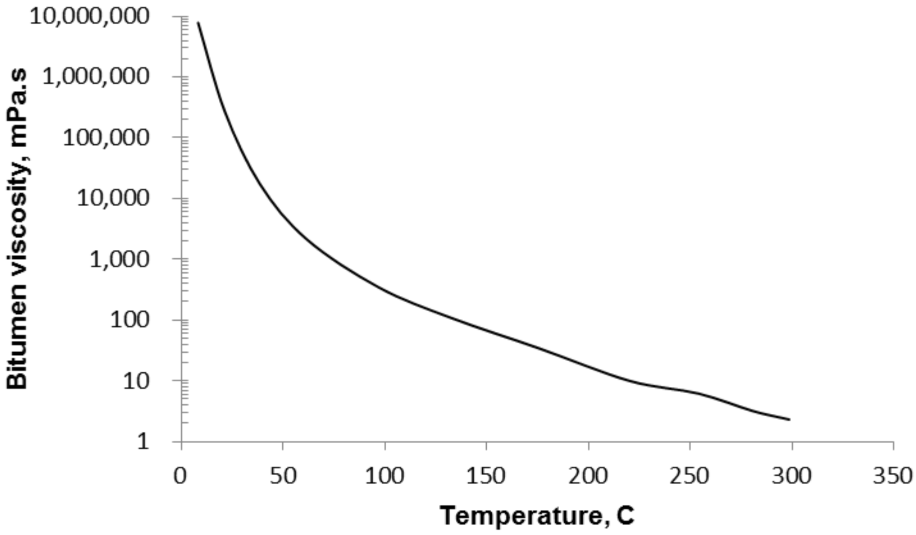

Figure 4.6 Viscosity variation with temperature (after Chalaturnyk, 1996)

4.5.2 Geomechanical model of oil sands

Isotropic stress-strain behavior was assumed for Quaternary Deposits, McMurray formation, and Devonian limestone while intrinsic anisotropic behavior was considered for the Clearwater shale and Wabiskaw member.

4.5.2.1 Elastic properties

Stress-dependent elasticity is commonly observed in oil sands and more generally in granular materials. Therefore, the modulus of elasticity varies as a function of effective confining stress. Li and Chalaturnyk (2005) showed that following relationship is appropriate to represent the modulus of elasticity variation of oil sands in Athabasca oil sands, Alberta.

$$E = -950 P_a (\acute{\sigma}_3 / P_a)^{0.5} \tag{59}$$

where E is Young's modulus; $\acute{\sigma}_3$ is the minimum principal effective stress, and P_a is atmospheric pressure.

Figure 4.7 shows the variation of module of elasticity against minimum effective principal stress.

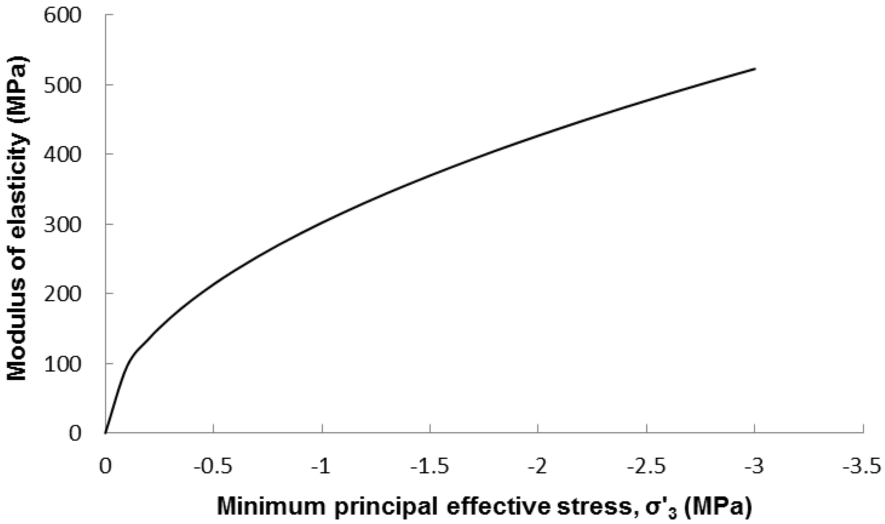

Figure 4.7 Variation of the modulus of elasticity versus minimum principal effective stress for McMurray oil sands (after Li and Chalaturnyk, 2005)

4.5.2.2 Yield surface

We used a bilinear Mohr-Coulomb yield function, which was also used by Nouri et al. (2009). Li and Chalaturnyk (2005) showed that the friction and dilation angle of oil sands are dependent on minimum effective principal stress. They proposed the following equations for the friction angle and dilation angle of oil sands.

$$\varphi = 55 + 14.93\, log(\acute{\sigma}_3/P_a) \tag{60}$$

$$\psi = 25.8 + 12.05\, log(\acute{\sigma}_3/P_a) \tag{61}$$

Based on the relations proposed by Li and Chalaturnyk (2005), failure function and potential functions for McMurray oil sands are shown in Figure 4.8 and Figure 4.9.

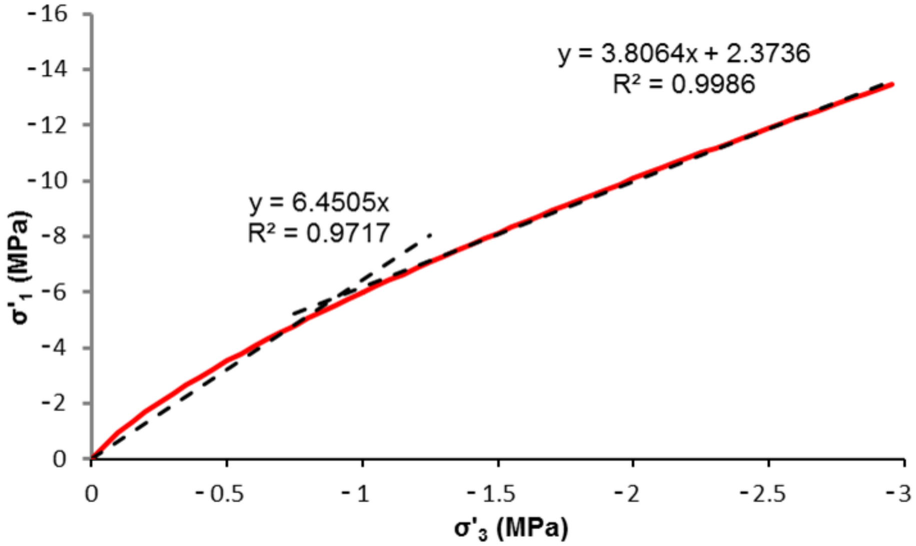

Figure 4.8 Failure envelope of McMurray oil sands (after Li and Chalaturnyk, 2005)

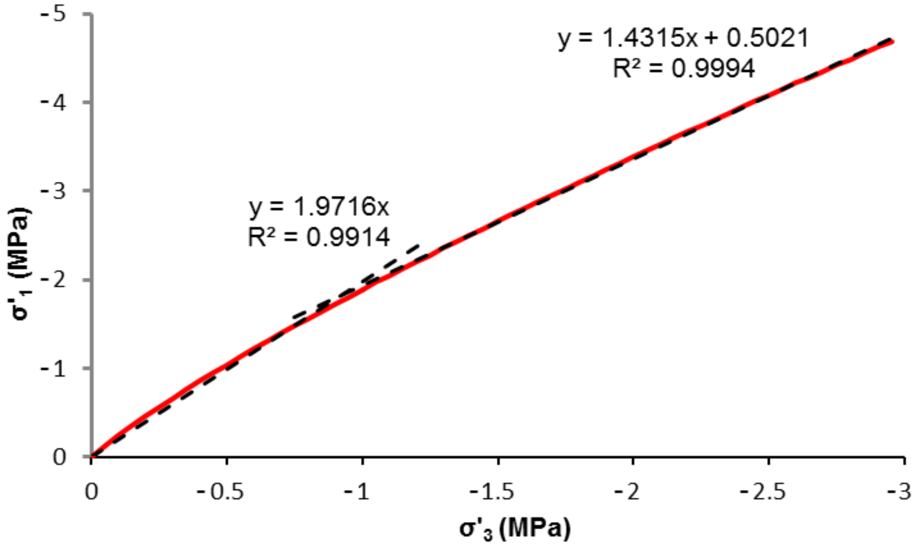

Figure 4.9 Potential function envelope of McMurray oil sands (after Li and Chalaturnyk, 2005)

The dashed lines in Figure 4.8 and Figure 4.9 show the bilinear fit to the Mohr-Coulomb curve for oil sands. Based on the figures, friction angle and dilation angle for Low Effective Confining Stress (LECS) and High Effective Confining Stress (HECS) are presented in Table 4.4.

Table 4.4 Mechanical properties of McMurray oil sands

Zone	LECS	HECS
Friction angle (°)	47	35.7
Dilation angle (°)	19	10.2
Cohesion (kPa)	0	610

4.5.3 Anisotropic mechanical properties

The AU constitutive model was used for describing the behavior of Clearwater and Wabiskaw shale. In this chapter, the effect of NFs is neglected and only the intrinsic anisotropy is assumed. Isotropic Mohr-Coulomb model was applied for all other layers (Quaternary Deposits, McMurray formation and Devonian limestone). As anisotropic properties were not available for the caprock shales, anisotropic values were assumed based on existing data and correlations for other shales.

Sone (2012) proposed the following empirical formula to calculate the ratio of horizontal to vertical Young's modulus for shales with clay content in the range of 5% and 65%:

$$\frac{E_x}{E_y} = 3.1exp\left(-0.0195E_y(GPa)\right) \tag{62}$$

where E_x and E_y are horizontal and vertical Young's moduli, respectively.

Eq. (62) was used to calculate the horizontal Young's modulus at different effective confining pressures for Clearwater and Wabiskaw shale assuming the Young's moduli in Table 4.3 were obtained for vertical core plugs. Table 4.5 lists

Poisson's ratio of Clearwater and Wabiskaw shales assuming transverse isotropy. The Poisson's ratio (ν_{xy}) was calculated from Eq. (63) (Puzrin, 2012). The Poisson's ratio (ν_{xz}) was observed to be close to (ν_{yx}) according to experimental data provided by Sone (2012). In this study, $\nu_{xz,}$ and ν_{yx} were assumed to be equal.

$$\frac{\upsilon_{xy}}{\upsilon_{yx}} = \frac{E_x}{E_y} \tag{63}$$

Table 4.5 Transversely isotropic properties of anisotropic layers

Layer's name	**Parameter**	**Value**
Clearwater shale	Poisson's ratio (υ_{xy})	0.40
	Poisson's ratio ($\upsilon_{yx}, \upsilon_{xz}$)	0.13
Wabiskaw shale	Poisson's ratio (υ_{xy})	0.45
	Poisson's ratio ($\upsilon_{yx}, \upsilon_{xz}$)	0.15

Correlations by McLamore and Gray (1967) were adopted to calculate the cohesion and friction angle in different directions for Clearwater and Wabiskaw shales. The strength properties of anisotropic layers are presented in Figure 4.10. In this figure, θ is the angle between the maximum principal stress and the horizontal direction. In Figure 4.10, the strength properties for the vertical direction (θ=90°) were adopted from Table 4.3. The calibration parameters for the cohesion and friction angle (see Eq. (38) and (39), Chapter 3) for the Clearwater and Wabiskaw shales were assumed to be the same as those of Green River shale (Table 4.6).

Table 4.6 Calibration parameters for anisotropic layers

Parameter	**Clearwater shale**	**Wabiskaw shale**	**Parameter**	**Clearwater shale**	**Wabiskaw shale**
A_1	2.5e5	1.34e6	C_2	0.466	0.349
A_2	2e5	1.085e6	D_1	0.06	0.051
B_1	9e4	4.88e5	D_2	0.056	0.045
B_2	4.3e4	2.32e5	**m**	6	6
C_1	0.475	0.355	**n**	6	6

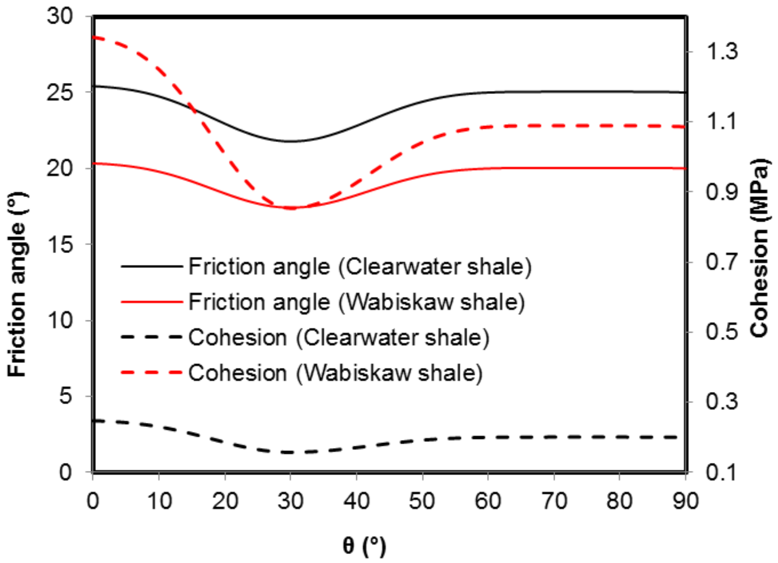

Figure 4.10 Friction angle and cohesion assigned to anisotropic Clearwater and Wabiskaw shales

4.5.4 In-situ stresses

Figure 4.11 shows the principal stress directions in relation to the wellbore trajectory in the area of interest. Pad-C wells were drilled parallel to the maximum horizontal stress.

The stress and pore pressure profiles for each stratigraphic zone in this area are shown in Figure 4.12. In this figure, solid lines represent the work of Walters et al. (2012), but dashed lines are based on educated assumptions. The gradient for vertical stress and pore pressure were kept constant for the entire model including the underburden as vertical stress usually follows the overburden weight. Bell and Babcock (1986) proposed 350 m and 2,500 m as the approximate threshold for the change in the stress state from thrust to strike slip and strike slip to normal, respectively, in Western Canada Basin. We could not find any in-situ stress measurement for the underburen and assumed the stress profiles at greater depths based on the conclusion made by Bell and Babcock (1986), which is the minimum and maximum horizontal stresses cross the vertical stress at 350 m and 2500 m depth, respectively.

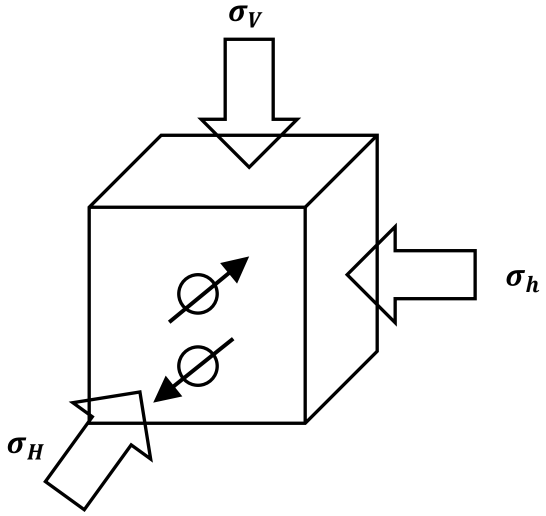

Figure 4.11 Principal stress directions

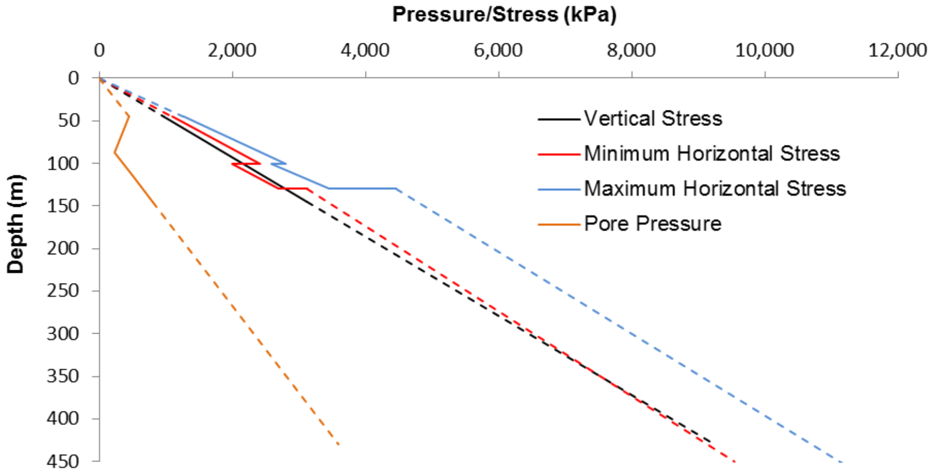

Figure 4.12 In-situ stress and pore pressure profiles

4.5.5 Operational conditions

In this study, we simulated five years of field operations. Steam quality, temperature, and pressure were reported to be 95%, 200 °C and 1,650 kPa, respectively (Suncor Energy, 2009). Steam circulation for this project commenced in September 2002 (Petro-Canada Corp., 2005a).

Actual injection-production data were used for the first 5 years of the operation. After that, a hypothetical pressure ramp-up for injectors was considered to find the caprock failure pressure as discussed later in this chapter.

Figure 4.13-16 show the measured and calculated Bottom Hole Pressure (BHP) of injectors, BHP of producers, steam injection rate of injectors, and production rate of producers. Steam injection rates and fluid production rates in Figure 4.15 and Figure 4.16 are reported per meter of wellbore length. Actual injection BHP data were used for the first five years of operation and the calculated and measured steam injection rates were found to have similar trends (Figure 4.17). In the simulations, actual injection pressures and actual production rates were used as boundary conditions, and the injection rates and production pressures were calculated and compared with the measured data. According to Figure 4.17, the values of calculated and measured injection rates in early stages are close. However, the difference is higher in later times, which could be due to uncertainties associated with the input parameters, including the calibration parameters for the permeability variation (Eq. (57)).

A pressure ramp-up phase was considered after five years of operation by increasing the injection pressure in the injection wells and considering a constant drawdown pressure between the injectors and producers to find the MOP. Each pressure ramp-up step was kept for six months and injection pressure was increased by 10% of initial injection pressure in each step.

A sensitivity study was performed to investigate the effect of the duration of each pressure ramp-up on the MOP. Results showed the same MOP for 6- to 24-month increment durations for the pressure ramp-up.

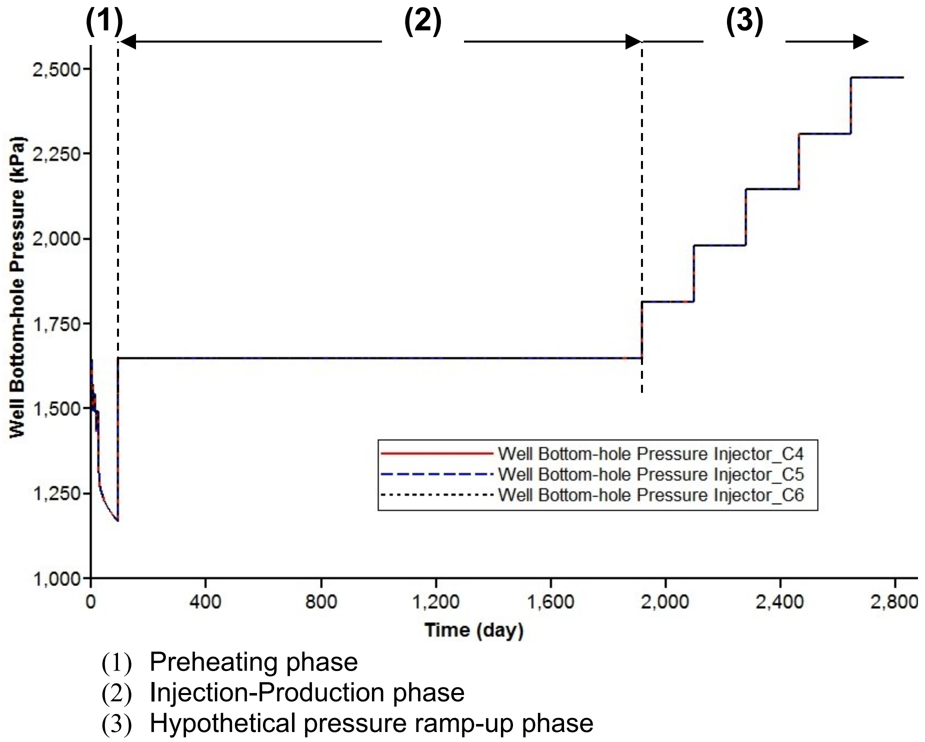

Figure 4.13 BHP versus time for injectors (measured for the first five years) applied as boundary condition

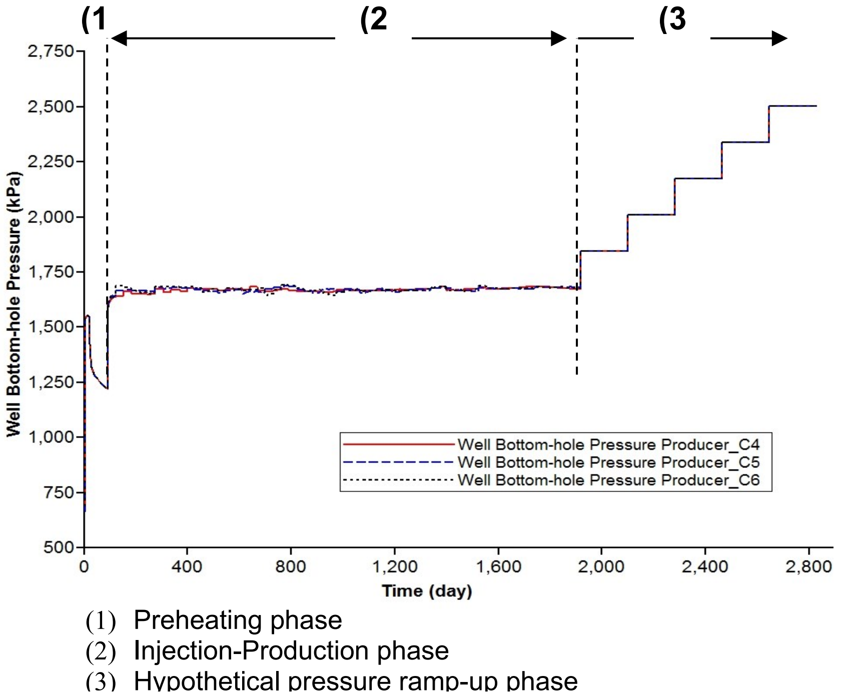

Figure 4.14 Calculated BHP versus time for producers

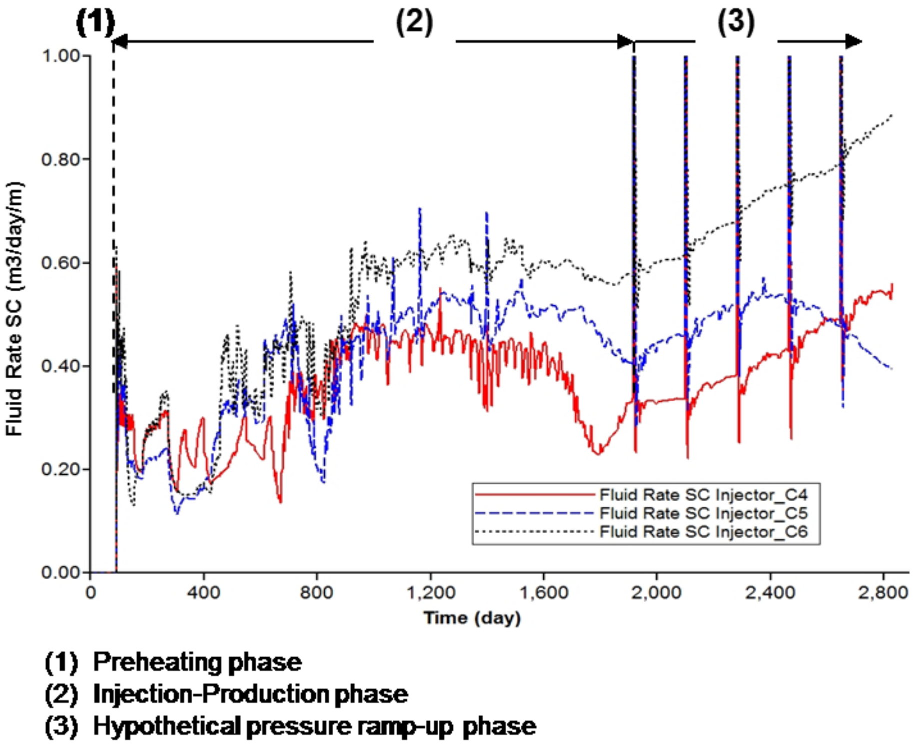

Figure 4.15 Calculated injection rates versus time for injectors

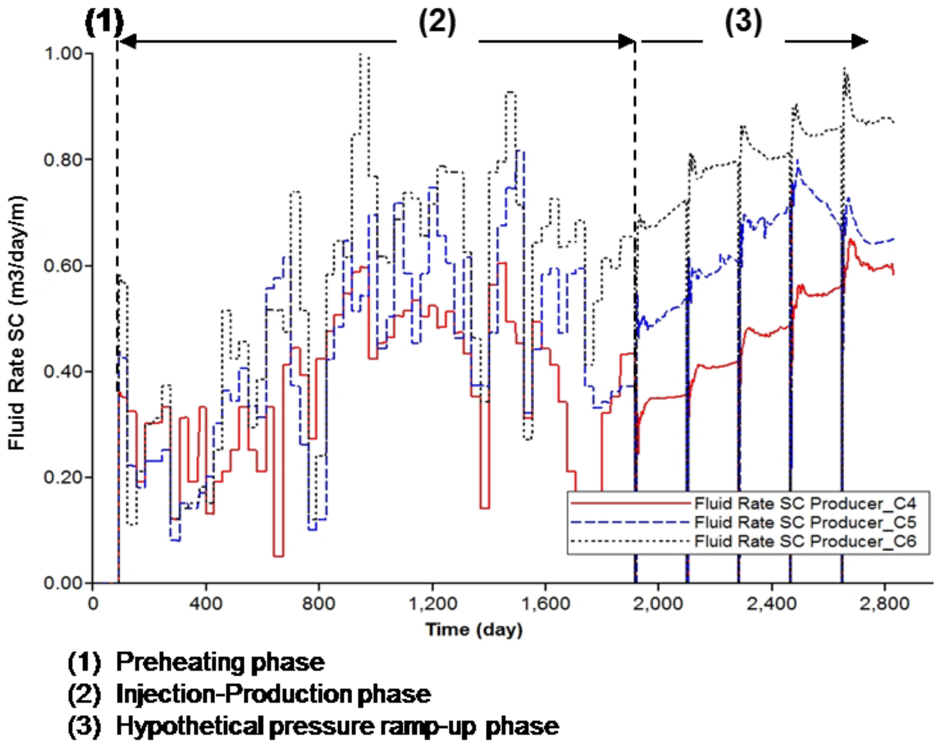

Figure 4.16 Measured (for the first five years) production rates versus time applied as boundary condition for producers

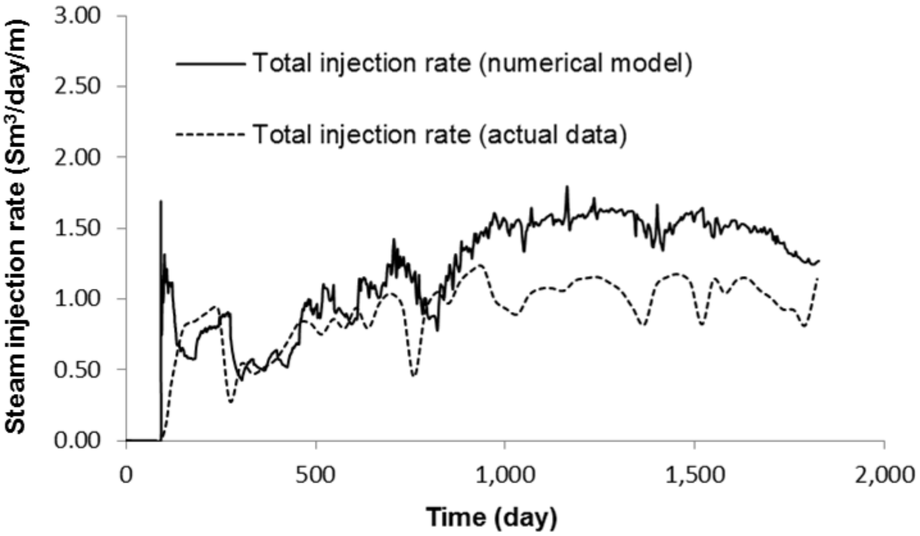

Figure 4.17 Comparison between calculated and measured steam injection rates

4.6 Results and discussion

The coupled hydro-thermo-mechanical model was used to investigate the caprock integrity and determine the MOP for the case study problem. Numerical simulations were performed for both AU and isotropic models for five years of pad operation to evaluate the impact of the anisotropic behavior of the caprock shale on the MOP.

4.6.1 Model validation

Measured surface heave data (Suncor Energy, 2009) were used to validate the model (Figure 4.18). As depicted in Figure 4.18, the displacements from the AU model show a better agreement with the measured data than those of the isotropic model. As injection and production continues, the AU model results in higher heave displacement at the surface and demonstrates a better agreement with the measured data.

Although predicted displacements with AU model are in better agreement with measured heave displacements, it seems that all calculated displacements in Figure 4.18 are smaller than measured data. Reasons could be, for instance, the possible use of smaller coefficient of thermal expansion or higher Young's modulus than the actual values. It may also be associated with the effect of temperature on cohesion, friction and Young's modulus, which have not been considered in the analysis. As mentioned before, the input data were obtained from published data not necessarily for this particular site. Therefore, we are not looking for a perfect match.

The difference between the vertical displacements for the isotropic and AU models could be explained noting different values for caprock horizontal stiffnesses. The Young's modulus in the horizontal direction for the AU model is about three times larger than the same in the isotropic model. Figure 4.19 compares the predicted horizontal displacements in the AU and isotropic models, which indicates smaller horizontal displacement in the reservoir for the AU model than the isotropic model. Therefore, for the same amount of reservoir expansions, the AU model results in larger vertical displacement in the reservoir and, consequently, larger heave at the surface.

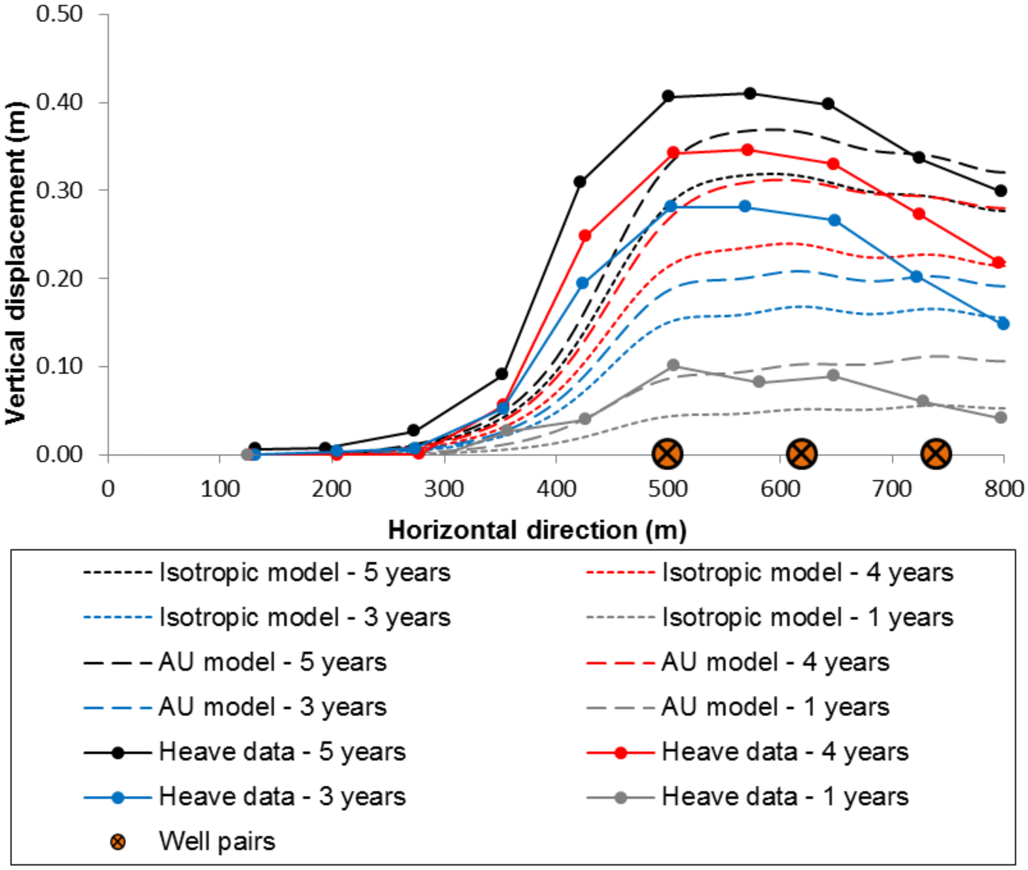

Figure 4.18 Comparison between the measured and calculated heave data

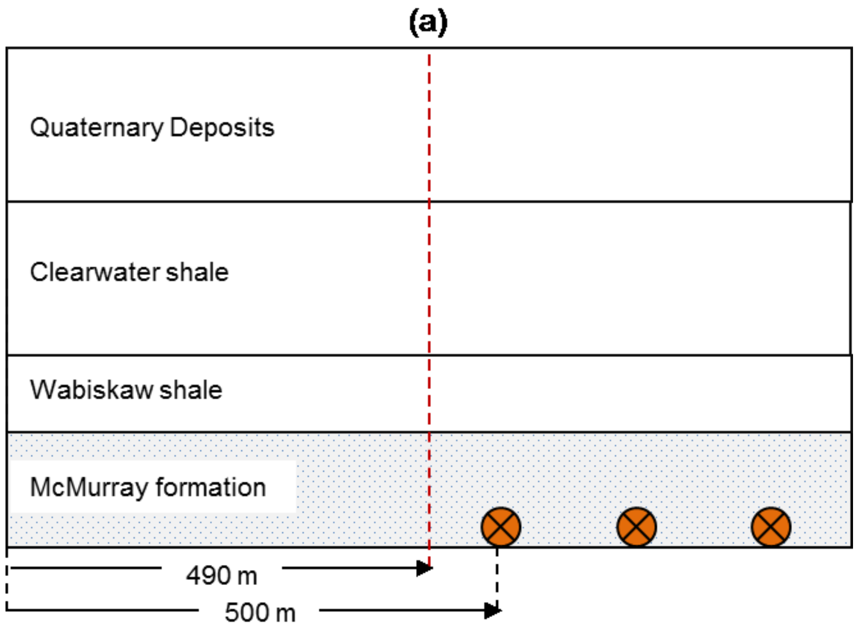

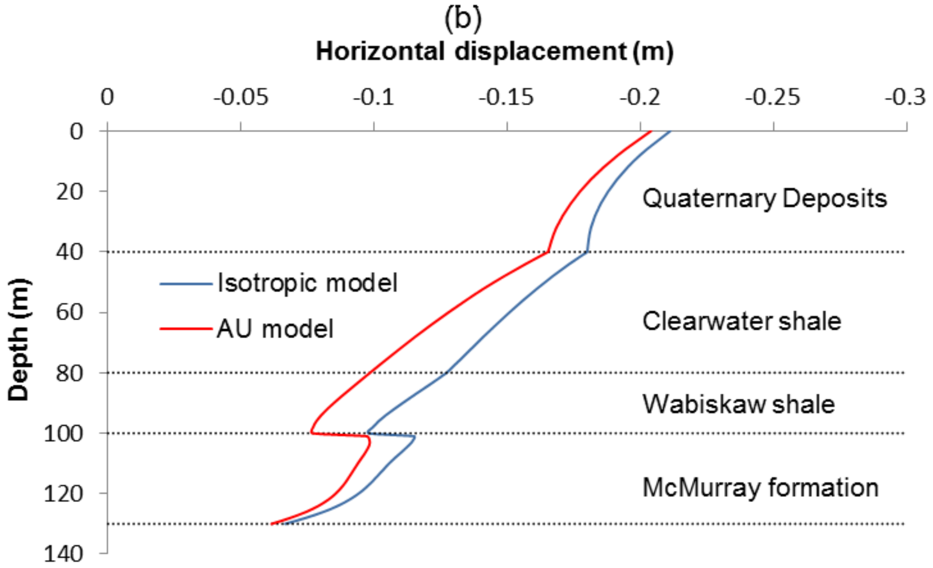

Figure 4.19 Horizontal displacements in a vertical cross section; a) location of the vertical cross section, and b) horizontal displacement for isotropic and AU models

4.6.2 Growth of steam chamber

Pore pressure and temperature are among the main parameters that change during the SAGD operation. Steam injection causes the expansion of the steam chamber and evolution of the pore pressure and temperature during the operation (Figure 4.20 and Figure 4.21). Results show the increase of reservoir pore pressure from the in-situ level of 500 kPa to 1,650 kPa (injection pressure) during the growth of steam chamber (Figure 4.20). Little pore pressure change is observed in the caprock during five years of operation, due to the low permeability of caprock shales, allowing minimal diffusion. The permeability of Wabiskaw C sand is large defusing any pore pressure build-up due to the increase in temperature.

Unlike pore pressure, temperature has changed noticeably during the SAGD operation in both caprock shales and underburden limestone (see Figure 4.21).

Temperature in Wabiskaw shale has increased by up to 110 °C right above the steam chamber. The temperature change is negligible for the points closer to the interface of Wabiskaw and Clearwater shale. The temperature increase in the reservoir also affects the underburden rock. The temperature at the interface of Devonian limestone and the reservoir has increased by up to 120 °C. It is worth pointing out that the temperature change in the underburden limestone is limited to the close vicinity (approximately 20 m) of the reservoir.

Figure 4.22 shows the water saturation maps in different years of SAGD operation. The figure shows that the rate of growth of the steam chamber is high in the first years but decreases as the SAGD operation continues.

By comparing the pore pressure (Figure 4.20), temperature (Figure 4.21), and saturation maps (Figure 4.22), we can see that the pore pressure front is ahead of the temperature front and the latter is ahead of the saturation front.

From the figures, it can be seen that the thermal front is ahead of the saturation front. This can be explained by the existence of convective and conductive heat flux in the SAGD operation. Conductive heat influx causes thermal front to diffuse ahead of the steam chamber. Furthermore, by comparing pressure maps (Figure 4.20) with temperature maps (Figure 4.21), it can be seen that pore pressure front is ahead of the thermal front. The pore pressure in the reservoir goes up due to the chamber pressing on the flank, and the flank being in undrained condition before it is heated up because of high viscosity of bitumen in low temperatures according to Figure 4.6. This phenomenon was also detected by Aherne and Birrel (2002) from field measurements in UTF Phase B project.

a) Pressure (kPa), Time=0 year

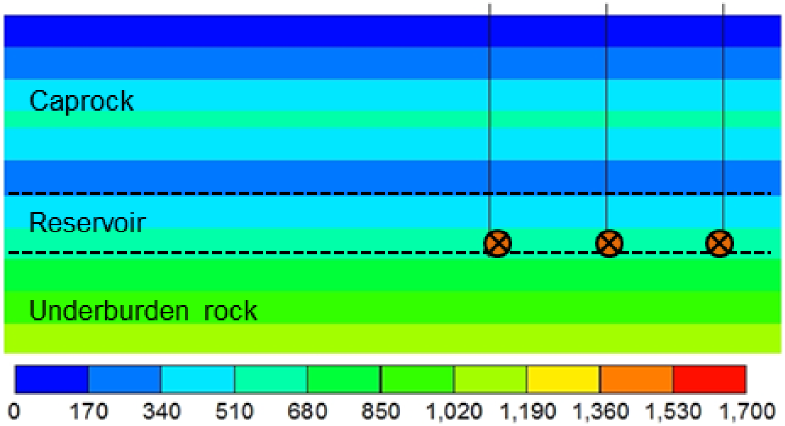

b) Pressure (kPa), Time=1 year

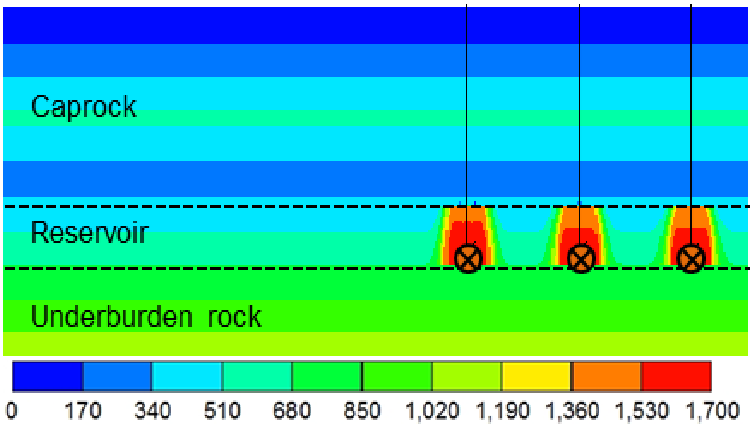

c) Pressure (kPa), Time=2 years

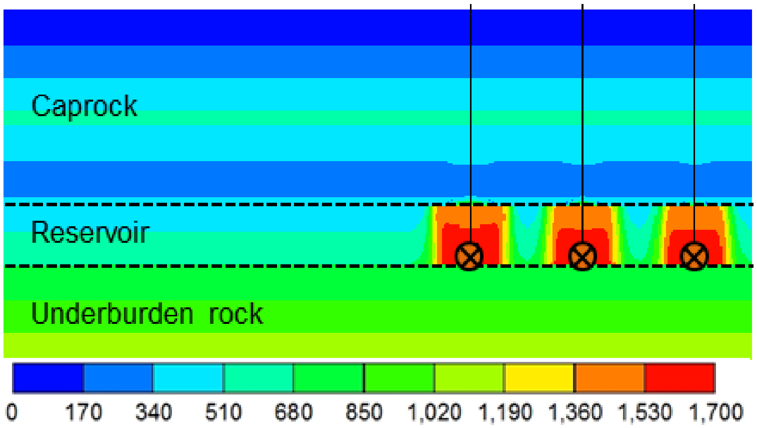

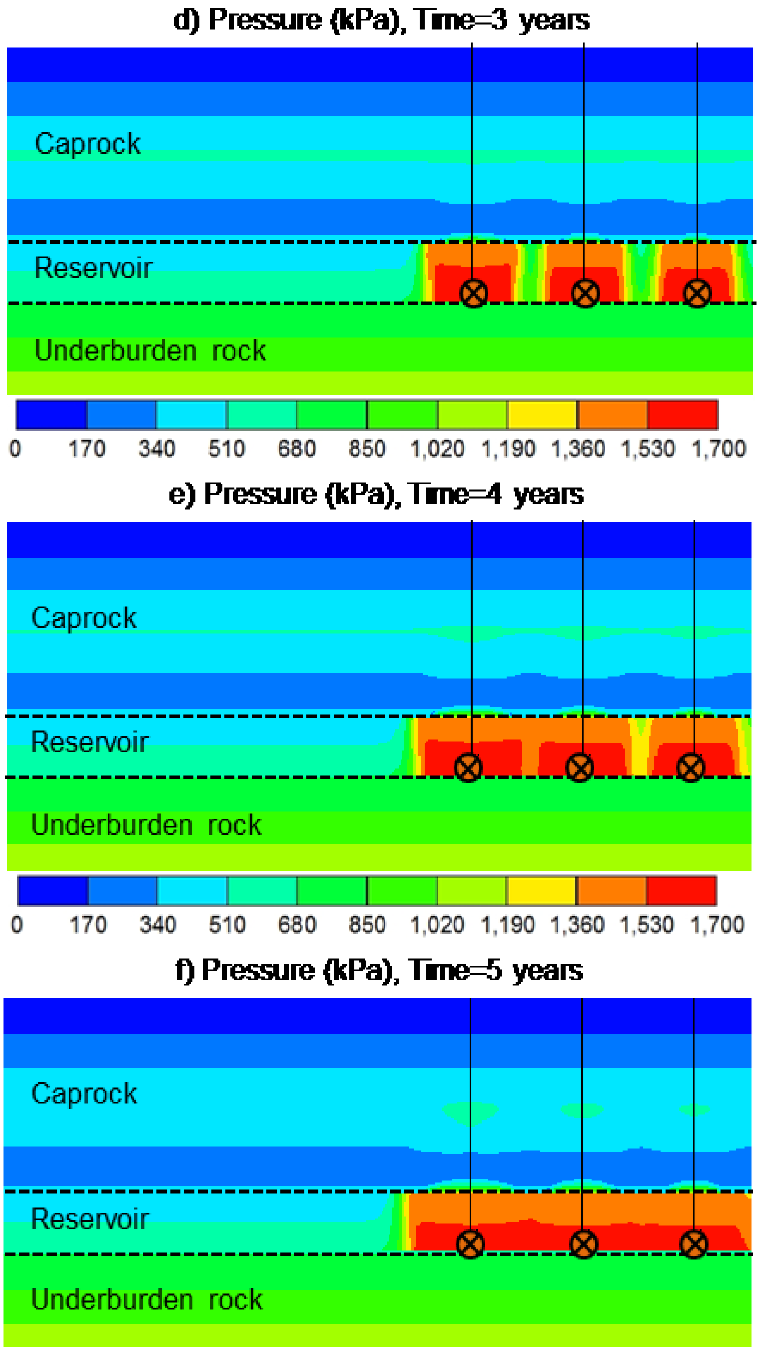

Figure 4.20 Pore pressure distribution in the model for five years of production (maps are plotted for depths shallower than 180 m)

a) Temperature (C), Time=0 year

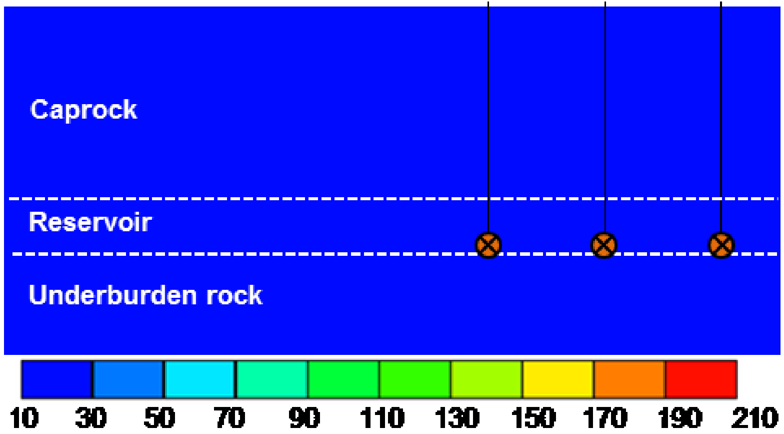

b) Temperature (C), Time=1 year

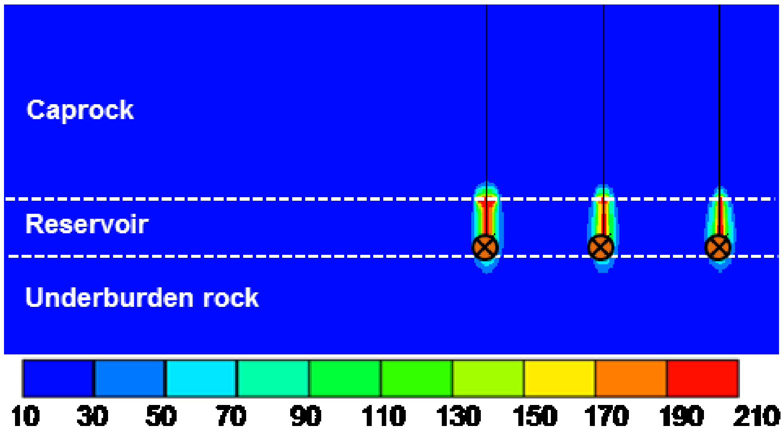

c) Temperature (C), Time=2 years

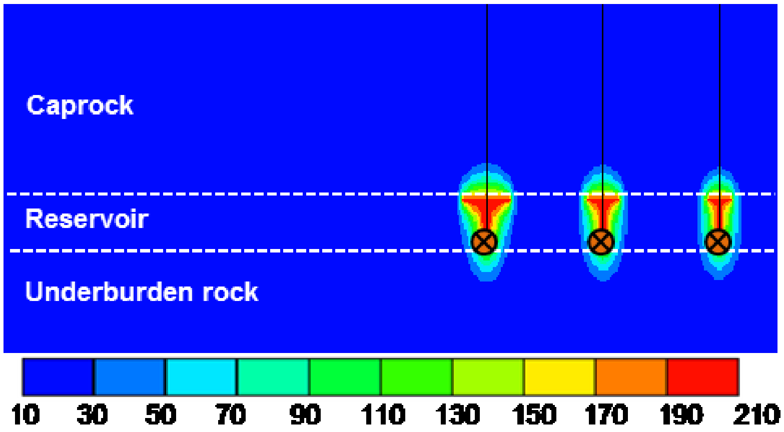

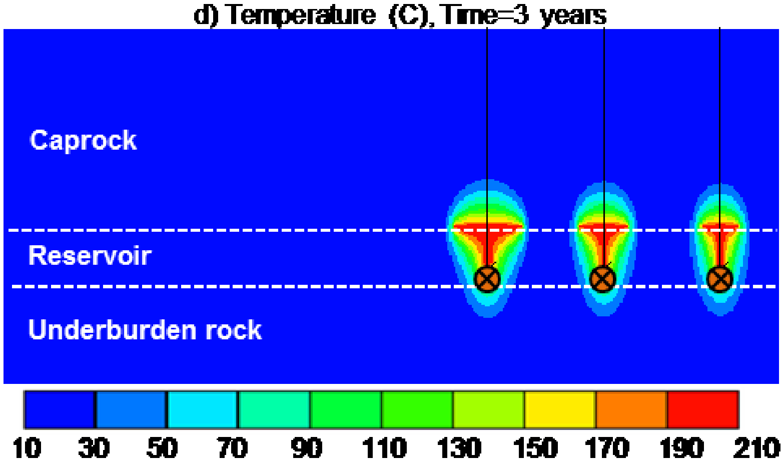

d) Temperature (C), Time=3 years

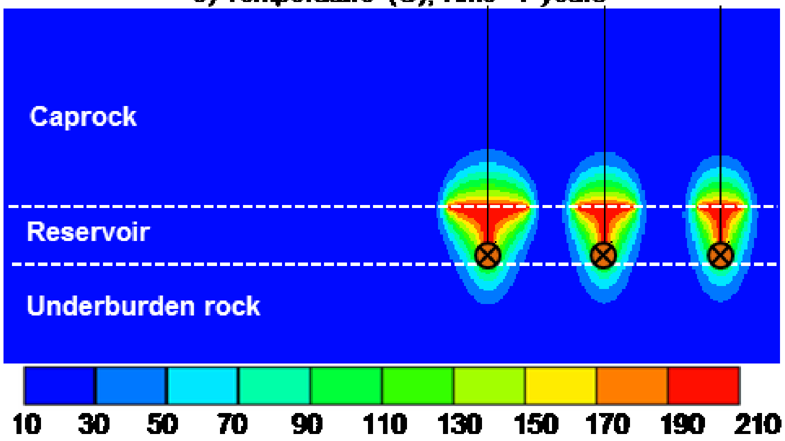

e) Temperature (C), Time=4 years

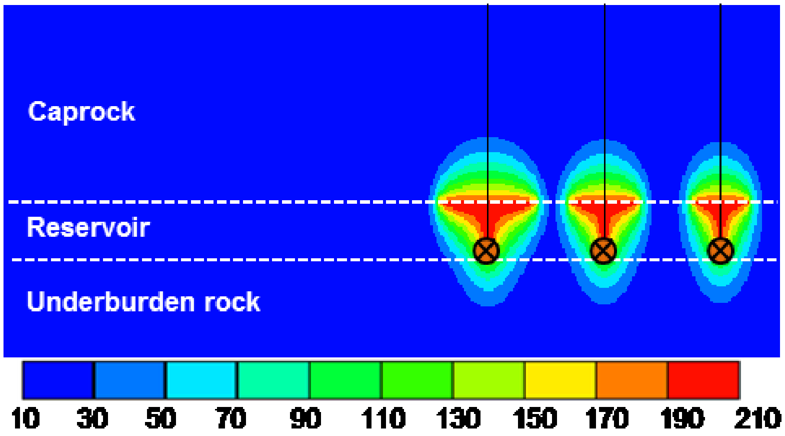

f) Temperature (C), Time=5 years

Figure 4.21 Temperature distribution in the model for five years of production (maps are plotted for depths shallower than 180 m)

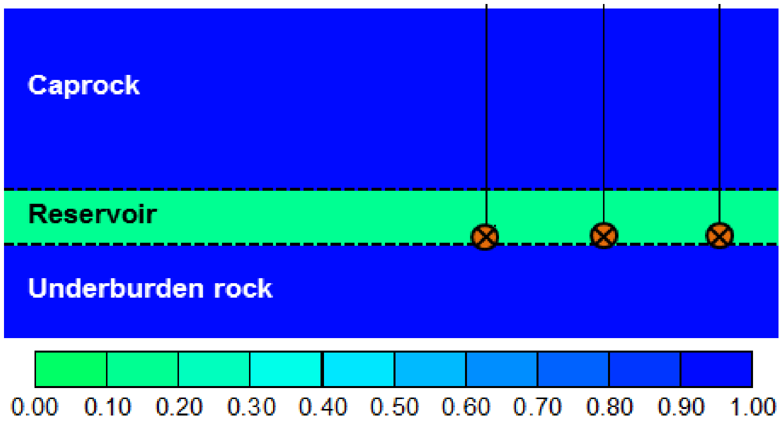
a) Water saturation, Time=0 year

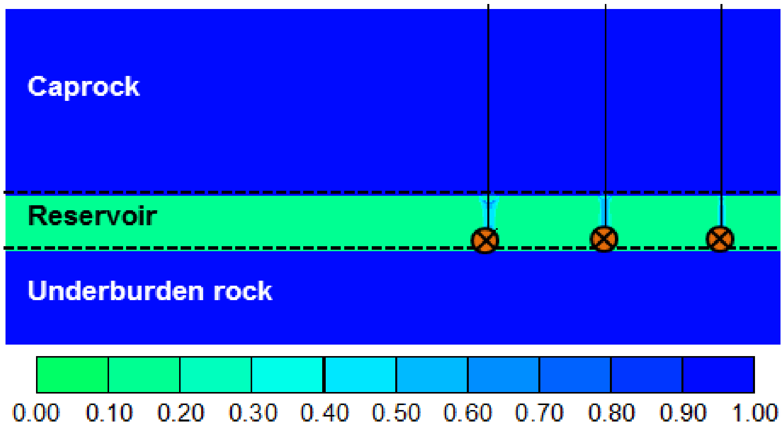
b) Water saturation, Time=1 year

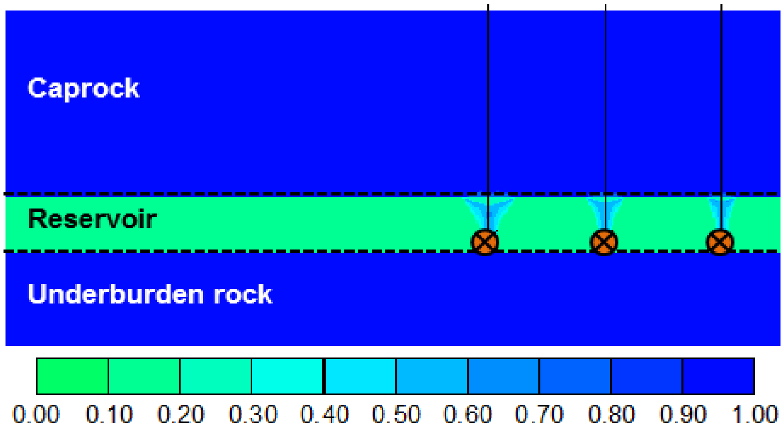
c) Water saturation, Time=2 years

d) Water saturation, Time=3 years

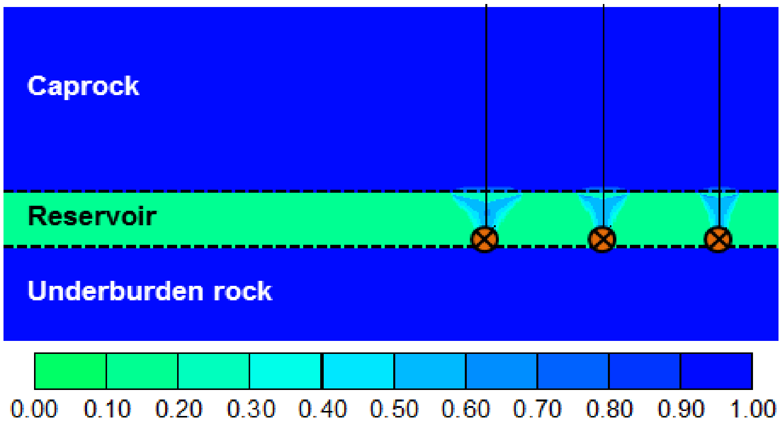

e) Water saturation, Time=4 years

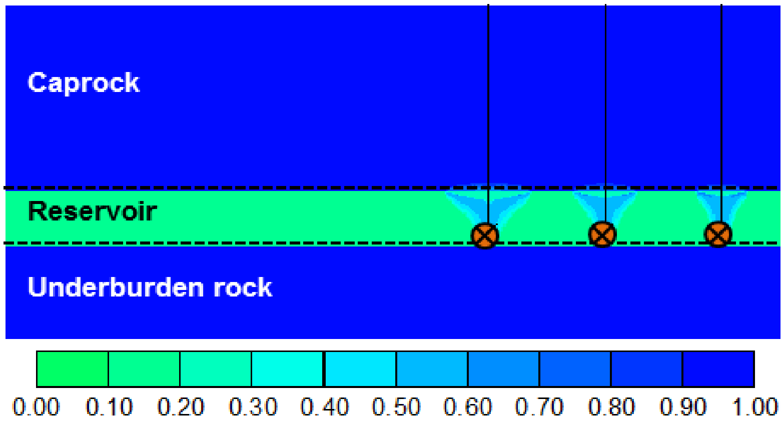

f) Water saturation, Time=5 years

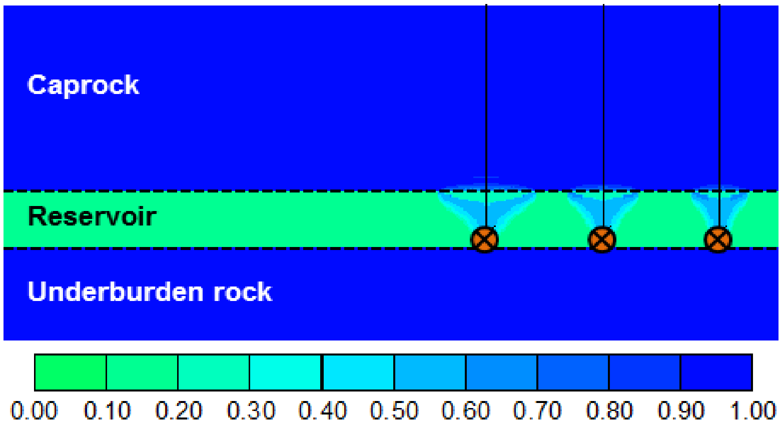

Figure 4.22 Water saturation distribution in the model for five years of production (maps are plotted for depths shallower than 180 m)

4.6.3 Induced stresses in and around the reservoir

SAGD operation changes the ground stresses. The stress changes are primarily caused by the increased reservoir pressure and the thermal expansion of the reservoir.

Figure 4.23 depicts the total horizontal stress profile for different vertical sections at different distances of 250 m, 450 m, 500 m and 550 m from the left boundary of the model. Stress profile for Section A, which is 250 m from the last well pair, is relatively close to the in-situ stress profile. For the other three sections (B, C, and D), the horizontal stress increases at the reservoir interval due to the pore pressure increase, dilative expansion of the reservoir sand in shear, and the thermal expansion of the reservoir. Total horizontal stresses in the overburden and underburden layers decrease from the in-situ values to compensate for the increased horizontal stresses at the reservoir interval. The AU model resulted in smaller horizontal stresses in Clearwater shale and slightly higher horizontal stresses in Wabiskaw shale, in comparison with the isotropic model. Both models predict similar horizontal stress trends for Quaternary Deposits, the reservoir, and the underburden layers. In the figure, the maximum difference for horizontal stresses between the isotropic and AU models is as large as 29% with respect to the horizontal in-situ stress.

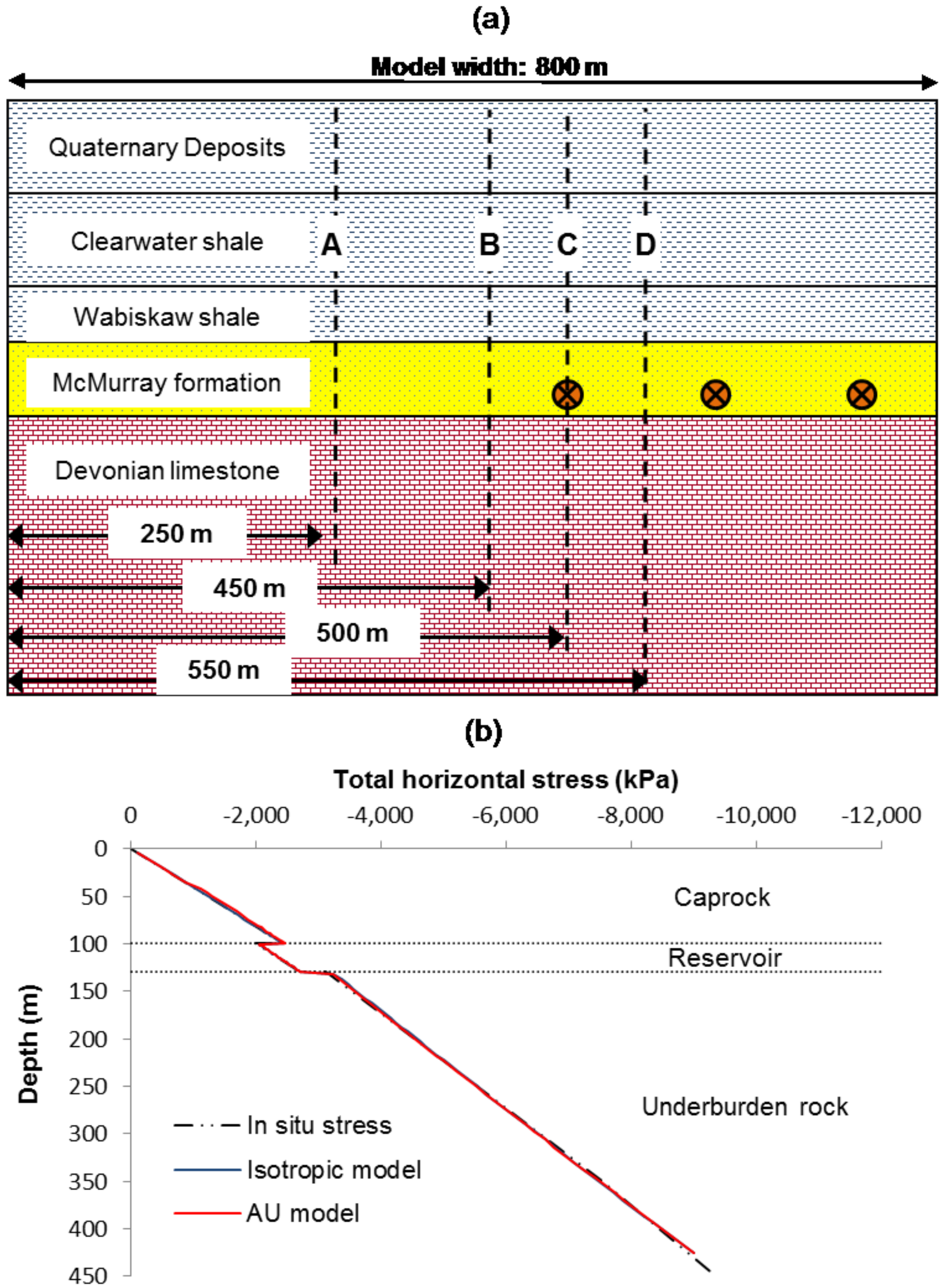
(a)
Model width: 800 m
Quaternary Deposits
Clearwater shale
Wabiskaw shale
McMurray formation
Devonian limestone
A
B
C
D
250 m
450 m
500 m
550 m
(b)
Total horizontal stress (kPa)
0
-2,000
-4,000
-6,000
-8,000
-10,000
-12,000
Depth (m)
0
50
100
150
200
250
300
350
400
450
Caprock
Reservoir
Underburden rock
In situ stress
Isotropic model
AU model

(c)

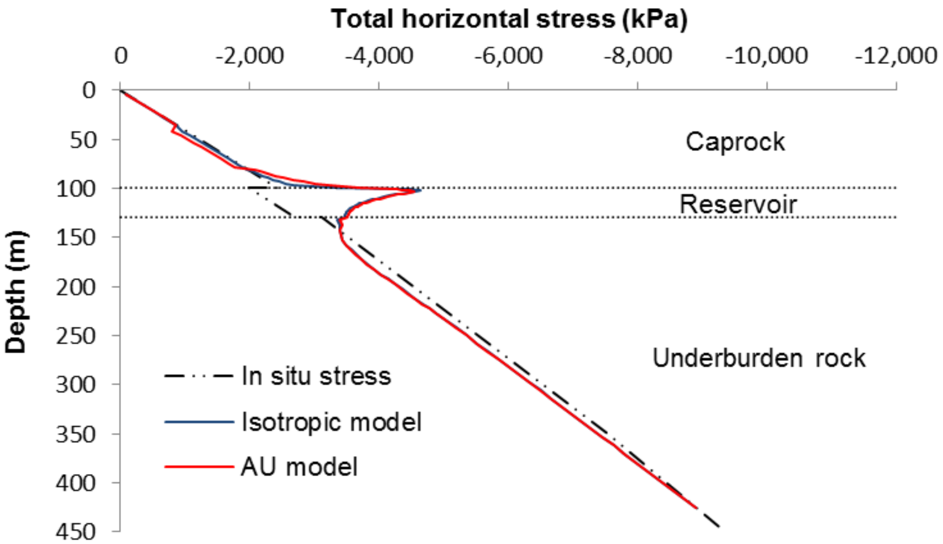
Total horizontal stress (kPa)
0
-2,000
-4,000
-6,000
-8,000
-10,000
-12,000
Depth (m)
0
50
100
150
200
250
300
350
400
450
Caprock
Reservoir
Underburden rock
In situ stress
Isotropic model
AU model

(d)

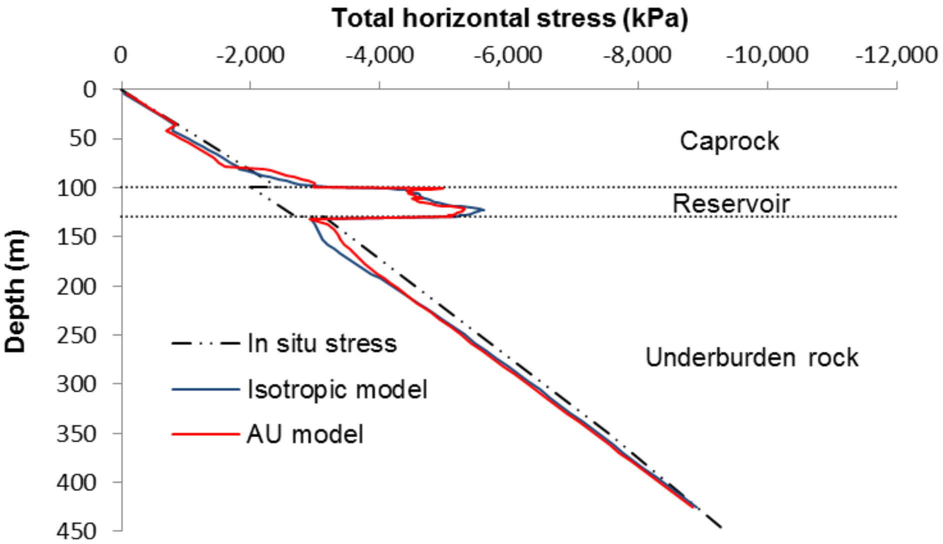
Total horizontal stress (kPa)
0
-2,000
-4,000
-6,000
-8,000
-10,000
-12,000
Depth (m)
0
50
100
150
200
250
300
350
400
450
Caprock
Reservoir
Underburden rock
In situ stress
Isotropic model
AU model

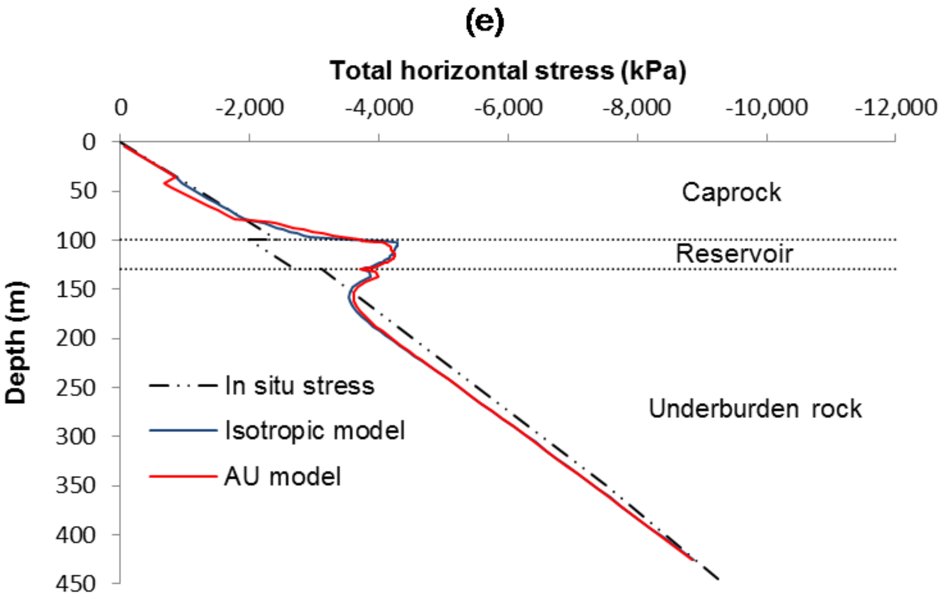

Figure 4.23 Total horizontal stress profile for vertical sections after five years of operation a) Vertical cross section locations, b) Total horizontal stress at cross section A, c) Total horizontal stress at cross section B, d) Total horizontal stress at cross section C, e) Total horizontal stress at cross section D

Figure 4.24 shows the total vertical stress profiles at different horizontal sections. Results indicate the vertical stresses in the cap shale are disturbed during the SAGD operations. Further, higher maximum and lower minimum for the vertical stress profiles result for the AU model. Generally, the vertical stresses above the chamber increase while the same at the reservoir flanks decrease, a phenomenon, which is known as thermal jacking (Collins, 2006). This is because of the expansion of the reservoir sand in the chambers, which result in stronger compressive forces on the caprock in places directly above the wells. The stress drop at the reservoir flanks for the AU model is found to be more significant than the same for the isotropic model. As expected far from the reservoir, stresses in both models converge to in-situ stresses representing the fact that the model is large enough to avoid any boundary effects.

(a)

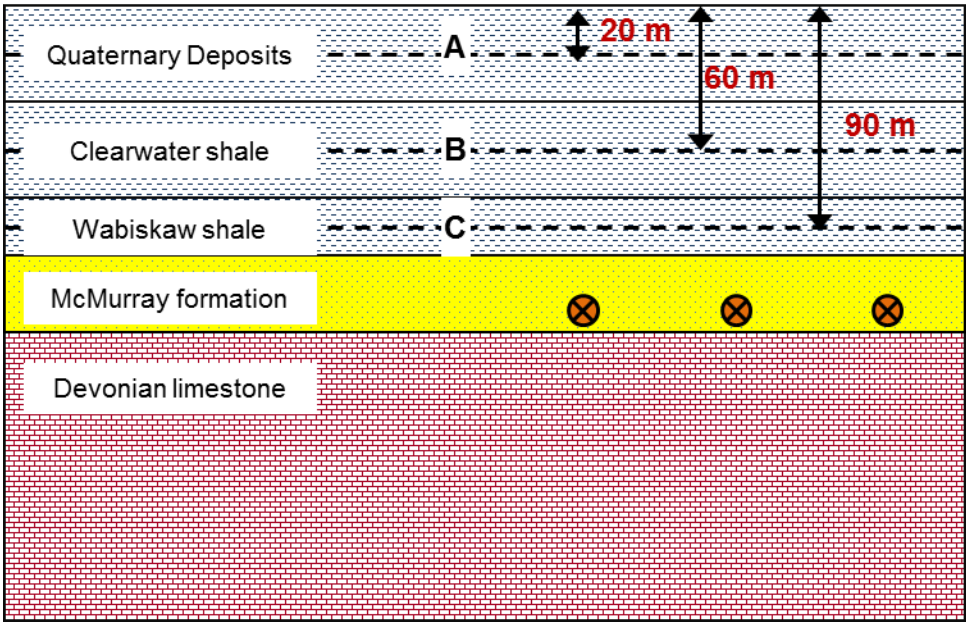
Quaternary Deposits
A
20 m
60 m
90 m
Clearwater shale
B
Wabiskaw shale
C
McMurray formation
Devonian limestone

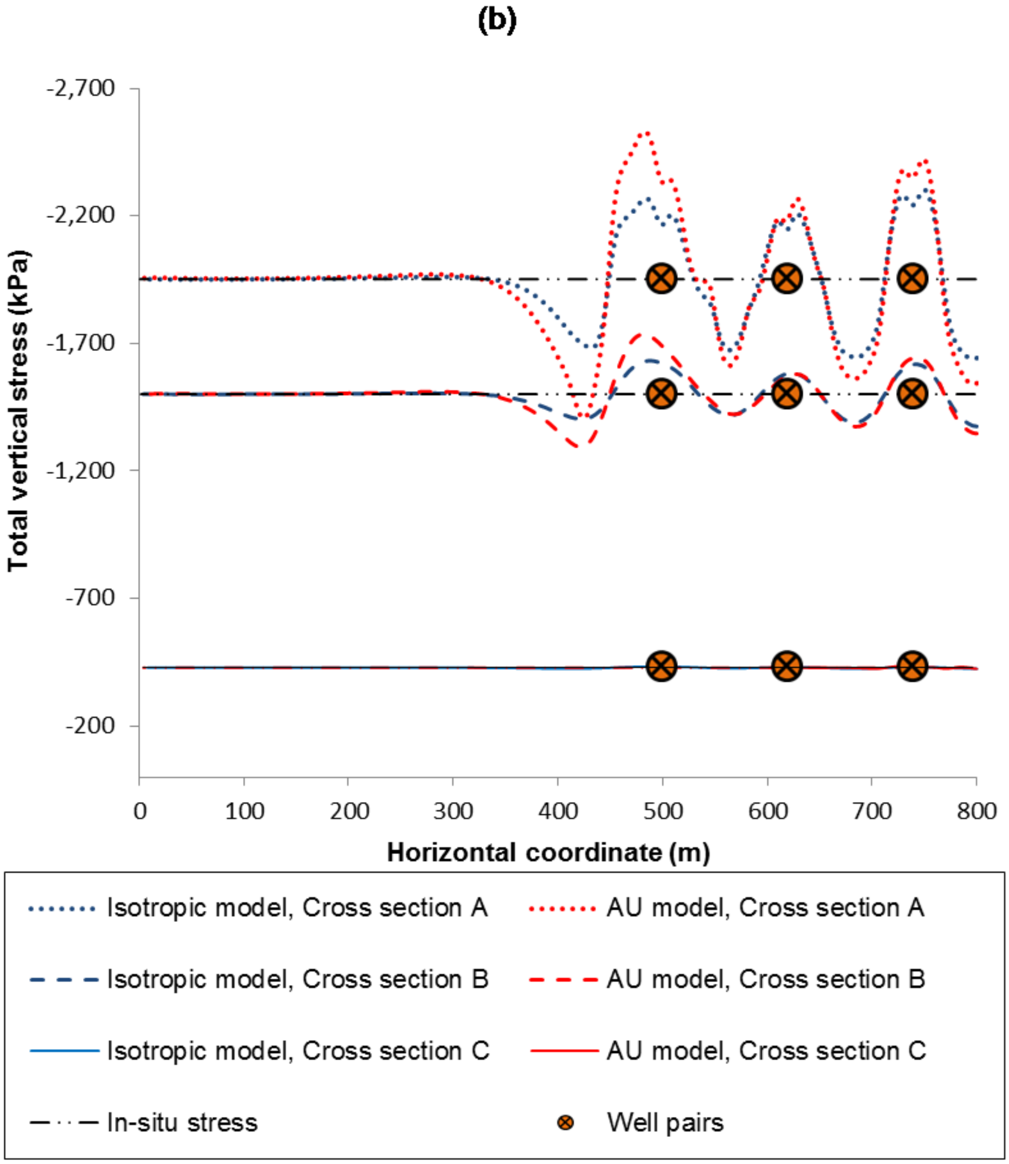

Figure 4.24 Total vertical stress at different horizontal sections, a) Horizontal cross section locations, b) total vertical stress at different cross sections after five years for both isotropic and AU models

Figure 4.25 and Figure 4.26 show the total horizontal and vertical stress contour maps for the AU model, respectively. For early stages of injection (Figure 4.25b and Figure 4.26b) steam chambers are separate and thermal jacking is apparent as vertical stresses are higher than the in-situ stresses above the well pairs and lower between the well pairs. Horizontal stresses in the reservoir are significantly larger than the in-situ stresses. Accordingly, horizontal stresses in the cap and base rocks are lower than in-situ stress to satisfy the force equilibrium. As injection-production continues, steam chambers further expand and eventually join together (Figure 4.25c, d and e).

a) Horizontal stress (Time=1 year)

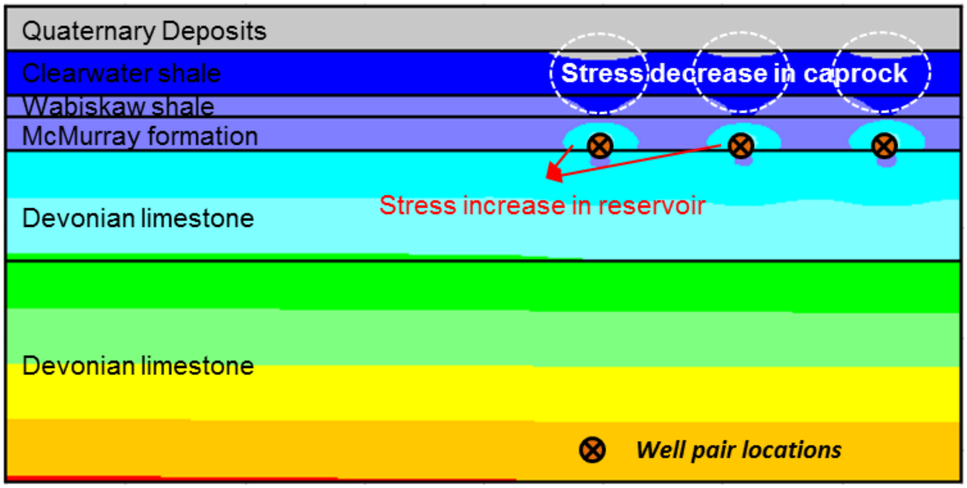

b) Horizontal stress (Time=2 years)

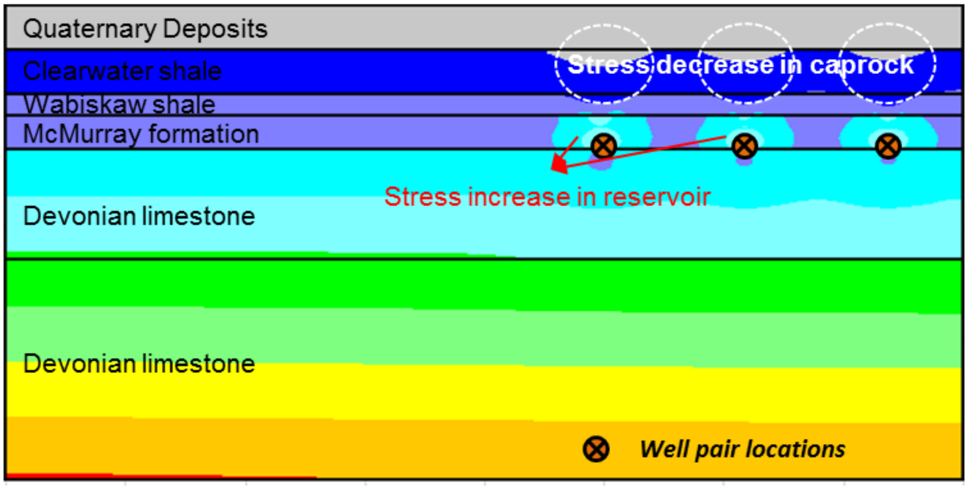

c) Horizontal stress (Time=3 years)

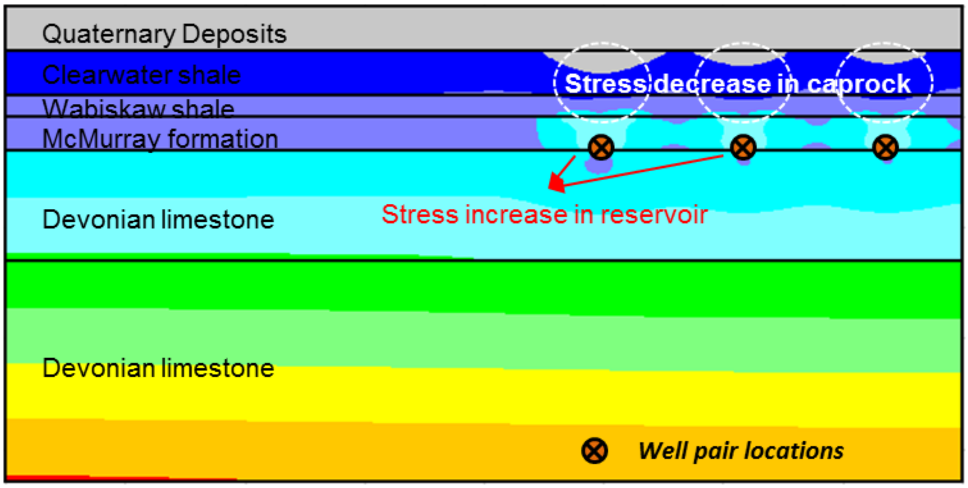

d) Horizontal stress (Time=4 years)

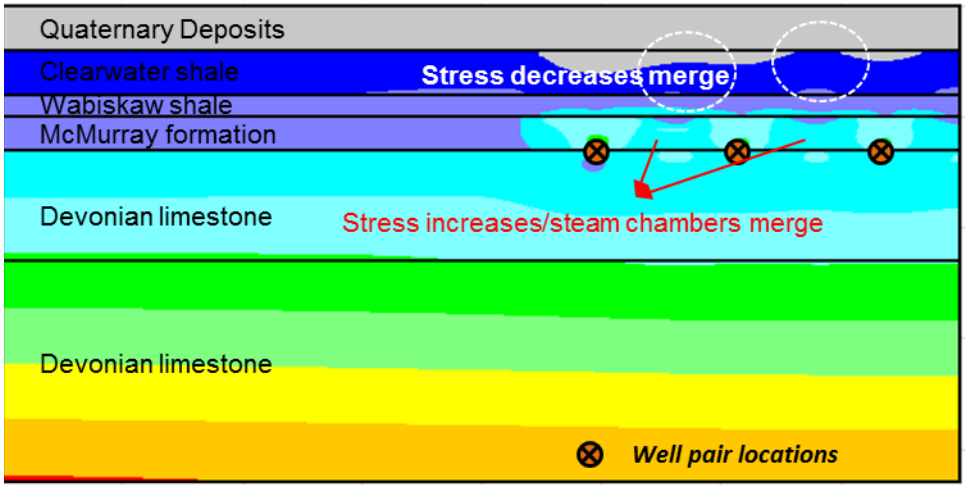

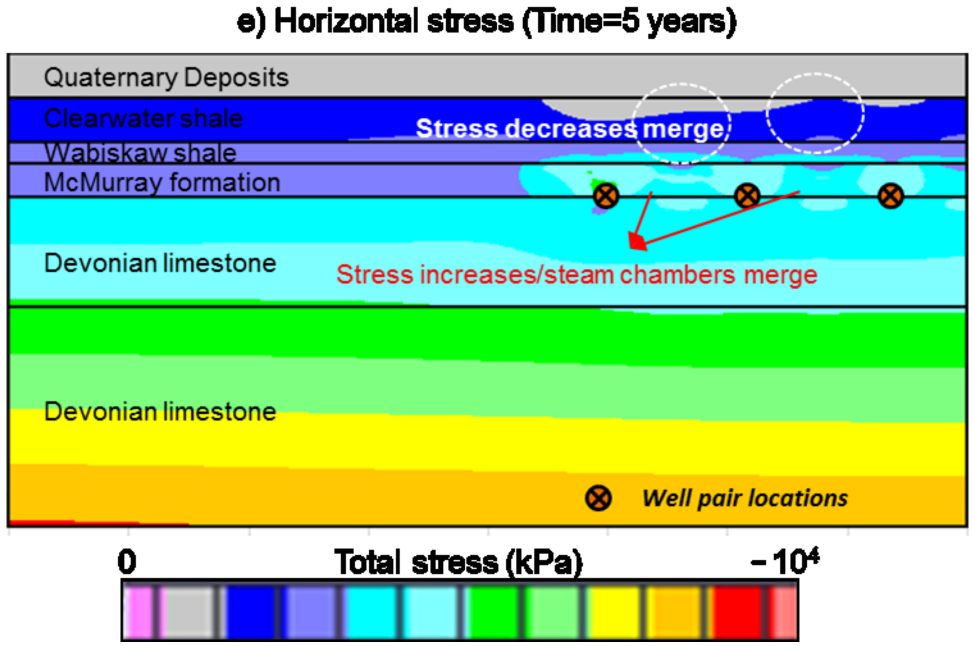

Figure 4.25 Total horizontal stress contour maps for AU model during the production

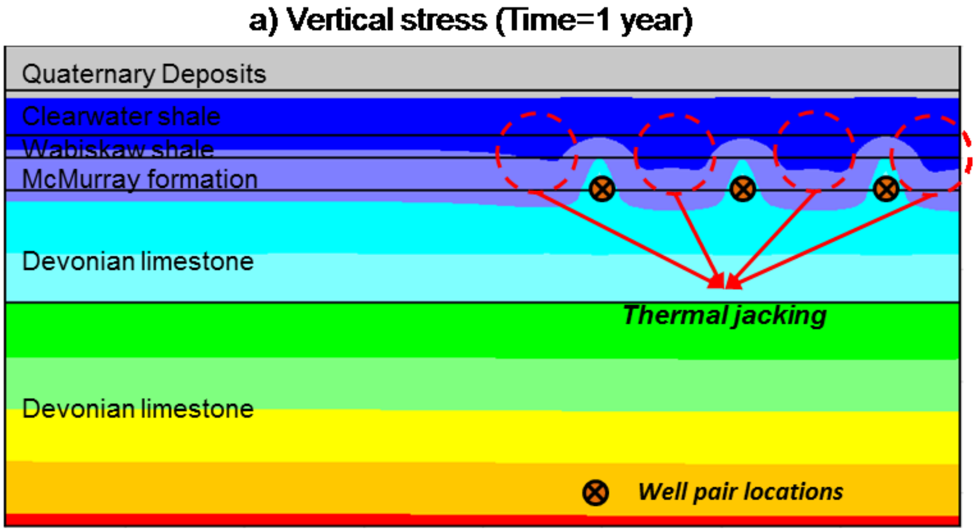

b) Vertical stress (Time=2 years)

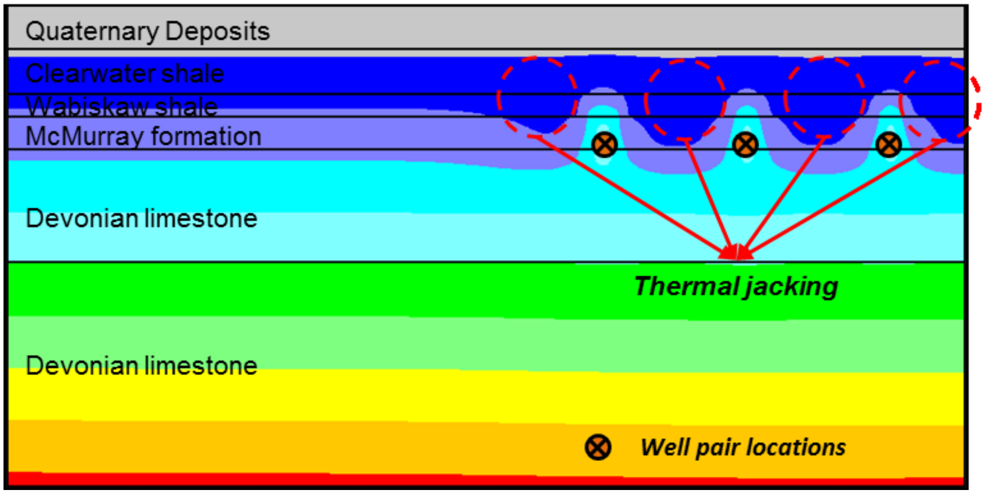

c) Vertical stress (Time=3 years)

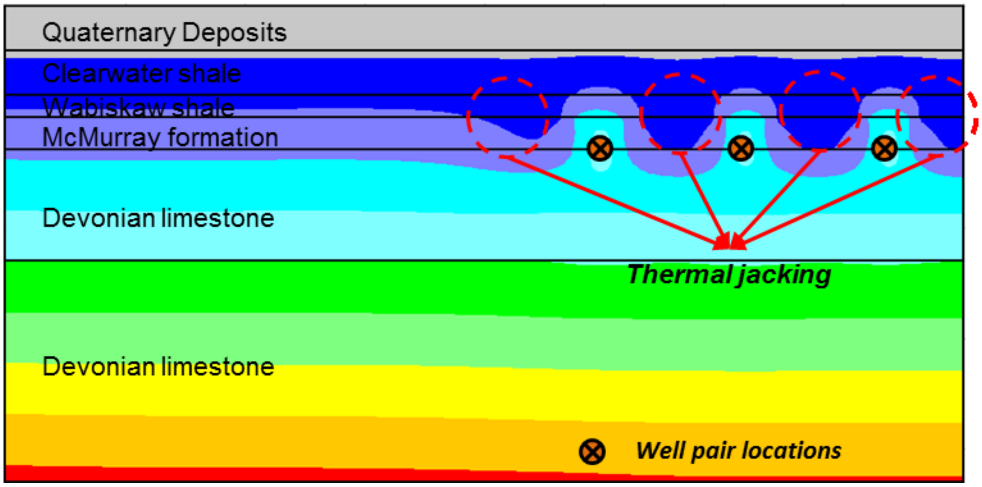

d) Vertical stress (Time=4 years)

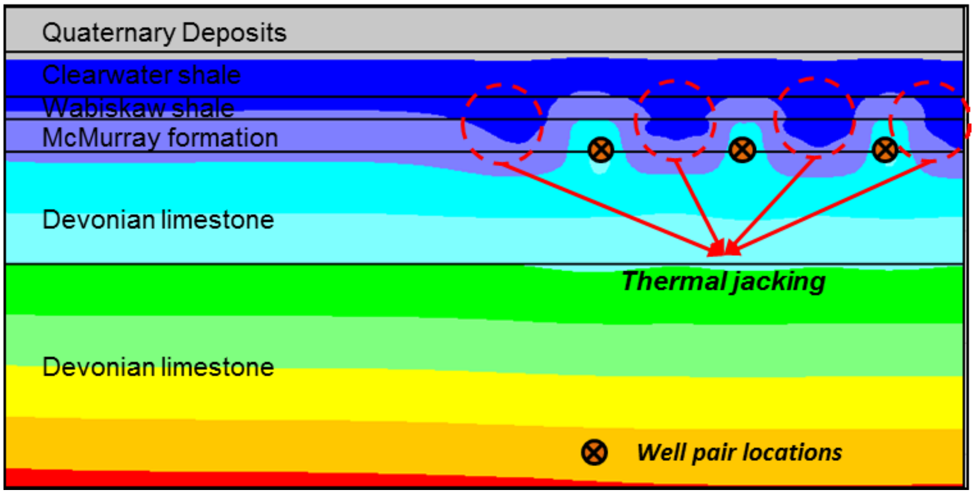

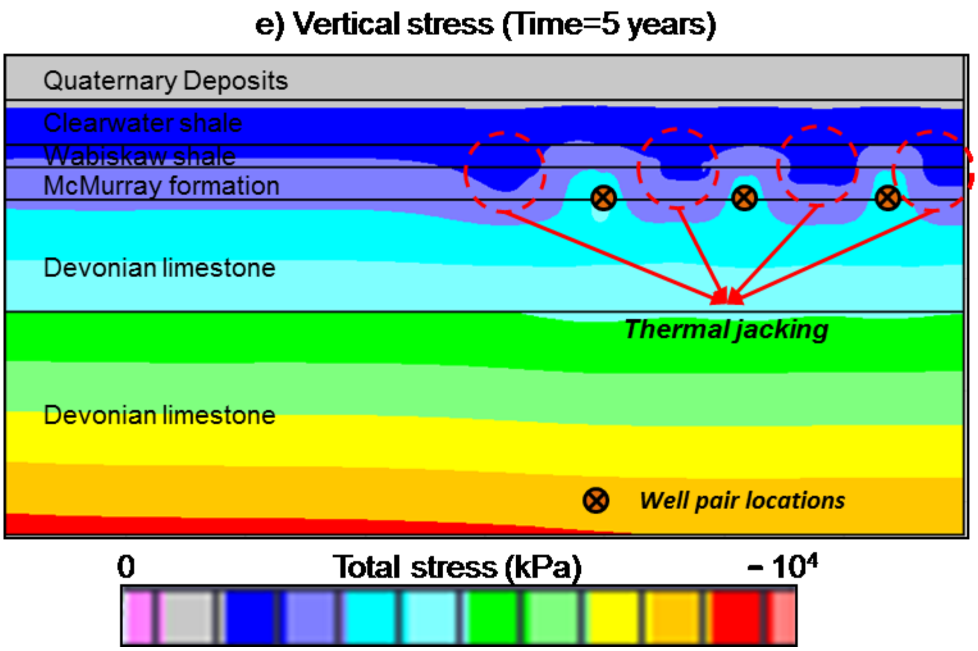

Figure 4.26 Total vertical stress contour maps for AU model during the production

4.6.4 Determination of failure pressure

The main focus of this study was the determination of the injection pressure associated with the breach of caprock integrity (failure pressure). Simulation results indicate the injection pressures Suncor had used during the years 2002-2007 did not compromise the caprock. In an effort to determine the failure pressure, we increased the injection pressures in the simulations beyond the actual levels (see Figure 4.27). The injection pressures were increased in 10% steps (10% of the initial injection pressure at the end of five years of operation) and the pressure at each step was kept constant for six months. Injection pressures were increased until the caprock integrity was compromised, which meant the failure zone had extended from the reservoir-caprock interface to the caprock-quaternary deposits interface. To obtain a more accurate prediction of failure pressure, after the occurrence of caprock breach, the numerical model for the last increment was repeated at 5% and 2.5% increments of the injection pressure, rendering failure pressure with higher accuracy than 40 kPa.

A sensitivity analysis was performed on the duration of each injection step for the isotropic model (6, 12, and 24 months) to see if this duration influenced the failure pressure. The failure pressure for different time intervals was found to be the same. It was observed that the initiation of caprock failure and the full expansion of the failure in the caprock thickness occurred within the first 3 and 6 months of the interval, respectively.

According to Figure 4.27, the AU model failed at lower injection pressure than the isotropic model (2,392 kPa vs. 2,557 kPa). The failure pressure for the AU and isotropic models were approximately 45% and 55% higher than the maximum operating injection pressure that had been exercised in the field, respectively. Figure 4.28 shows the growth of the failure zone for the injection pressure of 2,392 kPa, which resulted in the breach of caprock integrity for the AU model. Figure 4.28 shows the size of the yielded zone gradually increases under the same injection pressure after the initiation of failure in the caprock. According to Figure 4.28a, failure initiated from the interface of Quaternary Deposits and Clearwater shale. This is due to lower effective stresses at shallower depths of the Clearwater shale. Figure 4.28b shows gradual growth of the size of the yielded zone with the continued injection. After 5 months, the yielded zone grows across the entire caprock from the reservoir-Wabiskaw to the Clearwater-Quaternary interface. Additional reservoir expansion occurs as the injection continues and reservoir oil sands further expand resulting in higher shear stresses in the caprock.

With further expansion of the failure zone in the caprock, the thickness of the intact shale in the caprock decreases. The combination of higher shear stresses and thinner intact shale result in a fast growth of the yielded zone in the caprock. Figure 4.29 shows the growth of the yielded zone for the injection pressure of 2,557 kPa for the isotropic caprock.

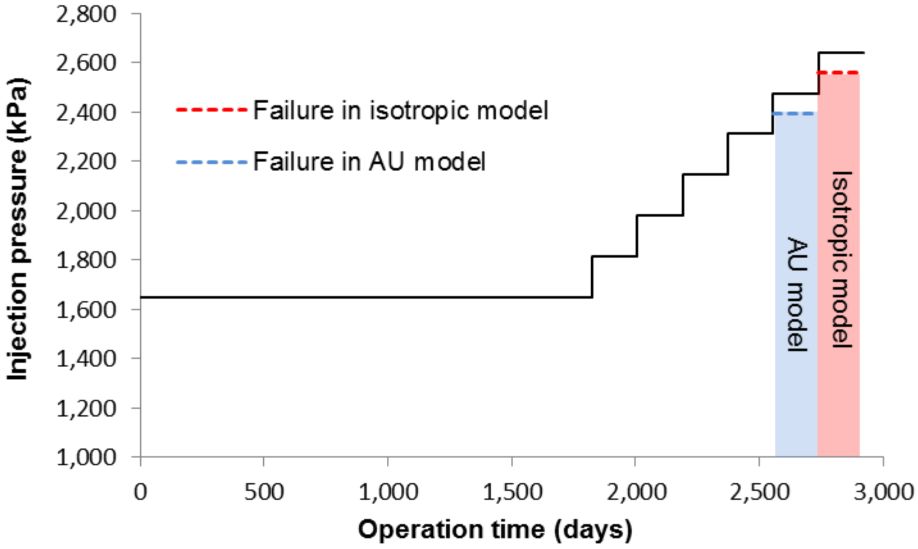

Figure 4.27 Sequences of injection pressure in both isotropic and AU model

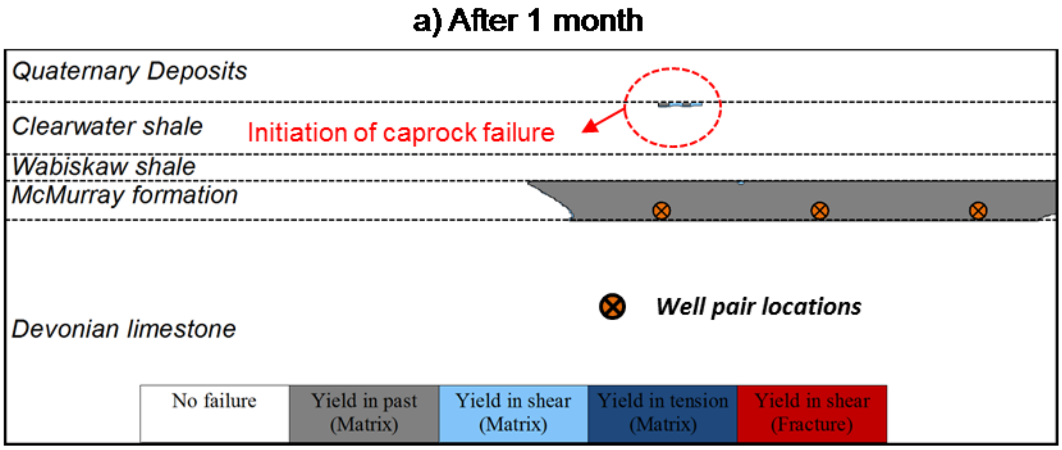
a) After 1 month

b) After 3 months

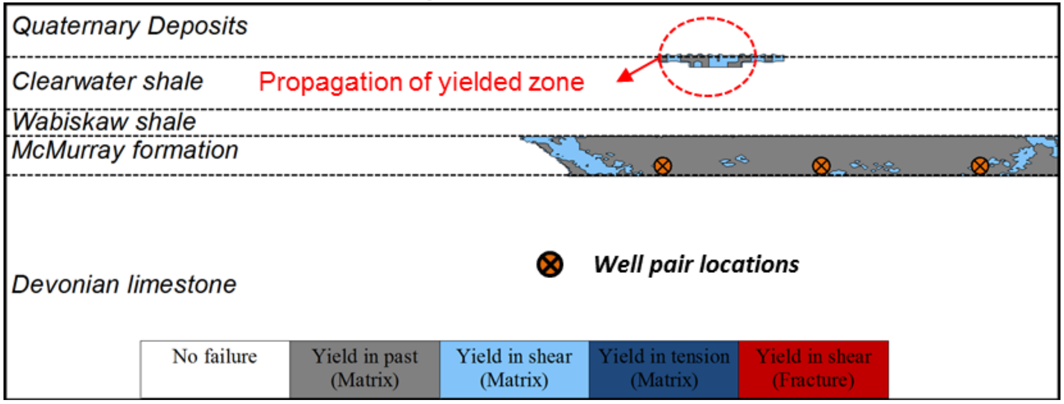

c) After 5 months

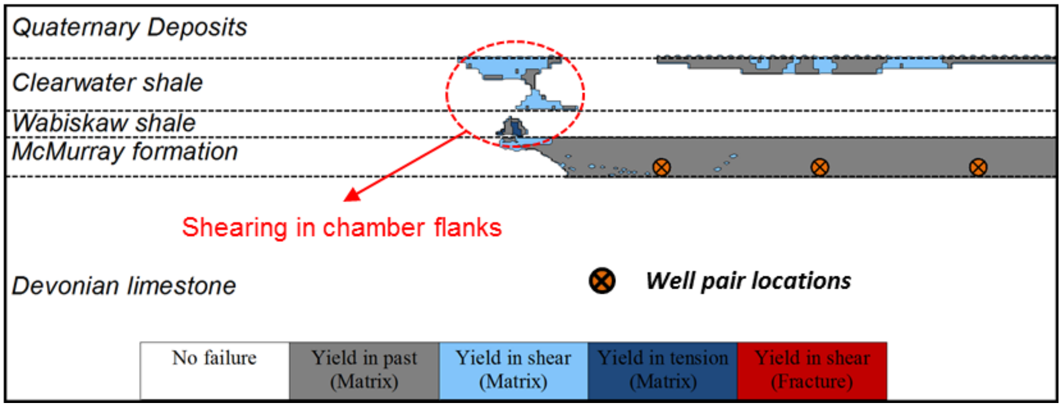

d) After 6 months

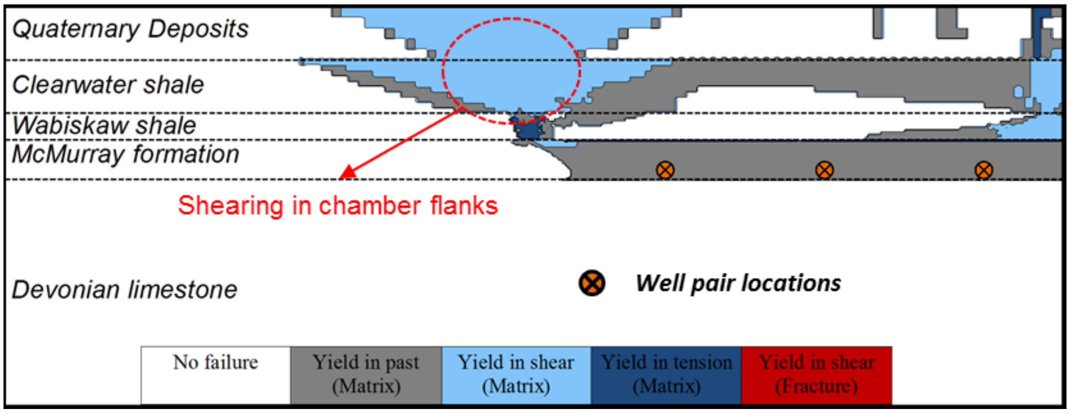

Figure 4.28 Failure zones for AU model at injection pressure of 2,392 kPa: a) after 1 month, b) after 3 months, c) after 5 months, and d) after 6 months

a) After 1 month

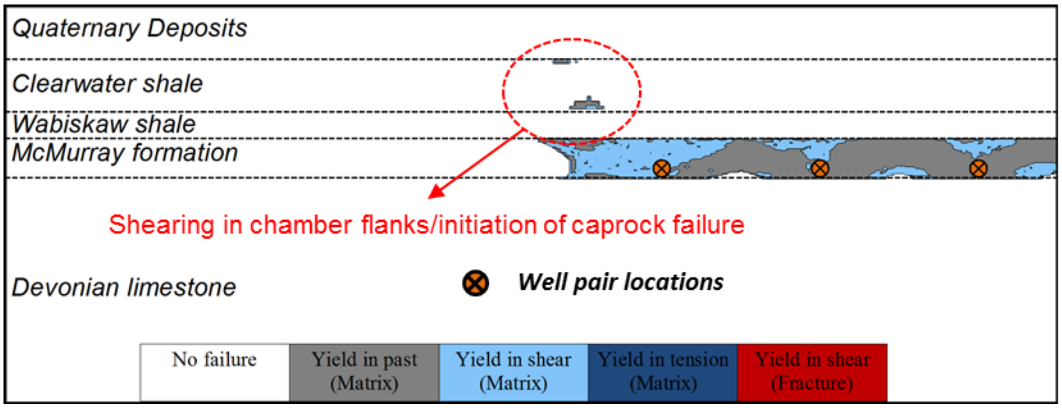

b) After 3 months

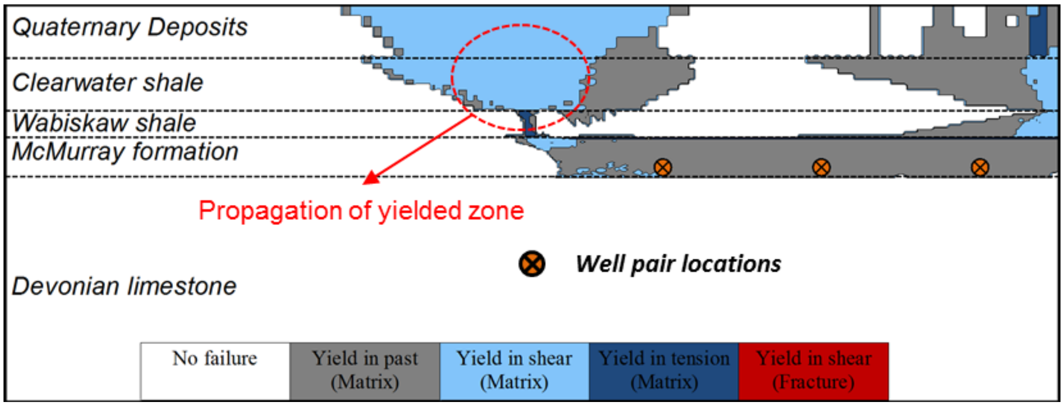

c) After 5 months

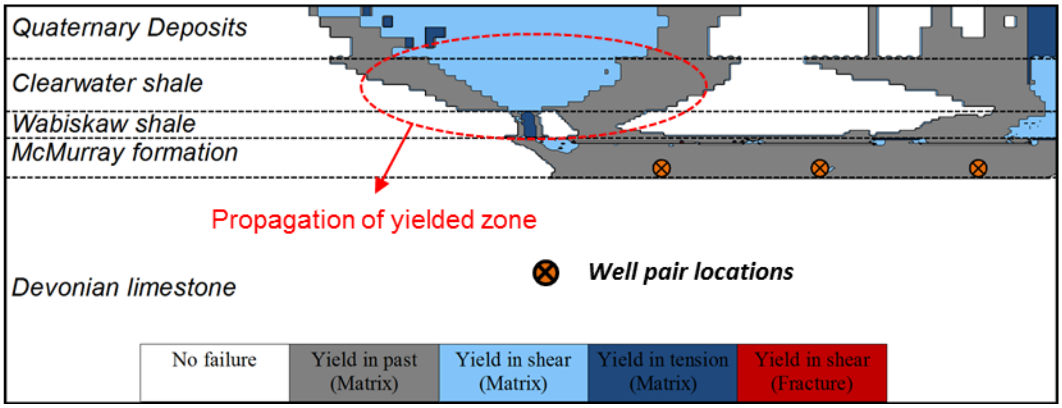

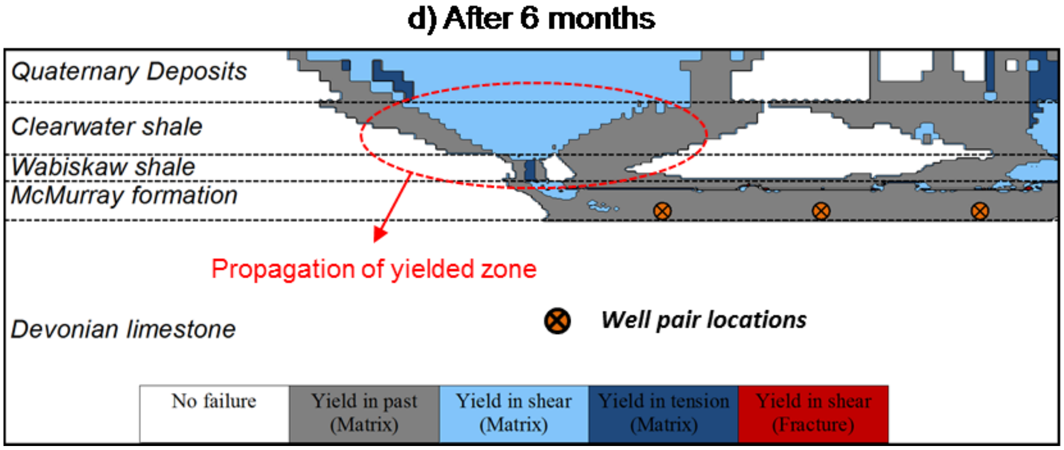

Figure 4.29 Failure zones for the isotropic model at injection pressure of 2,557 kPa: a) after 1 month, b) after 3 months, c) after 5 months, and d) after 6 months

Table 4.7 presents the failure pressure for different sensitivity cases. Failure pressures in Table 4.7 are influenced by the assumptions in the numerical model and uncertainties in the input data. One should consider a safety factor to convert the failure pressures to the Maximum Operating Pressure (MOP). The MOPs in Table 4.7 were calculated by applying the safety factor of 1.25 to the failure pressure. The safety factor of 1.25 is considered by the Alberta Energy Regulator (AER) for calculating the MOP for shallow thermal in-situ oil sands applications (AER Bulletin, 2014).

Table 4.7 Injection pressures at failure

Model	**MOP (kPa)**	**Failure pressure (kPa)**
Isotropic	2,045	2,557
AU	1,913	2,392

4.6.5 Discussion on the effect of anisotropy on failure pressure

The aim of this section is to explore the underlying reasons for the smaller failure pressure for the anisotropic caprock in SAGD. The hypothesis is that due to the higher stiffness in the horizontal direction for the AU model, the amount of the decrease in the minimum principal effective stress in the caprock for the AU model is higher than the same in the isotropic model. Consequently, the amounts of shear stresses in the caprock at corresponding states for the AU model are higher than the same in the isotropic model, hence, the lower failure pressure for the AU model. Herein, the stress paths and Mohr's circle representations for two sample points in the caprock are compared for both models to verify above hypothesis.

Figure 4.30a shows the locations of SP1 and SP2. These two points were selected in zones that were prone to shear yielding. SP1 is at the middle depth of Clearwater shale to the left side of the well pairs, close to the left flank of the steam chamber. The second observation point, SP2, was selected at the top of Clearwater shale above the C5 well pair.

In Figure 4.30b-e, stress paths are only plotted until the start of caprock failure as the numerical model didn't converge after the failure initiation due to the continued propagation of failure at constant injection pressure. For the AU model, the failure envelope depends on the angle between the maximum principal stress direction and the bedding direction. As such, only the lowest and highest envelopes are depicted.

Figure 4.30b shows the Mohr circles for SP1 for (1) the time before the start of the operation, (2) after five years of operation, and (3) at the start of caprock failure. Note, the injection pressures for the caprock failure for the isotropic and AU models do not coincide.

It can be seen from Figure 4.30b that Mohr circles for both AU and isotropic models move towards the failure envelope as the minimum and maximum principal effective stresses for both models decrease during the SAGD operation. However, the amount of drop for the minimum principal stress is more severe compared to the maximum principal stress for both models. These trends are expected as the higher horizontal stiffness for the AU model than the isotropic model should result in a larger drop in the horizontal stresses for the same amount of reservoir expansion.

Figure 4.30c shows the stress path for SP1 in the p-q space. The figure indicates a faster growth of shear stresses in the AU model than the same in the isotropic model. This is consistent with the Mohr circle results which indicate larger difference between the minimum and maximum principal stresses for the AU model than the same at the same state in the isotropic model. Figure 4.30d-e presents similar results for SP2.

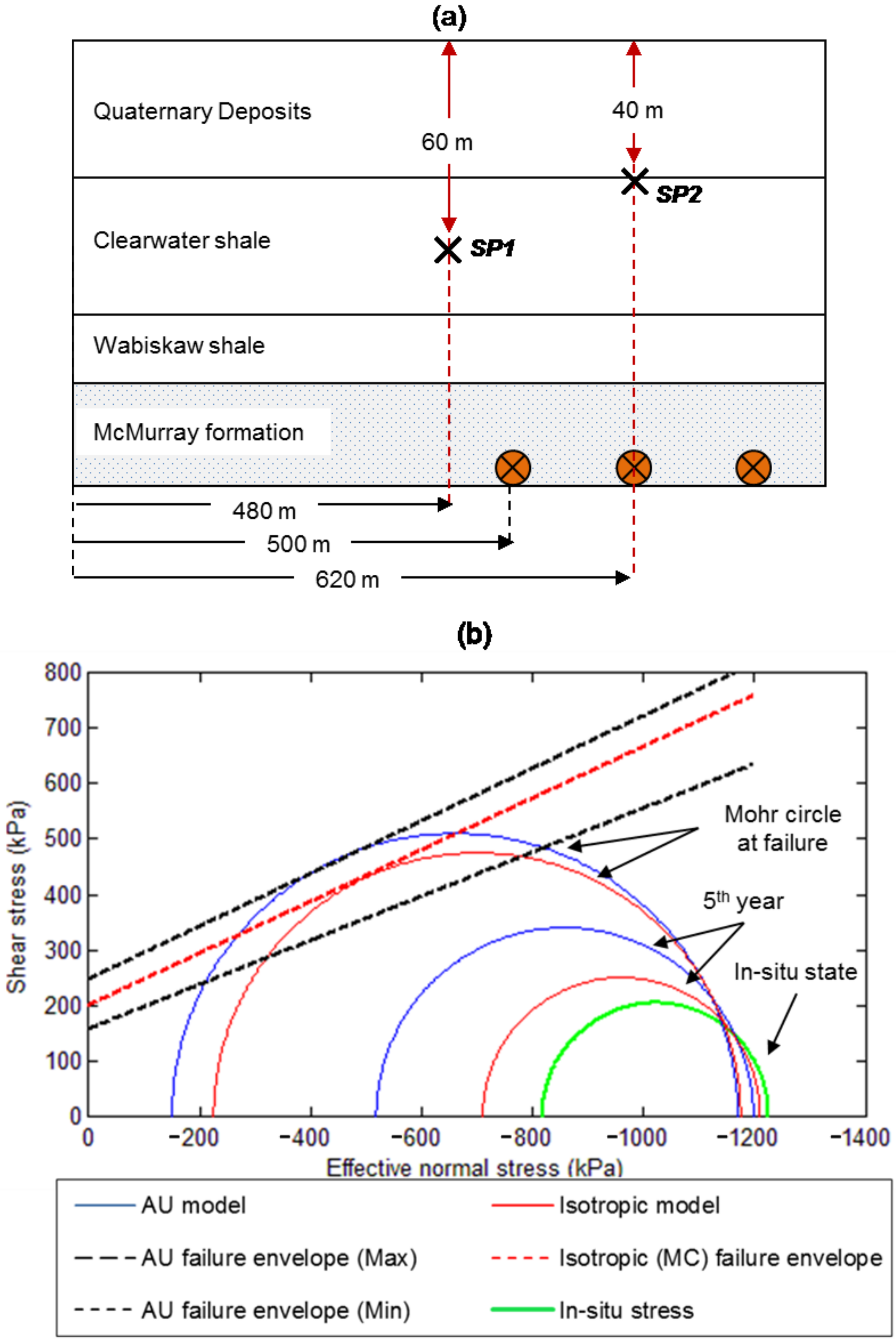
(a)
Quaternary Deposits
60 m
40 m
Clearwater shale
SP1
SP2
Wabiskaw shale
McMurray formation
480 m
500 m
620 m
(b)
Shear stress (kPa)
800
700
600
500
400
300
200
100
0
0
-200
-400
-600
-800
-1000
-1200
-1400
Effective normal stress (kPa)
Mohr circle at failure
5th year
In-situ state
AU model
AU failure envelope (Max)
AU failure envelope (Min)
Isotropic model
Isotropic (MC) failure envelope
In-situ stress

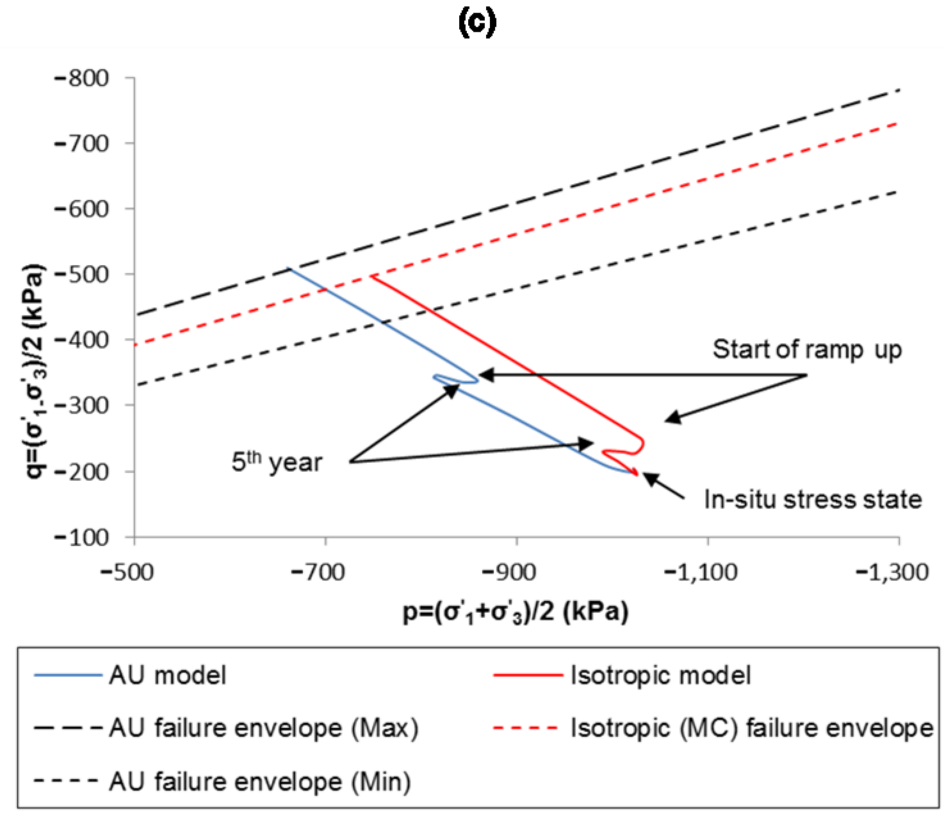
(c)
−800
−700
−600
−500
−400
−300
−200
−100
q=(σ'1-σ'3)/2 (kPa)
−500
−700
−900
−1,100
−1,300
p=(σ'1+σ'3)/2 (kPa)
Start of ramp up
5th year
In-situ stress state
AU model
Isotropic model
AU failure envelope (Max)
Isotropic (MC) failure envelope
AU failure envelope (Min)

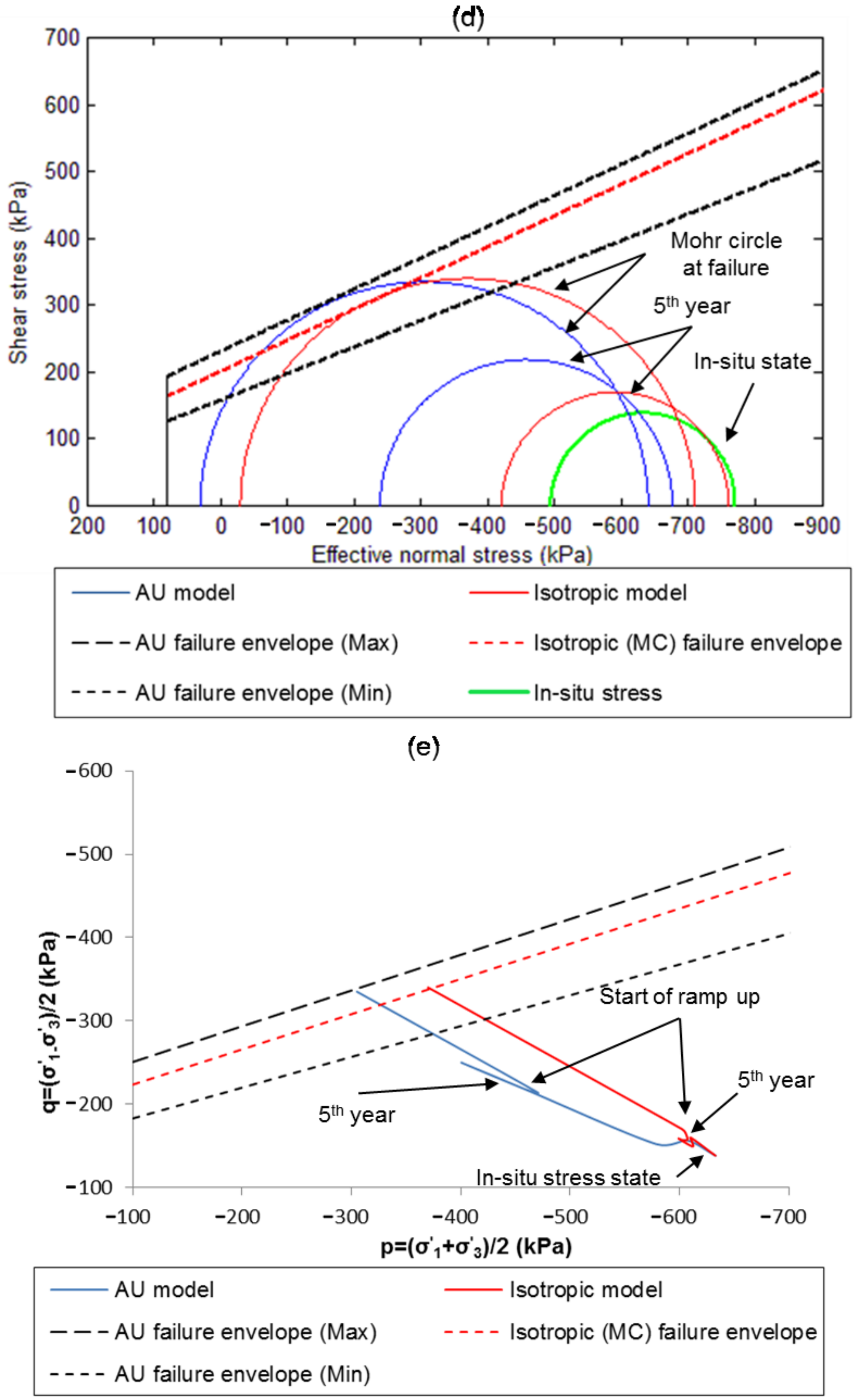

Figure 4.30 a) Locations of SP1 and SP2 in the caprock, b) Mohr's circles at SP1 for different times, c) p-q plot for SP1, d) Mohr's circle at SP2 for different times, and e) p-q plot for SP2

4.7 Conclusion

The coupled hydro-thermo-mechanical model (discussed in Chapter 3) was employed in a case study to determine the failure pressure for a SAGD case study. Two cases were considered with isotropic and anisotropic cap shales to study the effect of neglecting shale intrinsic anisotropy on the MOP. Surface heave displacements were used to validate the model. The AU model predicted closer surface heave displacement to the measurements.

Injection pressures during five years of operation did not result in the loss of caprock integrity for this case study for either of isotropic and AU models. To determine the MOP, a scenario was designed to sequentially increase the injection pressure beyond the maximum operating pressure that had been exercised in the field. Each injection pressure was kept for six months. Results show that the MOP for this case study was 45% and 55% higher than the peak operating injection pressure for AU and isotropic models, respectively. As such, anisotropic behavior of caprock shales cannot be ignored as common isotropic models provide an optimistic assessment of the MOP.

Chapter 5: Numerical assessment of the Maximum Operating Pressure for SAGD projects considering shale anisotropy and natural fractures

5.1 Introduction

Natural fractures have been observed in SAGD caprocks in Alberta (Chou, 2014). Natural fractures could provide preferential flow paths through the caprock for the escape of bitumen and injected steam and compromise the caprock integrity. These fractures could be triggered and connected to form larger fractures that can compromise the caprock integrity. Natural fractures also influence the caprock response by inducing structural anisotropy in the caprock.

Past mathematical models for caprock integrity studies have not considered the natural fractures. Several researchers have studied caprock integrity in SAGD projects assuming isotropic elasto-plastic behavior for the caprock and neglecting the effect of NFs and discontinuities in caprock layers (Smith, 1997; McLellan and Gillen, 2000; Collins, 2007; Chalaturnyk, 2011; Khan et al., 2011; Rahmati et al., 2013). Rahmati et al. (2015) studied the effect of intrinsic anisotropy of cap shale on caprock integrity. They concluded that neglecting intrinsic anisotropy for a case study overestimated the MOP by 7%. They did not include enough physics to incorporate NFs in the caprock integrity assessment.

This chapter presents a coupled hydro-thermo-mechanical model for the MOP assessment considering both intrinsic anisotropy and NFs. The effect of NFs was incorporated by using the AU constitutive model for shale (discussed in Chapter 3).

The coupled tool was used in conjunction with the AU model for a case study based on published data for MacKay River SAGD project (Suncor Energy, 2009). Suncor Energy (2013) performed fracture characterization study in the area of interest. They reported the existence of fractures in the caprock shales. However, the possible effect of NFs on the MOP is yet to be addressed.

In this chapter, different case scenarios in terms of fracture density, dip angle, and height were simulated to investigate their effect on the MOP in SAGD projects. Comparing the result of different case scenarios with those of conventional isotropic models highlights the need to include the intrinsic and structural anisotropy of the cap shale in caprock integrity studies.

Results of the coupled tool show that neglecting natural fractures can result in the overestimation of the MOP. The MOP was found to be highly sensitive to the fracture density, direction, and height. For the case study, results displayed horizontal fractures had minor effect on the MOP while fractures with the dip angle between 25° to 65° significantly dropped the MOP and could not be neglected.

5.2 Definitions

In this chapter, fractures are characterized by the number of fracture sets, fracture density, dip direction and angle, height, and length. A fracture set consists of a set of parallel systematic fractures (Singhal et al., 2010). Fracture density is defined as the number of fractures of a particular set per unit length measured in a direction perpendicular to the fracture plane (Singhal et al., 2010). Dip direction is defined as the direction of the horizontal trace of the line of the dip, measured clockwise from north (Wyllie et al., 2004). Fracture's dip angle is defined as the deviation of the fracture plane from the horizontal plane (Singhal et al., 2010). Fracture spacing describes the average perpendicular distance between two adjacent fractures of the same set and is equal to the inverse of fracture density (Singhal et al., 2010). Fracture height is the trace extent of the fractures in a sampling area normal to the fracture length (see Figure 5.1). Fracture length is a measure of the extent of development of fracture surface (Singhal et al., 2010).

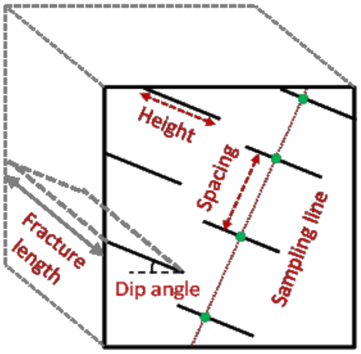

Figure 5.1 Definition of the attributes of natural fractures

5.3 Numerical model

The coupled hydro-thermo-mechanical model was used in conjunction with the AU constitutive model to capture the effect of intrinsic and structural anisotropy of the cap shale. The coupled tool and AU model are described in Chapter 3.

The model geometry, boundary conditions, operational constraints, and the mesh design of the model are the same as those in Chapter 4. Two-dimensional plane strain condition was assumed in this work as in the previous chapter. The plane strain assumption here is appropriate because (1) the length of wellbores is large in comparison with the distance between the wells; (2) thermocouple measurements show uniform distribution of temperature along the producers (Suncor Energy, 2013); and (3) the assumption was that all NFs in the caprock were parallel to the wellbores.

5.4 Case study

The importance of including cap shale's NFs in the caprock integrity is demonstrated by presenting the results of a case study.

5.4.1 Input data

Public data related to Pad C MacKay River SAGD project were used for this study to ensure consistent data. The work is an extension of what was presented in Chapter 4, with the only difference that the effects of NFs are included.

5.4.1.1 Natural fracture data

Suncor Energy (2013) reported the existence of NFs in Clearwater formation and Wabiskaw member in MacKay River SAGD project. They indicated that there was no mineralization or bitumen staining in the fractures in the core samples examined to date. They observed higher fracture density for the lower part of Clearwater Shale and Wabiskaw A shale than for the Wabiskaw D mudstone. They also observed that Wabiskaw A shale was the most fractured unit (2.6 frac./m), followed by Clearwater formation (2.4 frac./m). Wabiskaw-D Mudstone is the least fractured unit (0.2 frac./m). The geological evidence for the existence of NFs warrants the consideration of NFs in the caprock integrity analysis.

Information about the dip angle and dip direction of NFs in Wabiskaw member and Clearwater shale were not publicly available and should be assumed. These assumptions are not representative of the actual fractures for this particular site. The analysis is solely to show how the existence of NFs can impact the value of MOP. In this study, it was assumed that NFs are uniformly distributed. For the base case, linear fracture density of $2.5\,\mathrm{frac./m}$ was considered for both Clearwater and Wabiskaw shale. We assumed the fractures were systematic (not random) and assumed NE-SW direction (dip direction of 315°) (parallel to the SAGD wells) and the dip angle of 40-50° for them.

5.4.2 Strength properties of ubiquitous fractures

An important issue for this study was to determine the strength parameters of ubiquitous fractures. A series of hypothetical numerical direct shear tests was performed with FLAC to calculate the strength properties of elements containing fractures. The main purpose of this hypothetical numerical model was to smear the NF effect to the rock mass due to the relatively small fracture width in comparison with the size of numerical grid blocks. The results of numerical direct shear test were verified against analytical solution proposed by Wittke (1990).

5.4.2.1 Numerical direct shear test

Hypothetical numerical direct shear tests were performed to evaluate the rock mass properties for Clearwater and Wabiskaw shales considering the NFs. A schematic of the direct shear test under constant normal load (CNL) is presented in Figure 5.2. The normal load was applied vertically to the upper block and this load was kept constant during the test. The lower block was kept stationary during the test and a horizontal velocity of 1e-7 m/s was applied to the upper block. Direct shear tests were modeled assuming 2-D plane strain conditions. The plane strain assumption here seems appropriate because the fracture strikes are perpendicular to the test plane.

The sample size for direct shear test was selected 4 m by 4 m (Figure 5.1) based on a Representative Elementary Volume (REV) assessment for these fractures (Section 5.4.2.3). The REV is the smallest volume over which a measurement can be made that will yield a value representative of the whole (Hill, 1963).

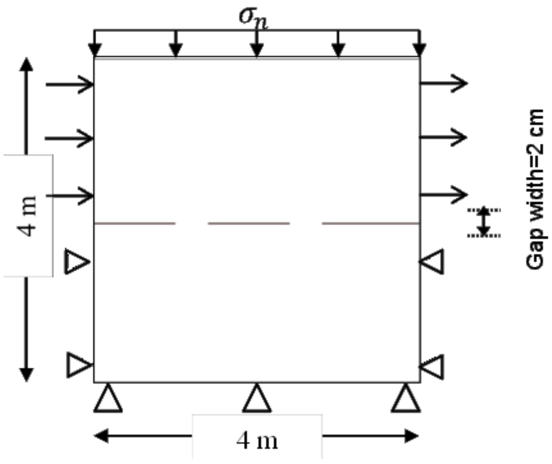

Figure 5.2 Schematic of numerical direct shear test

Different fracture densities (1.75 to 8.5 frac./m) were considered to evaluate the strength properties of the rock mass. The thickness of elements containing fractures (fracture thickness) is considered to be 2 cm. Fractures are uniformly distributed throughout the solid, as shown in Figure 5.3 where fractures are shown as black lines. Niven and Duestch (2010) asserted that conventional random fracture distribution, which is commonly used for Discrete Fracture Networks (DFNs), does not represent realistic fracture distribution with tectonic origin. They studied two NF maps for outcrop rocks in Northern Alberta and Vernazza, Italy. They concluded that for both examples, NFs were not distributed randomly; rather they were created according to in-situ stress directions and magnitudes. However, other causes of NFs (e.g., Glacio-tectonic disturbance, Gravity slumping, and Diagenetic mineral conversion) have also been observed in Alberta (Tsui et al., 1988; Gregor, 1997; Ding et al., 2012).

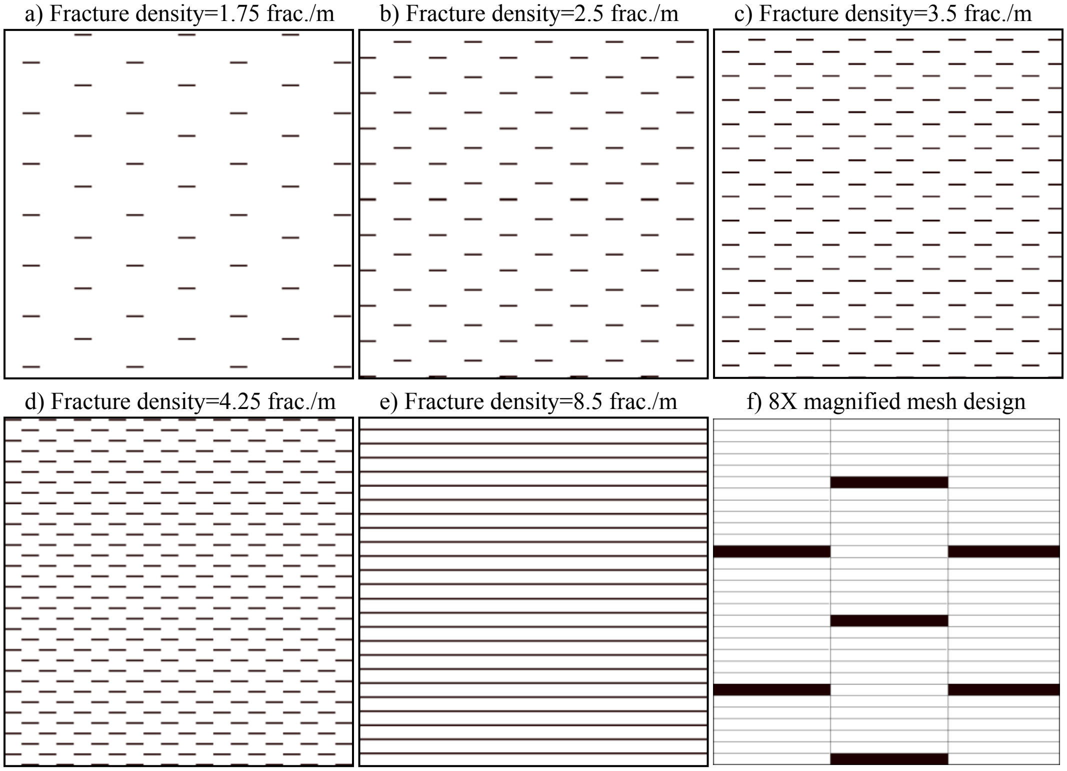

Figure 5.3 (a-e) Schematic of assumed NF distribution for different fracture densities and (f) magnified mesh design

The strength properties for Clearwater and Wabiskaw shales were obtained from Table 4.3. As most of the fractures for the studied area have no infill materials

(Suncor Energy, 2013), cohesion and tensile strength were assumed to be zero for the NFs. The friction angle of NFs was assumed to be 15°. The author is not aware if hard measurements have been conducted for this property for Clearwater and Wabiskaw shales particularly for this site.

5.4.2.2 Verification of direct shear test

The numerical direct shear test described in the previous section was verified by comparing the result of the shear test with the analytical solution proposed by Wittke (1990). Wittke (1990) analytically calculated the shear strength of samples with non-persistent, regularly ordered, open discontinuities. Non-persistent discontinuity is a discontinuity that is interrupted by rock bridges. Figure 5.4 shows a one-dimensional model of a non-persistent discontinuity.

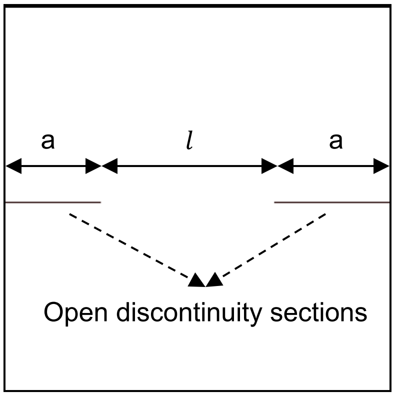

Figure 5.4 Schematic of discontinuities (after Wittke, 1990)

Wittke (1990) proposed Eq. (64)-(65) to calculate the shear strengths of rock mass. Cohesive strength of the fractures in the proposed equations is considered to be zero.

$$\varphi_{RM} = atan\big((1 - K_l)tan\varphi_{IR} + K_l tan\varphi_D\big) \tag{64}$$

$$c_{RM} = (1 - K_l)c_{IR} \tag{65}$$

where φ_{RM} and c_{RM} are friction angle and cohesion of rock mass, respectively; φ_{IR} and c_{IR} are friction angle and cohesion of intact rock; φ_D is the friction angle of discontinuity; and K_l is called the linear degree of separation and is defined as follows:

$$K_l = \frac{2a}{2a + l} \tag{66}$$

where a and l are the extent of the discontinuities and the separation between two consecutive discontinuities, respectively.

The agreement of the shear strength parameters obtained from the numerical tests and analytical solutions were examined to verify the numerical model. Different degrees of separation (K_l) between the fractures were considered ($K_l = 0, 0.25, 0.5, 0.75, 1$). Figure 5.5 shows the samples with different degrees of separation for the verification work. The model length is the same as that in the previous section (4 m × 4 m).

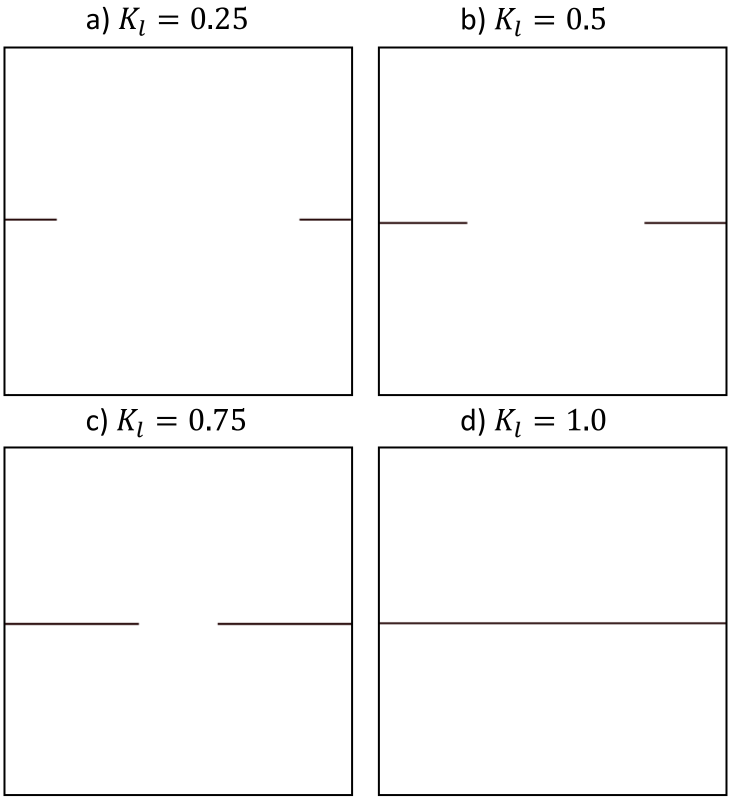

a) $K_l = 0.25$ b) $K_l = 0.5$

c) $K_l = 0.75$ d) $K_l = 1.0$

Figure 5.5 Schematic of samples with different degree of seperations

The properties of Clearwater shale were used in the verification model. Equivalent cohesion and friction angle for different samples, calculated from the analytical and numerical solutions are presented and compared in Figure 5.6 and 7. The results show close agreement between the numerical direct shear test results and analytical solutions with the maximum difference of 6.67 %.

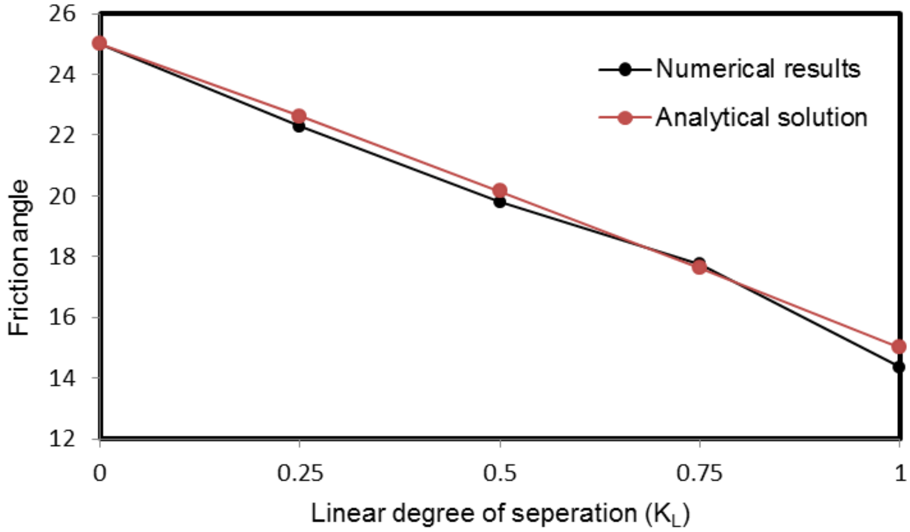

Figure 5.6 Equivalent friction angle for different degree of separations

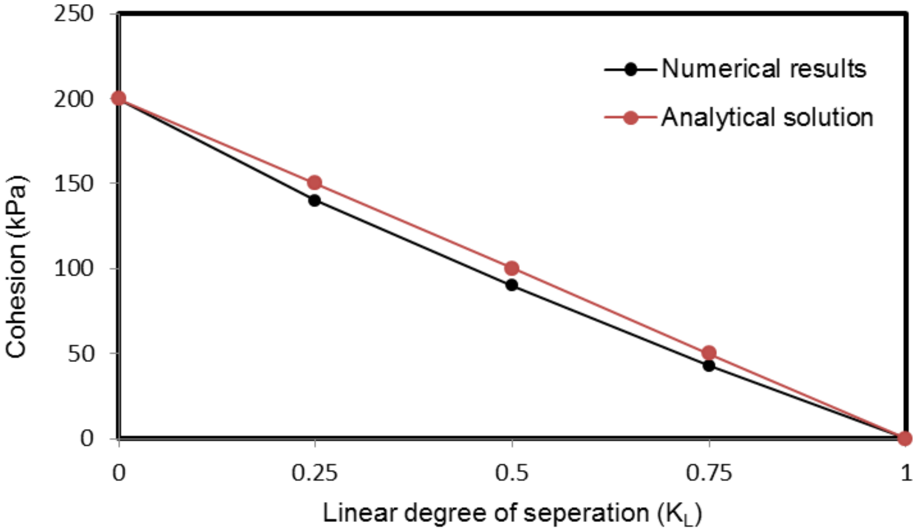

Figure 5.7 Equivalent cohesion for different degrees of separation

5.4.2.3 REV assessment

The Representative Elementary Volume (REV) (also called the Represent Volume Element (RVE) or the unit cell) is the smallest volume over which a measurement can be made that will yield a value representative of the whole (Hill, 1963). In continuum mechanics, for a fractured material, REV is considered as a volume that represents all fractures that exist in the rock. It must however remain small enough to be considered as a volume element of continuum mechanics.

In order to establish the properties of a given fractured medium, different sample sizes for the fractured medium were examined. If the sample is too small, the readings tend to oscillate. As the sample size is enlarged, the oscillations begin to damp out. Eventually the sample size would become large enough that the readings are consistent. This sample size is referred as the REV. If the sample size is increased, measurement would stay stable.

REV assessment was performed in this study by varying the sample size from 1 m^2 to 64 m^2. The samples were assumed to be square and fractures were distributed uniformly throughout the samples. Mechanical properties of Clearwater shale were considered for the samples. Constant fracture density of 2.5 frac./m was considered for all samples. Figure 5.8 shows the schematic of different samples used for the REV assessment.

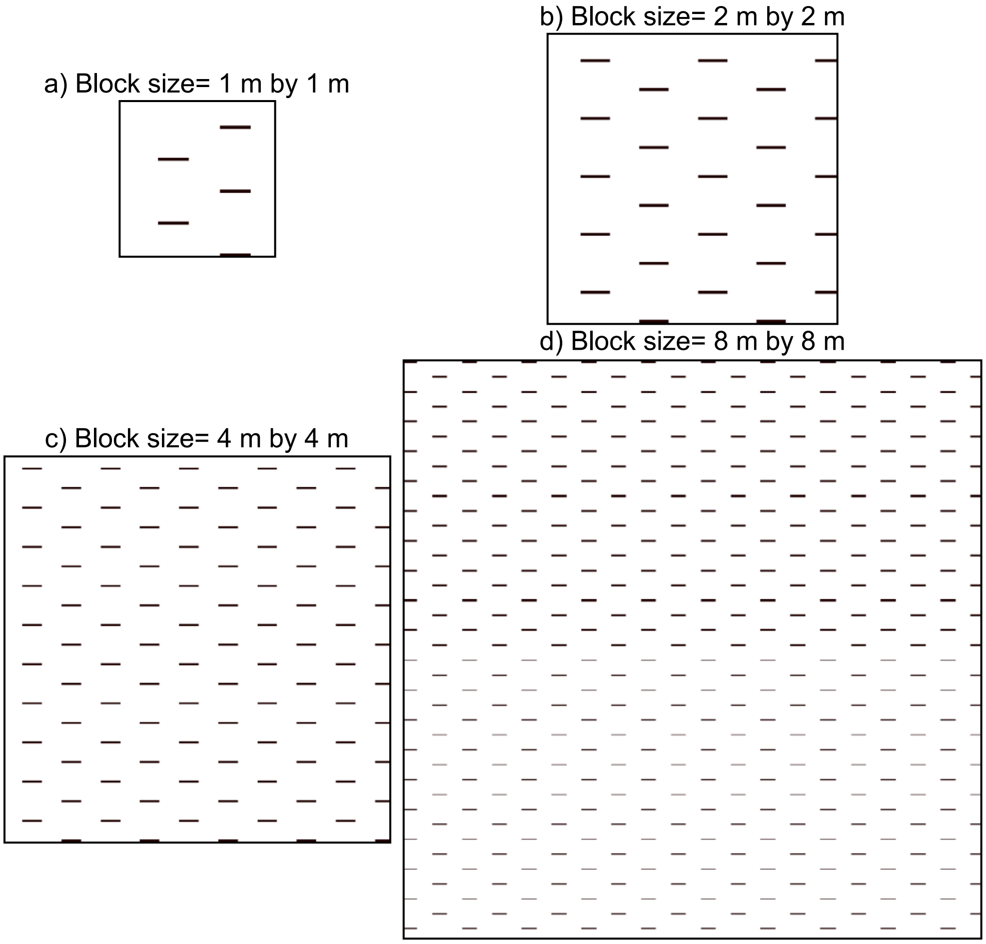

Figure 5.8 Schematic of samples with different sizes and constant fracture density

Figure 5.9 presents the results of shear test for different block sizes and with constant fracture density of 2.5 frac./m. Results show that the equivalent friction angle and cohesion for block sizes less than 4 m by 4 m tend to oscillates and for block sizes larger than that the readings are consistent. Therefore, the REV equal to 4 m by 4 m was selected for these fractures. In this study, the REV was assumed to be constant for different fracture densities (4 m × 4 m).

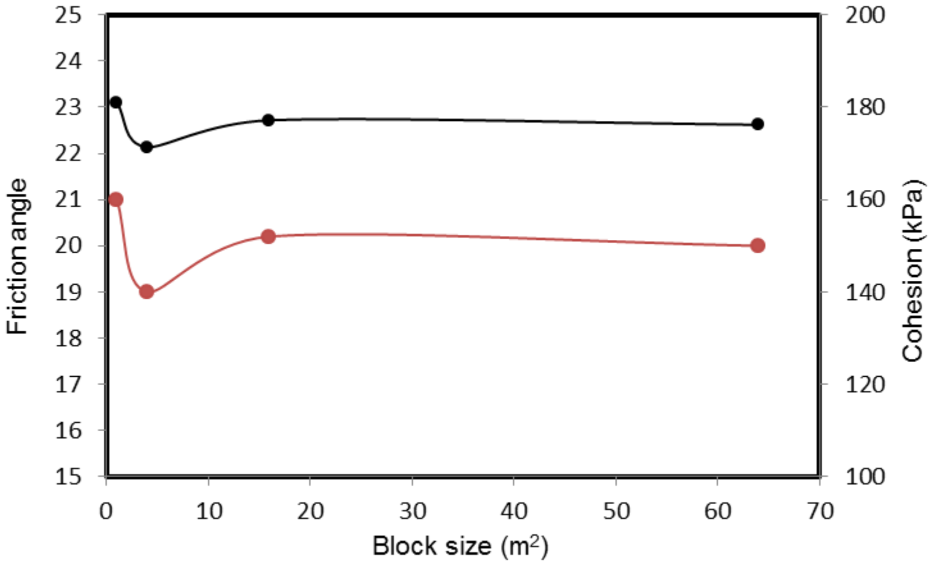

Figure 5.9 Equivalent friction angle and cohesion for different block sizes

5.4.2.4 Results of direct shear test for Clearwater shale

The results of numerical direct shear tests are presented in terms of shear stress and horizontal displacement for Clearwater shale. The shear stress in this section is defined as the average shear stress of the elements located in the gap row (see Figure 5.2). The horizontal displacement is measured as the horizontal movement of the left boundary in the upper block (see Figure 5.2). Normal stress is defined as the vertical stress (σ_n) applied on the top boundary of the shear block in Figure 5.2.

Shear tests simulations were carried out for fracture densities of 1.75, 2.5, 3.5, and 4.25 frac./m. Peak shear stresses were plotted against normal stresses for each fracture density. Equivalent friction angle and cohesion were determined by using the MC failure criterion. The results of the shear tests for Clearwater shale are presented in Figure 5.10-17.

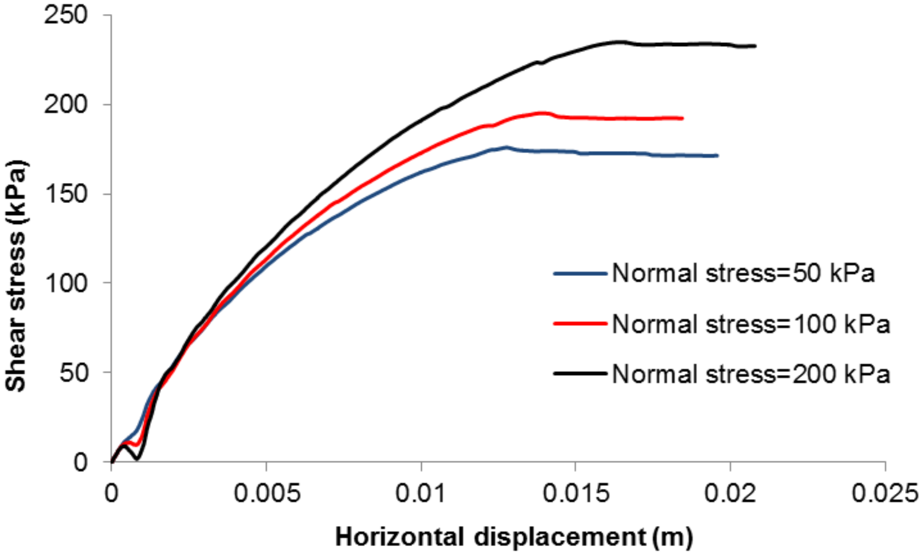

Figure 5.10 Shear stress vs. horizontal displacement for fracture density of 1.75 frac./m

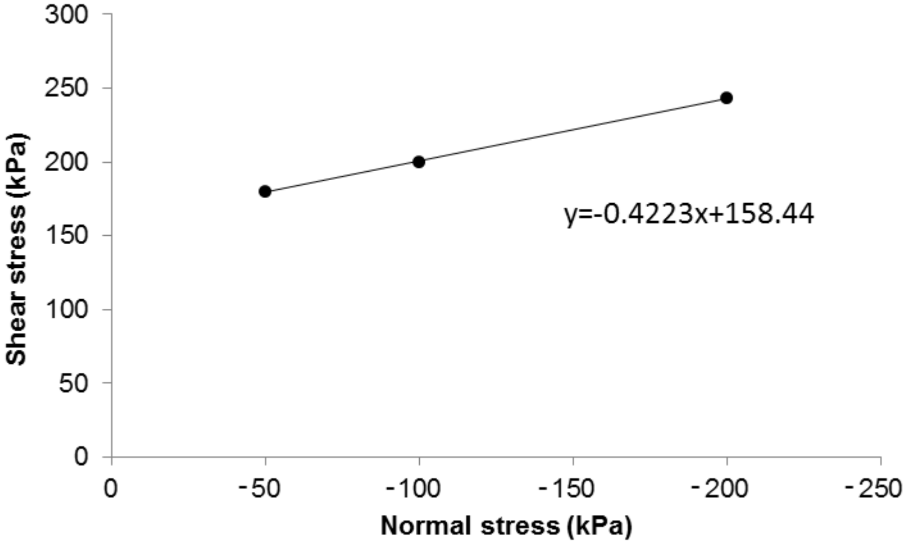

Figure 5.11 Shear stress vs. normal stress for fracture density of 1.75 frac./m

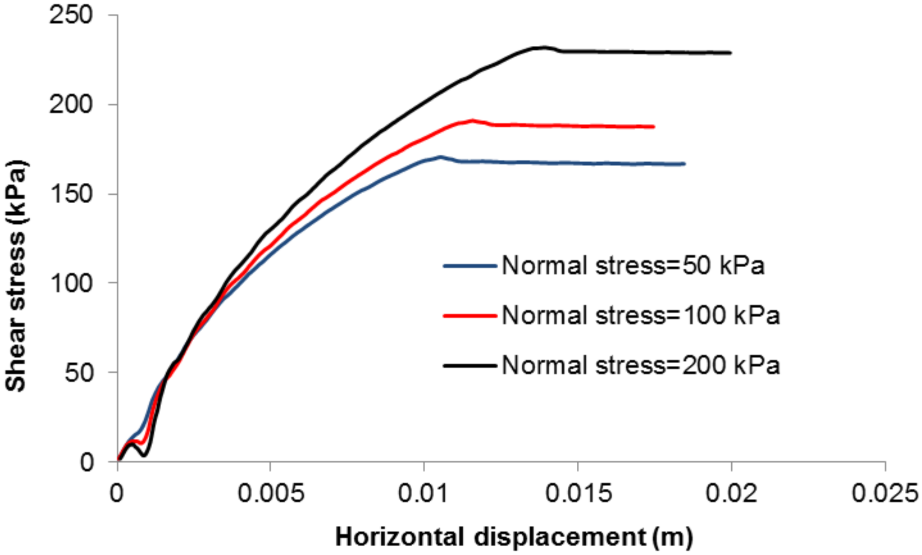

Figure 5.12 Shear stress vs. horizontal displacement for fracture density of 2.5 frac./m

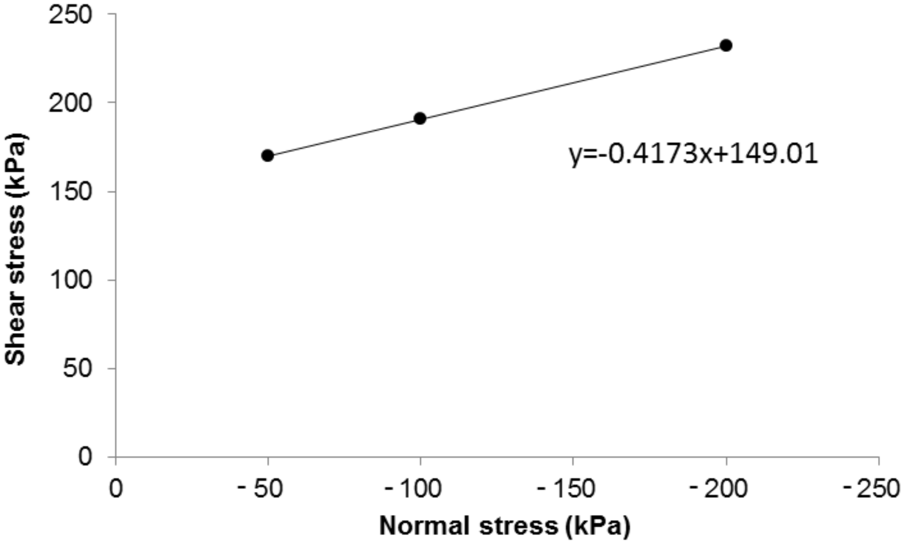

Figure 5.13 Shear stress vs. normal stress for fracture density of 2.5 frac./m

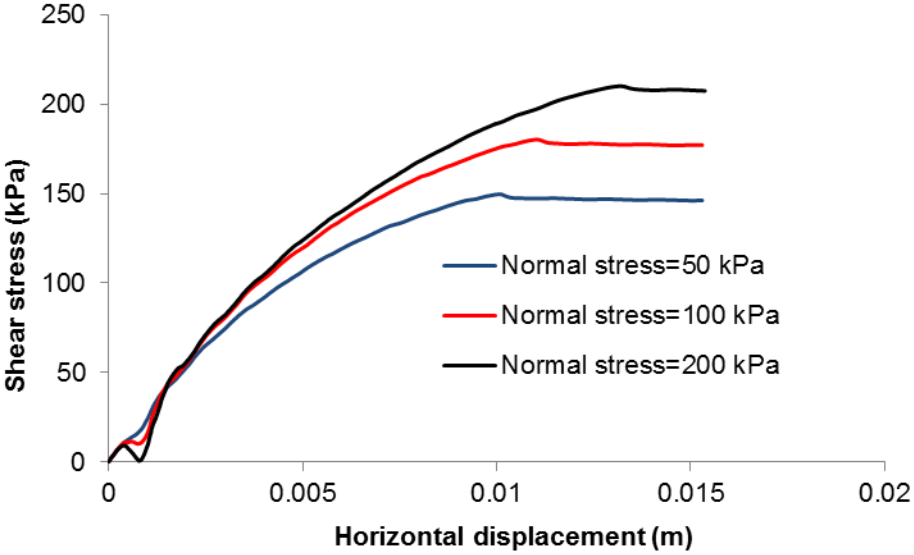

Figure 5.14 Shear stress vs. horizontal displacement for fracture density of 3.5 frac./m

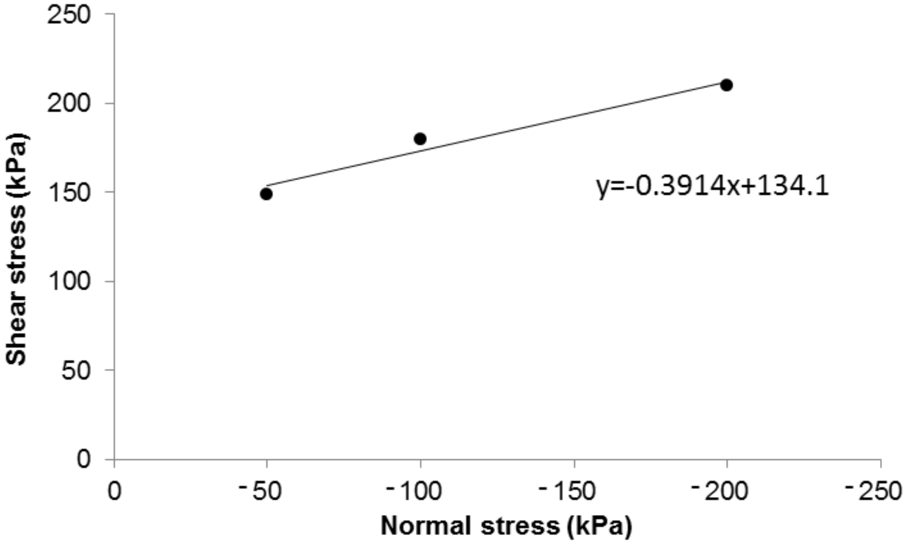

Figure 5.15 Shear stress vs. normal stress for fracture density of 3.5 frac./m

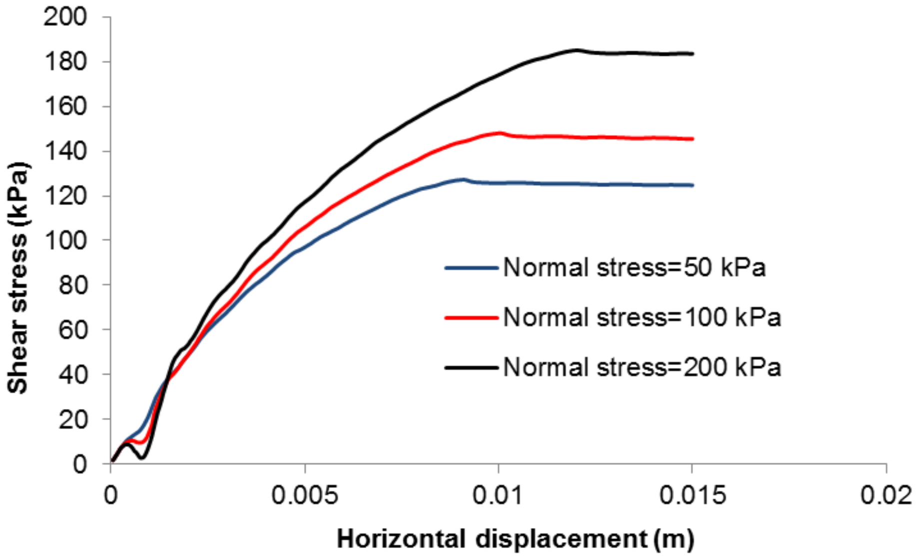

Figure 5.16 Shear stress vs. horizontal displacement for fracture density of 4.25 frac./m

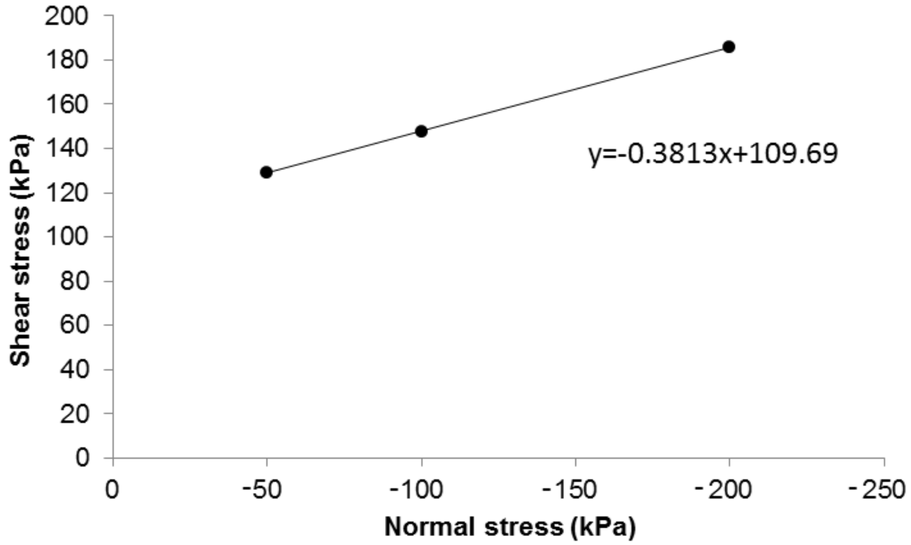

Figure 5.17 Shear stress vs. normal stress for fracture density of 4.25 frac./m

5.4.2.5 Results of direct shear test for Wabiskaw shale

The results of numerical direct shear tests are presented in terms of shear stresses and horizontal displacements for Wabiskaw shale. Shear test simulations were performed for fracture densities of 1.75, 2.5, 3.5, and 4.25 frac./m. The results of the shear tests for Wabiskaw shale are presented in Figure 5.18-25.

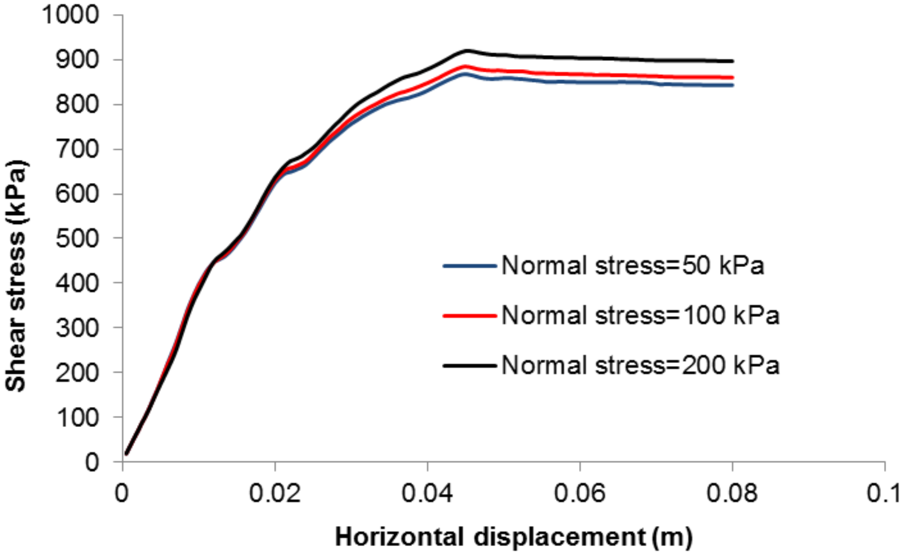

Figure 5.18 Shear stress vs. horizontal displacement for fracture density of 1.75 frac./m

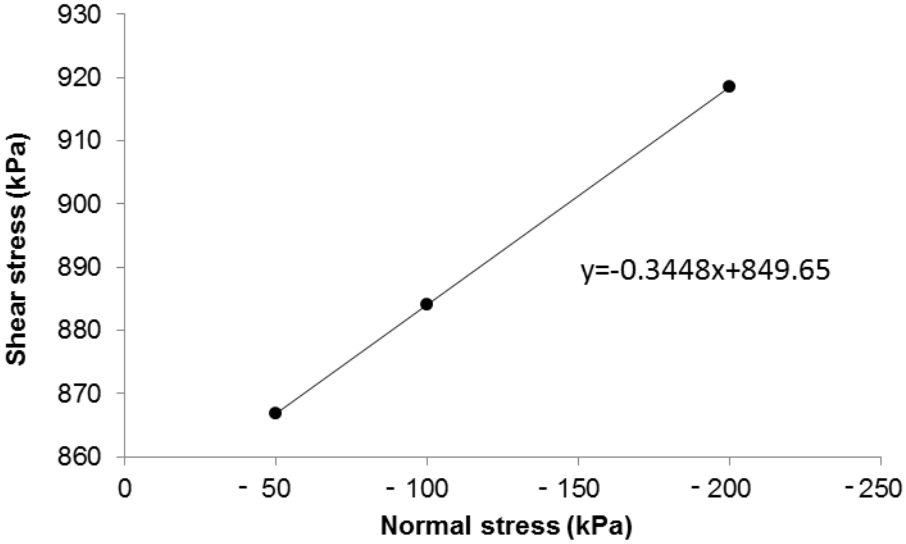

Figure 5.19 Shear stress vs. normal stress for fracture density of 1.75 frac./m

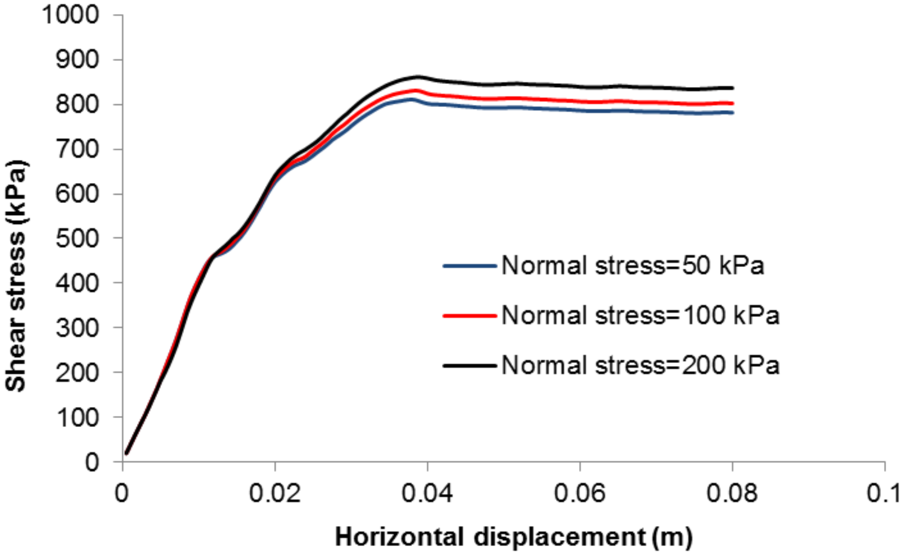

Figure 5.20 Shear stress vs. horizontal displacement for fracture density of 2.5 frac./m

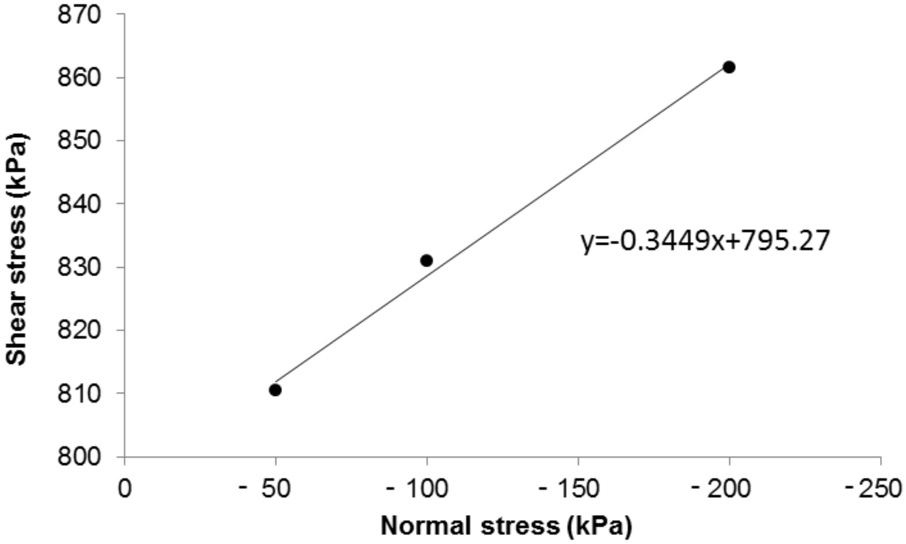

Figure 5.21 Shear stress vs. normal stress for fracture density of 2.5 frac./m

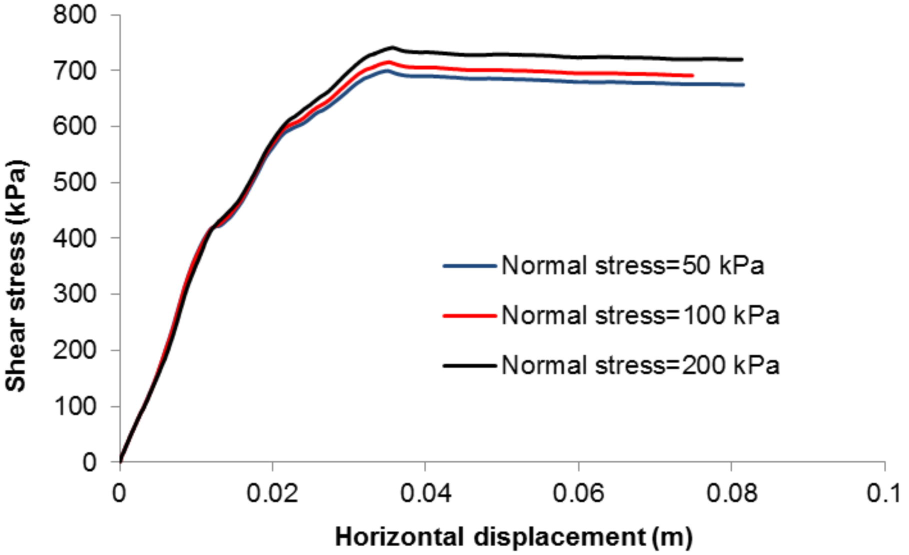

Figure 5.22 Shear stress vs. horizontal displacement for fracture density of 3.5 frac./m

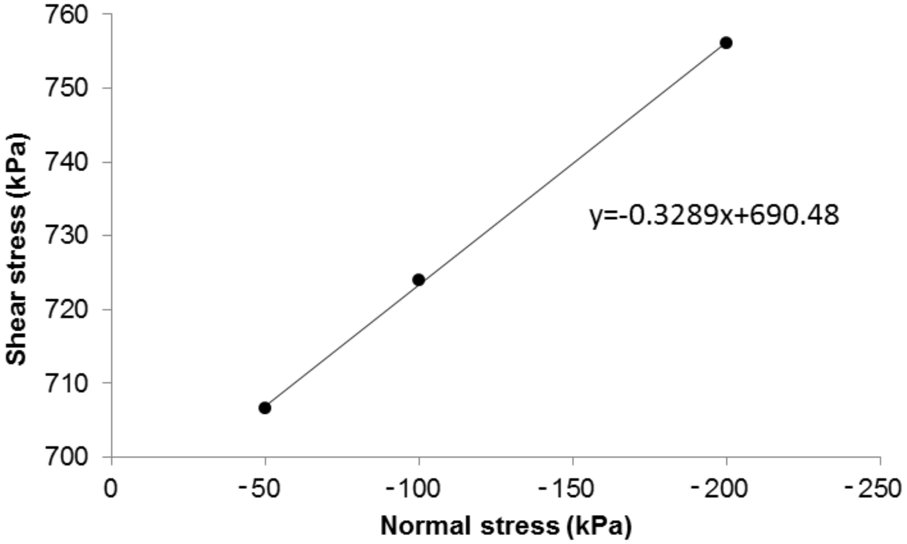

Figure 5.23 Shear stress vs. normal stress for fracture density of 3.5 frac./m

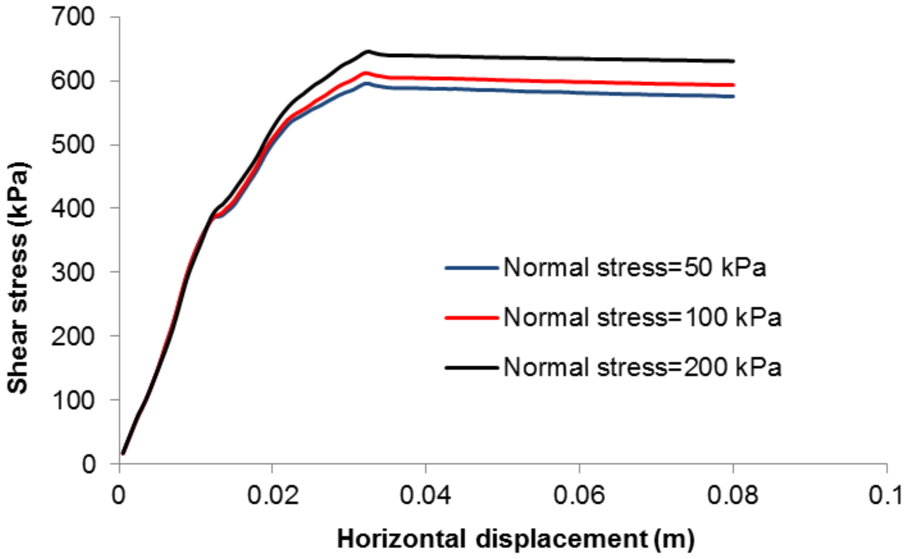

Figure 5.24 Shear stress vs. horizontal displacement for fracture density of 4.25 frac./m

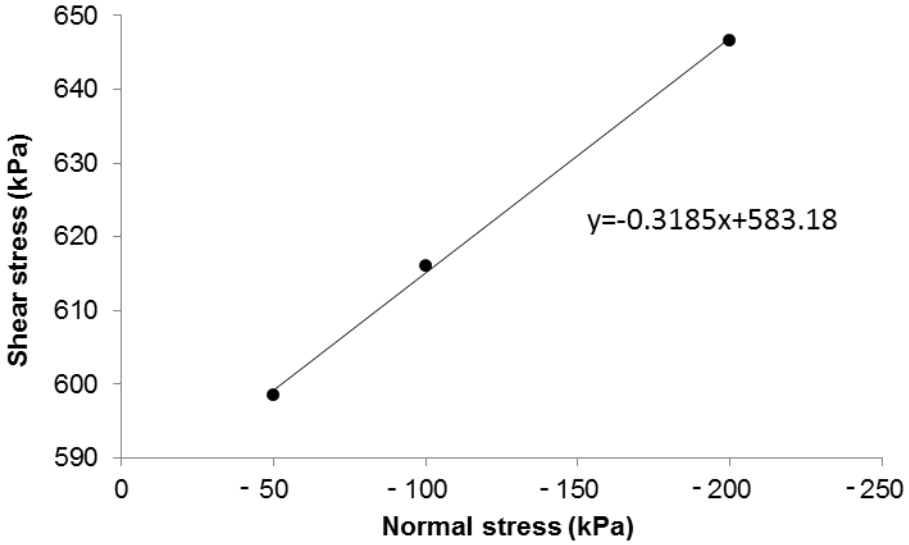

Figure 5.25 Shear stress vs. normal stress for fracture density of 4.25 frac./m

5.4.2.6 Equivalent cohesion and friction angle for Clearwater/Wabiskaw shale

Equivalent cohesion and friction angle for different fracture densities were calculated based on the result of numerical direct shear test. Figure 5.26 shows the equivalent friction angle and cohesion for different fracture densities.

Figure 5.26 shows that the equivalent cohesion and friction angle for low densities follow the matrix strength properties and, with the increase of density, equivalent strength properties converge to the strength properties of the NFs.

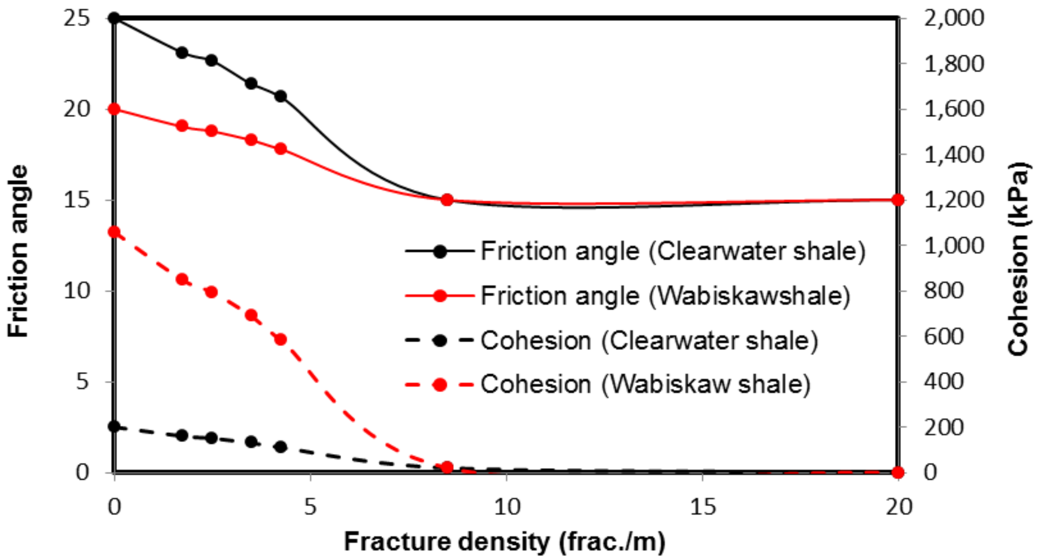

Figure 5.26 Equivalent friction angle and cohesion for different fracture intensities in Clearwater and Wabiskaw shales

5.4.2.7 Effect of gap size on direct shear test results

The gap size in the direct shear test affects the calculated strength properties of the specimen. In this study, the gap size was assumed to be 2 cm (see Figure 5.2). A sensitivity analysis was conducted with respect to the gap size which was varied from 1 cm to 10 cm. In this part, fracture density of 2.5 frac./m was assumed for the samples and Clearwater shale strength properties were considered.

Figure 5.27-28 present the results of direct shear test for different gap sizes. Note, in all simulations only one row of NFs is positioned inside of the gap (see Figure 5.3b). Results show that with the increase of gap size, peak yield stress increases slightly. This can be attributed to the fact that with the increase of the gap size, the ratio of rock matrix to fracture thickness in the gap interval increases. Thus, the calculated strength properties follow more predominantly the rock matrix strength properties thus the higher peak strength in the direct shear test.

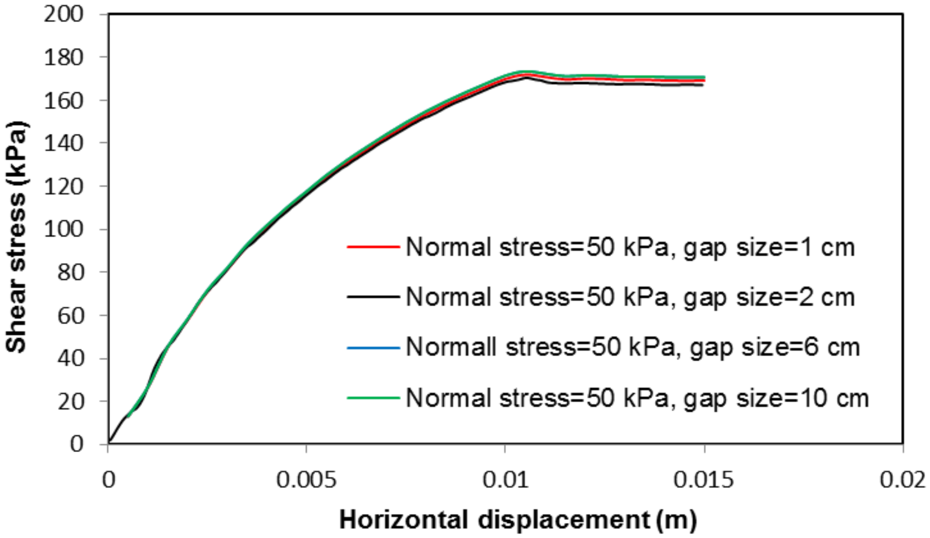

Figure 5.27 Shear stress vs. horizontal displacement for normal stress of 50 kPa

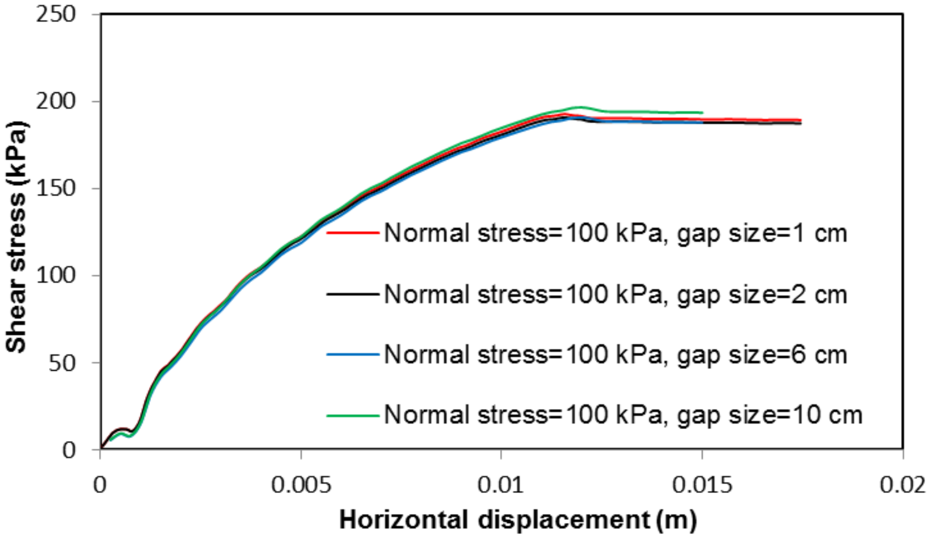

Figure 5.28 Shear stress vs. horizontal displacement for normal stress of 100 kPa

5.4.3 Effect of fracture attributes on strength properties of ubiquitous fractures

Considering the fact that a comprehensive fracture characterization has not been published for the case study area, we performed a parametric study by varying the number of fracture sets, fracture density, and fracture height and dip angle to investigate their effect on the MOP (Table 5.1). The base case was considered to be the intrinsically anisotropic model with no NF. To study the effect of fracture density on the MOP, two cases were tested with the fracture density of 2.5 and 3.5 frac./m.

Table 5.1 Simulation matrix to investigate the effect of NFs on MOP

Category	**Number of simulations**	**Fracture density (frac./m)**	**Fracture dip angle (ξ)**	**Fracture height (cm)**	**Number of fracture sets**
[1]Non-fractured cases	2	--	--	--	0
Fracture density	5	2.5 and 3.5	[2]0°, 45° and 90°	20	1
Fracture dip angles	5	2.5 and 3.5	[2]0°, 45° and 90°	20	1
Fracture height	2	2.5	45° for single set/25°,45° and 65° for 3 sets	20 and 100	3
Fracture interaction	2	2.5	45° for single set/25°,45° and 65° for 3 sets	20	1 and 3

[1] Non-fractured cases do not include fracture sets. Isotropic and intrinsically anisotropic models are considered for caprock layers.

[2] The case of 0° dip angle for fractures was not run for the density of 3.5 frac./m, as the case with the density of 2.5 frac./m showed that fractures with such dip angle have no contribution to failure.

5.5 Results of coupled hydro-thermo-mechanical model

The coupled numerical model was used to determine the failure pressure for the cases specified in Table 5.1. At the end of five years of operations, field injection pressures did not compromise the caprock. As such, injection pressures were increased beyond the actual levels to find the failure pressure that is defined here as the injection pressure of injector wells at the time of caprock breach. Injection pressure was increased stepwise by 10% of the total pressure in the previous step and kept constant for six months. Injection pressures were increased until the caprock breached which meant the yielded zone extended from the reservoir-caprock interface to the caprock-quaternary deposits interface. To obtain a more accurate prediction of failure pressure, after the occurrence of caprock breach, the numerical model for the last increment was repeated at 5% and 2.5% steps rendering failure pressure with accuracy higher than 40 kPa.

5.5.1 Simulation results

This section presents the results of the parametric analysis for the analysis cases reflected in Table 5.1.

5.5.1.1 Fracture density and dip angle

Figure 5.29 shows the yielded zone for the case with horizontal NFs ($\xi = 0°$) and fracture density of 2.5 frac./m. Failure pressure was found to be 2,392 kPa, which is the same as that of the model that considered only intrinsic anisotropy (no NFs). Figure shows that the caprock failure is due to shear yielding in the rock matrix.

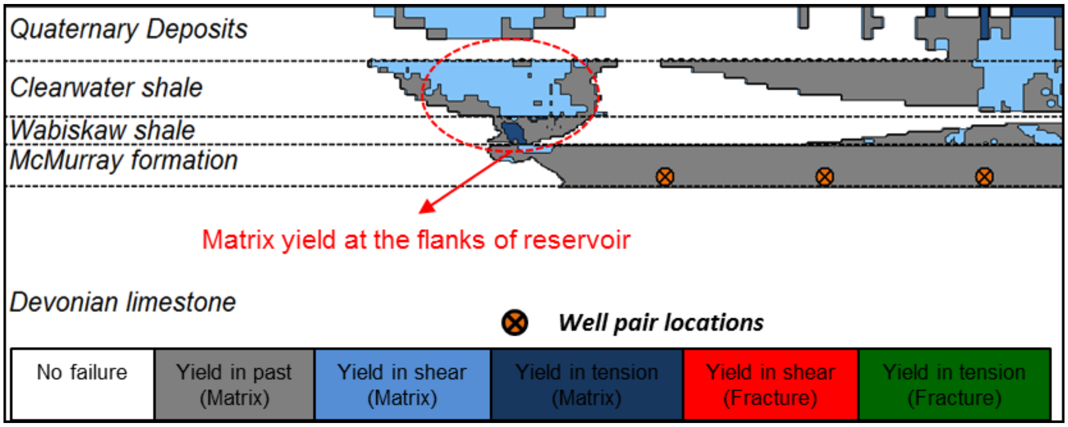

Figure 5.29 Yielded zones for fracture density=2.5 $frac./m$ and fracture dip angle=0°

Figure 5.30 displays the yielded zones for the case with oblique fractures (ξ = 45°) and fracture density of 2.5 frac./m. Results show that the Clearwater shale is in shear yield across the caprock due to the NFs. In this case study, failure pressure dropped from 2, 392 kPa with no NFs (intrinsically anisotropic case) to 2, 145 kPa for the case with the NFs. The NFs for this case decrease the failure pressure by 11%, which indicates that the oblique fractures (ξ = 45°) have significant effect on failure pressure.

Figure 5.31 shows the yielded zone for vertical fractures (ξ = 90°) and fracture density of 2.5 frac./m. The figure shows that there is a small zone with yielded fracture at the bottom of Clearwater shale and the rest of the caprock failed due to shear matrix yield. The assumption of no additional hydraulic conductivity for the fractures compared to the matrix could be the main reason that the vertical fractures showed minor effect on caprock failure pressure. Another reason could be due the fact that the NFs growth was not considered in this study. Failure pressure in this case was found to be 2,351 kPa. The failure pressure for this case is 1.7% less than the case without considering NFs (intrinsically anisotropic case).

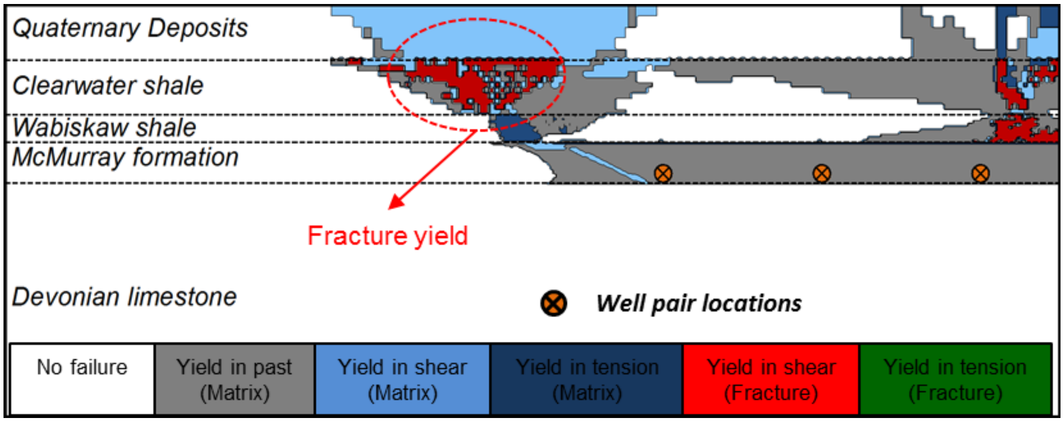

Figure 5.30 Yielded zones for fracture density=2.5 $frac./m$ and fracture dip angle=45°

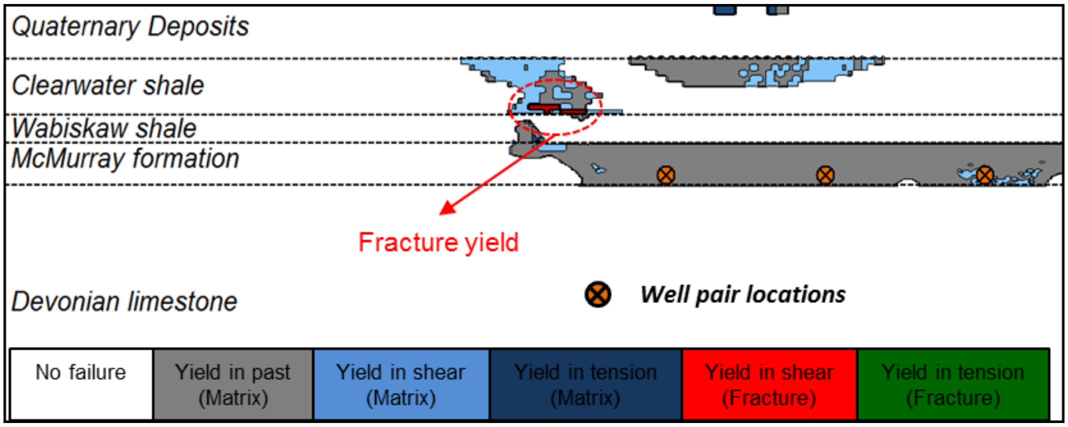

Figure 5.31 Yielded zones for fracture density=2.5 $frac./m$ and fracture dip angle=90°

Figure 5.32 presents the yielded zone for the case of fracture density of 3.5 frac./m and oblique fractures (ξ = 45°). Results show that the Clearwater shale was breached due to fracture yield mainly. Failure pressure in this case significantly dropped to 1,980 kPa. The figure shows the development of a pervasive flow path network due to the NFs yield in the full thickness of the Clearwater shale. The comparison of failure pressure for this case (fracture density of 3.5 frac./m and ξ = 45°) and the case with the fracture density of 2.5 frac./m and the same fracture dip angle indicates significant impact of fracture density on the failure pressure. Increasing the fracture density in this case from 2.5 to 3.5 frac./m decreased the failure pressure by 8%.

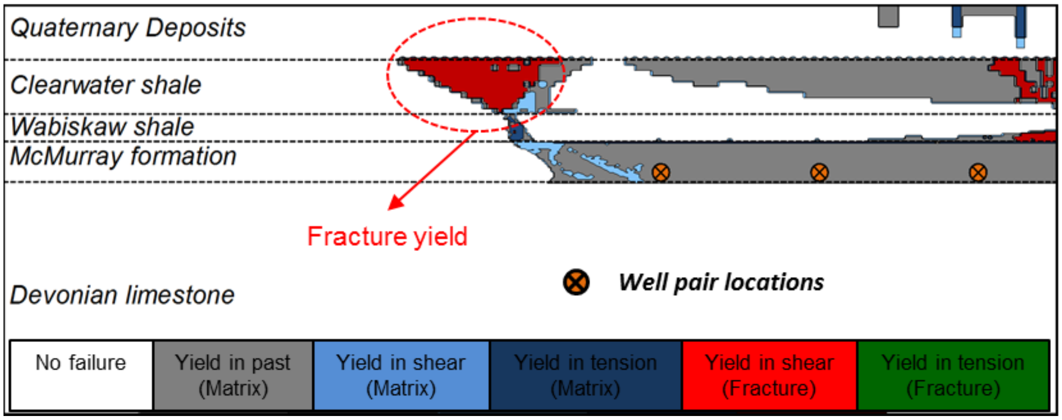

Figure 5.32 Yielded zones for fracture density=3.5 $frac./m$ and fracture dip angle=45°

Figure 5.33 illustrates the yielded zones for the case of vertical fractures, ($\xi = 90°$) and fracture density of 3.5 frac./m. This figure shows a yielded zone due to the NFs. Failure pressure for this case was found to be 2,310 kPa and it is close to the case with vertical fractures and fracture density of 2.5 frac./m (failure pressure = 2,351 kPa). The results show that the fracture density has minor effect on the failure pressure of vertical fractures for this case study. In this case, failure pressure was lower by only 1% due to 40% increase in fracture density. Also, the results indicate that vertical fractures have minor effects on caprock integrity for the ranges of fracture density considered here. Vertical fractures could have significant effects on caprock integrity if (1) the in-situ horizontal stress is the minimum principal stress (versus the study case in which vertical stress is the minimum principal stress, and (2) they possess high hydraulic conductivity that can lead to hydraulic fracturing.

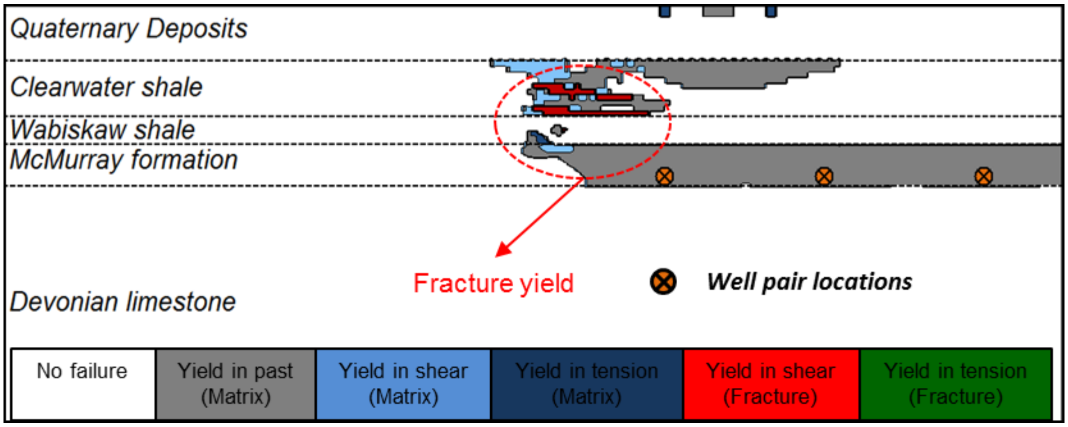

Figure 5.33 Yielded zones for fracture density=3.5 $frac./m$ and fracture dip angle=90°

5.5.1.2 Interaction between different fracture sets

The results shown before were only with the consideration of one set of fractures. To investigate the possible interaction of different fracture sets, a case was considered with three fracture sets with 25°, 45° and 65° dip angles. Fracture height and total density were kept at 20 cm and 2.5 frac./m for all fracture sets combined. Fracture density for fracture sets with dip angles of 25°, 45°, and 65° were assumed to be 0.5,1, and 1 frac./m. Therefore, the total fracture density in different dip angles is equal to 2.5 frac./m.

Results show that caprock breaches at 2,227 kPa, which is higher than the failure pressure for single fracture set with 45^{o} dip angle (2,145 kPa). The failure pressure in this case is 3.6% higher than the case with 45^{o} dip angle considering only one set of NFs with the same fracture density. This is because, for this case study, NFs with 45^{o} dip angle are more prone to failure than 25^{o} or 65^{o} NFs. Figure 5.34 shows the yielded zones for the case with three fracture sets. Yielded fractures are seen to have conical shape with more spread at shallower depths, due likely to smaller normal stresses on NF planes at shallower depth. The yielded zone in this case shows a network of yielded NFs and it could be a potential flow path for injected fluid and bitumen through the caprock.

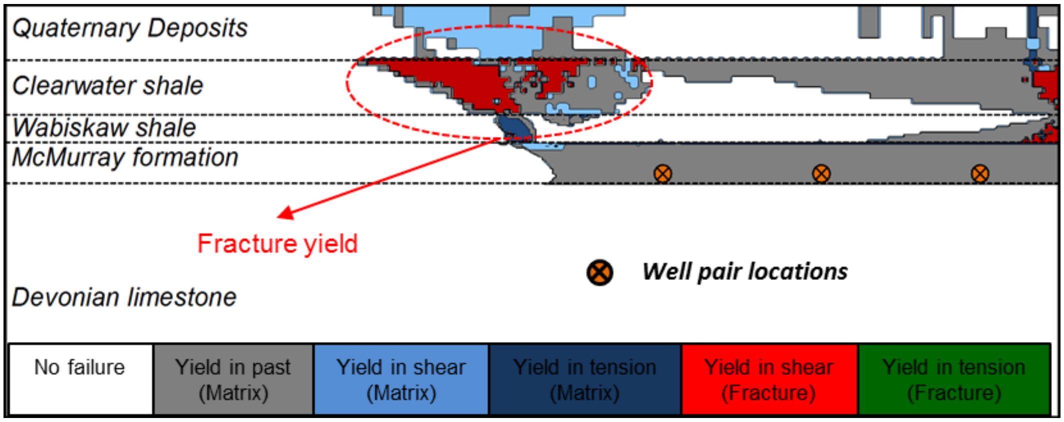

Figure 5.34 Yielded zones for three sets of the fractures with 25°, 45° and 65° dip angle of fracture density=2.5 $frac./m$ and fracture height=20 cm

5.5.1.3 Fracture height

Fracture height was assumed to be 20 cm for all previous cases. To investigate the effect of fracture height on failure pressure, a case was considered with three sets of fractures with dip angle of 25°, 45° and 65° and fracture height of 100 cm. As expected, caprock was more prone to failure in this case due to the longer fractures. The result was caprock failure in the third year of production with the existing operating pressure (injection pressure of 1,650 kPa). Figure 5.35 depicts the yielded zone for this case that shows shear yielded fractures across the Clearwater shale. Figure shows yielded NFs in the Clearwater shale above the steam champers and also at the flanks. By comparing the failure pressure of this case (1,650 kPa) with the case with fracture height of 20 cm (2,227 kPa), it can be concluded that the failure pressure is highly affected by the length of NFs. Failure pressure in this case dropped by 26% in comparison with the case with the fracture height of 20 cm. Results show the importance of accurate characterization of NFs in terms of the height and dip angle.

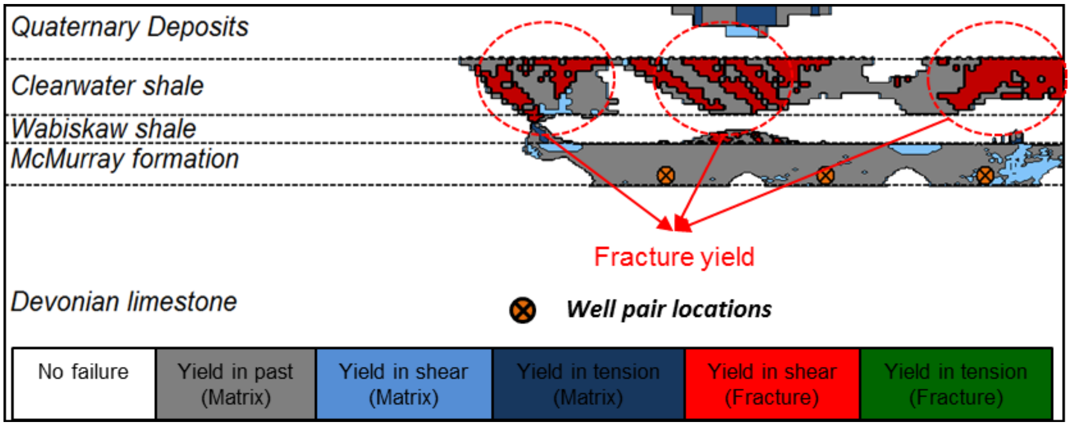

Figure 5.35 Yielded zones for three sets of the fractures with 25°, 45° and 65° dip angle of fracture density=2.5 $frac./m$ and fracture height=100 cm

5.5.2 Comparison with models with no NFs

To highlight the effect of including NFs in the constitutive model, calculated failure pressures are compared with those of isotropic and intrinsically anisotropic models.

Figure 5.36 shows the injection pressures for caprock breach for different cases. The figure indicates the lowest failure pressure among the cases with 20 cm fracture height belongs to the case with the dip angle of 45° and fracture density of 3.5 frac./m. The highest failure pressure can be observed for the model with the assumption of isotropic material for the caprock. This figure indicates conventional isotropic models can overestimate the failure pressure. The predicted failure pressure for the case of 100 cm fracture was low as results indicated caprock failure in the 3rd year of production with the operating pressure that was exercised in the field.

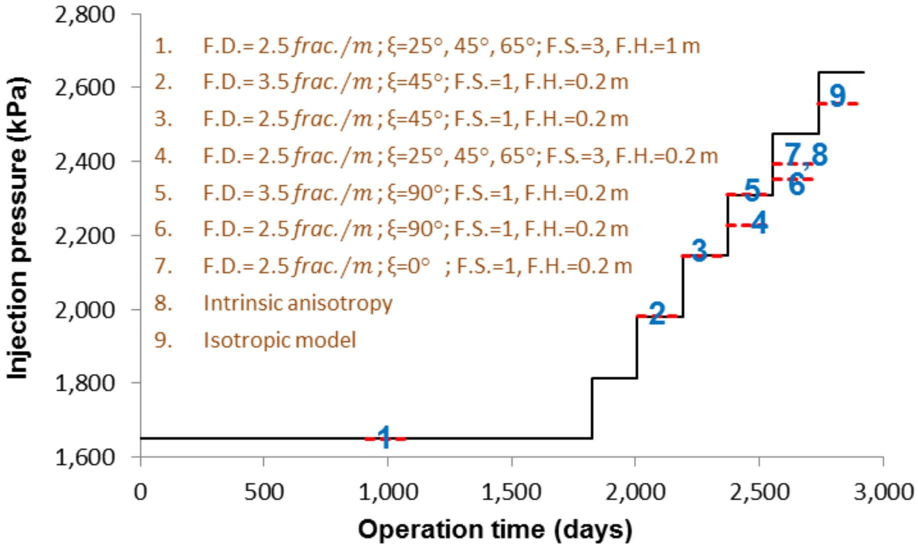

Figure 5.36 Injection pressures at caprock failure for Injector wells (F.D., F.S. and F.H. stand for fracture density, number of fracture sets and fracture height, respectively)

Table 5.2 presents the failure pressures for different sensitivity cases in terms of injector well pressure. Failure pressures in Table 5.2 are affected by the assumptions in the numerical model and uncertainties for the input data. One should consider a safety factor to convert the failure pressures to the MOP. The MOPs in Table 5.2 were calculated by applying the safety factor of 1.25 to the failure pressure. The safety factor of 1.25 is considered by the Alberta Energy Regulator (AER) for calculating MOP for shallow thermal in-situ oil sands applications (AER Bulletin, 2014).

By comparing different cases in Table 5.2 and considering the case with isotropic caprock as the base case, it can be seen that:

- Neglecting intrinsic anisotropy overestimated the MOP by 6.8%;
- For the sensitivity cases attempted, neglecting structural anisotropy (i.e., NFs) overestimated the MOP by up to 30.9% compared with the intrinsically anisotropic model.

- Oblique NFs had a major effect while horizontal NFs showed little effect on the MOP. Vertical fractures showed minor effect on the MOP (1.7%-3.4% compared with the case with intrinsically anisotropic assumption without NFs).
- Including multiple sets of NFs (instead of assuming NFs in one dip angle) has significant effect on the MOP of injector wells. For the specific case study of this research and the same fracture density, the MOP increased by 3.6% when considering three sets of NFs in comparison with the case with one set of NFs and fracture density of 2.5 frac./m.
- Fracture height has significant effect on the MOP of injector wells. The results show that with the increase of the fracture height from 20 cm to 100 cm, the MOP dropped by 35%. Therefore, accurate characterization of NFs is essential for caprock integrity studies.
- Fracture density affects the MOP in SAGD operations. The MOP decreased by the increase of fracture density. In this study, the MOP decreased by 8% with 40% increase of fracture density for the case of oblique NFs with 45° dip angle.

Table 5.2 Injection pressures at failure for injector wells

Category		Fracture density $(frac./m)$	Fracture height	Fracture sets	Fracture dip angle	[2]MOP	Failure pressure (*kPa*)	Difference with the base model[3]
	Fracture height	2.5	100	3	ξ=25°,45° and 65°	1,320	[1]1,650	31%
Fracture interaction		2.5	20	3	ξ=25°,45° and 65°	1,781	2,227	6.9%
	Fracture density and dip angle	2.5	20	1	ξ=45°	1,716	2,145	10.3%
		2.5	20	1	ξ=0°	1,913	2,392	0%
		2.5	20	1	ξ=90°	1,880	2,351	1.7%
		3.5	20	1	ξ=45°	1,584	1,980	17.2%
		3.5	20	1	ξ=90°	1,848	2,310	3.4%
	Non-fractured cases	Isotropic model	20	0	-	2,045	2,557	6.8%
		[3]Intrinsic Anisotropy	20	0	-	1,913	2,392	0%

[1] Model failed after three years of operation with the current operating injection pressure.

[2] MOP was calculated considering 1.25 safety factor.

[3] Intrisically anisotropic model is the base case model and other cases are compared with it.

5.6 Conclusions

Numerical direct shear tests were performed on samples with different fracture densities to find the equivalent strength parameters for ubiquitous fracture sets. Results showed that with the increase of fracture density, equivalent friction angle and cohesion for the sample dropped.

A series of coupled numerical models was performed to evaluate the failure pressure for a case study considering intrinsic and structural anisotropy (NFs) of shale formations. Failure pressure was defined as the pressure that results the expansion of yielded zone from reservoir-caprock interface up to the caprock-quaternary deposits interface. A sensitivity analysis was performed for different fracture densities, heights, dip angles and number of fracture sets. The maximum operating pressure was calculated by dividing the failure pressure by the safety factor of 1.25.

Results for the case study showed that the intrinsically anisotropic model (with no NFs) overestimated the MOP by 1.7% to 31% depending on fracture density and dip angle. Results showed that the inclined fractures with the dip angle of 45° had significant effect on the MOP, where the MOP dropped by 17.2% and 10.3% for fracture density of 3.5 and 2.5 frac./m, respectively, compared to those estimated using the intrinsically anisotropic model. Vertical fractures did not show significant effect on the MOP due to the specific in-situ stress pattern and negligible hydraulic conductivity of NFs in the case study.

In this study, the hydraulic contribution of the NFs was neglected as published reports indicated little hydraulic conductivity for the NFs. Natural fractures could act as significant channels for fluid flow when triggered by applied stresses. The model could be improved by including the hydraulic contribution of triggered NFs.

Chapter 6: Conclusions and recommendations for further studies

6.1 Summary and conclusions

This thesis has described the numerical assessment of the MOP for SAGD projects considering the effect of intrinsic and structural anisotropy of cap shales. The research methodology consists of the construction, verification and validation of a coupled hydro-thermo-mechanical model, implementation of a constitutive law capable of capturing shale intrinsic and structural anisotropy in the coupled model along with its verification, and an investigation of the effect of intrinsic and structural anisotropy on the MOP in SAGD reservoirs. This chapter summarizes the key findings in this research based on a case study for a SAGD reservoir.

Two cases were considered with isotropic and anisotropic cap shales to study the effect of shale intrinsic anisotropy on the MOP. The effect of NFs was neglected in this stage. Surface heave displacements were used to validate the model. Results show neglecting shale intrinsic anisotropy leads to a higher MOP prediction (7% higher MOP for the case study).

The effect of existence of NFs (structural anisotropy) on the MOP was studied by performing a sensitivity analysis for different fracture densities, heights, dip angles and number of fracture sets for the same case study.

Numerical direct shear tests were performed on samples with different fracture densities to find the equivalent strength parameters for ubiquitous NF sets. Results showed that with the increase of fracture density, equivalent strength properties for the sample dropped.

Results of the coupled tool indicate neglecting NFs can result in significant overestimation of the MOP. Results for the case study showed that the intrinsically anisotropic model (with no NFs) overestimated the MOP by 1.7 % to 31% depending on fracture density and dip angle. The MOP was found to be highly sensitive to the fracture density, direction, and height. For the case study, results displayed horizontal fractures had minor effect on the MOP while fractures with the dip angle between 25° to 65° significantly dropped the MOP and could not be neglected. Also, vertical fractures did not show significant effect on the MOP due to the specific in-situ stress pattern and negligible hydraulic conductivity of the NFs in the case study.

The results in this thesis have shown that the intrinsic and structural anisotropic behavior of the caprock shales cannot be ignored. Common isotropic models provide an optimistic assessment of the MOP as they overestimate the MOP. Overestimation of MOP may result in loss of caprock integrity and irrecoverable consequences for the reservoir and the environment.

6.2 Recommendations for future work

The following research works are recommended for further research in caprock integrity assessment for SAGD reservoirs:

- Injected heat into the reservoir can diffuse in the caprock strata and affect the shale strength properties. Use of constitutive models that can capture the effect of temperature on the strength properties and characterization of temperature dependent strength properties will improve the accuracy of the model predictions.

- Diffusion of water in the cap shale increases the water content in the shale zones adjacent the reservoir. Increased water content is known to reduce shale's strength, thus, is expected to adversely impact the caprock integrity.
- Natural fractures may act as channels for fluid flow when triggered by stresses. The model can be improved by including the hydraulic contribution of triggered NFs.
- This research did not capture the potential effects of hydraulic and thermal anisotropies. It is evident that shale permeability along the bedding and NFs is significantly higher than the same in the perpendicular direction.

A challenge in this project was the long computational time for the numerical model. A sequential coupling scheme was used to link the fluid flow and geomechanics simulators. The numerical stability and convergence rate are the key issues for the success of the sequential scheme. Several attempts to find stable and efficient sequential scheme methods for coupled poromechanics have been pursued in the geotechnical and computational mechanics communities (Kim et al., 2009). Four solution strategies for sequential schemes have been proposed: drained, undrained, fixed- strain, and fixed-stress solutions (Kim et al., 2009). All schemes can be applied to linear and nonlinear problems such as elastoplasticity (Kim et al., 2009). The stability and convergence rate of each of the sequentially coupled models for coupled fluid flow and reservoir geomechanics problems are different. Investigating the convergence rate of each solution scheme was out of the scope of this study, but can have immediate and widespread applicability in the design of reservoir flow simulators that account for geomechanics.

Bibliography

AER, 2014. *Geological Characterization of the Lower Clearwater Shale in the Athabasca Oil Sands Area, Townships 87-99, Ranges 1-13, West of the Fourth Meridian.* Retrieved from http://www.ags.gov.ab.ca/publications/OFR/PDF/OFR_2014_04.PDF.

AER Bulletin, 2014. *Regulatory Approach for Shallow Thermal In Situ Oil Sands Applications in the Wabiskaw-McMurray Deposit of the Athabasca Oil Sands Area*. January, Retrieved from https://www.aer.ca/documents/bulletins/AER-Bulletin-2014-03.pdf.

Aherne, A.L., and Birrell, G.E. 2002. Observations Relating to Non-Condensable Gasses in a Vapor Chamber: Phase B of the Dover Project. In SPE International Thermal Operations and Heavy Oil Symposium and International Horizontal Well Technology Conference, Calgary, Canada. Society of Petroleum Engineers, 4-7 November, SPE-79023.

Alqahtani, A.A. 2013. Effect of Mineralogy and Petrophysical Characteristics on Acoustic and Mechanical Properties of Organic Rich Shale. Unconventional Resources Technology Conference (URTEC, Denver, Colorado. Society of Petroleum Engineers), 12-14 August, SPE-168899-MS. http://dx.doi.org/10.1190/URTEC2013-045.

Ansari, S., Haigh, R., Khosravi, N., et al. 2012. Caprock Integrity Case Study for Non-thermal Polymer Flooding Project Using 4D Reservoir Coupled Geomechanical Simulation. In SPE Heavy Oil Conference, Calgary, Alberta. Society of Petroleum Engineers, 12-14 June, SPE-157912-MS. http://dx.doi.org/10.2118/157912-MS.

AOS (Alberta Oilsands Inc.), 2010. *Application for Alberta Oilsands Inc. Clearwater West LP-SAGD Pilot Project.* Retrieved form http://www.aboilsands.ca/_pdfs/AOS-ERCB-Project-Update-Dec-13.pdf.

Azad, A., and Chalaturnyk, R.J. 2011. Numerical Study of SAGD: Geomechanical-Flow Coupling for Athabasca Oil Sands Reservoirs. In 45th US Rock Mechanics/Geomechanics Symposium, San Francisco, California, 26-29 June. ARMA-11-414.

Babcock, E.A. 1973. Regional Jointing in Southern Alberta. *Canadian Journal of Earth Sciences*, **10**(12): 1769-1781. http://dx.doi.org/10.1139/e73-173.

Babcock, E.A. 1975. Fracture Phenomena in the Waterways and McMurray Formations, Athabasca Oil Sands Region, Northeastern Alberta. *Bulletin of Canadian Petroleum Geology*, **23**(4): 810-826.

Bell, J.S. and Babcock, E.A. 1986. The Stress Regime of the Western Canadian Basin and Implications for Hydrocarbon Production. *Bulletin of Canadian Petroleum Geology*, **34**(1): 364-378.

Bieniawski, Z.T. 1976. Rock Mass Classification in Rock Engineering. In Exploration for Rock Engineering, Proc. of the Symp., (ed. Z.T. Bieniawski) 1, 97-106. Cape Town, Balkema.

Butler, R.M. 1997. *Thermal Recovery of Oil and Bitumen*. Calgary, GravDrain.

CMG, 2006. *STARS 2006.11*, User Manual.

Butler, R.M., McNab, G.S., and Lo, H.Y. 1981. Theoretical Studies on the Gravity Drainage of Heavy Oil during In-Situ Steam Heating. *Canadian Journal of Chemical Engineering*, **59**(4): 455-460. http://dx.doi.org/10.1002/cjce.5450590407.

Butler, R.M. and Stephens, D.J. 1981. The Gravity Drainage of Steam Heated Heavy Oil to Parallel Horizontal Wells. *Journal of Canadian Petroleum Technology*, **20**(02): 90-96, PETSOC-81-02-07. http://dx.doi.org/10.2118/81-02-07.

Caddell, R. M., Raghava, R. S., and Atkins, A.G. 1973. A Yield Criterion for Anisotropic and Pressure Dependent Solids such as Oriented Polymers. *Journal of Materials Science*, **8**(11): 1641-1646. http://dx.doi.org/10.1007/BF00754900.

Canadian Natural Resources Limited, 2014. *Primrose Flow to Surface Causation Report*. Retrieved from https://www.cnrl.com/upload/media_element/819/01/initial-causation-review-report.pdf.

CAPP, 2011. *The Facts on Oil Sands. Upstream Dialogue*. Retrieved from: http://www.capp.ca/Upstream Dialogue/Oilsands/Pages/default.aspx.

Cazacu, O., Shao, J.F., Henry, J.P., and Cristescu, N.D. 1996. Elastic/viscoplastic Constitutive Equation for Anisotropic Shale. In 2nd North American Rock Mechanics Symposium, Montreal, Quebec. American Rock Mechanics Association, 19-21 June, ARMA-96-1681.

Cengel, Y.A. 2007. *Heat and Mass Transfer: A Practical Approach, 3rd ed.* New York, McGraw-Hill.

Chalaturnyk, R.J. 1996. *Geomechanics of the Steam-Assisted Gravity Drainage Process in Heavy Oil Reservoirs*. PhD thesis, University of Alberta, Edmonton, Canada (April 1996).

Chalaturnyk, R.J. 2011. Observations on SAGD Caprock Integrity. In Recovery–2011 CSPG CSEG CWLS Convention.

Chan, D. 2014. *Foundation on Expansive Soils* [Class handout]. Civil and Environmental Department, University of Alberta, Edmonton, Alberta, Canada.

Chan, A.W., and Zoback, M.D. 2002. Deformation Analysis in Reservoir Space (DARS): A Simple Formalism for Prediction of Reservoir Deformation with Depletion. In SPE/ISRM Rock Mechanics Conference, Irving, Texas. Society of Petroleum Engineers, 20-23 October, SPE-78174-MS. http://dx.doi.org/10.2118/78174-MS.

Chen, H., and Teufel, L.W. 2001. Reservoir Stress Changes Induced by Production/Injection, In SPE Rocky Mountain Petroleum Technology Conference, Keystone, Colorado. Society of Petroleum Engineers, 21-23 May, SPE-71087-MS. http://dx.doi.org/10.2118/71087-MS.

Chenevert, M.E., and Gatlin C. 1965. Mechanical Anisotropies Laminated Sedimentary Rocks. *Society of Petroleum Engineering Journal*, **5**(1): 66-67. SPE-890-PA. http://dx.doi.org/10.2118/890-PA.

Chou, Q. 2011. Clearwater Formation Natural Fracture Characterization from Cores and Image Logs, Athabasca Oil Sands, Alberta. In Recovery–2011 CSPG CSEG CWLS Convention.

Clark, I.H. 2006. Simulation of Rock mass Strength Using Ubiquitous Joints. In: R. Hart & P. Varona (eds), Numerical Modeling in Geomechanics-2006; Proc. 4th International FLAC Symposium, Madrid, May 2. Paper No. 08-07.

Colak, K., and Unlu, T. 2004. Effect of Transverse Anisotropy on the Hoek–Brown Strength Parameter 'mi'for Intact Rocks. *International Journal of rock mechanics and mining sciences*, **41**(6): 1045-1052.

Collins, P.M. 2007. Geomechanical Effects on the SAGD Process. *SPE Reservoir Evaluation and Engineering.* **10**(4): 367-375. SPE-97905-PA. http://dx.doi.org/10.2118/97905-PA.

Dell'Amico, J.J., Captain F.K., and Chansky, S.H. 1967. *Characterization and Thermal Conductivities of Some Samples of Conasauga Shale*, ORNL-MIT-20, Oak- Ridge National Laboratory, Mar. 29.

Ding, W., Li, C., Li, C., Xu, C., et al. 2012. Fracture Development in Shale and Its Relationship to Gas Accumulation. *Geoscience Frontiers*, **3**(1): 97-105. http://dx.doi.org/10.1016/j.gsf.2011.10.001.

Donath, F.A. 1964. *Strength Variation and Deformational Behavior in Anisotropic Rock*. State of the Earth in the Earth's Crust. New York: Elsevier, 281-98.

Dusseault, M.B., and Rothenburg, L. 2002. Analysis of Deformation Measurements for Reservoir Management. *Oil & Gas Science and Technology*, **57**(5): 539-554.

Duveau, G., Tiantang, Y., and Shao, J.F. 2001. Modelling of Anisotropy in Elastoplastic Sedimentary Rocks. In DC Rocks 2001, the 38th US Symposium on

Rock Mechanics (USRMS), Washington, D.C. American Rock Mechanics Association, 7-10 July, ARMA-01-1517.

Edmunds, N. R., and Gittins, S. D. 1993. Effective Application of Steam Assisted Gravity Drainage of Bitumen to Long Horizontal Well Pairs. *Journal of Canadian Petroleum Technology*, **32**(6): 49-55, PETSOC-93-06-05. http://dx.doi.org/10.2118/93-06-05.

eFunda, 2014. *Orthotropic Definition*. Retrieved from: http://www.efunda.com/formulae/solid_mechanics/mat_mechanics/hooke_orthotropic.cfm.

ERCB, 2010. *ERCB Staff Review and Analysis: Total E&P Canada Ltd., Surface Steam Release of May 18, 2006, Joslyn Creek SAGD Thermal Operation*. Retrieved from https://www.aer.ca/documents/reports/ERCB_StaffReport_JoslynSteamRelease_2010-02.pdf.

ERCB, 2011. *Oil Sands Fact sheets "talk about oil sands"*, Retrieved from: www.oilsands.alberta.ca.

ERCB. 2013. *Canadian Natural Resources Ltd. Primrose East Bitumen Emulsion Release January 3, 2009. ERCB Investigation Report*. Retrieved from: https://www.aer.ca/documents/reports/IR_20130108_CNRLPrimrose.pdf.

Erteckin, T., and Abou-Kassem, J.H., et al. 2001. *Basic Applied Reservoir Simulation*. Tx, Richardson.

Eshelby, J.D. 1957. The Determination of the Elastic Field of an Ellipsoidal Inclusion, and Related Problems. *Proceedings of the Royal Society of London. Series A. Mathematical and Physical Sciences*, **241**(1226): 376-396.

Eshelby, J.D. 1959. The Elastic Field outside an Ellipsoidal Inclusion. *Proceedings of the Royal Society of London. Series A, Mathematical and Physical Sciences*, **A252**(1271): 561-569.

Fjaer, E., Holt, R. M., Raaen, A. M., Risnes, R., et al. 2008. *Petroleum Related Rock Mechanics*, Elsevier, Amsterdam.

Gautam, R., and Wong, R. C. 2006. Transversely Isotropic Stiffness Parameters and Their Measurement in Colorado Shale. *Canadian geotechnical journal*, **43**(12): 1290-1305. http://dx.doi.org/10.1139/t06-083.

Geertsma, J. 1966. Problems of Rock Mechanics in Petroleum Production Engineering. In 1st ISRM Congress, Lisbon, Portugal. International Society for Rock Mechanics, 25 September-1 October, ISRM-1CONGRESS-1966-099.

Goodman, R.E., and Smith, H.R. 1980. RQD and Fracture Spacing. *Journal of the Geotechnical Engineering Division*, ASCE, **106**(2): 191-193.

Gregor, V.A. 1997. Mannville Linears in the Lloydminster Heavy Oil Area and Their Relationship to Fractures and Fluid Flow in the Western Canada Sedimentary Basin. *Canadian society of Petroleum Geologists*, 428-474.

Gutierrez, M., Lewis, R.W., and Masters, I. 2001. Petroleum Reservoir Simulation Coupling Fluid Flow and Geomechanics. *SPE Reservoir Evaluation & Engineering*, **4**(3): 164-172, SPE-72095-PA. http://dx.doi.org/10.2118/72095-PA.

Hemsing, D.B. 2007. *Laboratory Determination of Seismic Anisotropy in Sedimentary Rock from the Western Canadian Sedimentary Basin*. MS thesis, University of Alberta, Edmonton, Canada (Fall 2007).

Hill, R. 1948. A Theory of the Yielding and Plastic Flow of Anisotropic Metals. Proceedings of the Royal Society of London. *Series A. Mathematical and Physical Sciences*, **193**(1033): 281-297.

Hill, R. 1963. Elastic Properties of Reinforced Solids: Some Theoretical Principles. *Journal of the Mechanics and Physics of Solids*, **11**(5): 357-372. http://dx.doi.org/10.1016/0022-5096(63)90036-x.

Hill, R. 1993. A User-Friendly Theory of Orthotropic Plasticity in Sheet Metals. *International Journal of Mechanical Sciences*, **35**(1): 19-25. http://dx.doi.org/10.1016/0020-7403(93)90061-X.

Hoek, E. 1964. Fracture of Anisotropic Rocks. *Journal of the South African Institute of Mining and Metallurgy*, **64**(10):510–518.

Hoek, E., and Brown, E.T. 1997. Practical Estimates of Rock Mass Strength. *International Journal of Rock Mechanics and Mining Sciences*, **34**(8): 1165-1186.

Hoek, E. and Marinos, P. 2000. Predicting Tunnel Squeezing. *Tunnels and Tunnelling International*. Part 1 – November 2000, Part 2 – December 2000.

Hoek, E., Wood, D. and Shah S. 1992. A Modified Hoek-Brown Criterion for Jointed Rock Masses. Proc. Rock Characterization, Symp. Int. Soc. Rock Mech.: Eurock '92, (ed. J.A. Hudson), 209-214. London, Brit. Geotech. Soc.

Horino, F.G. and Ellickson, M.L. 1970. *A Method for Estimating Strength of Rock Containing Planes of Weakness*. Vol. 7449. US Dept. of Interior, Bureau of Mines.

Hosford, W.F. 1985. Comments on Anisotropic Yield criteria. *International Journal of Mechanical Sciences*, **27**(7-8): 423-427. http://dx.doi.org/10.1016/0020-7403(85)90032-3.

ICG. 2011. FLAC (Fast Lagrangian Analysis of Continua) User's Guide. 5th. Vol. 7. Minneapolis, Minnesota: Itasca Consulting Group Inc.

Imam, R. 1998. *Constitutive Modelling of Anisotropic Sands for the Analysis of Static Liquefaction*. Ph.D. thesis, University of Alberta, Canada (Spring).

Islam, M.A., and Skalle, P. 2013. An Experimental Investigation of Shale Mechanical Properties Through Drained and Undrained Test Mechanisms. *Journal of Rock Mechanics and Rock Engineering*. **46**: 1391-1413. http://dx.doi.org/10.1007/s00603-013-0377-8.

Jaeger, J.C. 1960. Shear Failure of Transversely Isotropic Rock. *Geology Magazine*, **97**: 65-72.

Jaeger, J.C., Cook, N.G., and Zimmerman, R. 2009. *Fundamentals of Rock Mechanics*. John Wiley & Sons.

Japan Petroleum Exploration Co. Ltd. (JAPEX), n.d., *Oil Sands Development Utilizing the SAGD Process*, Retrieved from https://www.japex.co.jp/english/business/oversea/sadg.html.

Jun, X., Nathan, D., Chalaturnyk, R.J., and Xiaolan H., 2012. Reservoir Geomechanical Analysis for Caprock Integrity Evaluation during Oilsand Development. *Disaster Advances*, **5**(4): 1713-1717.

Karakul, H., Ulusay, R. and Isik, N.S. 2010. Empirical Models and Numerical Analysis for Assessing Strength Anisotropy Based on Block Punch Index and Uniaxial Compression Tests. *International Journal of Rock Mechanics and Mining Sciences*, **47**(4): 657-665. http://doi:10.1016/j.ijrmms.2010.03.006.

Khan, S., Han, H., Ansari, S., and Khosravi, N. 2010. An Integrated Geomechanics Workflow for Caprock Integrity Analysis of a Potential Carbon Storage. In SPE International Conference on CO2 Capture, Storage, and Utilization, New Orleans, Louisiana. Society of Petroleum Engineers, 10-12 November, SPE-139477-MS. http://dx.doi.org/10.2118/139477-MS.

Khan, S., Han, H., Vishteh, M. et al. 2011. Caprock Integrity Analysis in Thermal Operations: An Integrated Geomechanics Approach. In WHOC-609 Proceedings for the 2011 World Heavy Oil Congress, Edmonton, Alberta. WHOC-11-609.

Khan, M., Teufel, L.W., Zheng, Z., and Baker, A. 2000. Determining the Effect of Geological and Geomechanical Parameters on Reservoir Stress path through Numerical Simulation. In SPE Annual Technical Conference and Exhibition, Dallas, Texas. Society of Petroleum Engineers, 1-4 October, SPE-63261-MS.

Kim, J., Tchelepi, H. A., and Juanes, R. 2009. Stability, Accuracy and Efficiency of Sequential Methods for Coupled Flow and Geomechanics. In SPE Reservoir Simulation Symposium, Woodlands, Texas. Society of Petroleum Engineers, 2-4 February, SPE-119084.

Kosar, K.M. 1989. *Geotechnical Properties of Oil Sands and Related Strata*. PhD thesis, University of Alberta, Edmonton, Canada (January 1989).

Kwasniewski, M.A. 1993. Mechanical Behavior of Transversely Isotropic Rocks. *Comprehensive Rock Engineering*, Vol. 1., pp. 285–312, New York: Oxford, Pergamon Press.

Laubach, S.E., Olson, J.E., Eichhubl, P., et al. 2010. Natural Fractures from the Perspective of Diagenesis. CSEG RECORDER, Focus Article, September.

Lekhnitskii, S.G. 1981. *Theory of Elasticity of an Anisotropic Body*, translated from the revised 1977 Russian edition, Mir, Moscow.

Li, P., and Chalaturnyk, R.J. 2005. Geomechanical Model of Oil Sands. In PS-CIM/CHOA International Thermal Operations and Heavy Oil Symposium, Calgary, Alberta, 1–3 November. SPE-97949-MS. http://dx.doi.org/10.2118/97949-MS.

Li, P. and Chalaturnyk, R.J. 2009. History Match of the UTF Phase a Project with Coupled Reservoir Geomechanical Simulation. *Journal of Canadian Petroleum Technology*, **48**(1): 29-35. http://dx.doi.org/10.2118/09-01-29.

Li, P., Chalaturnyk, R.J., and Tan, T.B. 2006. Coupled Reservoir Geomechanical Simulations for the SAGD Process. *Journal of Canadian Petroleum Technology*, **45**(1): 33-40, PETSOC-2003-083. http://dx.doi.org/10.2118/2003-083.

Lo, T.W., Coyner, K.B., and Toksöz, M.N. 1986. Experimental Determination of Elastic Anisotropy of Berea Sandstone, Chicopee Shale, and Chelmsford Granite. *Geophysics*, **51**(1): 164-171. http://dx.doi.org/10.1190/1.1442029.

Love, A.E.H. 1944. *A Treatise on the Mathematical theory of elasticity*. Dover Publications, New York.

Malvern, L.E. 1969. *Introduction to Mechanics of a Continuous Medium*. Englewood Cliffs, New Jersey: Prentice Hall.

MATLAB software. 2014, Version R2014a, The MathWorks Inc., MA, USA.

Marinos. P, and Hoek, E. 2001. Estimating the Geotechnical Properties of Heterogeneous Rock Masses such as Flysch. Accepted for publication in the Bulletin of the International Association of Engineering Geologists.

McLamore, R., and Gray, K.E. 1967. The Mechanical Behavior of Transversely Isotropic Sedimentary Rocks. *Journal of Engineering for Industry*, **89**(1): 62–73.

McLellan, P., and Gillen, K. 2000. Assessing Caprock Integrity for Steam-Assisted Gravity-Drainage Projects in Heavy-Oil Reservoirs. GEM Presentation, prepared for presentation at the (2000).

Melaku, M.T. 2007. *Velocity Anisotropy of Shales and Sandstones from Core Sample and Well Log on the Norwegian Continental Shelf*. Master's thesis, University of Oslo, Norway (fall).

Michiel H. 2001, *Spline interpolation*, Encyclopedia of Mathematics, Springer, ISBN 978-1-55608-010-4.

Mindlin, R.D., and Cheng, D.H. 1950. Nuclei of Strain in the Semi-Infinite Solid. *Journal of Applied Physics*, **21**(9): 926-930.

Mohamadi, M., Gong, X., and Wan, R.G. 2013. Laboratory and Constitutive Modeling of Colorado Shale at High Pressure and Temperature. In 47th US Rock Mechanics/Geomechanics Symposium, San Francisco, California, American Rock Mechanics Association, 23-26 June, ARMA-2013-651.

Morita, N., Whitfill, D.L., Nygaard, O., and Bale, A. 1989. A Quick Method to Determine Subsidence, Reservoir Compaction, and In-Situ Stress Induced by Reservoir Depletion. *Journal of Petroleum Technology*, **41**(1): 71-79, SPE-17150-PA. http://dx.doi.org/10.2118/17150-PA.

Mura, T. 1982. *Micromechanics of Defects in Solids*. Martinus Nijhoff Publishers, The Hague, Netherlands.

Nasseri, M.H., Rao, K.S., and Ramamurthy, T. 1997. Failure Mechanism in Schistose Rocks. *International Journal of Rock Mechanics and Mining Sciences*, **34**(3): 219-e1.

Niandou, H. 1994. *Etude du Comportement rheologiques et Modelisation de l'argilite de Tournemire*. Application a la stabilite des ouvrages souterrains, These de Doctorat, USTL Lille, France.

Niandou, H., Shao, J. F., Henry, J. P., and Fourmaintraux, D. 1997. Laboratory Investigation of the Mechanical Behaviour of Tournemire Shale. *International*

Journal of Rock Mechanics and Mining Sciences, **34**(1): 3-16. http://dx.doi.org/10.1016/S1365-1609(97)80029-9.

Nikiforuk, A. 2013. Next Oil Sands Threat: Cracking Caprock. Retrieved August 7, 2015, from http://www.resilience.org/stories/2013-10-23/next-oil-sands-threat-cracking-caprock.

Nikiforuk, A. 2014. Salt Formations New-found Threat to Oilsand Projects. Retrieved August 7, 2015, from https://nbharbinger.wordpress.com/2014/07/28/salt-formations-new-found-threat-to-oilsand-projects/.

Niven, R.B., and Duestch, C.V. 2010. On the Randomness of Natural Fractures. CCG Annual Report 12, 207.

Nottenburg R. et al., 1978. Measurement of Thermal Conductivity of Green River Oil Sha1es by a Thermal Comparator Technique, *Fuel*, **57**.

Nouri, A., Kuru, E., and Vaziri, H. 2009. Elastoplastic Modelling of Sand Production Using Fracture Energy Regularization Method. *Journal of Canadian Petroleum Technology*, **48**(04): 64-71.

Ochs D.E., Chen, H., and Teufel, L.W. 1997. Relating In-Situ Stresses and Transient Pressure Testing for a Fractured Well. In SPE Annual Technical Conference and Exhibition, San Antonio, Texas, Society of Petroleum Engineers, 5-8 October, SPE-38674-MS. http://dx.doi.org/10.2118/38674-MS.

Oda, M. 1993. *Comprehensive Rock Engineering*. Vol. 1, Pergamon Press, New York, USA, pp. 185-200.

Oldakowski, K. 1994. *Stress Induced Permeability Changes of Athabasca Oil Sands*. MS thesis, University of Alberta, Edmonton, Canada (April 1994).

Petro-Canada Corp., 2005a. *Amendment Application for MacKay River Expansion: Project Description*. Retrieved from http://citeseerx.ist.psu.edu/viewdoc/download?doi=10.1.1.116.729&rep=rep1&type=pdf.

Petro-Canada Corp., 2005b. *MacKay River Oilsands Progress Report*, Retrieved from http://www.aer.ca/data-and-publications/activity-and-data/in-situ-performance-presentations.

Pettijohn, F. J. 1957, *Sedimentary rocks*, New York: Harper and Row, Third edition.

Potter, P.E., Maynard, J.B. and Depetris, P.J. 2005. *Mud and Mudstones*. Vol. 1, Springer, N.Y., U.S., 297.

Puzrin, A.M. 2012. *Constitutive Modelling in Geomechanics*. Zurich, Switzerland: Springer. http://DOI 10.1007/978-3-642-27395-7.

Rahmati, E., Nouri, A., and Fattahpour, V, Trivedi, J. 2015. Numerical Assessment of the Maximum Operating Pressure for Anisotropic Caprock in SAGD Projects. In SPE Heavy Oil Conference, Calgary, Alberta, 9-11 June. SPE-174509-MS.

Rahmati, E., Nouri, A., and Fattahpour, V. 2014. Caprock Integrity Analysis during a SAGD Operation Using an Anisotropic Elasto-Plastic Model. In SPE Heavy Oil Conference, Calgary, Alberta, 10-12 June. SPE-170114-MS. http://dx.doi.org/10.2118/170114-MS.

Rahmati, E., Nouri, A., and Rahmati, H. 2013. Numerical Assessment of Caprock Integrity in SAGD Operations. In SPE Heavy Oil Conference, Calgary, Alberta, 11-13 June. SPE-165422-MS. http://dx.doi.org/10.2118/165422-MS.

Ramamurthy, T. 1993. Strength and Modulus Responses of Transversely Isotropic Rocks, *Comprehensive Rock Engineering*, Vol. 1, pp. 313-329 U.K.: Pergamon Press.

Robertson, E.C. 1979. *Thermal Conductivity of Rocks*. USGS Open File Report 79-356, U.S. Geological Survey.

Saeidi, O., Rasouli, V., Vaneghi, R.G., et al. 2014. A Modified Failure Criterion for Transversely Isotropic Rocks. *Geoscience Frontiers*, **5**(2): 215-225.

Samier, P., Onaisi, A., and Fontaine, G. 2006. Comparisons of Uncoupled and Various Coupling Techniques for Practical Field Examples. *SPE Journal*, **11**(01): 89-102, SPE-79698-PA. http://dx.doi.org/10.2118/79698-PA.

Saroglou, H., and Tsiambaos, G. 2008. A Modified Hoek–Brown Failure Criterion for Anisotropic Intact Rock. *International Journal of Rock Mechanics and Mining Sciences*, **45**(2): 223-234. http://dx.doi.org/10.1016/j.ijrmms.2007.05.004.

Segall, P. 1985. Stress and Subsidence Resulting from Subsurface Fluid Withdrawal in the Epicentral Region of 1983 Coalinga Earthquake. *Journal of Geophysical Research*, **90**(B8): 6801-6816. http://dx.doi.org/10.1029/JB090iB08p06801.

Segall, P. 1992. Induced Stresses due to Fluid Extraction from Axisymmetric Reservoirs. *Pure and Applied Geophysics*, **139**(3-4): 535–560.

Segall, P., and Fitzgerald, S.D. 1998. A Note on Induced Stress Change in Hydrocarbon and Geothermal Reservoirs. *Tectonophysics*, **289**(1-3): 117-128.

Settari, A. 2005. Geomechanics and Subsidence. In 8th International Forum on Reservoir Simulation, Borromees, Italy, June.

Settari, A., and Walters, D.A. 2001. Advances in Coupled Geomechanical and Reservoir Modeling with Applications to Reservoir Compaction. *SPE Journal*, **6**(03): 334-342, SPE-74142-PA. http://dx.doi.org/10.2118/74142-PA.

Singhal, B.B.S., and Gupta, R.P. 2010. *Applied Hydrogeology of Fractured Rocks*. Springer Science & Business Media, Springer Dordrecht Heidelberg London New York.

Sladek, T.A. 1971. *A Determination of the Composition and Temperature Dependencies of Thermal Conductivity Factors for Green River Oil Shale*. Ph.D. thesis, Colorado School of Mines, USA (Fall).

Smith, R.J. 1997. *Geomechanical Effects of Cyclic Steam Stimulation on Casing Integrity*. MS thesis, University of Calgary, Calgary, Canada (Fall 1997).

Sone, H. 2012. *Mechanical Properties of Shale Gas Reservoir Rocks and Its Relation to the In-situ Stress Variation Observed in Shale Gas Reservoirs*. PhD thesis, Stanford University, California, US (March 2012).

Soreide, O. K., Bostrom, B., and Horsrud, P. 2009. Borehole Stability Simulations of an HPHT Field Using Anisotropic Shale Modeling. In 43rd US Rock Mechanics Symposium & 4th US-Canada Rock Mechanics Symposium, Asheville, North Carolina, American Rock Mechanics Association, 28 June-1 July, ARMA-09-185.

Southern Pacific Resource Corp. 2011. *STP McKay Thermal Project, Part B-Project Description*. November, Retrieved from http://www.shpacific.com/SAGD2-2012/November2011/Volume1/02PartB-Project%20Description.pdf.

Southern Pacific Resource Corp. 2012. *Annual Performance Presentation McKay River Thermal Project*. Retrieved from http://www.aer.ca/documents/oilsands/in situ-presentations/2012AthabascaSouthernPacificMckaySAGD11461.pdf.

Stauffer, M.R., Gendzwill, D.J., and Sauer, E.K. 1990. Ice-Thrust Features and the Maymont Landslide in the North Saskatchewan River Valley. *Canadian Journal of Earth Sciences*, **27**(2): 229-242. http://dx.doi.org/10.1139/e90-023.

Suncor Energy Inc. 2009. *MacKay River Performance Presentation*. Retrieved from http://www.aer.ca/documents/oilsands/in situ-presentations/2009AthabascaSuncorMacKayRiver8668.pdf.

Suncor Energy Inc., 2013. *2013 AER Performance Presentation: Surface Commercial Scheme Approval No. 8668*. Retrieved from http://www.aer.ca/documents/oilsands/insitu-presentations/2013SuncoreMacKayRiver8668.pdf.

Thomas, S., and Sands, I.S.O. 2010. *Re: Project Update for Alberta Oilsands Inc. Clearwater West LP-SAGD Pilot Project*. Retrieved from http://www.aboilsands.ca/_pdfs/AOS-ERCB-Project-Update-Dec-13.pdf.

Touhidi-Baghini A. 1998. *Absolute Permeability of McMurray Formation Oil Sands at Low Confining Stresses*. PhD thesis. University of Alberta, Edmonton, Canada (October 1998).

Townend, J., and Zoback, M.D. 2000. How Faulting Keeps the Crust Strong. *Geology*, **28**(5): 399-402.

Tran, D., Nghiem, L., and Buchanan, L. 2005. Improved Iterative Coupling of Geomechanics with Reservoir simulation. In SPE Reservoir Simulation Symposium Houston, Texas. Society of Petroleum Engineers, 31 January-2 Feburary, SPE-93244-MS. http://dx.doi.org/10.2118/93244-MS.

Tsui, P.C., Cruden, D.M., and Thomson, S. 1988. Mesofabric, Microfabric, and Submicrofabric of Ice-Thrust Bedrock, Highvale Mine, Wabamun Lake Area, Alberta. *Canadian Journal of Earth Sciences*, **25**(9): 1420-1431. http://dx.doi.org/10.1139/e88-136.

Tutuncu, A.N. 2010. Anisotropy Compaction and Dispersion Characteristics of Reservoir and Seal Shales. In 44th US Rock Mechanics Symposium and 5th US-Canada Rock Mechanics Symposium, Salt Lake City, Utah. American Rock Mechanics Association, 27-30 June, ARMA-10-344.

Uwiera-Gartner, M., Carlson, M.R., Walters, D.A. et al. 2011. Geomechanical Simulation of Caprock Performance for a Proposed Low Pressure Steam-Assisted Gravity Drainage Pilot Project. In Canadian Unconventional Resources Conference, Calgary, Alberta, 15-17 November. SPE-148886-MS. http://dx.doi.org/10.2118/148886-MS.

Walsh, J.B., and Brace, W.F. 1964. A Fracture Criterion for Brittle Anisotropic Rock. *Journal of Geophysical Research*, **69**(16): 3449-3456. http://dx.doi.org/10.1029/JZ069i016p03449.

Walters, D.A., Wang, J. and Settari, A. 2012. A Geomechanical Methodology for Determining Maximum Operating Pressure in SAGD Reservoirs. In SPE Heavy Oil Conference Calgary, Alberta. Society of Petroleum Engineers, 12-14 June, SPE-157855-MS. http://dx.doi.org/10.2118/157855-MS.

Wenlong, D., Bowen, Z., and Taiming, L. 2003. Formation of Non-Tectonic Fractures in Mudstones in Gulong Depression. *Oil and Gas Geology*, **24**(1): 50-54.

Wyllie, D. C., and Mah, C. 2004. *Rock Slope Engineering*. CRC Press, 4th edition.

Wittke, W. 1990. *Rock Mechanics: Theory and Applications with Case Histories*. Springer-Verlag, Berlin.

Wong, R.C.K. 1996. A Model for Highly Anisotropic Swelling Shales. In 2nd North American Rock Mechanics Symposium, Montreal, Quebec. American Rock Mechanics Association, 19-21 June, ARMA-96-1295.

Wong, R.C.K. 1998. Swelling and Softening Behaviour of La Biche Shale. *Canadian Geotechnical Journal*, **35**(2): 206-221. http://dx.doi.org/10.1139/t97-087.

Wong, R.C.K, and Lau, J. 2008. Surface Heave Induced by Steam Stimulation in Oil Sand Reservoirs. *Journal of Canadian Petroleum Engineering*, **47**(1): 13-17, PETSOC-08-01-13-TN. http://dx.doi.org/10.2118/08-01-13-TN.

Xiong, J., Chalaturnyk, R.J., and Deisman, N., 2012. Reservoir Geomechanical Analysis for Caprock Integrity Evaluation during Oilsand Development. *Disaster Advances*, **5**(4): 1713-1717.

Xu, L., Ren, Q., Chen, Z. and Wu, J. 2010. An Anisotropic Elastoplastic Constitutive Model for Layered Rock Masses and Its Implementation in ABAQUS. *Earth and Space 2010 Engineering, Science, Construction, and Operations in Challenging Environments, ASCE*, pp.: 305-318. http://dx.doi.org/10.1061/41096(366)32.

Xu, B., Yang, B., and Yuan, Y. 2013. Caprock Integrity Analysis, Cenovus's Christina Lake SAGD Project. BitCan Geosciences & Engineering Inc., February. Retrieved from http://www.cenovus.com/operations/docs/christinalake/phase-h/1c/appendices-iv-1-caprock.pdf.

Zeuch, D. H. 1983. The Mechanical Behavior of Anvil Points Oil shale at Elevated temperatures and Confining Pressures. *Canadian Geotechnical Journal*, **20**(2): 344-352. http://dx.doi.org/10.1139/t83-037.

Zhang, Z., Wang, J., and Yale, D. P. 2012. Overburden Stability under Varying Pressure Loading. In American Rock Mechanic Association, Chicago, Illinois. ARMA, 24-27 June, ARMA-2012-669.

Appendix A: Formulation of the AU constitutive model

This appendix presents the incremental formulation of the AU constitutive model. AU constitutive model in this project is used in conjunction with FLAC software to capture the intrinsic and structural anisotropic behavior of shale formations. Explicit solution scheme is used for the constitutive model. The advantage of this scheme is the ability in following the evolution of a geologic system in a realistic manner without concerns about numerical instability problems.

The AU constitutive model incorporates an incremental numerical algorithm. In this algorithm, the stress state for the current time (t) is given. Also, the total strain increment for the current time step (Δt) is given. The purpose is to determine the stress increment for the time Δt and, therefore, new stress state at time $t + \Delta t$. In the case of plastic deformations, only the elastic part of strain increment $(\Delta e_{ij}^{e\,\Delta t})$ contributes to the stress increment $(\Delta \acute{\sigma}_{\iota\jmath}{}^{\Delta t})$. In this case, a correction must be made to the elastic stress increment as calculated from the total strain increment, in order to obtain the actual stress at the end of the time step $(\Delta \acute{\sigma}_{\iota\jmath}{}^{\mathrm{t}+\Delta t})$.

The description of AU constitutive model is presented next. The yield criterion is defined as:

$$f(\acute{\sigma}_{\iota}) = 0 \tag{A.1}$$

where f is the yield function and $\acute{\sigma}_{\mathrm{I}}$ is the compontent of effective stresses.

The relation expressing the decomposition of strain increments into the sum of elastic and plastic parts is as follow:

$$\Delta e_{ij}^{total} = \Delta e_{ij}^{e} + \Delta e_{ij}^{p} \tag{A.2}$$

where Δe_{ij} is the strain increment and superscripts 'e' and 'p' denote the elastic and plastic parts, respectively.

The elastic relation between elastic strain increment and stress increment is as follows:

$$\Delta \acute{\sigma}_{ij} = \sum_{k,l} K_{ijkl} \Delta e_{kl} \tag{A.3}$$

where $\Delta \acute{\sigma}_{ij}$ is the incremental effective stress component, K_{ijkl} are elastic constants, and Δe_{kl} is the incremental strain compontent.

The flow rule specifiying the direction of the plastic strain increment vector as that normal to the potential surface is defined as:

$$\Delta e_{i}^{p} = \lambda \frac{\partial g}{\partial \acute{\sigma}_{i}} \tag{A.4}$$

where g is the potential function and λ is a constant.

One requirement for the new stress state ($\acute{\sigma}_{ij}{}^{t+\Delta t}$) is that it should satisfy the yield function.

$$\acute{\sigma}_{ij}{}^{t+\Delta t} = \acute{\sigma}_{ij}{}^{t} + \Delta \acute{\sigma}_{ij}{}^{\Delta t} \tag{A.5}$$

$$f\left(\acute{\sigma}_{ij}{}^{t+\Delta t}\right) = 0 \Longrightarrow f\left(\acute{\sigma}_{ij}{}^{t} + \Delta \acute{\sigma}_{ij}{}^{\Delta t}\right) = 0 \tag{A.6}$$

Substitution of the expression for the elastic starin increment derived from (A.2) into to the elastic relation (A.3) yields,

$$\begin{aligned} K_i \Delta e_i^{total^{\Delta t}} &= K_i \Delta e_i^{e^{\Delta t}} + K_i \Delta e_i^{P^{\Delta t}} \Rightarrow K_i \Delta e_i^{e^{\Delta t}} \\ &= K_i \Delta e_i^{total^{\Delta t}} - K_i \Delta e_i^{P^{\Delta t}} \overset{A.3}{\Rightarrow} \Delta \acute{\sigma}_{\imath}{}^{\Delta t} \\ &= K_i \Delta e_i^{total^{\Delta t}} - K_i \Delta e_i^{P^{\Delta t}} \end{aligned} \tag{A.7}$$

In further expressing the plastic strain increment by means of the flow rule (A.4), this equation becomes:

$$\Delta \acute{\sigma}_{\imath}{}^{\Delta t} = K_i \Delta e_i^{total^{\Delta t}} - K_i \Delta e_i^{P^{\Delta t}} \overset{A.4}{\Rightarrow} \Delta \acute{\sigma}_{\imath}{}^{\Delta t} = K_i \Delta e_i^{total^{\Delta t}} - \lambda K_i \left(\frac{\partial g}{\partial \acute{\sigma}_{\imath}} \right) \tag{A.8}$$

In the special case of AU constitutive model, where f is the linear function of the effective stress components ($\acute{\sigma}_1$ and $\acute{\sigma}_3$), Eq. (A.6) can be expressed as:

$$f\left(\acute{\sigma}_{\imath}{}^{t} + \acute{\Delta} \sigma_{\imath}{}^{\Delta t} \right) = 0 \Rightarrow f\left(\acute{\sigma}_{\imath}{}^{t} \right) + f^{*}\left(\Delta \acute{\sigma}_{\imath}{}^{\Delta t} \right) = 0 \tag{A.9}$$

where f* represents the function f minus its constant term:

$$f^{*}(.) = f(.) - f(\underline{0}) \tag{A.10}$$

where f($\underline{0}$) represents the constant terms in the yield function.

For a stress point on the yield surface (Eq. (A.9)) after substitution of the expression Eq. (A.8) for the stress increment, it becomes

$$f^{*}\left(K_i \Delta e_i^{total^{\Delta t}} \right) - \lambda f^{*} \left[K_i \left(\frac{\partial g}{\partial \acute{\sigma}_{\imath}} \right) \right] = 0 \tag{A.11}$$

New stress components ($\acute{\sigma}_{\imath}{}^{N}$) and initial elastic stress guesses ($\acute{\sigma}_{\imath}{}^{I}$) are defined as:

$$\acute{\sigma}_{\imath}{}^{t+\Delta t^{N}} = \acute{\sigma}_{\imath}{}^{t} + \Delta \acute{\sigma}_{\imath}{}^{t+\Delta t} \tag{A.12}$$

$$\acute{\sigma}_{\iota}{}^{t+\Delta t^{I}} = \acute{\sigma}_{\iota}{}^{t} + K_i \Delta e_i^{total^{\Delta t}} \tag{A.13}$$

Note that the term $\mathrm{K_i \Delta e_i^{total^{\Delta t}}}$ in Eq. (A.13) is the component i of the stress increment introduced by the total strain increment in case no increment of plastic deformation takes place. That is the reason the Eq. (A.13) called initial guess.

An expression for λ in terms of f can be derived form Eq. (A.10) and (A.11) as follows:

$$\lambda = \frac{f\left(\acute{\sigma}_{\iota}{}^{t+\Delta t^{I}}\right)}{f\left[K_i\left(\frac{\partial g}{\partial \acute{\sigma}_{\iota}}\right)\right] - f(\underline{0})} \tag{A.14}$$

Using the expression of the stress increment, Eq. (A.8), and the definition of the elastic guess, Eq. (A.13), the new stress state can be written as:

$$\acute{\sigma}_{\iota}{}^{t+\Delta t^{N}} = \acute{\sigma}_{\iota}{}^{t+\Delta t^{I}} - \lambda K_i \left(\frac{\partial g}{\partial \acute{\sigma}_{\iota}}\right) \tag{A.15}$$

Finally, new stresses are calculated based on the following equation by combining Eq. (A.13), Eq. (A.14), and Eq. (A.15).

$$\acute{\sigma}_{\iota}{}^{t+\Delta t^{N}} = \acute{\sigma}_{\iota}{}^{t} + K_i \Delta e_i^{total^{\Delta t}} - \frac{f\left(\acute{\sigma}_{\iota}{}^{t+\Delta t^{I}}\right)}{f\left[K_i\left(\frac{\partial g}{\partial \acute{\sigma}_{\iota}}\right)\right] - f(\underline{0})} K_i \left(\frac{\partial g}{\partial \acute{\sigma}_{\iota}}\right) \tag{A.16}$$

Note that in above formula, for each time step, $\acute{\sigma}_{\iota}{}^{t}$ is the initial sress state and $\Delta e_i^{total^{\Delta t}}$ is the total strain increment for each time step. Both parameters are known in the calculations. The total strain increments are calculated from the force equiblirium equations in each time step and based on them, effective stresses are updated.